Tailoring light-matter interactions in waveguide networks for computing applications

Ross Glyn MacDonald

Supervisor: Dr. Victor Pacheco Peña
Co-supervisor: Prof. Alex Yakovlev

School of Engineering &
School of Mathematics, Statistics and Physics
Newcastle University

This dissertation is submitted for the degree of

Doctor of Philosophy

March 2024

Abstract

Computing with electromagnetic waves has, in recent years, emerged as an interesting alternative computing paradigm. This is due to the inherent high-speed (computing at the speed of light in the medium) and the potential for parallelization of electromagnetic wave-based computing systems. Multiple examples of electromagnetic wave-based structures, such as metamaterials, metasurfaces and gratings, have been proposed and demonstrated to perform computing operations. This includes the emulation of digital logic gates and the calculation of operations such as differentiation, integration and convolution.

In this PhD thesis, interconnected networks of parallel plate waveguides are exploited to enable high-speed electromagnetic wave-based computing processes. To begin with an introduction to electromagnetism, waveguides and transmission line theory is presented in chapter 1. This is followed in chapter 2 by the outline of an algorithm developed to assist in the characterisation of waveguide networks. In chapter 3, we then explore how waveguide networks may be exploited to emulate conventional computing techniques. Here, we demonstrate how by tailoring the splitting and superposition of transverse electromagnetic pulses at waveguide junctions one can compute the outputs of decision-making processes (i.e., *if… then… else…* statements). We also exploit the linear superposition of monochromatic waves within waveguide networks to emulate logic operations such as AND and OR logic gates. In chapter 4, transmission line filtering techniques will be exploited to perform m^{th} order differentiation in the time domain using the Greens function approach. This includes the calculation of fractional derivatives in which m may be a positive non-integer value. In chapter 5, it is shown how periodic networks of waveguide-based metatronic circuits may be used to calculate the solutions partial differential equations. This is done with a focus on partial differential equations in the form of the Helmholtz wave equation. Finally, chapter 6 presents a list of the main conclusions of this thesis and potential future work.

Acknowledgements

First and foremost, I would like to thank my supervisor Dr. Victor Pacheco-Peña for all the support he has provided in the past three and a half years. His insightful advice and guidance has pushed me to overcome many challenges over the course of my PhD. My gratitude also extends to my second supervisor Prof. Alex Yakovlev, who always offers a unique and profound perspective. Without this support, the completion of this project would have been a much more difficult task. I could not wish for a better supervisory team.

Secondly, I would also like to express my appreciation to my colleagues in the Metamaterials and Plasmonics Group: Wasem Al Juaid, Joseph Riley, Tony Knighley, Alex Ventisei, Will Rogers and Dr. Christian Johnson-Richards for their support and encouragement. The future may lead us on diverging paths, but I sincerely hope we meet again. We have had some unforgettable experiences with this group. From outside the PhD world, I cannot forget to mention my wonderful friends who have stuck by my side since undergrad—or even before that. I won't name names, as I might miss someone by mistake, but you know who you are. You have made these past years the best of my life.

Finally, I am forever grateful to my wonderful family and my partner Rachel. To Rachel, I have to say sorry for the long nights I spent working on this thesis. To my mother Mary, thank you for all the support over the years and for pushing me to achieve as much as I possibly can do. To my sister Fiona, thank you so much for handling so much of the family business while I have been preoccupied with the thesis. I also must give a very special thanks to my Nanna Sheila, who is undoubtably my biggest cheerleader. Though she may be too old to do the dance moves now. And finally, I would like to honour the memory of my departed family. My farther Douglas MacDonald, my poppy Ken MacDonald, my grandfather John Brown and my Oma Anna Brown. Although we can't share in this success, I hope that I have made you proud.

Declaration

I hereby declare that except where specific reference is made to the work of others, the contents of this dissertation are original and have not been submitted in whole or in part for consideration for any other degree or qualification in this, or any other university. This dissertation is my own work and contains nothing which is the outcome of work done in collaboration with others. This dissertation contains fewer than 65,000 words including appendices, bibliography, footnotes, tables and equations and has fewer than 150 figures.

Ross Glyn MacDonald

March 2024

Table of Contents

List of Figures

List of Tables

Nomenclature

EM	Electromagnetic
TL	Transmission line
PEC	Perfect electrical conductor
PPW	Parallel plate waveguides
TEM	Transverse electric-magnetic
TE	Transverse electric
TM	Transverse magnetic
MZI	Mach-Zehnder Interferometer
SOA	Semiconductor optical amplifier
ADC	Analogue to digital converter
DAC	Digital to analogue converter
FL	Focal length
GRIN	Graded-index
MOSFET	Metal-oxide-semiconductor-field-effect-transistor
QWT	Quarter-wave transformer
WPD	Wilkinson power divider
RMSE	Root mean square error
FWHM	Full width half maximum
PDE	Partial differential equation
FEM	Finite element method
PML	Perfectly matched layer
FIT	Finite integration technique

Chapter 1. Introduction

Further advancements in computational technologies are required to keep pace with modern computing requirements for speed and energy efficiency. Historically, conventional semiconductor-based computing technologies have been able to keep pace with demands[1], due to their tremendous scalability[2]. However, this is a task that is becoming increasingly challenging, as semiconductor manufacturing techniques begin to approach the atomic scales[3,4]. This has led many scientists and industry experts to suggest that new paradigms in computing are required[5–7]. Several interesting alternative computing paradigms have been presented including biological computing systems[8–10], spintronics[11,12], quantum computing systems[13–17] and advanced architectures[6,18–20], among others. One promising computing paradigm is computing with electromagnetic (EM) waves, in which calculations are performed with light instead of electrons. Some of the benefits of EM wave-based computing are an inherent high speed (computing at the speed of light in the medium) and the potential of parallel operations (associated with exploiting different wavelengths or polarizations of light[21]). In this realm, EM wave-based computing systems have been demonstrated performing digital operations such as elementary logic gates[22] and analogue computing operations[21]. These works and the methods exploited to implement them are discussed in Section 1.4 of this thesis.

The purpose of this PhD thesis is to explore how the splitting and superposition of EM signals within networks of EM waveguides may be exploited to enable EM wave-based computing operations[23–27]. To this end, this thesis will present theoretical calculations and numerical simulations of waveguide-based structures designed to implement both digital and analogue operations. This initial chapter provides the relevant background and theory, starting with an introduction to EM wave propagation within a media and wave-matter interactions. It then provides an overview of transmission line (TL) theory, which is used to model the waveguide-based structures presented throughout. It also gives an overview of metatronic circuits which are exploited in chapter 5 to design a waveguide network capable of solving partial differential equations. Finally, a summary of devices found in the literature and their operating principles is presented. This section includes a brief introduction to and history of analogue computing, with the aim to put the thesis in context.

1.1 EM Wave Propagation in Materials and Maxwell's Equations

To study how light may be exploited for computing processes, it is important to first understand how light propagates and interacts with matter. Take for example, Fig. 1.1, which shows the schematic representation of a propagating EM wave. As it can be seen, the wave consists of two fields, the electric E-field in red and the magnetic H-field in blue. The direction of propagation of the wave is calculated[28] as:

$$\boldsymbol{S} = \boldsymbol{E} \times \boldsymbol{H} \tag{1.1}$$

where $\boldsymbol{S}$ is the Poynting vector describing the direction of energy propagation. Fig. 1.1 shows an example of a linearly polarized planewave, meaning that both the $\boldsymbol{E}$ and $\boldsymbol{H}$ fields oscillate on orthogonal planes perpendicular to the direction of propagation.

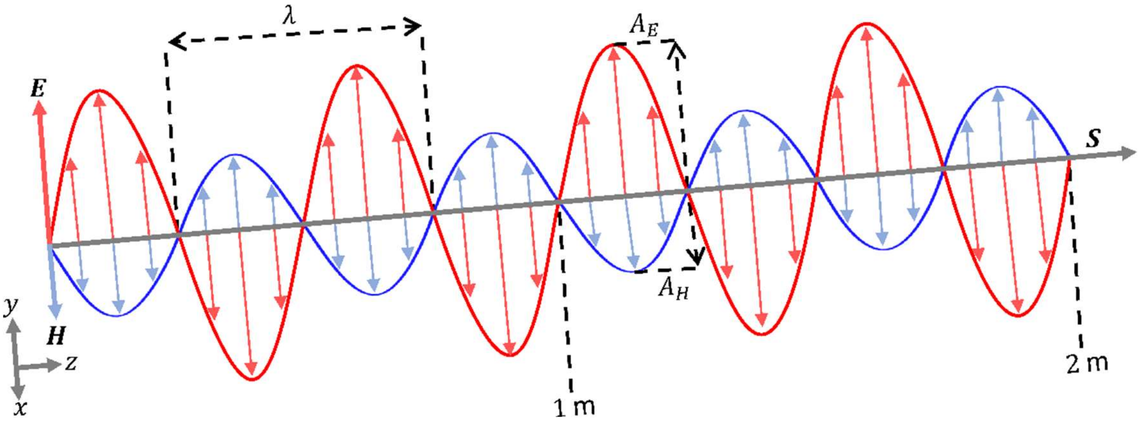

Figure 1.1 An illustration of a linearly polarized propagating EM wave.

An EM wave may be classified into different regions of the EM spectrum based on wavelength λ and common applications. For instance, radio waves, microwaves, infrared and visible are different regimes with applications in the regimes including with radio communication[29], mobile phone communication[30], thermal imaging[31], and optics[32], respectively, to name a few. Throughout this thesis, EM waves in the microwave regime will be exploited. In this realm, microwave circuits based on networks of microwave waveguides are commonly exploited to produce antennas[33], filters[34], and sensors[35], among other applications. As it will be discussed, microwave design techniques and principles may also be applied to computing systems.

1.1.1 Maxwell's Equations

In classical EM theory, light-matter interactions are described by four equations collectively referred to as Maxwell's equations[28]. These are as follows:

$$\nabla \times \boldsymbol{E} = \frac{-\partial \boldsymbol{B}}{\partial t} \tag{1.2a}$$

$$\nabla \times \boldsymbol{H} = \frac{\partial \boldsymbol{D}}{\partial t} + \boldsymbol{J} \tag{1.2b}$$

$$\nabla \cdot \mathbf{D} = \rho_f \tag{1.2c}$$

$$\nabla \cdot \mathbf{B} = 0 \tag{1.2d}$$

where $\boldsymbol{B}$, $\boldsymbol{D}$ and $\boldsymbol{J}$ are the magnetic flux density, electric displacement field and current density vectors, respectively. ρ_f is the free charge density and t is time. Eq. 1.2a and Eq. 1.2b are Faraday's and Ampère's laws, respectively. They describe the induction of an electric/magnetic field due to a time varying magnetic/electric field and the generation of a magnetic field due to an electrical current. Eq. 1.2c and Eq. 1.2d are Gauss's law for electricity and magnetism. Eq. 1.2c describes the generation of electric fields due to electrical charge while Eq. 1.2d describes the absence of magnetic sources and sinks, i.e., the absence of magnetic charge.

As light interacts with a material, new sources of $\boldsymbol{E}$ and $\boldsymbol{B}$ are generated in that material as the atoms and molecules within them become polarized and magnetized by the external fields. This is expressed as:

$$\boldsymbol{D} = \varepsilon_0 \boldsymbol{E} + \boldsymbol{P} = \varepsilon_0 (1 + \chi_e) \boldsymbol{E} \tag{1.3a}$$

$$\boldsymbol{B} = \mu_0 \boldsymbol{H} + \boldsymbol{M} = \mu_0 (1 + \chi_m) \boldsymbol{H} \tag{1.3b}$$

where $\boldsymbol{P}$, $\boldsymbol{M}$ are the polarization and magnetization vectors, χ_e, χ_m are the electric and magnetic susceptibilities of the material and ε_0, μ_0 are the permittivity and permeability of free space, respectively ($\varepsilon_0 = 8.854 \times 10^{-12}$ F/m, $\mu_0 = 4\pi \times 10^{-7}$ H/m). Eq. 1.3 describes the scenario where light is interacting with a linear isotropic material, meaning that only the first order susceptibility terms are significant. In this scenario, it is typical to rewrite Eq. 1.3 as follows:

$$\boldsymbol{D} = \varepsilon_0 \varepsilon_r \boldsymbol{E} = \varepsilon \boldsymbol{E} \tag{1.4a}$$

$$\boldsymbol{B} = \mu_0 \mu_r \boldsymbol{H} = \mu \boldsymbol{H} \tag{1.4b}$$

where ε_r and μ_r are the relative permittivity and permeability values of the material given by $\varepsilon_r = (1 + \chi_e)$ and $\mu_r = (1 + \chi_m)$. Eq. 1.4 is still commonly used to describe the response of non-linear materials[36,37], such as active media[38–40] or materials with a high third order Kerr susceptibility[41–44]. However, when modelling non-linear materials ε_r and μ_r are no longer independent of the applied $\boldsymbol{E}$ and $\boldsymbol{H}$, fields. Furthermore, anisotropic media may also be described by Eq. 1.4, if ε_r and μ_r are rewritten as tensors[28,30]. In fact all materials will exhibit some level of non-linearity and anisotropy, however in most cases these effects are negligible and the material may be approximated as linear and isotropic. Additionally, most natural materials (and all those considered in this thesis) are non-magnetic, meaning that it is the permittivity which dominates the response of a material, i.e. $\mu_r = 1$.

1.1.2 Material and structural dispersion

The EM properties of a material (ε_r, μ_r) are determined by the interaction of an incident wave with various material resonances. Different models may be used to describe the variation of ε_r, depending on the type of material and the resonances present within it. For instance, the Lorentz model is commonly used to describe the EM response of dielectrics[45]. In this model, bound electrons within atoms are modelled as damped harmonic oscillators with the applied EM signal as an external force. The relative permittivity of this model is as follows[46]:

$$\varepsilon_r(\omega) = \varepsilon_\infty + \omega_p^2 \sum_a \frac{f_a}{\omega_{0,a}^2 - \omega^2 - i\omega\gamma_a} \tag{1.5}$$

where ω_p, ε_∞ is the plasma frequency and high frequency permittivity of the material and $\omega_{0,a}$, γ_a, f_a are the resonant frequency, damping frequency, and oscillator strength of the ath resonance in the material. Throughout this thesis, dielectrics will be used in the microwave frequency regime. This regime is far from the material resonances discussed above. Using Eq. 1.5, it can be seen that at frequencies far from material resonances, dielectrics are transparent materials with low losses.

At low frequencies (below the plasma frequency of metals[47], generally <10THz) metals may be characterized by a finite conductivity σ, which describes the relationship between an electric field and the current density inside the metal via Ohms law:

$$\boldsymbol{J} = \sigma\,\mathbf{E} \tag{1.6}$$

Substituting Eq. 1.6 into Eq. 1.2, the complex permittivity of a metal is expressed as:

$$\varepsilon_r = 1 + i\frac{\sigma}{\omega\varepsilon_0} \tag{1.7}$$

One of the consequences of Eq. 1.7 is that, due to the highly conductive nature of metals at low frequencies, the permittivity is dominated by the imaginary (lossy) component. This means that waves cannot penetrate far into a metal as they quickly decay, characterized by the skin depth $\delta = \sqrt{2/(\omega\mu_0\mu_r\sigma)}$. At these frequencies (<10 THz) it is often convenient to treat a metals as "perfect electric conductors" (PEC), meaning a material with infinite conductivity. In this scenario the incident field may not penetrate the metal at all and is thus be entirely reflected at the boundary. This approximation is not valid at higher frequencies[48,49] (approaching and above the plasma frequency of the metal, generally >10 THz) as metals become transparent. In this realm a metal may instead be described by the Drude model[50,51]:

$$\varepsilon_r = 1 - \frac{\omega_p^2}{\omega^2 + i\gamma\omega} \tag{1.8}$$

In practice, materials with intricate permittivity functions, such as gold[52], may be modelled by a combination of Eq. 1.5 and Eq. 1.8 referred to as the Drude-Lorentz model[52].

The models presented in Eq. 1.5 and Eq. 1.7 described the EM response of a natural material. In this scenario, the values of ε_r and μ_r are determined by the arrangement of atoms and molecules within the material (See Fig. 1.2A). Similar principles can also be used to describe a structural response, where effective EM properties (ε_{reff}, μ_{reff}) are instead determined by the materials and geometry of the structure. One of the first examples of effective materials were artificial dielectrics[53–55] which exploited metallic obstacles to tailor the permittivity value of a structure. In later works, the introduction of metamaterials (artificial media whose EM properties may be controlled to achieve EM responses not easily available in nature) would extend this control to the permeability, without the need for magnetic materials[56]. To do this, metamaterials exploit a periodic (or sometimes aperiodic) arrangement of subwavelength structures, called meta-atoms. Due to the small size (compared to the wavelength of the incident signal) and high density of the meta-atoms, an incident wave does not see the individual meta-atoms. Instead, when it interacts with the structure it sees a homogenised material with effective values of ε_r and μ_r ($\varepsilon_{r,eff}$ and $\mu_{r,eff}$). A schematic example of the difference between natural and artificial media is presented in Fig. 1.2, showing how for a natural material with permittivity and permeability values ε_r and μ_r, an effective medium may be designed to produce the same effective response ε_{reff} and μ_{reff}.

The first example of a metamaterial with a magnetic response ($\mu_r \neq 1$) was the split-ring-resonator[56]. One interesting feature of this structure is that it was shown to exhibit an effective negative permeability at a designed frequency. Shortly thereafter a combination of conducting rods and split-ring-resonator meta-atoms would be exploited to design a metamaterial with simultaneously negative permittivity and permeability[57]. These structures are referred to a double negative[58] or left-handed[59] materials and possess some extraordinary features not seen in natural media. These include negative refraction[60,61] and backwards waves[62]. In the context of EM wave-based computing, metamaterials and other effective media structures have been exploited in the literature due to the arbitrary control they enable over the propagation of light in both space and time[63–68]. A discussion of the application of metamaterials to EM wave-based computing systems is presented in Section 1.4 of this thesis.

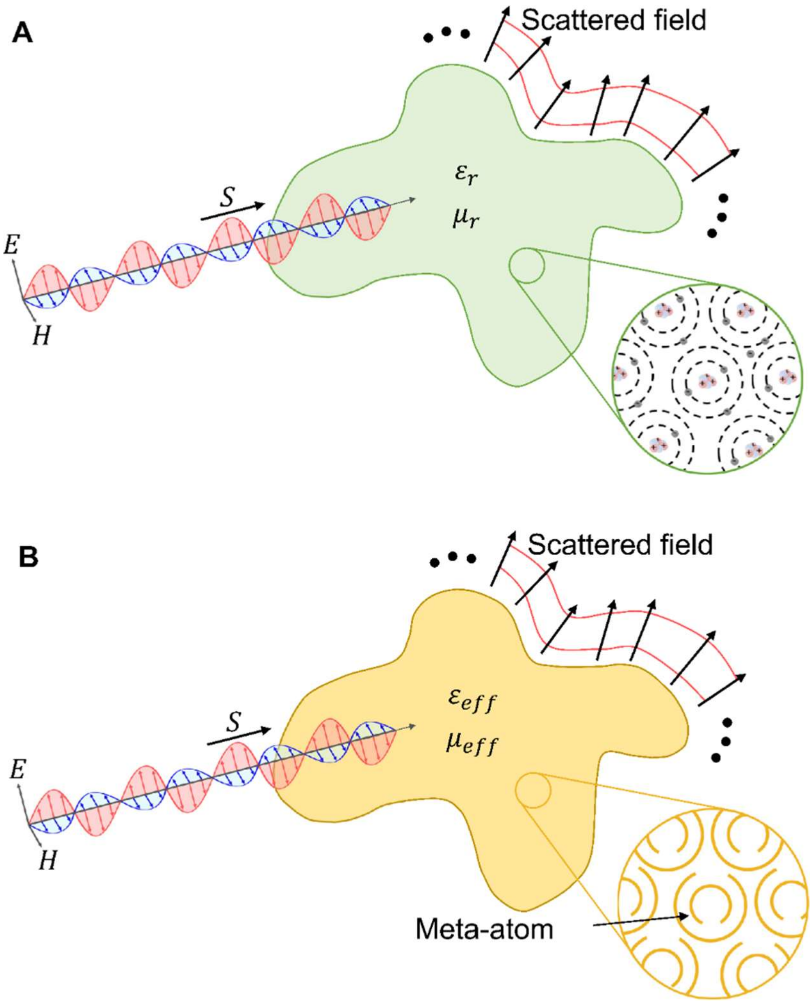

Figure 1.2 Schematic representation of the differences between **A** natural media and **B** effective media. **A.** An EM wave interacts with an arbitrarily shaped obstacle with natural EM properties ε_r and μ_r to produce a scattered field. **B.** Same scenario as in **A** now with a metamaterial constructed from a periodic arrangement of meta-atoms. This hypothetical structure has effective EM properties $\varepsilon_{r,eff}$ and $\mu_{r,eff}$, producing the same scattered field as in **A**.

1.2 Introduction to Waveguides and Transmission Lines

Waveguides and TLs are an incredibly important technology allowing for the low-loss transmission of power from one location to another[30,69]. This is done by confining the EM waves within the waveguide such that it follows the path of the waveguide though space. Throughout this thesis, waveguides modelled as TLs will be exploited extensively to perform EM wave-based computing operations. In this section, the main properties of waveguides, TLs and the methods used to model them are described.

1.2.1 The lumped element model of a TL

The propagation of waves within waveguides may be analysed and understood using TL theory where a section of waveguide is represented by an equivalent circuit of lumped elements[30,69]. The primary difference between circuit theory and TL theory is the scale of the system being modelled. Circuit theory considers electrically small elements, such that the phase variation of signals across the elements is almost negligible. On the other hand, waveguides are typically comparable in size to the wavelength of the signals within them, and therefore the phase variation must be considered.

In TL theory, this is achieved by using distributed circuit elements: resistance R, inductance L, capacitance C and conductance G, which are now per unit length parameters[30,70]. This can be seen in Fig. 1.3 in which a small section (length Δz) of an electrically large hypothetical waveguide, modelled as an ideal TL (Fig. 1.3A), is represented by the equivalent circuit shown in Fig. 1.3B. This representation is valid so long as the Δz is chosen to be sufficiently smaller than the wavelength of the signal within the waveguide ($\Delta z \ll \lambda$ where λ is the wavelength inside the waveguide filling medium). The waveguide as a whole is then modelled by considering multiple of these circuits periodically arranged in a line, as is shown in Fig. 1.3C. Considering Kirchhoff's laws[71] for the splitting of current in the circuit, the equations for the voltage and current in this circuit are written as follows:

$$V(z,t) - R\Delta z I(z,t) - L\Delta z \frac{\partial I(z,t)}{\partial t} - V(z+\Delta z) = 0 \tag{1.8a}$$

$$I(z,t) - G\Delta z V(z+\Delta z,t) - C\Delta z \frac{\partial V(z+\Delta z,t)}{\partial t} - I(z+\Delta z,t) = 0 \tag{1.8b}$$

where $V(z,t)$ and $I(z,t)$ are the voltage and current values at position z along the TL at time t.

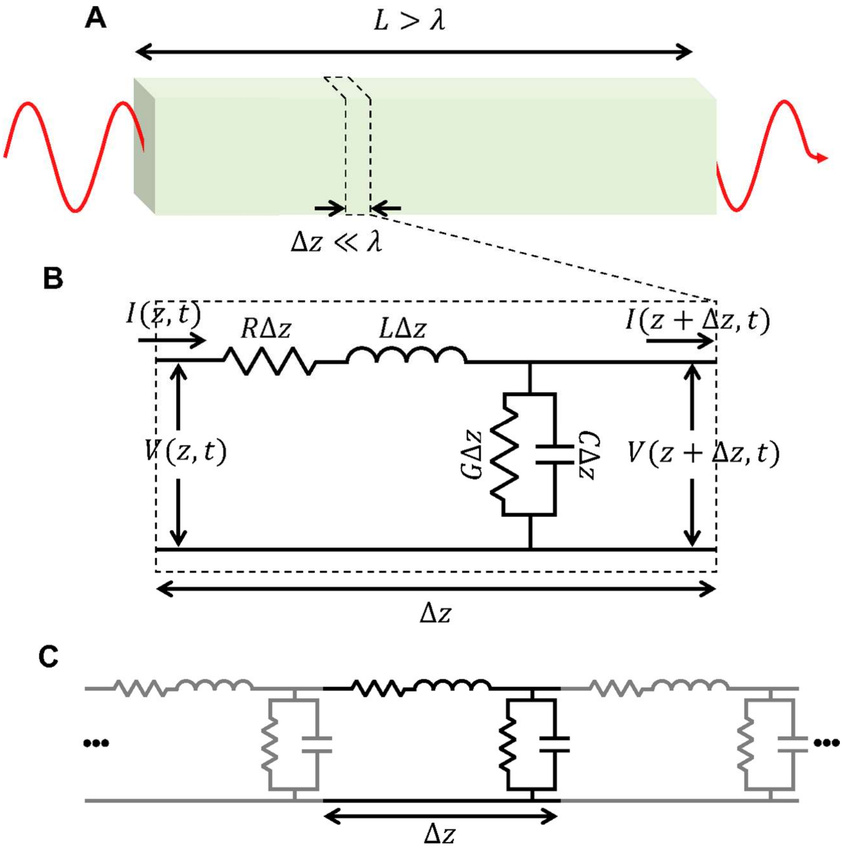

Figure. 1.3 Lumped element representation of a transmission line. **A.** An electrically long section of waveguide with a propagating wave. **B.** Circuit theory representation of the highlighted section of waveguide in **A**. **C.** Schematic showing how the circuits shown in **B** may be connected in a row to model the entire waveguide shown in **A**.

1.2.2 Wave propagation on a TL

One of the main uses of TL theory is to model the propagation of waves within waveguides. This is done by drawing an analogy between the solutions to Eq. 1.8 and Eq. 1.2, when certain restrictions are applied[70]. Consider the consequences of Eq. 1.8 in the limit when Δz approaches 0. In this scenario, Eq. 1.8 may be represented as a system of linear differential equations, known as the *telegrapher's equations* in space and time. For signals with a simple harmonic time dependence $e^{-i\omega t}$ this may then be rewritten as follows[30]:

$$\frac{\partial^2 V(z)}{\partial z^2} - \gamma^2 V(z) = 0 \tag{1.9a}$$

$$\frac{\partial^2 I(z)}{\partial z^2} - \gamma^2 I(z) = 0 \tag{1.9b}$$

where γ is the complex propagation constant of the medium. γ is expressed as:

$$\gamma = \alpha - i\beta = \sqrt{(R - i\omega L)(G - i\omega C)} \tag{1.10}$$

where α and β are the attenuation, and propagation constants of the TL, respectively. Solutions to Eq. 1.9 can be written as a superposition of two traveling waves:

$$V(z) = V^{+}e^{-\gamma z} + V^{-}e^{\gamma z} \tag{1.11a}$$

$$I(z) = I^{+}e^{-\gamma z} + I^{-}e^{\gamma z} = \frac{1}{Z}(V^{+}e^{-\gamma z} + V^{-}e^{\gamma z}) \tag{1.11b}$$

where the $+, -$ superscripts indicate a wave traveling from negative to positive z (referred to a right to left) and vice versa. Z is the characteristic impedance of the waveguide defined as:

$$Z = \sqrt{\frac{R - i\omega L}{G - i\omega C}} \tag{1.12}$$

which describes the relation between the voltage and current for a single traveling wave at any given point along the TL ($V = ZI$). From Eq. 1.11 it can be seen that α and β describe the amplitude loss and phase change of a wave as it propagates along the TL. Eq. 1.9-1.12 are used to model EM wave propagation problems by drawing an analogy between field quantities/EM properties and elements of circuit theory[70]. In this realm, the $\boldsymbol{E}$ and $\boldsymbol{H}$-fields are analogous to the voltage V and current I on the line. The permittivity $\varepsilon_r\varepsilon_0$, permeability $\mu_r\mu_0$, conductivity σ and intrinsic impedance η of the material are analogous to the distributed capacitance C, distributed inductance L, distributed conductivity G and characteristic impedance Z, respectively. Waves propagate along TLs at the phase velocity of the TL $v_p = \omega/\beta$ which for lossless TLs may be reduced to $v_p = 1/\sqrt{LC} = 1/\sqrt{\varepsilon_r\varepsilon_0\mu_r\mu_0}$ i.e., the speed of light in the medium. If the TL is also dispersionless (meaning that L, C, R and G do not vary with frequency) then v_p is the same for all frequencies. However, in general R, G, C and L will be frequency dependent quantities. In this scenario, different frequency components of a signal will travel at different velocities along the TL, potentially leading to a distortion[72]. In this scenario the overall propagation of the wave packet is instead described by the group velocity as $v_g = \partial\omega/\partial\beta$.

In TL theory, reflections are produced when a wave on the TL encounters a change in impedance, for instance at a mismatched load or at a boundary with another TL or medium. For a simple boundary where an input wave encounters a load the reflection coefficient is calculated as:

$$\Gamma = \frac{Z_1 - Z_L}{Z_1 + Z_L} \tag{1.13}$$

where $V^- = \Gamma V^+$ for a rightward traveling input signal and $Z_{1,L}$ is the impedance of the input TL and load, respectively. One of the advantages of modelling waveguides (and other systems) as TLs is that complex systems of many interactions may be represented by an equivalent circuit which is comparably simpler to solve analytically. This can be done by reducing the equivalent circuit into a single impedance Z_{in} which is seen by the input wave in the steady state. Consider for instance, the scenario presented in Fig. 1.4A. Here a plane wave propagating to the right inside a vacuum ($\varepsilon_r = \mu_r = 1$) encounters a dielectric slab of finite thickness. Even this comparably simple case will produce multiple reflections as signals bounce between the two vacuum-dielectric boundaries. In this scenario, the total steady state reflection and transmission may be calculated by considering the infinite sum of signals at either interface. However, for larger systems this may be a challenging task. Using TL theory, the total reflection in steady state is instead calculated by considering the total input impedance seen when looking into the system. This impedance is as follows:

$$Z_{in} = Z_0 \frac{Z_L - iZ_0 \tan{(\beta L)}}{Z_0 - iZ_L \tan{(\beta L)}} \tag{1.14}$$

where β,L is the propagation constant and length in the direction of propagation of the slab, respectively. In the scenario Z_L is the impedance of the load at the end of the slab (i.e. $Z_L = Z_0$) and the total reflection is calculated by substituting Eq. 1.14 into Eq. 1.13 with Z_L in Eq. 1.13 as Z_{in} in Eq. 1.14.

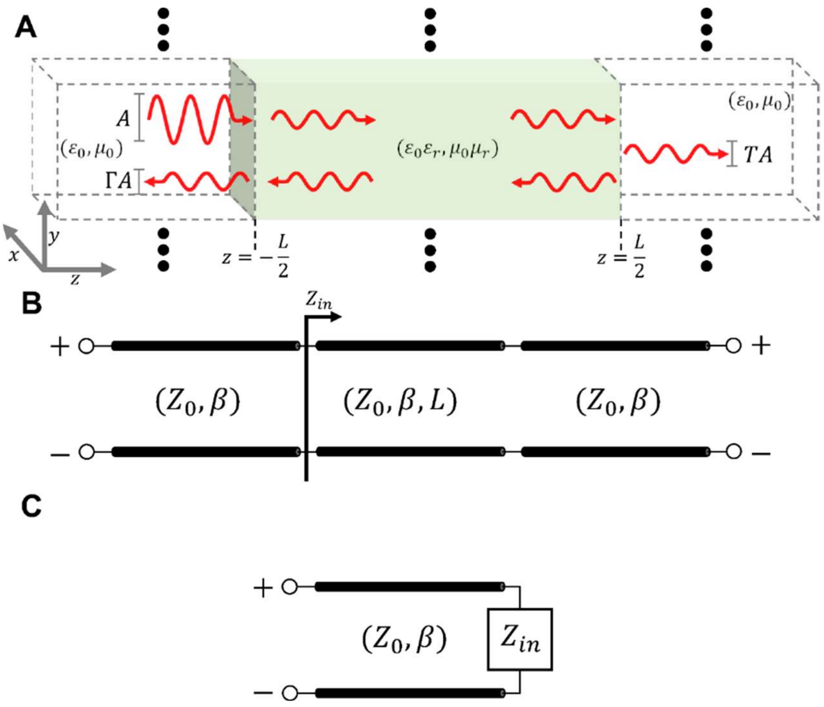

Figure. 1.4 Transmission and reflection in TL theory. **A.** Signal interacting with a dielectric slab in a vacuum, dielectric, vacuum system. The signal arrives from the left producing multiple reflections within the slab as well as an overall reflection and transmission to the left and right respectively. **B.** TL representation of the scenario depicted in **A**. **C.** reduction of the three TL system in **B** down to a single input impedance Z_{in}. Z_{in} encompasses the entire structure right of the arrow in **B**.

1.2.3 Propagating waveguide modes

In waveguides, propagating waves are confined within a finite number of guided modes. The nomenclature regarding guided modes references the component of light which is perpendicular to the direction of propagation. Consider for instance, parallel plate waveguides (PPWs), which will be used throughout this project (see Fig. 1.5A for a schematic representation). The fundamental mode of this structure is a TEM mode in which the $\boldsymbol{E}$-field spans the distance between the two metallic plates and the $\boldsymbol{H}$-field is oriented parallel along the transverse plane. This mode is classified as a TEM mode as both the $\boldsymbol{E}$ and $\boldsymbol{H}$-fields are simultaneously oriented perpendicular to the direction of propagation[73]. PPWs can also support TE_m and TM_m modes, where m is the mode number, in which the $\boldsymbol{E}$-field (TE_m) and $\boldsymbol{H}$-field (TM_m) are individually oriented perpendicular to the direction of propagation, but not simultaneously. A schematic representation of the TEM, TE_1 and TM_1 modes[73] of a PPW is presented in Fig. 1.5. Here the real component of the guided mode is presented at positions $\lambda/4$, $2\lambda/4$, $3\lambda/4$ and λ along the PPW, in the direction of propagation (see Fig. 1.5A). In this instance, λ is the wavelength of the mode being displayed.

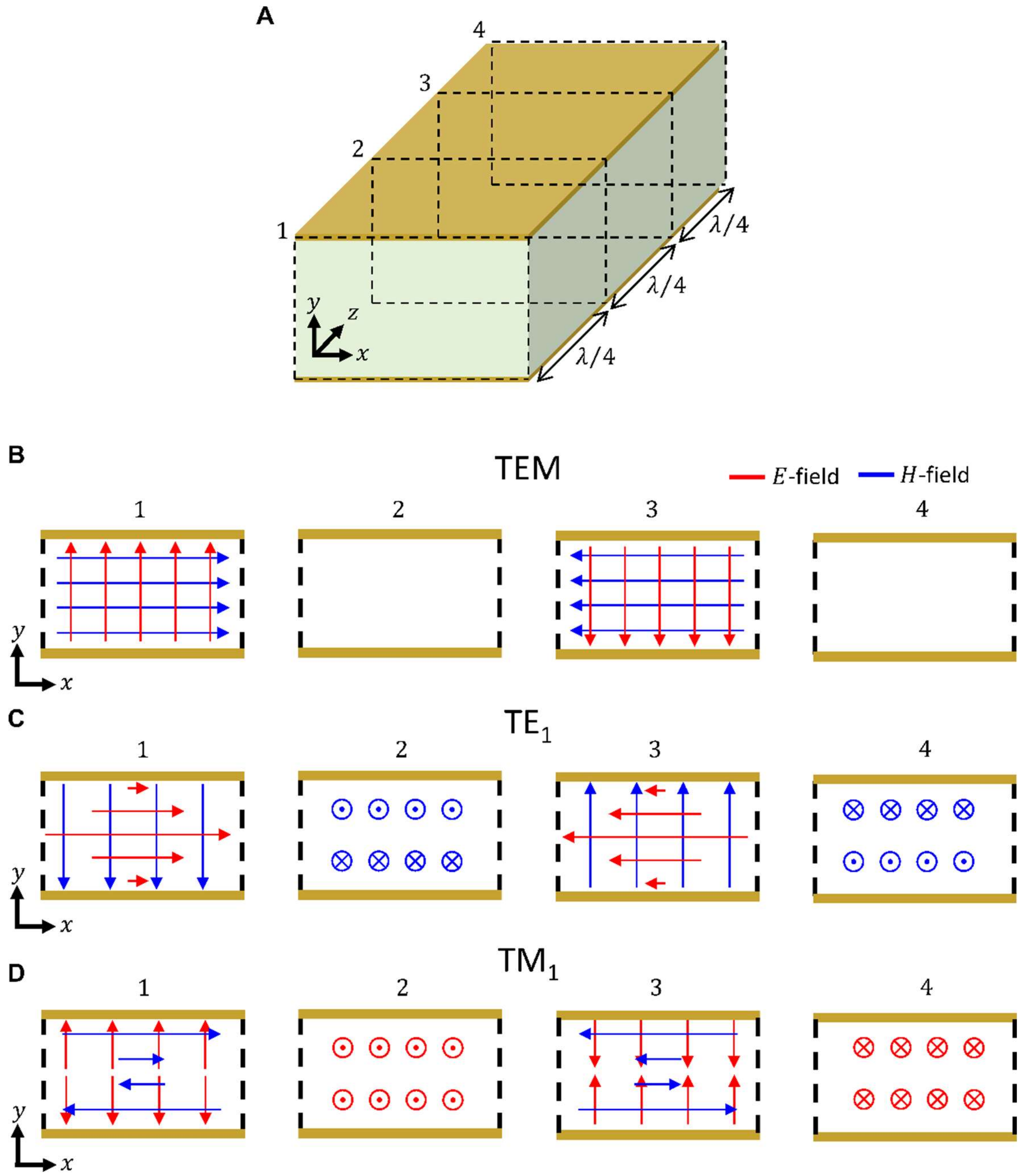

Figure. 1.5 Waveguide modes in a PPW. **A.** Schematic representation of a PPW with xy transversal plane and z propagation direction. **B.**, **C.**, **D.** TEM, TE_1 and TM_1 modes of a PPW sampled at the four positions highlighted in **A**.

In a PPW a wave may propagate in the TEM mode for all frequencies, however the TE_m and TM_m modes have an associated cutoff wavenumber below which they are evanescent[30]. This is as follows[30]: $k_c = m\pi/h$, where k_c is the wavenumber of the cutoff frequency and h is the separation between the metallic plates. Note that for PPWs this is the same for both TE and TM modes, however this is not the case for other structures. Additionally TE_m and TM_m modes are dispersive with a propagation constant of $\beta = \sqrt{k^2 - k_c^2}$, a fact which has been exploited in rectangular waveguides to produce an effective epsilon-near-zero response[74], when operating near the cutoff frequency. This can lead to the distortion of signals as they propagate along the waveguides, a feature which is often undesirable for computing purposes[75]. The PPWs used throughout this thesis are designed with $h \ll \lambda$. This is primarily to ensure the perfect splitting of signals at the junctions between waveguides[76,77], however it has the additional consequence that only the TEM mode is supported within the operating frequency range.

1.2.4 The ABCD matrix method

One method for modelling TLs which will be exploited throughout this thesis is the ABCD matrix method[30,78–80]. An ABCD matrix is defined as a 2×2 matrices which describe the relationship between voltages and currents at two ports in a system, port 1 and 2 respectively (see Fig. 1.6A), as follows:

$$\begin{pmatrix} V_1 \\ I_1 \end{pmatrix} = \begin{pmatrix} A & B \\ C & D \end{pmatrix} \begin{pmatrix} V_2 \\ I_2 \end{pmatrix} = \boldsymbol{ABCD} \begin{pmatrix} V_2 \\ I_2 \end{pmatrix} \tag{1.15}$$

where $\boldsymbol{ABCD}$ is the ABCD matrix with the matrix components A, B, C and D in positions $(1,1)$, $(1,2)$, $(2,1)$ and $(2,2)$ of $\boldsymbol{ABCD}$, respectively. $V_{1,2}$ and $I_{1,2}$ are the voltages and currents at ports 1 and 2, respectively. ABCD matrices may be used to model a wide range of two port EM systems, including electrical circuits, metatronic circuits and TLs. In this present thesis the ABCD matrix terms of specific systems will be presented as they become relevant, however the ABCD matrix representation of a TL will be used ubiquitously throughout. They are defined as follows[30]:

$$A = \cos(\beta L) \tag{1.16a}$$

$$B = -iZ\sin(\beta L) \tag{1.16b}$$

$$C = \frac{-i\sin(\beta L)}{Z} \tag{1.16c}$$

$$D = cos\,(\beta L) \tag{1.16d}$$

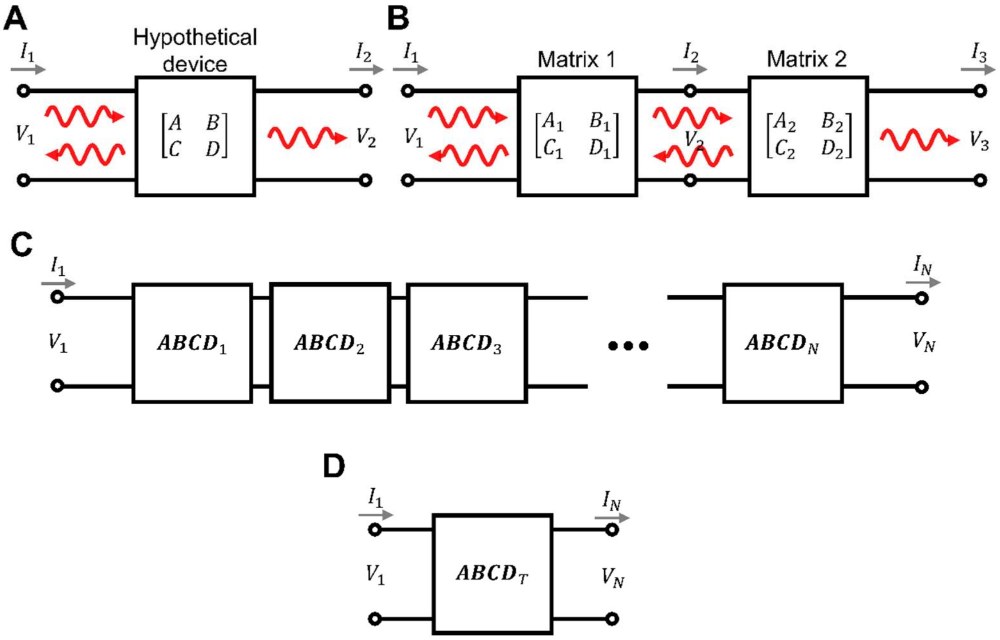

Figure. 1.6 Principles of ABCD matrices. **A.** An ABCD matrix representing a hypothetical device. **B.** Schematic showing how ABCD matrices may be connected. Here the right output of matrix 1 becomes the left input of matrix 2 and vice versa. **C.** Schematic showing how an arbitrary number of ABCD matrices may be cascaded together to describe complex systems. **D.** Reduced ABCD matrix form of the scenario presented in **C.**

for a segment of TL with length L, characteristic impedance Z and propagation constant β. For the PPWs considered throughout this thesis the characteristic impedance is calculated as follows:

$$Z = \frac{d}{h}\sqrt{\frac{\mu_r\mu_0}{\varepsilon_r\varepsilon_0}} \tag{1.17}$$

where d is the width of the parallel plate waveguides in the transverse plane and ε_r, μ_r are the permittivity and permeability of the waveguide filling material.

One benefit of the ABCD matrix method is the ability to cascade the ABCD matrices of individual systems/devices, in doing so producing a new ABCD matrix which describes the combined system. Consider for example, as two connected hypothetical devices described by $\boldsymbol{ABCD}_1$ and $\boldsymbol{ABCD}_2$, respectively. There are 3 position of interest inside this network (see Fig. 1.6B); positions 1 and 3 are inputs/outputs into $\boldsymbol{ABCD}_1$ and $\boldsymbol{ABCD}_2$, respectively, while position 2 is an input/output of both. The ABCD matrix of the combined structure is then found using Eq. 1.16 substituting $\boldsymbol{ABCD}_2$ to eliminate the terms describing the voltage and current at position 2 as:

$$\begin{pmatrix} V_1 \\ I_1 \end{pmatrix} = \begin{pmatrix} A_1 & B_1 \\ C_1 & D_1 \end{pmatrix} \begin{pmatrix} A_2 & B_2 \\ C_2 & D_2 \end{pmatrix} \begin{pmatrix} V_3 \\ I_3 \end{pmatrix} \tag{1.18}$$

where $A_{1,2}$, $B_{1,2}$,$C_{1,2}$ and $D_{1,2}$ are the matrix elements of $\boldsymbol{ABCD}_1$ and $\boldsymbol{ABCD}_2$, respectively. If multiple devices are connected, the overall response of the system is then found via repeated application of Eq. 1.18. Take for example, Fig. 1.6C, where N arbitrary devices, each described by an ABCD matrix $\boldsymbol{ABCD}_a$ with $a = 1,2,\ldots N$, are connected. The matrix which describes the overall system $\boldsymbol{ABCD}_T$ is:

$$\boldsymbol{ABCD}_T = \prod_{i}^{N} \boldsymbol{ABCD}_i \tag{1.19}$$

1.2.5 The scattering matrix

Throughout this present thesis, networks of waveguides interconnected together at junctions will be discussed. At these intersections, waveguides will intersect to form T, X or star shaped junctions, to name a few[76,77,81–83]. The input and output signals at the each of the waveguides of these junctions are x_a and y_a, respectively, where $a = 1,2,\ldots,N$ as the input waveguide for a junction constructed from N waveguides. In the TL representation of this system each waveguide is represented by a TL. The scattering and superposition of input signals from and between these TLs can be described by the scattering matrix $\boldsymbol{A}$ as[23]:

$$\boldsymbol{y} = \boldsymbol{A}\boldsymbol{x}^T \tag{1.20}$$

where $\boldsymbol{y} = [y_1,y_2,\ldots,y_N]^T$, $\boldsymbol{x} = [x_1,x_2,\ldots,x_N]$ are the vectors containing the output/input signals respectively and T as a superscript indicates the transpose operation. The matrix elements of $\boldsymbol{A}$ are $A_{b,a}$ with $A_{b,a} \in \mathbb{C}$ and $b = 1,2,\ldots, N$. They describe the scattering towards waveguide b from waveguide a. Similarly to the ABCD matrices for individual transmission lines, $\boldsymbol{A}$ can be considered as a black box which describes the relationship between input and output signals of a system but provides no information about the interaction of signals inside. Likewise, one can envision a scattering matrix which describes the inputs and outputs of any arbitrary N input/output system, such as a network of multiple interconnected waveguide junctions (see Fig. 1.7).

In a real scenario, the physics of the system being modelled must inform the values of A_{ji}, meaning they are not independent quantities[30]. For instance, if a system contains no active or non-reciprocal materials, as is the case for the waveguides and junctions considered in this thesis the following condition is also imposed[30]:

$$A_{ji} = A_{ij} \tag{1.21}$$

onto the possible values of the scattering matrix. Additionally, if the system is lossless the matrix must be unitary to represent the conservation of total energy, imposing a further condition:

$$\boldsymbol{A}^T \boldsymbol{A}^* = \boldsymbol{I} \tag{1.22}$$

where $\boldsymbol{A}^*$ indicated the complex conjugate of $\boldsymbol{A}$ and $\boldsymbol{I}$ is the $N \times N$ identity matrix.

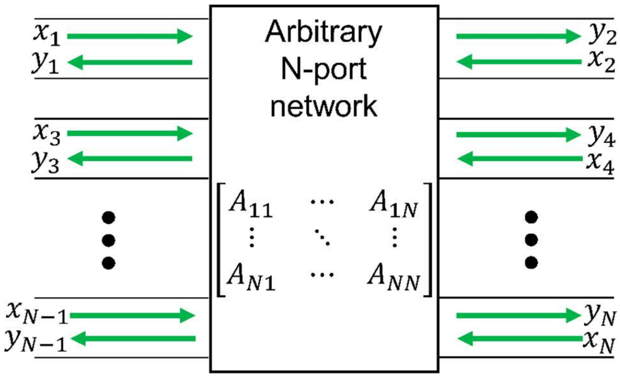

Figure. 1.7 Schematic representation of an N input/output system represented by an $N \times N$ scattering matrix.

1.2.6 Splitting and superposition at series and parallel waveguide junctions

Throughout this thesis junctions between PPWs are exploited in two configurations, parallel and series[23–25,84]. To illustrate the difference between these two scenarios, examples of junctions between 4 waveguides are presented in Fig. 1.8. First consider the parallel connection, as seen in Fig. 1.8A. In this configuration, the PPWs are oriented such that the metallic waveguides are above and below the junction plane, running parallel to it. This means that at the junction, the each of the top plates connect, forming a metallic cross shape, and likewise for the bottom plates. On the other hand, in the series configuration, seen in Fig. 1.8B, the metallic plates are orientated at either side of the waveguide, perpendicular to the junction plane. At the waveguide junction each plate connects to a single plate from an adjacent waveguide only, forming four L shaped corners.

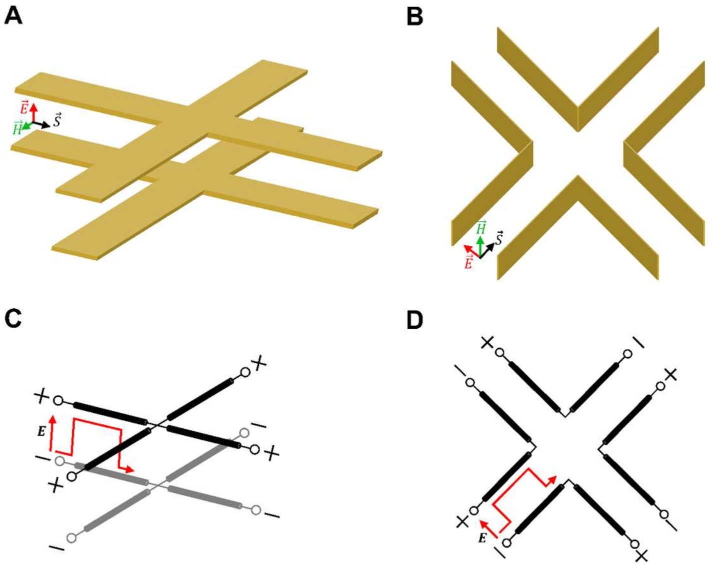

Figure. 1.8 A., **B.** Parallel and series junctions constructed from four PPWs. **C.**, **D.** TL representations of the structures shown in **A**, **B**.

Now consider for example, a single square incident pulse using the TEM mode arriving at the junction from one of the waveguides. The ideal TL representation of this scenario for the parallel and series configurations, is presented in Fig. 1.8C,D, respectively. This is a valid representation of the waveguide junction, provided that the junction is small enough compared to the wavelengths contained within the incident signal[26,76] to consider it as a perfect splitter. This pulse is assigned a polarity $+/-$ determined by the direction of the E-field component. In the parallel configuration, a pulse is assigned $+$ polarity if the E-field is pointed out of the junction plane and – if it is into it (see Fig 1.9a,c respectively). For the series configuration, the E-field is now in-plane with the junction[23–25,84]. In this case, polarity is assigned by looking at the direction of the E-field from above the junction. Here, one can envision a hypothetical circle, centred at the middle of the waveguide junction, extending out to the middle of the pulse such that the E-field component of pulse is tangential to this circle. Pulses with E-field pointed clockwise/anti-clockwise around the circle are then assigned $+/-$ polarity respectively[24,25,84] (see Fig. 1.9 B,D respectively).

As the incident pulse encounters the junction it is split, transmitted, and reflected at the junction, based on the material characteristics and geometry of the waveguides (characteristic impedance Z_0 in the TL representation). From TL theory, the scattering matrix components for this interaction in the parallel case are calculated as follows:

$$A_{ba} = \frac{2}{\sqrt{Z_a Z_b}\sum_{c=1}^{N}\frac{1}{Z_c}} - \delta_{ba} \tag{1.23}$$

where δ_{ji} is the Kronecker delta. And for the series case as:

$$A_{ba} = \delta_{ba} - \frac{-2\sqrt{Z_a Z_b}}{\sum_{c=1}^{N} Z_c} \tag{1.24}$$

From Eq. 1.23-1.24, as the pulse interacts with the junction N new outward traveling pulses are generated, one per waveguide with polarity and magnitude determined by Eq. 1.23 and Eq. 1.24.

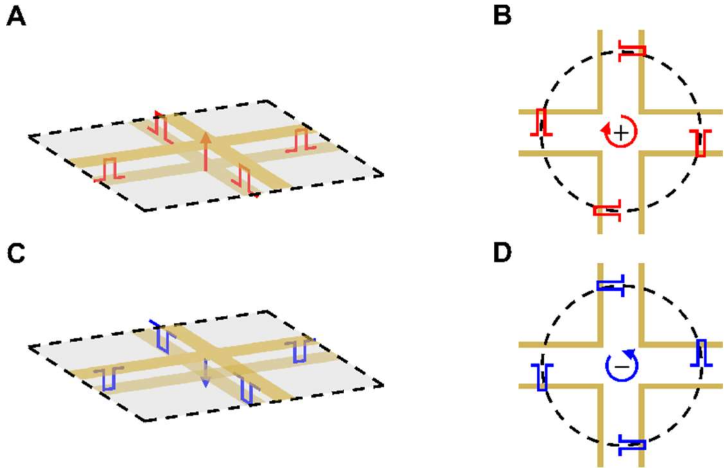

Figure. 1.9 Definition of pulse polarity in parallel and series waveguide junctions. **A.**, **C.** positive and negative polarity, respectively in parallel junctions. **B.**, **D.** positive and negative polarity, respectively in series junctions.

1.2.7 Perfect splitting with equal impedance waveguides

One special case occurs when all waveguides connected at the junction have the same materials and cross-section, meaning the characteristic impedance of the waveguides is the same. In this scenario, when a monochromatic source is applied from one of the input waveguides, the junction can be thought of as a radiating dipole with an equal amplitude signal supplied to each connected waveguide[76]. This is referred to as *perfect splitting* and has been recently exploited to perform fundamental computing operations such as the switching and routing of information[23–25,84,85], or the construction of resonant guided wave networks[77,82,83]. In this context, the concept of *perfect splitting* is different than power dividers[86,87] where an incident signal is transmitted from one port to many without reflections. Indeed, here the reflection of signals at a *perfect splitting* waveguide junction is exploited to perform switching as will be shown in Fig. 1.12

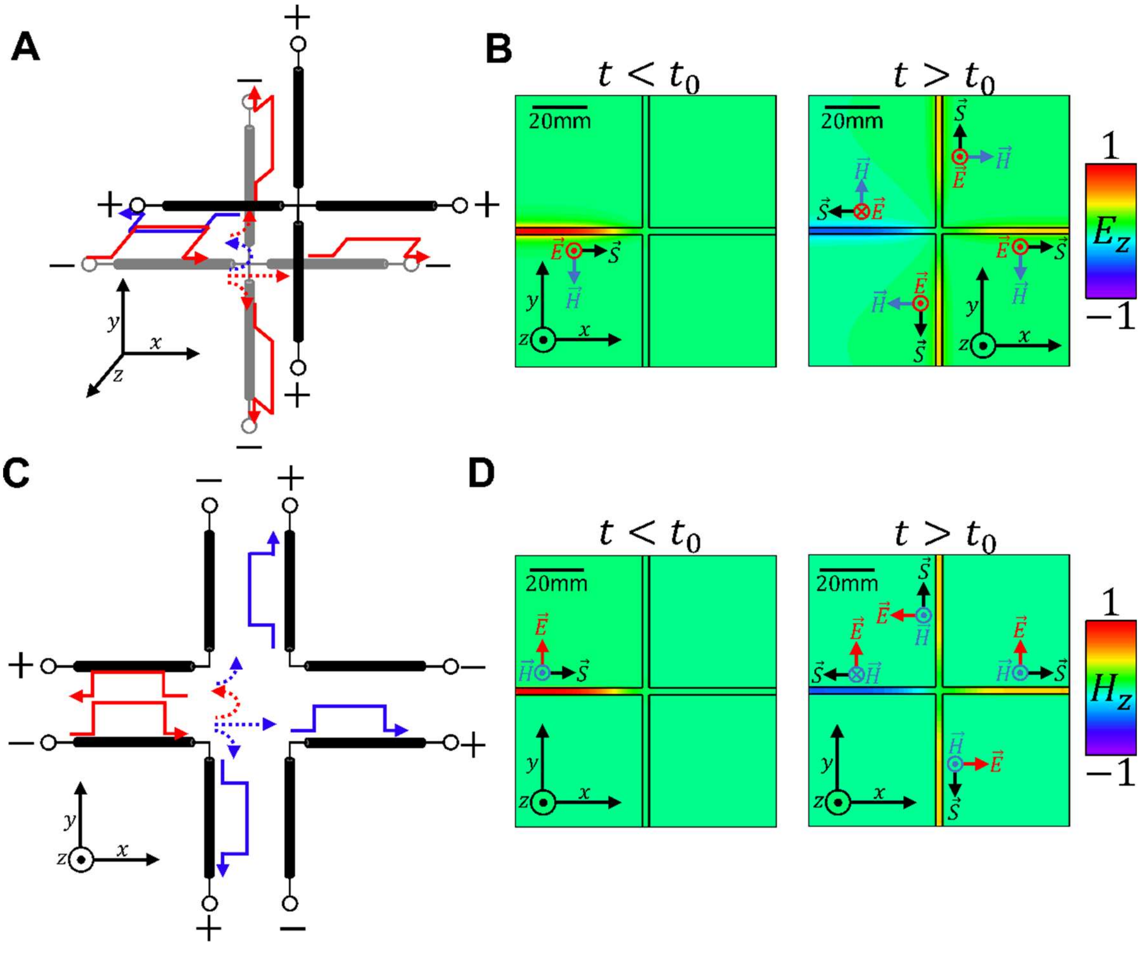

Figure. 1.10 Splitting of TEM pulses in parallel and series waveguide junctions with equal input impedances. **A.**, **C.** TL representation of the parallel and series junctions showing the input and output pulses with their respective polarities. **B.**, **C.** Numerical simulations of the out-of-plane electric and magnetic fields of the scenario presented in **A**, **C** respectively. (Left) Input pulse before $t = t_0$. (Right) Output pulses after the interaction with the junction.

The scattering matrix of an N-waveguide *perfect splitting* structure can be found by simply substituting $Z_i = Z_j = Z_0$ into Eq. 1. 23 or Eq. 1.24 and rearranging to receive:

$$\boldsymbol{A} = \pm(\boldsymbol{I} - \gamma\boldsymbol{J}) \tag{1.25}$$

where $\boldsymbol{I}$, $\boldsymbol{J}$ are the $N \times N$ identity and all-ones matrices, respectively and $\gamma = 2/N$ is the transmission coefficient towards a single waveguide, calculated from Eq. 1.23 or Eq. 1.24.The $+$ and $-$ cases in Eq. 1.25 represent the parallel and series cases respectively. Consider, for example, a *perfect splitting* structure, constructed from four waveguides[23,76]. The transmission coefficient of this structure is $\gamma = 1/2$. Likewise, the magnitude of the reflection coefficient (found using Eq. 1.25) is also $|\Gamma| = 1/2$. However, the polarity of the reflected signal is opposite to the transmitted in both cases. This means that the total energy of the input signal will be divided between all four connected waveguides, with each receiving 25% of the total input energy. The scattering matrix of this structure is as follows:

$$\boldsymbol{A} = \pm\frac{1}{2}\begin{pmatrix} -1 & 1 & 1 & 1 \\ 1 & -1 & 1 & 1 \\ 1 & 1 & -1 & 1 \\ 1 & 1 & 1 & -1 \end{pmatrix} \tag{1.26}$$

Numerical simulations of this scenario are presented in Fig. 1.10 showing both the parallel and series cases. These simulations are produced using the commercial simulation software CST Studio Suite®. Here the input pulse is applied at the leftmost waveguide with positive polarity. Fig. 1.10.B,D shows the normalized out-of-plane E and H-fields of the two scenarios. By observing the magnitude and polarity of the pules after the pulse has been scattered by the junction, it can be seen how in both scenarios, all output pulses have the same magnitude, however there is a polarity flip between the respective pulses in the two cases.

1.2.8 *TEM pulse-based processor and elementary switching operations*

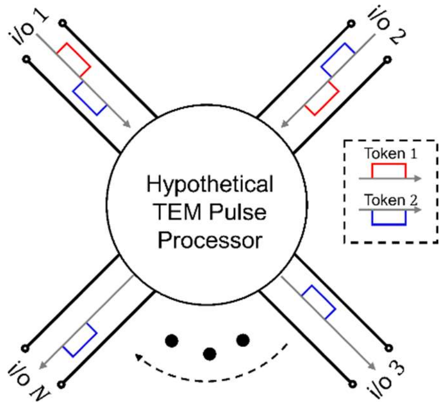

Figure. 1.11 TEM pulse-based processor. Here tokens of data (see figure insert) are encoded into the amplitude or polarity of incident TEM pulses. Computation is performed based on the splitting and superposition of pulses within the TEM pulse processor.

Recently, the concept of a TEM pulse processor for high-speed computing has been proposed[23]. In this realm, information is encoded into either the amplitude or polarity of TEM pulses and elementary switching operations can then be performed based on the constructive or destructive superposition of these signals at waveguide junctions[23]. This premise of the TEM pulse processor is presented in Fig. 1.11A. As an example, consider the scenario presented in Fig. 1.10, now with two incident pulses. Both pulses have the same magnitude, which for the incident pulses is 1 (arbitrary units). In this scenario, by tailoring the polarity relation between the two input signals (same polarity or opposite polarity), the constructive/destructive nature of the interaction between the two signals is controlled. Using Eq. 1.25 with Eq. 1.20, it can be seen that when two pulses of the same polarity are excited at two different waveguides, the pulses transmitted to the other waveguides (without an input pulse) constructively interfere, producing a pulse with the same polarity as the input and a magnitude of 1.On the other hand, the pulses transmitted/reflected towards the input waveguides destructively interfere and completely cancelling out.. This is reversed when the two input pulses have opposite polarities. This means that the direction of the pulse propagation after the interaction with the junction is controlled by the polarity relationship between the two pulses. This is an elementary switching operation, which is analogous to an XNOR gate, here emulated with an analogue system. Numerical simulations of these two scenarios, produced using the commercial simulation software CST Studio Suite® (see Appendix. A for more details) are presented in Fig. 1.12B,D showing input pulses with the same and opposite polarities, respectively. Here, series junctions have been exploited, but the technique may also be applied to parallel junctions[23].

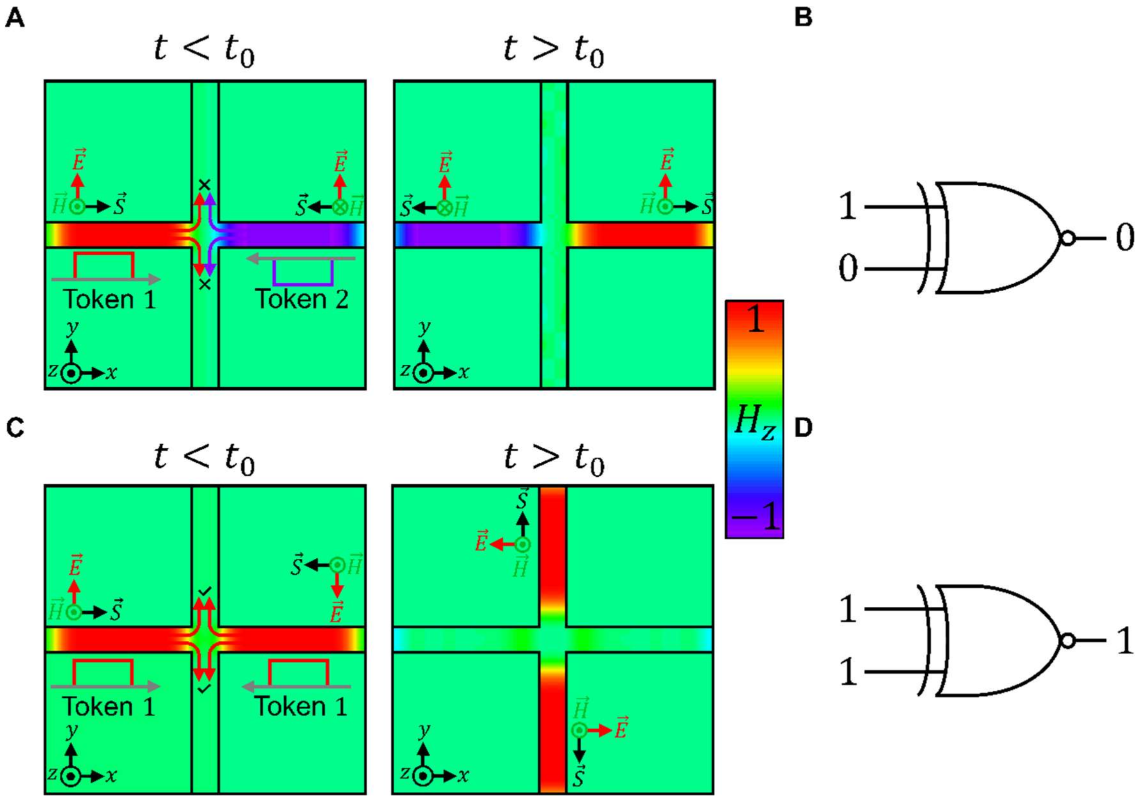

Figure. 1.12 Example of an XNOR style operation emulated using TEM pulses at a series four-wave waveguide junction**. A.**, **C.** Numerical simulations of the out-of-plane magnetic field of the (1,0) and (1,1) input cases. **B.**, **D.** Logic gate representation of the examples provided in **A**, **C**. Here t_0 is the time at which the pulses arrive at which TEM pulse arrives at the waveguide junction.

1.3 Metatronic Circuits

Metatronic circuits are subwavelength structures which emulate the performance of electrical lumped elements at higher frequencies[88–91]. Metatronic circuits have been exploited for applications such as, sensing[92,93], filtering[94–96], impedance matching[97] and antennas[98], to name a few. The operating principle behind metatronic elements is presented in Fig. 1.13. A simple metatronic element may be constructed from a single dielectric or metallic plane[90,96,99], as is presented in Fig. 1.13A. For an incident signal at normal incidence, such as a plane wave or a TEM signal in a waveguide, this structure emulates the performance of a lumped element if the thickness of the slab in the direction of wave propagation is sufficiently smaller than the wavelength of the incident signal inside the medium[96]. The impedance Z of the metatronic element is calculated as follows[96]:

$$Z = \frac{i}{\omega \varepsilon_0 \varepsilon_r(\omega) d} \tag{1.27}$$

where ω is the angular frequency of the incident signal, while $\varepsilon_r(\omega)$ and d are the dispersive relative permittivity and width of the slab in the direction of propagation, respectively. From Eq. 1.27, the type of lumped element emulated by the metatronic element, is determined by the sign of the ε_r. If for instance, the slab is a dielectric with $Re\{\varepsilon_r\} > 0$, then the metatronic element will behave as a capacitor[88] in parallel with the TLs representing the input and output medium (vacuum $\varepsilon_r = \mu_r = 1$ in Fig. 1.13). On the other hand, if $Re\{\varepsilon_r\} < 0$, such as when operating near a Lorentzian resonance, the slab will instead behave as an inductor[88] (See Fig. 1.13B).

It has also been demonstrated that impedance transformers may be exploited in the context of metatronic circuits, for instance to assist in filtering[96], or impedance matching[97]. One method of implementing an impedance transformation is to embed the dielectric/metallic slab into a host medium, such as vacuum or air, with an impedance Z_h and a length L_h on either side of the slab, in the direction of propagation. In this scenario, the whole structure then emulates the performance of a new lumped element. The impedance is found by applying an impedance transformation (for instance by using Smith's chart[97,100]) to Eq. 1.27. Consider for instance, the structure presented in Fig. 1.13C, here L_h has been chosen as $\lambda_h/4$, where λ_h is the wavelength of the incident signal in the host medium. In this scenario, the parallel impedance is transformed into a series impedance[30], representing the whole structure Z' with $Z' = Z_h^2/Z$. Using Eq. 1.27 the value of the series impedance is calculated as:

$$Z' = -i\omega\varepsilon_0\varepsilon_r d Z_h^2 \tag{1.28}$$

From Eq. 1.28 and Fig. 1.13 it can be seen how a slab with $Re\{\varepsilon_r\} > 0$ or $Re\{\varepsilon_r\} < 0$ now emulate either series inductors or capacitors, respectively.

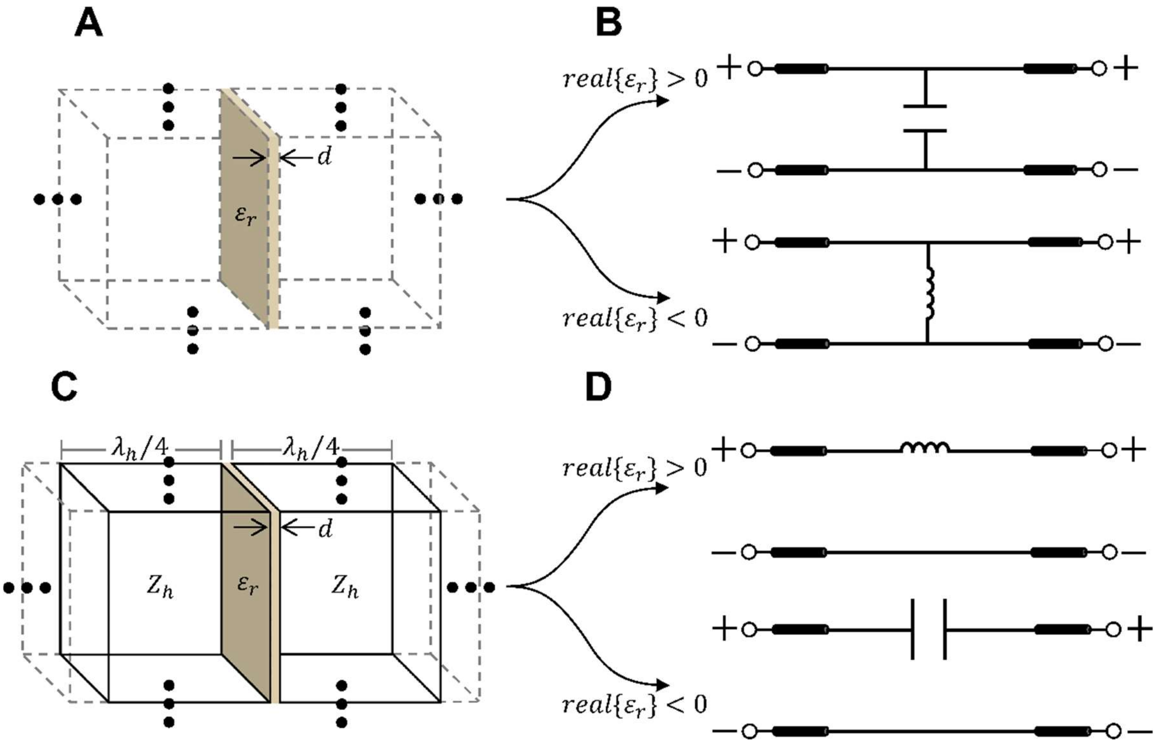

Figure. 1.13 Principles of metatronic circuit design. **A.** Example of an metatronic element constructed from a single dielectric/metallic slab with permittivity ε_r and width d. **B.** Circuit theory representation of **A** when $real\{\varepsilon_r\} > 0$ (top) and $real\{\varepsilon_r\} < 0$ (bottom), respectively. **C.** Implementation of series metatronic element using smith chart impedance transforms. **D.** Same as **B.** now showing the circuit theory representation of **C.**

Fig. 1.14 shows an example of how metatronic circuits and impedance transformations may be exploited for impedance matching purposes. In this figure an incident signal, propagating in vacuum ($\varepsilon_r = \mu_r = 1, Z_0 = 120\pi\ \Omega$) encounters a dielectric ($\varepsilon_r = 10$, $\mu_r = 1, Z_1 = 119\ \Omega$) at normal incidence. To minimize the reflections produced in this scenario, two dielectric slabs have been introduced as an impedance matching layer. These slabs are designed to emulate a parallel metatronic capacitor ($Z_c = 256.04i\ \Omega$) and series metatronic inductor ($Z_L = -175.22i\ \Omega$), respectively. The simulated normalized impedance of this structure when viewed from the left is presented in Fig. 1.14B. As it can be seen, at the designed frequency ω_d, the impedance mismatch between the vacuum region and the total structure is minimized, thus reducing the reflection seen in the vacuum region.

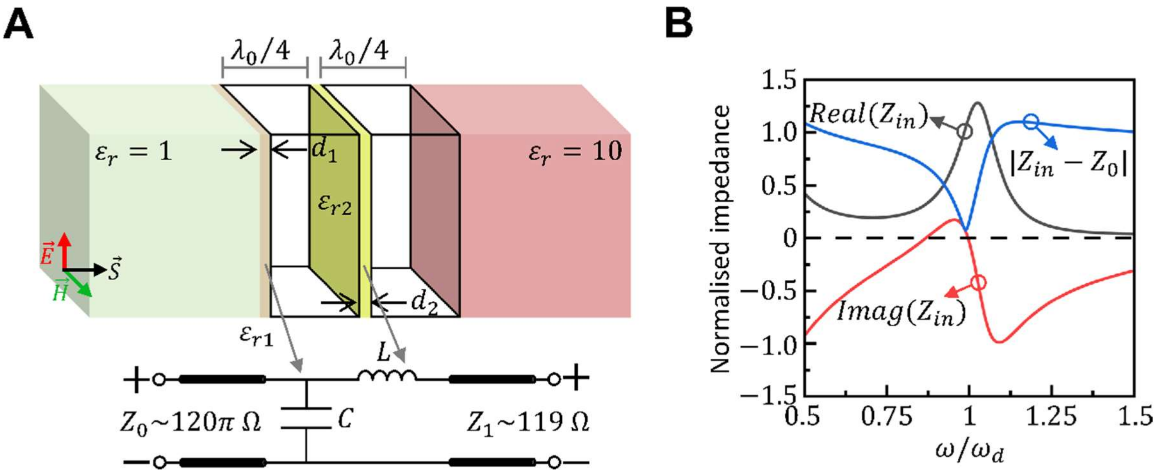

Figure. 1.14 Impedance matching with an LC metatronic circuit. **A.** Impedance matching structure (top) and the TL representation (bottom). **B.** Normalized input impedance Z_{in} of the structure in **A.** as viewed from the left.

1.4 Computing with EM Waves: Motivation and Background

1.4.1 Digital switching techniques with EM waves

Optical/EM wave-based logic gates have been investigated over the recent decades as a means to overcome the challenges of conventional semiconductor-based computing technology. The core premise of any EM logic gate is to encode binary information into wave features (amplitude, phase, wavelength, or polarization), and to perform Boolean operations by controlling the propagation of that wave. In this realm EM logic gates have been demonstrated by exploiting a variety of structures/interaction mechanisms. These devices may be classified based on the method they use to control the propagation of light though the system[22] as follows:

Electro-optical/Thermo-optical switching

One technique which has been exploited to enable EM logic gates is to control the propagation of light via the use of electro-optical or thermo-optical elements[101–105]. These being devices capable of changing their permittivity in response to an electrical signal or heat. These devices are commonly used within structures such as Mach-Zehnder Interferometer networks (MZI) to control the constructive/destructive nature of interference of multiple signals by inducing phase difference between them[106–108]. This technique has the benefits of being relatively simple to implement, as MZI networks are well known, and has the potential of being reconfigurable[105]. However, the use of an electrical input signal and an optical output signal necessitates conversions between the two regimes when cascading operations together. Additionally, devices based on MZI architecture require a relatively large footprint[22], compared to other techniques.

All optical switching with non-linear elements

Another technique is to control the propagation of EM waves based on intensity, or via an external EM signal. To do this with arbitrary control necessitates a highly non-linear system[109]. In this realm, the non-linear properties of semiconductor optical amplifiers (SOAs) have been exploited to design logic gates, either on their own[110–114] or in conjunction with another system such as an MZI network[115–118]. Another method is to exploit materials with a high third order Kerr susceptibility as a source of non-linearity. To achieve this, structures such as plasmonic waveguides or photonic crystal waveguides have been exploited[119–126] due to their highly confined modes, allowing for regions of high intensity inside cavities and resonators. Meaning the impact of the non-linear term on the overall permittivity is increased.

All optical switching without non-linearity

Elementary switching operations, such as universal logic gates, have also been demonstrated using interferometric techniques, without exploiting non-linearity, here called "*linear logic gates*"[127,128]. In this realm, elementary logic gates have been designed, exploiting guided wave structures. Examples include networks of dielectric waveguides[129], including MZI networks[130], plasmonic waveguide networks[82,131–135], photonic crystal waveguides and topological waveguides[136]. Additionally, inverse design and topological optimization techniques have also been applied to assist in designing switching structures[137].

1.4.2 Introduction to analogue computing

Computing with EM waves has also been exploited in unconventional computing paradigms such as analogue computing. Unlike conventional digital computing, in this realm information is not encoded into bits. Instead, calculations are performed using continuous input and output functions. An illustration of the difference between the two computing approaches is presented in Fig. 1.15. Here, an input signal (for instance, information from a microphone or camera) is received by a computing system (digital top, analogue bottom). In the digital system, to perform operations with this data, it is first converted into a digital representation using an analogue to digital converter[21] (ADC). The desired operation is then performed in the digital regime before converting the information back into an analogue format using a digital to analogue converter (DAC) (for instance, in order to output towards a speaker). In contrast in the analogue computing approach the input signal is not converted between regimes, instead the analogue processor performs operations directly onto the waveform of the incident signal, in this case computing the function $g_2(x)$ from the hypothetical input function $g_1(x)$. Analogue computing as an alternative computing paradigm has the potential to enable a computation speedup over conventional digital computing systems due to the one-shot nature[21] of the calculations and the lack of ADC/DACs[21].

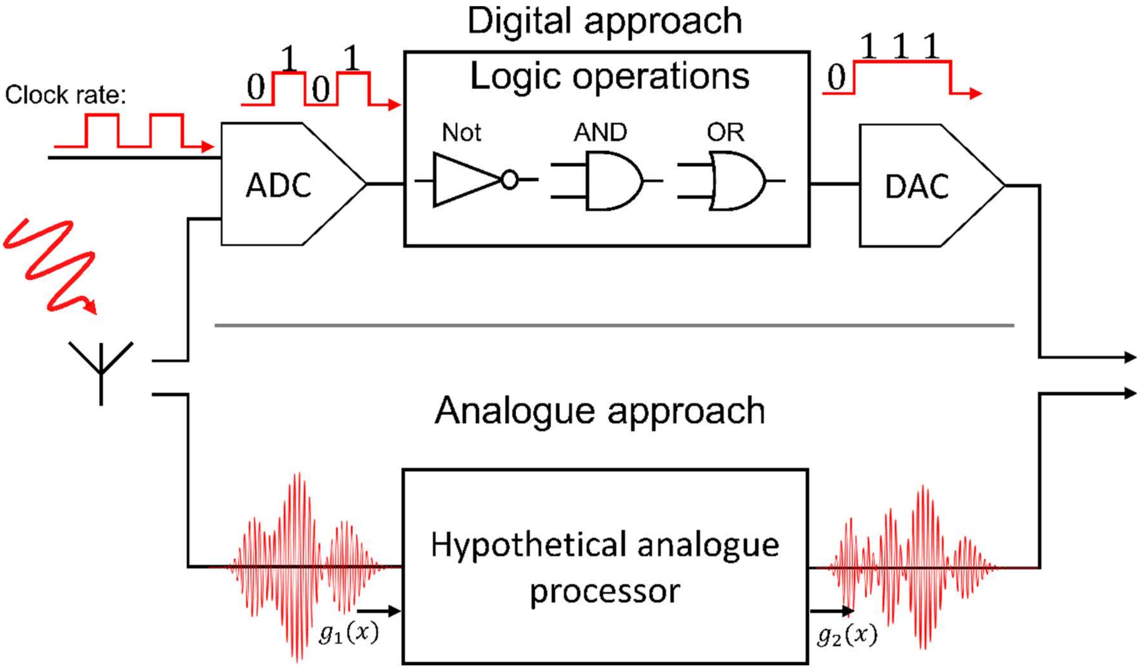

Figure. 1.15 Schematic representation of the difference between digital (top) and analogue (bottom) approaches to computing operations.

Early analogue computing devices can be traced back to over two millennia ago with the earliest known device being the Antikythera mechanism[138], theorized to have been invented as early as 200BC[138]. Other historic computing tools include an abacus[139], Napier's bones[140] or a slide rule[141]. Modern analogue computing, much like digital computing, can be traced back to the early 20th century[142]. Analogue computing devices from this era, such as the Hartree differential analyzer[143], were mechanical in nature using gear networks to calculate the solutions to integral equations. Mechanical analogue computers would later be largely replaced by their electrical counterparts[144], in part due to higher speed and lower fabrication/operation costs[144]. These devices would use networks of electrical elements, both active and passive, to perform signal processing tasks[142] as well as comparably complex tasks such as partial differential equation (PDE) solving[145,146].

Although analogue computing has advantages, early analogue computers have not seen the same widespread adoption as digital computers. One significant contributing factor to this is the tremendous scalability of semiconductor devices allowing them to outpace the development of analogue computing systems[1,2]. Another is the inherent resilience to noise of digital systems in comparison to analogue[21] as the accuracy of a calculation is determined by how many bits are used and the time allowed for the calculation. In an analogue computing system, the accuracy instead depends on the fabrication tolerances of the computing structure[21]. Despite this, analogue computing is an interesting alternative paradigm as modern photonic systems (metamaterials, waveguides, plasmonic) allow for the advantages of computing with EM waves to be exploited in an analogue computing context.

1.4.3 Analogue computing techniques with EM waves

In the realm of analogue computing with EM waves, different techniques have been exploited to design the analogue processors. Two example techniques which are commonly used are: 1) Fourier optics and 2) The Green’s function method. In this section, a brief overview of both techniques including some advantages and disadvantages of each, will be presented.

Fourier optics.

The first technique is to use Fourier optics to perform operations in the spatial domain. This technique exploits the well-known fact that a converging lens may be exploited to calculate the Fourier transform of an incident signal. In this realm, differential operations are conducted by converting spatial domain signals into the frequency domain where differential operations can instead be calculated as multiplications. Consider for example a four focal length system, as is shown in Fig. 1.15. An input image, in this case an image of a dog representing the function $g(x, y)$, is applied one focal length FL away from a converging lens. At the other side of the lens (also one focal length away) is a metasurface[147–151] analogue processor. The image as seen from the left-hand side of the metasurface is the Fourier transform of the input image $g(x, y)$. Operations are then applied onto the input signal in the frequency domain by carefully engineering the transmission coefficient of the metasurface $T(x, y)$. The second lens then applies the reverse Fourier transform to convert the signal back to the spatial domain. The overall output of the system is:

$$g'(x, y) = \mathcal{F}^{-1}\{T(x, y)\mathcal{F}[g(x, y)]\} \tag{1.29}$$

where $\mathcal{F}$ is the Fourier transform operation. Differential operations such as differentiation or integration are then calculated by tailoring the shape of $T(x, y)$ to resemble the operation in the frequency domain. One challenge of this method is that the system is bulky by necessity, requiring four focal lengths at minimum. To tackle this challenge graded-index[152] (GRIN) metamaterials have be exploited to implement the Fourier transform operation over a shorter distance[149] thus reducing the overall footprint of the device.

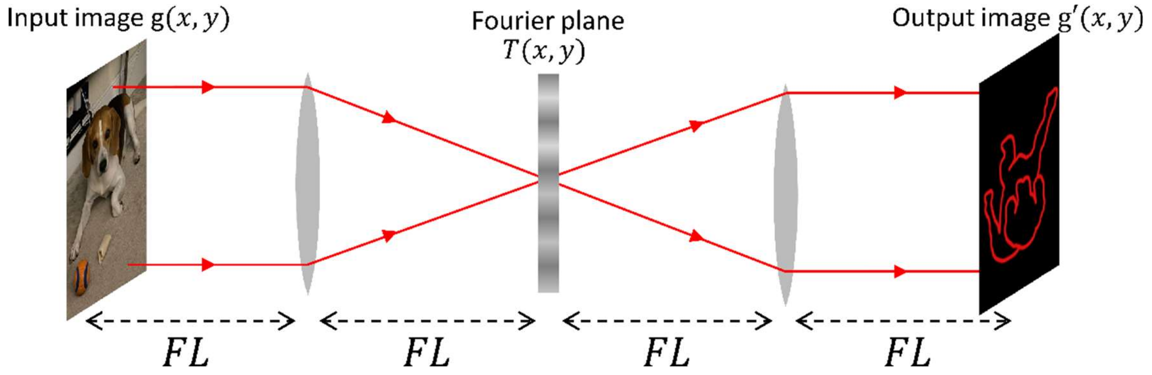

Figure. 1.16 Fourier optics approach to spatial optical computing using a four-focal-length system. The example provided is of edge enhancement on a picture of a dog.

The Green's function approach.

Another commonly exploited method of analogue computing with EM waves is the Greens function approach. In this method analogue processors may be designed to apply operations in either spatial or temporal domains by applying operations directly onto the wavefront or temporal profile of an incident signal. This is done without the use of Fourier transforming blocks meaning processors designed with this method may be smaller than those designed using the Fourier optics approach[21]. A schematic representation of this method is presented in Fig. 1.17 in which a hypothetical analogue processor is shown calculating the first derivative of an incident signal in both space (Fig. 1.17A) and time (Fig. 1.17B). Consider the temporal case as an example. Here an incident signal with a temporal profile $g_{in}(t)$ and a carrier frequency f_0

interacts with the hypothetical analogue processor. For a linear system the signal transmitted though the structure is calculated as:

$$g_{out}(t) = \mathcal{F}^{-1}\{T(f)\mathcal{F}[g_{in}(t)]\} \tag{1.30}$$

where f is frequency and $T(f)$is the frequency dependent transmission coefficient. Eq. 1.30 can then be used to perform differential operations in the temporal domain by tailoring the shape of $T(f)$ similarly to $T(x, y)$ in the Fourier optics method. Like in the spatial domain the angular response ($T(\theta_i)$, where θ_i is the angle of incidence) of the structure is tailored to instead perform operations onto the angular spectrum of an incident signal. Analogue processors based on the Greens function approach have been designed by exploiting structures such as metamaterials[149,153], metasurfaces[154,155], plasmonic structures[156–158], gratings[159–161] and multilayered media[149,162] among others[26,163–168].

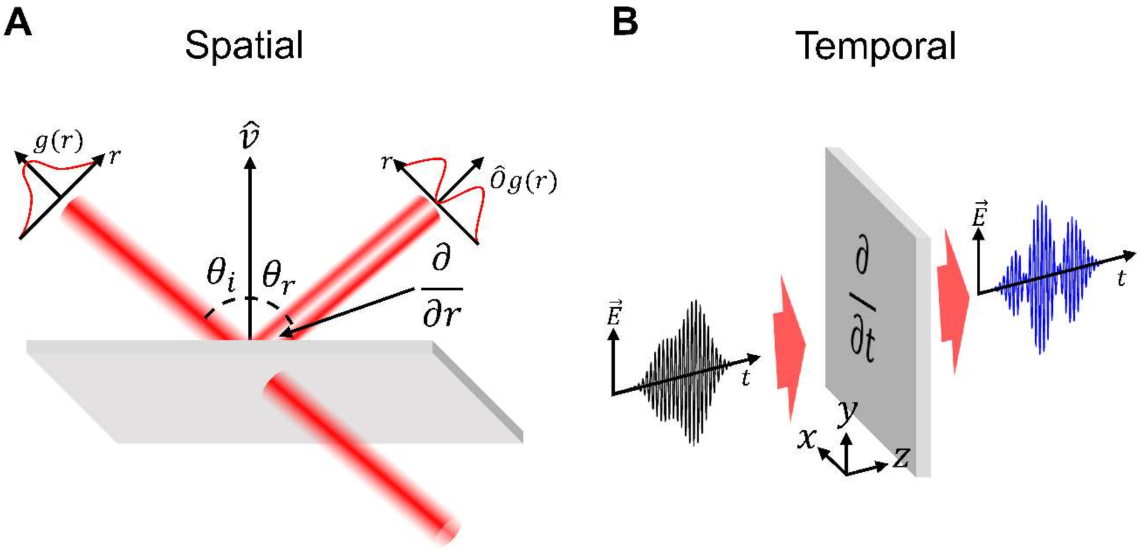

Figure. 1.17 Schematic representation of Greens functions based analogue computing in **A.** spatial and **B.** temporal domains.

1.5 Chapter 1 conclusions

In this chapter, background and theory regarding computing with EM waves has been presented. This included an overview of Maxwells Equations (the equations which govern the behaviour of EM waves at the length scales considered in this thesis), material/structural dispersion, an introduction to waveguides, TL theory and metatronic circuits. The mathematical framework presented in this Chapter will be exploited throughout this thesis when designing and modelling networks of waveguide junctions for computing applications.

Chapter 2. Modelling Arbitrarily Connected Waveguide Networks

This project explores how the splitting and superposition of EM waves within interconnected networks of waveguide junctions may be exploited for computing purposes. The behaviour of light within these networks may be understood by modelling the waveguides as TLs and exploiting the TL techniques outlined in section 1.2. For simpler networks, such as the examples provided in section 1.2.4-1.2.8, the governing equations of the network may be expressed and solved by hand. However, as the complexity and connectivity of the networks studied grows, this quickly becomes an unfeasible task. Thus, early in the project, it was identified that an automated tool capable of evaluating the performance of an arbitrary waveguide would be required, to aid in the design of waveguide networks. This chapter will explain the algorithm developed for this task.

2.1 Applying graphical modelling techniques to interconnected waveguide networks.

2.1.1 Graphical representation of arbitrary waveguide networks

When developing the algorithm, the first task is to express the connections between waveguide junctions in a form which may be interpreted by a computer. In this realm, microwave networks have been modelled using graphical techniques such as signal flow diagrams[30,169] or petri-nets[84]. When using signal flow diagrams, the inputs, and outputs of a system (x_a and y_a, respectively where $a = 1,2,3\ldots$ is the input/output number) are represented by nodes of a graph. The scattering between inputs and outputs (S-parameters) of the system is represented by arrows. These arrows represent the direction in which a signal will flow through a system. They are weighted with the corresponding S-parameter values of the input/output combination connected by each of the arrows. In this sense the scattering matrix of a system is also the adjacency matrix[170] of the signal flow diagram. As an example, the signal flow diagram of a four-port perfect-splitting waveguide junction[23,24,76,171] is presented in Fig. 2.1. Here it can be seen that each waveguide port is represented by two nodes, describing the incoming and outgoing signals from that port respectively. Due to the perfect splitting nature of the structure[76,85], this signal flow diagram is fully connected, meaning that each input is connected to each output of the graph.

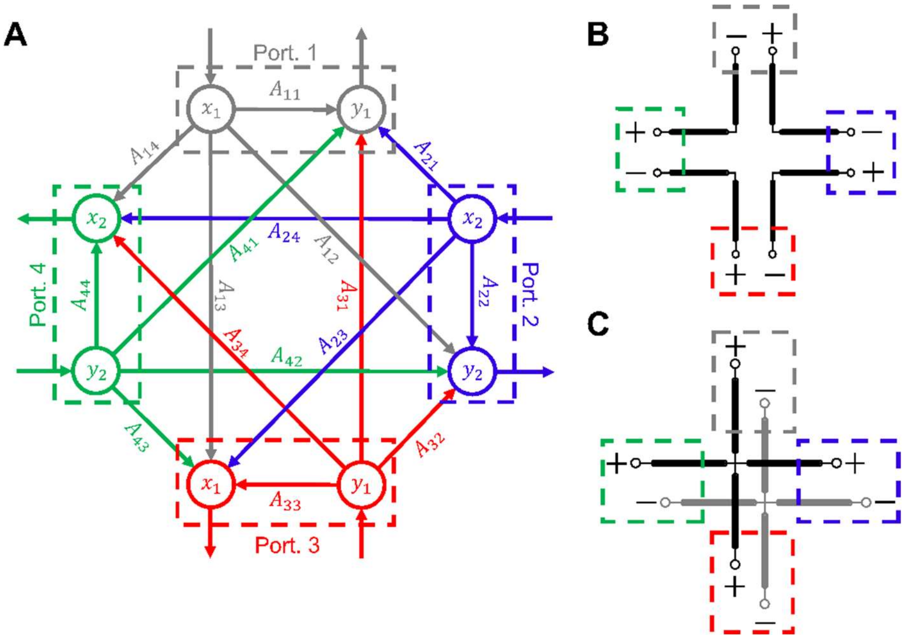

Figure 2.1 Signal flow diagram representation of a four-port perfect splitting structure. **A**. generic signal flow diagram for a four-port network. **B.** series and **C.** parallel TL models of a four-port perfect splitting structure. Plots have been colour coordinated between to show the equivalent ports in **A**, **B**, and **C**.

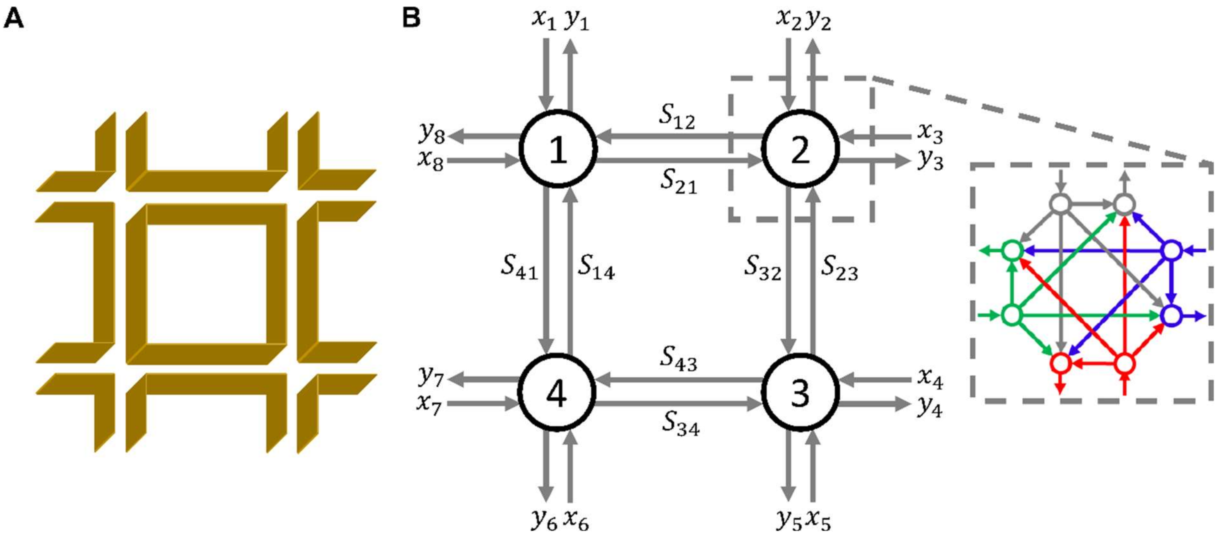

Figure. 2.2 Graphical representation of a waveguide network. **A.** Example waveguide network consisting of four four-waveguide junctions arranged in a square. **B.** Graphical representation of the network constructed in **A**. Here each node of the network represents a junction, which may also be represented by a signal flow diagram (seen inside the grey box).

Now, consider how this technique may be applied to a larger network of many interconnected waveguide junctions. Following the same procedure outlined above, by representing the waveguide junctions as the nodes of a graph (similar to the inputs/outputs in a signal flow diagram) then the connections between them may be expressed by a weighted arrow. In doing so, a larger graph describing the connections of the entire network (not just one system) is created. This graph may be expressed by its adjacency matrix[170]. As an example, a waveguide network and the corresponding connectivity graph is presented in Fig. 2.2. In this scenario four four-waveguide junctions are connected in a square-shaped network, with 8 external inputs/outputs (see Fig. 2.2A). The graphical representation of this structure is shown in Fig. 2.2B. As it can be seen, each node of the graph is itself a signal flow diagram representing the scattering matrix of the four-waveguide junction. For this particular network, the connections between junctions are simple waveguides meaning that the weightings assigned to the connections are as follows:

$$S_{a,b} = S_{b,a} = e^{-i\gamma_{ab}L_{ab}k} \tag{2.1}$$

where $a, b = 1, 2, 3$ and 4 are the nodes of the network, $S_{a,b}$ is the weighting of the connection between node a and b (i.e. the S-parameters of the waveguide between a and b). γ_{ab} and L_{ab} are the propagation constant and length of the waveguides connecting nodes a and b. Note that since the waveguides in this example are reciprocal $\gamma_{ab} = \gamma_{ba}$ and $L_{ab} = L_{ba}$. k is the wavenumber in free space of the signal being investigated. The adjacency matrix $\boldsymbol{Adj}$ constructed from this graph is as follows[170]:

$$\boldsymbol{Adj} = \begin{pmatrix} 0 & S_{12} & 0 & S_{14} \\ S_{21} & 0 & S_{23} & 0 \\ 0 & S_{32} & 0 & S_{34} \\ S_{41} & 0 & S_{43} & 0 \end{pmatrix} \tag{2.2}$$

2.1.2 Premise of the waveguide network reducing algorithm

As discussed in chapter 1, the coupling between inputs and outputs of a waveguide junction may be described by the scattering matrix $\boldsymbol{A}$. Likewise, a scattering matrix $\boldsymbol{A}_{total}$ may also be defined to instead describe the coupling between the inputs and outputs of the entire waveguide network. Now, given the adjacency matrix of the network and the scattering matrices of the individual junctions/nodes, how can one calculate the $\boldsymbol{A}_{total}$? To answer this, consider the network presented in Fig. 2.3A. This is the graphical representation of a 5 junction network with 4 external input/output waveguides. In this scenario, $\boldsymbol{A}_{total}$ is a 4×4 matrix and each junction has an associated scattering matrix $\boldsymbol{A}_a$ for $a = 1,2,3,4$ and 5. For the purposes of this example, $\boldsymbol{A}_a$ are arbitrary matrices which are not necessarily representative of a four-waveguide junction. Now, consider splitting this network into two regions by, for instance, drawing a circle around junction 1 and 2. Then, if an $\boldsymbol{A}_{total}$ may be calculated for the five-junction network, it must also be possible to calculate an $\boldsymbol{A}_{total}$ which describes the scattering of signals in the two-junction subnetwork containing only junctions 1 and 2. This is called $\boldsymbol{A}_{12}$. The challenge of calculating $\boldsymbol{A}_{12}$ is addressed in section 2.2. Using $\boldsymbol{A}_{12}$ the graph representation of the overall network may now be redrawn to represent junctions 1 and 2 now as a single node. This is shown in Fig. 2.3B in which the five-node graph from Fig. 2.3A has been reduced to a four-node graph. The process of splitting the graph into regions may then be applied to the new four-node graph, at this stage constructing a node which is representative of 3 waveguide junctions, as is the case in Fig. 2.3C. In fact, this process may be systematically repeated, at each stage adding another junction to the combined node and calculating a scattering matrix, until all junctions in the network are included into the combined node and in doing so $\boldsymbol{A}_{total}$ has been calculated. For a graph with N nodes (a network of N junctions or N connected scattering matrices) this occurs after at most $N - 1$ iterations.

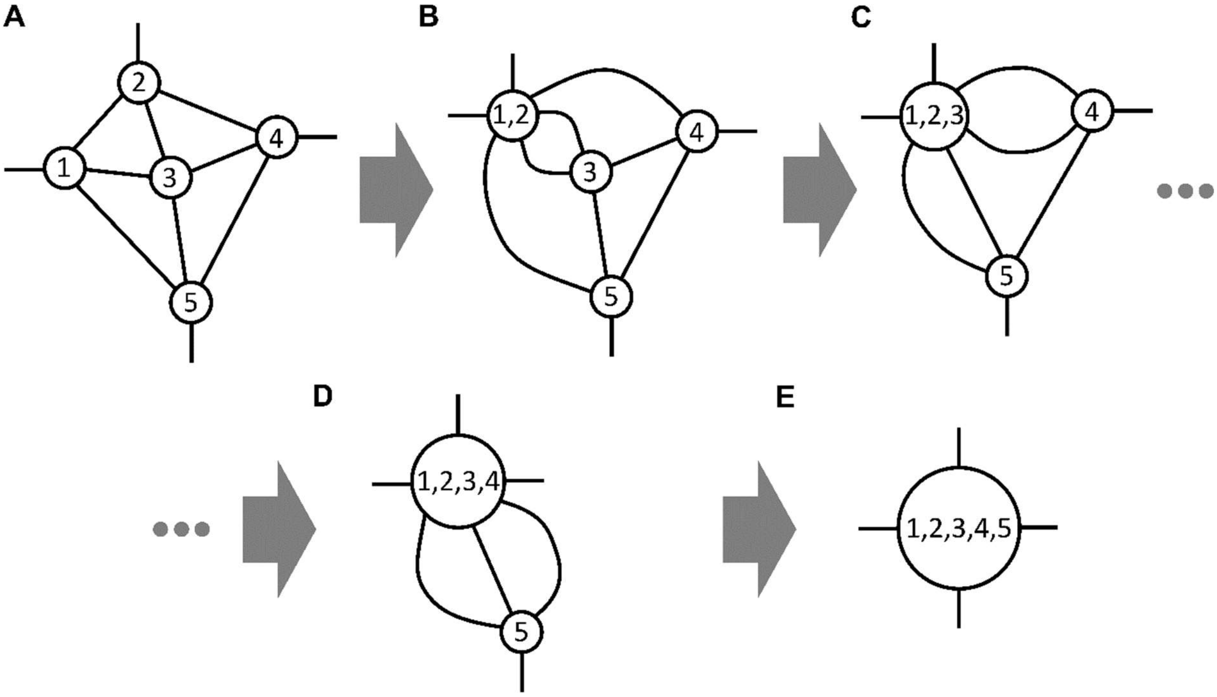

Figure. 2.3 Premise of the waveguide network solving algorithm **A.** Graphical representation of the hypothetical 5-waveguide network. **B.** Graph after 1 iteration, nodes 1 and 2 have been combined into a single node, labelled 1,2. **C.** After 2 iterations. **D.** After 3 iterations. **E.** Final iteration showing the overall scattering matrix of the structure.

2.2 Combining Two Connected Scattering Matrices

The implementation of the algorithm discussed in section. 2.1.2 relies on the ability to combine two scattering matrices together into a single scattering matrix which describes both structures. After this, the rest of the algorithm can be implemented by repeatedly applying this operation. There are a few requirements of this operation; 1) The two scattering matrices to be combined should be arbitrary so that a general solution can be calculated. 2) There may be multiple paths connecting the two scattering matrices. As seen in Fig. 2.3B-D, combining nodes together may produce multiple paths between two nodes. If the operation is to be applied iteratively, it must function in this scenario. 3) The ordering of terms in the scattering matrix should be preserved. This is important as the S-parameters of the scattering matrices calculated through this algorithm must be correctly associated with an input/output combination.

A schematic representation of this scenario is presented in Fig. 2.4. Here two systems described by the arbitrary scattering matrices $\boldsymbol{A}$ and $\boldsymbol{A'}$ are connected by M connections. The undashed and dashed systems have N and N' external inputs/outputs respectively (inputs which do not connect to the other scattering matrix). This means that $\boldsymbol{A}$ and $\boldsymbol{A'}$ are matrices of size $(N+M)\times(N+M)$ and $(N'+M)\times(N'+M)$ respectively. The input and output vectors of these systems are $\boldsymbol{x} = [x_1, x_2, \ldots, x_{N+M}]$, $\boldsymbol{y} = [y_1, y_2, \ldots, y_{N+M}]$ and $\boldsymbol{x}' = [x_1', x_2', \ldots, x_{N'+M}']$, $\boldsymbol{y}' = [y_1', y_2', \ldots, y_{N'+M}']$ for the undashed and dashed systems, respectively.

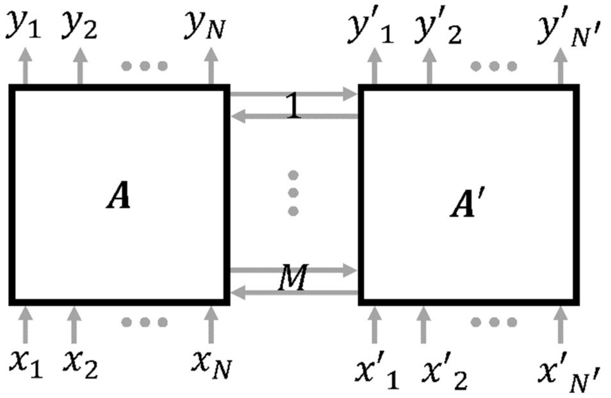

Figure 2.4 Schematic representation of two arbitrary scattering matrices connected by M connections.

2.2.1 Labelling convention

Importantly in the scenario depicted in Fig. 2.4, there have been no restrictions placed on the labelling/ordering of the terms of the two scattering matrices. Consequentially, a single connection may be labelled differently when viewed from either the dashed or undashed system. To assist in the calculation of the combined scattering matrix for this system, the following sets are defined: $\nu = \{a \mid x_a$ and y_a denotes an external input/output of the undashed system$\}$, $\nu' = \{a \mid x'_a$ and y'_a denotes an external input/output of the dashed system$\}$, $\xi = \{a \mid x_a$ and y_a denotes an input/output of the undashed system which connects to an input/output of the dashed system$\}$ and $\xi' = \{a \mid x'_a$ and y'_a denotes an input/output of the dashed system which connects to an input/output of the undashed system$\}$. With these sets Eq. 1.20 for $\boldsymbol{y}$ and $\boldsymbol{y}'$ may be rewritten as:

$$y_j = \sum_{a1=1}^{N} A_{j,\nu_{a1}} x_{\nu_{a1}} + \sum_{a2=1}^{M} A_{j,\xi_{a2}} x_{\xi_{a2}} \tag{2.3a}$$

$$y'_{j'} = \sum_{b1=1}^{N'} A'_{j',\nu'_{b1}} x_{\nu'_{b1}} + \sum_{b2=1}^{M} A'_{j',\xi'_{b2}} x_{\xi'_{b2}} \tag{2.3b}$$

where $j = 1,2,\ldots,N+M$ and $j' = 1,2,\ldots,N'+M$, respectively. ν_a, ν'_a, ξ_a and ξ'_a refer to the term at index a of the sets ν, ν', ξ and ξ', respectively. Both equations of Eq. 2.3 have two terms. These describe the scattering of signals towards output j or j' (in Eq. 2.3a and Eq. 2.3b, respectively) which originate from an external input and a connection between scattering matrices, for the first and second term respectively. Due to the connections between scattering matrices if $j \in \xi$ then an output signal from Eq. 2.3a will become an input signal in the second term of Eq. 2.3b. Likewise for an output signal from Eq. 2.3b and the second term of Eq. 2.3a if $j' \in \xi'$.

2.2.2 Describing the connections between two scattering matrices

To help envision the connections between scattering matrices, consider the example presented in Fig. 2.5. Here $\boldsymbol{A}$ and $\boldsymbol{A'}$ are both 7×7 matrices with $N = N' = 2$ and $M = 5$. In this example, $\nu = \{6{,}7\}$, $\xi = \{1{,}2{,}3{,}4{,}5\}$, $\nu' = \{4{,}5\}$ and $\xi' = \{1{,}2{,}3{,}6{,}7\}$. Looking at the inputs/output of the undashed system ($\boldsymbol{x}$ and $\boldsymbol{y}$), the vectors containing only the inputs/outputs from/towards the connections are $\boldsymbol{xc} = [x_1,x_2,x_3,x_4,x_5]$ and $\boldsymbol{yc} = [y_1,y_2,y_3,y_4,y_5]^T$, respectively. In general, this can be expressed as:

$$\boldsymbol{xc} = [x_a : a \in \mathbb{Z}^+_{N+M} \cap \xi\ ] \tag{2.4a}$$

$$\boldsymbol{yc} = [y_a : a \in \mathbb{Z}^+_{N+M} \cap \xi]^T \tag{2.4b}$$

where $\mathbb{Z}^+_{N+M} = 1{,}2{,}3{,}...{,}N + M$ is the set of positive integers from 1 to $N + M$. Likewise, the inputs and outputs from/towards the connections when viewed from $\boldsymbol{A'}$ are $\boldsymbol{xc'} = [x'_1,x'_2,x'_3,x'_6,x'_7]$ and $\boldsymbol{yc'} = [y'_1,y'_2,y'_3,y'_6,y'_7]^T$, respectively. In general, this is:

$$\boldsymbol{xc'} = [x'_a : a \in \mathbb{Z}^+_{N'+M} \cap \xi'\ ] \tag{2.5a}$$

$$\boldsymbol{yc'} = [y'_a : a \in \mathbb{Z}^+_{N'+M} \cap \xi']^T \tag{2.5b}$$

where $\mathbb{Z}^+_{N'+M} = 1{,}2{,}3{,}...{,}N' + M$ is the set of positive integers from 1 to $N' + M$.

Using the vectors defined in Eq. 2.4-2.5 the inputs from the connections can be expressed as:

$$\boldsymbol{xc} = \boldsymbol{C}\,\boldsymbol{yc'} \tag{2.6a}$$

$$\boldsymbol{xc'} = \boldsymbol{C'}\,\boldsymbol{yc} \tag{2.6b}$$

where $\boldsymbol{C}$ and $\boldsymbol{C'}$ are matrices which describe coupling between output vectors $\boldsymbol{yc'}, \boldsymbol{yc}$ and the input vectors $\boldsymbol{xc}$, $\boldsymbol{xc'}$, respectively. For the example presented in Fig. 2.5 $\boldsymbol{C}$ and $\boldsymbol{C'}$ are as follows:

$$\boldsymbol{C} = \boldsymbol{C'} = \begin{pmatrix} 0 & 0 & 1 & 0 & 0 \\ 0 & 1 & 0 & 0 & 0 \\ 1 & 0 & 0 & 0 & 0 \\ 0 & 0 & 0 & 0 & 1 \\ 0 & 0 & 0 & 1 & 0 \end{pmatrix} \tag{2.7}$$

In general, $\boldsymbol{C}$ and $\boldsymbol{C}'$ can be constructed using the following steps: 1) Initialize $\boldsymbol{C}$ and $\boldsymbol{C}'$ as all-zero matrices of size $M \times M$. 2) To construct $\boldsymbol{C}$, iterate over $a = 1,2,3,...,M$ at each step identifying the index of the term in $\boldsymbol{xc}$ which is connected to the output $\boldsymbol{yc}'_a$. This index is called idx. 3) Replace $C_{idx,a}$ with the transmission coefficient of the connection between $\boldsymbol{yc}'_a$ and $\boldsymbol{xc}_{idx}$. 4) To construct $\boldsymbol{C}'$ repeat the procedure outlined in 2) and 3), now swapping the dashed and undashed vectors, respectively. Using Eq. 2.6, Eq. 2.3 may be rewritten in general as:

$$y_j = \sum_{a1=1}^{N} A_{j,v_{a1}} x_{v_{a1}} + \sum_{a2=1}^{M} \sum_{c1=1}^{M} A_{j,\xi_{a2}} C_{a2,c1} y'_{\xi'_{c1}} \tag{2.8a}$$

$$y'_{j'} = \sum_{b1=1}^{N'} A'_{j',v'_{b1}} x_{v'_{b1}} + \sum_{b2=1}^{M} \sum_{c2=1}^{M} A'_{j',\xi'_{b2}} C'_{b2,c2} y_{\xi_{c2}} \tag{2.8b}$$

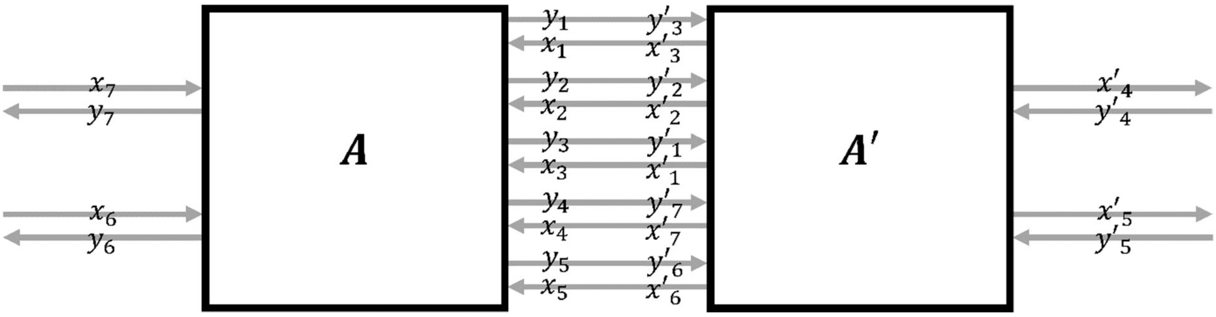

Figure 2.5 Example of two connected scattering matrices with mismatched indices for the connected input/outputs.

2.2.3 Constructing the combined scattering matrix

Examining Eq. 2.8, one can see that Eq. 2.8b now appears in the second term of Eq. 2.8a if $j' = \xi'_{c1} \in \xi'$. The same is true for Eq.2.8a and the second term of Eq. 2.8b if $j = \xi_{c2} \in \xi$. Using this observation Eq. 2.8a and Eq. 2.8b are combined as follows:

$$y_j = \sum_{a1=1}^{N} A_{j,v_{a1}} x_{v_{a1}} + \sum_{a2=1}^{M} \sum_{c1=1}^{M} \sum_{b1=1}^{N'} A_{j,\xi_{a2}} C_{a2,c1} A'_{\xi'_{c1},v'_{b1}} x_{v'_{b1}} \dots$$

$$\dots + \sum_{a2=1}^{M} \sum_{c1=1}^{M} \sum_{b2=1}^{M} \sum_{c2=1}^{M} A_{j,\xi_{a2}} C_{a1,c1} A'_{\xi'_{c1},\xi'_{b2}} C'_{b2,c2} y_{\xi_{c2}} \tag{2.9a}$$

$$y'_{j'} = \sum_{b1=1}^{N'} A'_{j',\nu'_{b1}} x_{\nu'_{b1}} + \sum_{b2=1}^{M} \sum_{c2=1}^{M} \sum_{a1=1}^{N} A'_{j',\xi'_{b2}} C_{b2,c2} A_{\xi_{c2},\nu_{a1}} x_{\nu_{a1}} \dots$$

$$\dots + \sum_{b1=1}^{M} \sum_{c2=1}^{M} \sum_{a2=1}^{M} \sum_{c1=1}^{M} A'_{j',\xi'_{b2}} C'_{b2,c2} A_{\xi_{c2},\xi_{a2}} C_{a2,c1} y'_{\xi'_{c1}} \tag{2.9b}$$

Note that if $j = \xi_{c2} \in \xi$ and $j' = \xi'_{c1} \in \xi'$, then Eq. 2.9 form a series of simultaneous equations. In this scenario, Eq. 2.9 may be rewritten as:

$$y_{\xi_l} = \sum_{a1=1}^{N} A_{\xi_l,\nu_{a1}} x_{\nu_{a1}} + \sum_{a2=1}^{M} \sum_{c1=1}^{M} \sum_{b1=1}^{N'} A_{\xi_l,\xi_{a2}} C_{a2,c1} A'_{\xi'_{c1},\nu'_{b1}} x_{\nu'_{b1}} \tag{2.10a}$$

$$+ \sum_{d1=1}^{M} B_{l,d1} y_{\xi_{d1}}$$

$$y'_{\xi'_l} = \sum_{b1=1}^{N'} A'_{\xi'_l,\nu'_{b1}} x_{\nu'_{b1}} + \sum_{b2=1}^{M} \sum_{c2=1}^{M} \sum_{a1=1}^{N} A'_{\xi'_l,\xi'_{b2}} C_{b2,c2} A_{\xi_{c2},\nu_{a1}} x_{\nu_{a1}} \tag{2.10b}$$

$$+ \sum_{d2=1}^{M} B'_{l,d2} y'_{\xi'_{d2}}$$

where $l = 1,2,\dots, M$ and $\boldsymbol{B}$, $\boldsymbol{B}'$ are a pair of $M \times M$ matrices with terms defined as follows:

$$B_{l,l'} = \sum_{a1=1}^{M} \sum_{c1=1}^{M} \sum_{b2=1}^{M} A_{l,\xi_{a1}} C_{a1,c1} A'_{\xi'_{c1},\xi'_{b2}} C'_{b2,l'} \tag{2.11a}$$

$$B'_{l',l} = \sum_{b1=1}^{M} \sum_{c2=1}^{M} \sum_{a2=1}^{M} A'_{l',\xi'_{b1}} C'_{b1,c2} A_{\xi_{c2},\xi_{a2}} C_{a2,l} \tag{2.11b}$$

where $l' = 1,2,\dots,M$. In solving Eq. 2.10, the output signals into the connected waveguides are expressed as:

$$y_{\xi_l} = \sum_{d1=1}^{M} \sum_{a1=1}^{N} (\boldsymbol{I} - \boldsymbol{B})^{-1}_{l,d1} A_{\xi_{d1},\nu_{a1}} x_{\nu_{a1}} \dots$$

$$\dots + \sum_{d1=1}^{M} \sum_{a2=1}^{M} \sum_{c1=1}^{M} \sum_{b1=1}^{N'} (\boldsymbol{I} - \boldsymbol{B})^{-1}_{l,d1} A_{\xi_{d1},\xi_{a2}} C_{a2,c1} A'_{\xi'_{c1},\xi'_{b1}} x_{\nu'_{b1}} \tag{2.12a}$$

$$y'_{\xi'_l} = \sum_{d2=1}^{M} \sum_{b1=1}^{N'} (\boldsymbol{I} - \boldsymbol{B}')^{-1}_{l,d2} A_{\xi'_{d2},\nu'_{b1}} x_{\nu'_{b1}} \dots$$

(2.12b)

$$\ldots + \sum_{d2=1}^{M} \sum_{b2=1}^{M} \sum_{c2=1}^{M} \sum_{a1=1}^{N} (\boldsymbol{I} - \boldsymbol{B}')^{-1}_{l,d2} A'_{\xi'_{d2},\xi'_{b2}} C_{b2,c2} A_{\xi_{c2},\nu_{a1}} x_{\nu_{a1}}$$

where $\boldsymbol{I}$ is the identity matrix of size $M \times M$. For clarity Eq. 2.12 is then rewritten as:

$$y_{\xi_l} = \sum_{a1=1}^{N} D_{l,a1}\, x_{\nu_{a1}} + \sum_{b1=1}^{N'} E_{l,b1} x_{\nu'_{b1}} \tag{2.13a}$$

$$y'_{\xi'_l} = \sum_{b1=1}^{N'} E'_{l,b1}\, x_{\nu'_{b1}} + \sum_{a1=1}^{N} D'_{l,a1}\, x_{\nu_{a1}} \tag{2.13b}$$

where $\boldsymbol{D}$, $\boldsymbol{D}'$ and $\boldsymbol{E}$, $\boldsymbol{E}'$ are matrices of size $(M \times N)$ and $(M \times N')$, respectively. The terms of $\boldsymbol{D}, \boldsymbol{D}'$, $\boldsymbol{E}$ and $\boldsymbol{E}'$ are calculated as follows:

$$D_{l,m1} = \sum_{d1=1}^{M} (\boldsymbol{I}{-}\boldsymbol{B})^{-1}_{,l} A_{\xi_l,m1} \tag{2.14a}$$

$$E_{l,m2} = \sum_{d1=1}^{M} \sum_{a2=1}^{M} \sum_{c1=1}^{M} (\boldsymbol{I} - \boldsymbol{B})^{-1}_{l,d1} A_{\xi'_{d1},\xi'_{a2}} C_{a2,c1} A_{\xi_{c1},m2'} \tag{2.14b}$$

$$D'_{l,m1} = \sum_{d2=1}^{M} \sum_{b2=1}^{M} \sum_{c2=1}^{M} (\boldsymbol{I} - \boldsymbol{B}')^{-1}_{l,d2} A'_{\xi'_{d2},\xi'_{b2}} C_{b2,c2} A_{\xi_{c2},m1} \tag{2.14c}$$

$$E'_{l,m2} = \sum_{d2=1}^{M} (\boldsymbol{I} - \boldsymbol{B}')^{-1}_{l,d2} A_{\xi'_{d2},m2'} \tag{2.14d}$$

where $m1 = 1{,}2{,}\ldots{,}N$ and $m2 = 1{,}2{,}\ldots{,}N'$, respectively.

To calculate the signals seen at the external outputs of either scattering matrix, Eq. 2.13a and Eq. 2.13b is substituted into Eq. 2.8b and Eq. 2.8a respectively to obtain:

$$y_j = \sum_{a1=1}^{N} \left[A_{j,\nu_{a1}} + \sum_{a2=1}^{M} \sum_{c1=1}^{M} A_{j,\xi_{a2}} C_{a2,c1} D_{c1,a1} \right] x_{\nu_{a1}} \ldots$$

$$\ldots + \sum_{a2=1}^{M} \sum_{c1=1}^{M} \sum_{b1=1}^{N'} A_{j,\xi_{a2}} C_{a2,c1} E_{c1,b1} x_{\nu'_{b1}} \tag{2.15a}$$

$$y'_{j'} = \sum_{b1=1}^{N'} \left[A'_{j',\nu'_{b1}} + \sum_{b2=1}^{M} \sum_{c2=1}^{M} A'_{j',\xi_{b2}} C_{b2,c2} E'_{c2,b1} \right] x_{\nu'_{b1}} \ldots$$

$$\ldots + \sum_{b2=1}^{m} \sum_{c2=1}^{m} \sum_{b1=1}^{N} A'_{j',\xi'_{b2}} C_{b2,c2} D'_{c2,b1} x_{\nu_{b1}} \tag{2.15b}$$

where Eq. 2.15a and Eq. 2.15b are the external output signals of the undashed and dashed systems, respectively. Both equations of Eq. 2.15 have two terms. The first term describes the scattering between an external inputs and outputs of the same system. The second describes the scattering between inputs and outputs of opposite systems (i.e., the signal that travels though the connections between the dashed and undashed system). Using Eq. 2.15, the scattering matrix of the combined system $\boldsymbol{A}''$ can be expressed as:

$$\boldsymbol{A}'' = \begin{pmatrix} \boldsymbol{A11} & \boldsymbol{A12} \\ \boldsymbol{A21} & \boldsymbol{A22} \end{pmatrix} \tag{2.16b}$$

where $\boldsymbol{A11}$, $\boldsymbol{A12}$, $\boldsymbol{A21}$ and $\boldsymbol{A22}$ are matrices of size $(N \times N)$, $(N \times N')$, $(N' \times N)$ and $(N' \times N')$, respectively. These matrices are extracted from Eq. 2.15 with $\boldsymbol{A11}$, $\boldsymbol{A22}$ and $\boldsymbol{A12}$, $\boldsymbol{A21}$ as the first and second terms from Eq. 2.15a, Eq. 2.15b, respectively. i.e.

$$\boldsymbol{A11}_{m1,m1'} = A_{m1,v_{m1'}} + \sum_{a2=1}^{M} \sum_{c1=1}^{M} A_{m1,\xi_{a2}} C_{a2,c1} D_{1,m1'} \tag{2.17a}$$

$$\boldsymbol{A12}_{m1,m2} = \sum_{a2=1}^{M} \sum_{c1=1}^{M} A_{m1,\xi_{a2}} C_{a2,c1} E_{c1,m2} \tag{2.17b}$$

$$\boldsymbol{A21}_{m2,m1} = \sum_{b2=1}^{M} \sum_{c2=1}^{M} A'_{m2,\xi'_{b2}} C_{b2,c2} D'_{c2,m1} \tag{2.17c}$$

$$\boldsymbol{A22}_{m2',m2} = A'_{m2',v'_{m2}} + \sum_{b2=1}^{M} \sum_{c2=1}^{M} A'_{m2',\xi_{b2}} C_{b2,c2} E_{c2,m2'} \tag{2.17d}$$

Where subscripts $m1' = 1,2,...,N$ and $m2' = 1,2,...,N'$. The input and output vectors of the combined system are $\boldsymbol{x}'' = [x_1'', x_2'', \dots, x_{N+N'}'']$ and $\boldsymbol{y}'' = [y_1'', y_2'', \dots, y_{N+N'}'']^T$, respectively. These vectors contain the combined external input/output terms of $\boldsymbol{x}$, $\boldsymbol{x}'$ and $\boldsymbol{y}$, $\boldsymbol{y}'$, respectively. In this formulation the first N terms of $\boldsymbol{x}''$ and $\boldsymbol{y}''$are the external input/output terms from $\boldsymbol{x}$ and $\boldsymbol{y}$. The remaining N' terms are the terms of the external input/output terms from $\boldsymbol{x}'$ and $\boldsymbol{y}'$ (i.e. $\boldsymbol{x}_{m1}'' = \boldsymbol{x}_{v_{m1}}$, $\boldsymbol{y}_{m1}'' = \boldsymbol{y}_{v_{m1}}$, $\boldsymbol{x}_{m2+N}'' = \boldsymbol{x}_{v'_{m2}}'$ and $\boldsymbol{y}_{m2+N}'' = \boldsymbol{y}_{v'_{m2}}'$).

2.3 Evaluating the Performance of the Waveguide Network Solving Algorithm

Using Eq. 2.17, the algorithm outlined in section. 2.1.2 may now be implemented to evaluate the performance of an arbitrary waveguide network. To parameterize the network, a list of waveguides and their respective properties is constructed. In this context, an individual waveguide is parameterized by 1) the labels of the junctions to which it is connected and 2) the geometrical and EM properties of the waveguide Z_c, γ and L which are the characteristic impedance, complex propagation constant and length of the waveguide. If the waveguide only connects to a single junction, then it is labelled as an external input/output waveguide. After these properties have been defined, the respective scattering matrices of each junction is calculated using Eq. 1.23 or Eq. 1.24 for a parallel or series junction, respectively. The adjacency matrix of the system is also calculated using Eq. 2.1. A flow diagram describing the full algorithm is presented in Fig. 2.6.

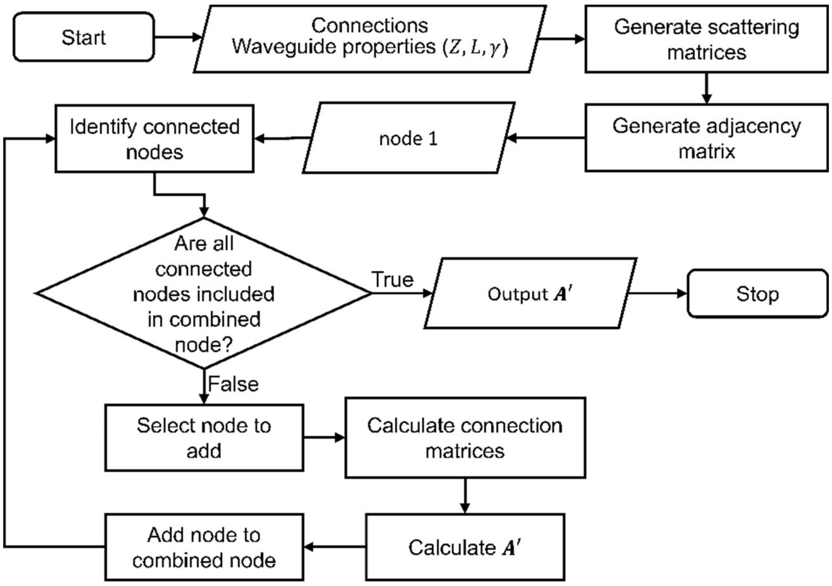

Figure. 2.6 Flow diagram of the waveguide network solving algorithm.

2.3.1 Comparison with full wave simulation results

To corroborate the validity of this method of extracting the theoretical S-parameters, an investigation was conducted to compare results produced by this method to those calculated using a commercial full-wave numerical simulation tool (in this case CST Studio Suite®, see Appendix A for more details). A schematic representation of the network constructed for this task is presented in Fig. 2.7. It is a rhombus-shaped network constructed from four series waveguide junctions. Here each waveguide has the same characteristic impedance and is filled with vacuum ($\varepsilon_r = \mu_r = 1$). The lengths of the waveguides which are the edges of the rhombus are all L_1. Another waveguide connects two of the corners of the rhombus together and has a length of L_2. An external input/output waveguide is connected to each of the junctions of the network.

To evaluate the validity of the algorithm, the S-parameters of this network are extracted for a range of L_1 and L_2 values. Here monochromatic probe signals are excited at input/output 1 of the network. In this simulation $f_0 = 10$ GHz. The reflected signal seen at input/output 1 and the signal transmitted to input/outputs 2 and 4 are then measured and used to calculate the first column of the scattering matrix of the network. The results of which are presented in Fig. 2.8 for the following length combinations: 1) $L_1 = \lambda_0$, $L_2 = \lambda_0$, 2) $L_1 = \lambda_0$, $L_2 = \lambda_0/2$ and 3) $L_1 = 2\lambda_0/3$, $L_2 = \lambda_0/2$, from left to right respectively. In all cases the S-parameters calculated by both methods are clearly in agreement with each other, indicating that the algorithm is accurately calculating the S-parameters as expected.

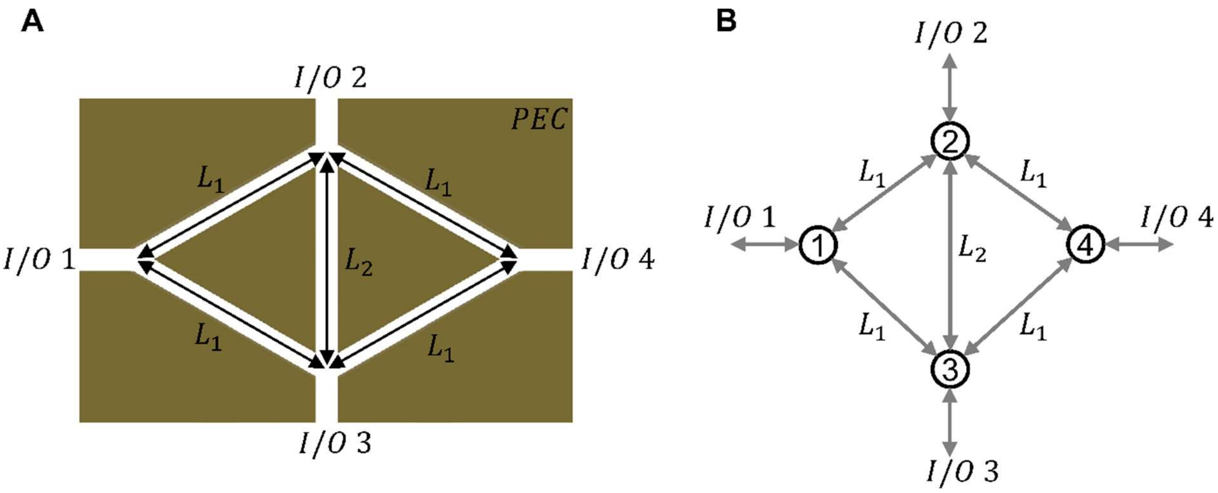

Figure. 2.7 Schematic representations of the waveguide network used to corroborate the performance of the network solving algorithm. **A.** Physical network as it was implemented in CST Studio Suite®. **B.** Graphical representation implemented in the waveguide network solving algorithm.

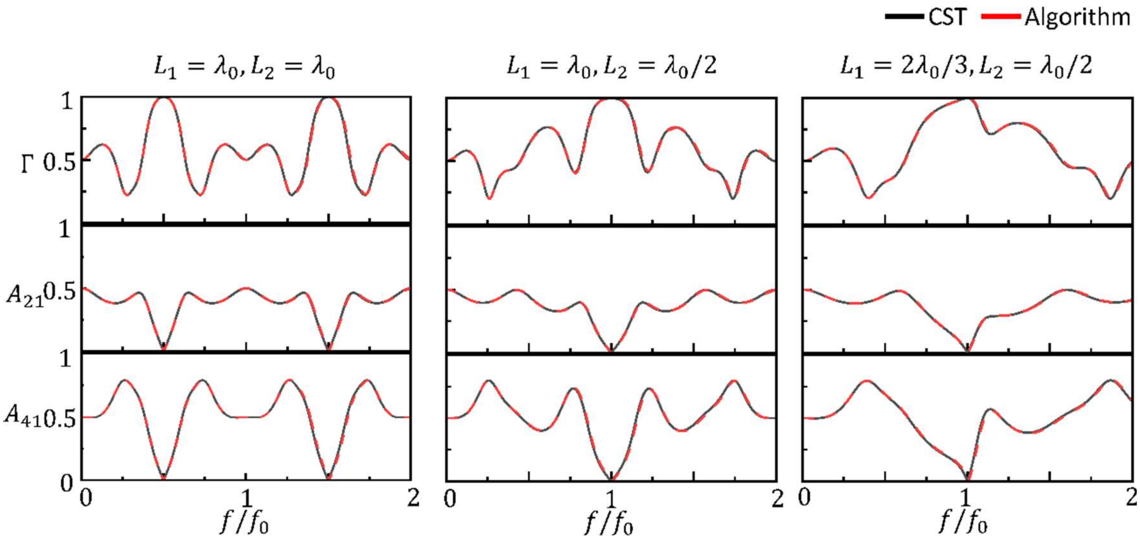

Figure. 2.8 Calculated S-parameters of the structure presented in Fig. 2.7. The reflection coefficient (top row), transmission towards port 2 (middle row) and transmission towards port 3 (bottom row) are presented for 3 combinations of L_1 and L_2.

2.4 Chapter 2 conclusions

This chapter has detailed the development of a mathematical tool for the modelling of large, interconnected networks of waveguides, based upon the combining of multiple connected scattering matrices into a single scattering matrix which captures the behaviour of the full combined system. For completeness, a full mathematical description of this technique is provided. The results produced by this tool have been validated by comparing the calculated S-parameters of a test network by the tool, to those extracted from a full-wave numerical simulation (using the commercial simulation solver CST Studio Suite®). The two datasets produced from this study are in excellent agreement with each other indicating that the tool is indeed accurate. This tool will be used throughout this thesis to aid in the design of waveguide networks for computing purposes as it enables for fast an efficient prototyping of network designs, without the need for full-wave simulation.

Chapter 3. Emulating Digital Switching with Linear Systems

In this chapter, methods of emulating the performance of digital computing systems by exploiting the linear superposition of EM pulses and waves within parallel plate waveguide networks will be exploited. To this end, two techniques will be discussed. The first technique is to emulate decision making processes in the form of $if \ldots then \ldots else \ldots$ statements by exploiting the splitting and superposition of polarized TEM pulses at series at parallel junctions. This technique is explored in Section 3.1. The results discussed in this section have also been published in the manuscript titled "Amplitude-Controlled Electromagnetic Pulse Switching Using Waveguide Junctions for High-Speed Computing Processes"[25].

The second method is to emulate the performance of conventional logic gates to calculate Boolean operations, using EM waves. This is explored in Section 3.2. Some of the methods which have been exploited in the literature for these purposes have been discussed in the introduction section of this thesis. These methods include exploiting systems with high non-linearity such as SOAs[112–114,117] or the optical Kerr effect[120,123,126]. However, in the context of this thesis these operations will instead be emulated by controlling the superposition of waves within a network of waveguide junctions i.e., a fully linear system. As will be discussed, by tailoring the structure of the waveguide network and the encoding scheme of the input data it is possible to emulate the performance elementary logical operations by exploiting the linear superposition of input signals.

3.1 Decision Making Processes with TEM Pulses of Non-constant Amplitude

Decision-making processes are a fundamental building block of computing systems. In this realm a stream (or multiple streams) of input information is categorized into output states based on how the information relates to a set of conditions. Essentially computing the solution to *if… then… else…* operations. In this section a method of performing decision making tasks based on the amplitude of incident pulses at waveguide junctions is presented. This section starts with an introduction to decision making processes with EM waves before presenting two examples of decision-making structures that can be constructed exploiting a three-waveguide junction. The first is called a *comparator*. As will be shown, this structure can be used to compare two numbers (φ_1 and φ_2) which are mapped to the amplitude of TEM pulses excited from two of the connected waveguides. The polarity of the pulse generated in the third waveguide is then determined by the relationship between φ_1 and φ_2 with a negative polarity if $\varphi_1 < \varphi_2$ and a positive polarity if $\varphi_1 > \varphi_2$ (when exploiting a parallel waveguide junction). The second is called a *pulse director*. In this structure, the reciprocal nature of waveguide junctions is exploited to perform decision making processes based on the interaction of many pulses. As will be demonstrated, when the amplitudes and polarities of the input pulses fulfil a *matched* condition, all the input energy will be directed into a single connected waveguide. However, if one or more inputs do not conform to this *matched* condition, then a portion of the input energy will instead be reflected towards one of the input junctions. This performs a decision-making process analogous to that of an AND gate, here emulated with an analogue linear system. This technique is presented firstly by exploiting a three-input junction, before extending to an N-input junction.

An example of an elementary decision-making process with TEM pulses is presented in Section 1.2.8. In that example, switching is performed by tailoring the polarity relationship between two incident signals of equal magnitude. Here, this technique is explored further to demonstrate different decision-making processes. These are enabled by exploiting many input pulses simultaneously or pulses with various input amplitudes. Unlike the example presented in Section 1.2.8, in this technique input pulses are not encoded using a binary two-state system (positive and negative polarity) and may instead possess a wide range of potential input values representative of many different tokens of data (See Fig. 3.1C). Decision making processes in the form of *if… then… else…* statements are then calculated based on the splitting and superposition of the various input pulses in parallel and series waveguide junctions (see Fig. 3.1A,B for an example of pulse interacting in a parallel or series junction, respectively).

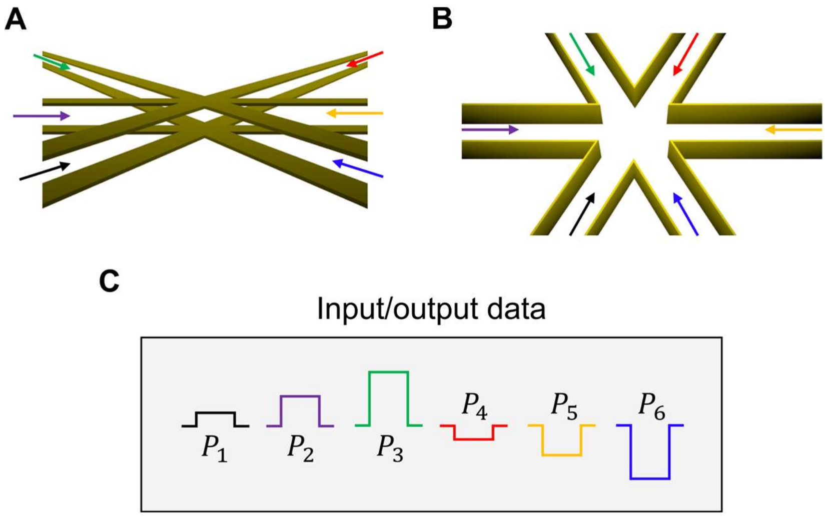

Figure 3.1 Computing with many TEM pulses of non-discretized amplitudes. **A.**, **B.** interaction of many pulses of various amplitudes in parallel and series junctions, respectively. **C.** Schematic representation of information encoded into the amplitudes and polarities of input pulses from P_1-P_6

To begin with, let us first consider the interaction of TEM square pulses within a three-waveguide junction. As in section 1.2.8, this junction is constructed using waveguides with the same geometry and materials (same characteristic impedance). This means that the scattering matrix of this system can be calculated using Eq. 1.25. In this instance as $N = 3$ (the number of connected waveguides) and $\gamma = 2/3$, meaning that the Eq. 1.20 for this system can be rewritten as:

$$\boldsymbol{y} = \pm \begin{pmatrix} \frac{-1}{3} & \frac{2}{3} & \frac{2}{3} \\ \frac{2}{3} & \frac{-1}{3} & \frac{2}{3} \\ \frac{2}{3} & \frac{2}{3} & \frac{-1}{3} \end{pmatrix} \begin{pmatrix} x_1 \\ x_2 \\ x_3 \end{pmatrix} = \pm \begin{pmatrix} \frac{-1}{3} x_1 + \frac{2}{3}[x_2 + x_3] \\ \frac{-1}{3} x_2 + \frac{2}{3}[x_1 + x_3] \\ \frac{-1}{3} x_3 + \frac{2}{3}[x_1 + x_2] \end{pmatrix} \tag{3.1}$$

where $+$ and $-$ refers to junctions connected in the parallel and series configurations, respectively. Now, consider the implications of Eq. 3.1 when two identical incident pulses, for instance from port 1 (P_1) and 2 (P_2), respectively, encounter the junction simultaneously at time t_0. In this scenario the output vector $\boldsymbol{y}$ is written as:

$$\boldsymbol{y} = \pm\frac{1}{3}\begin{pmatrix} 2x_2 - x_1 \\ 2x_1 - x_2 \\ 2[x_1 + x_2] \end{pmatrix} \tag{3.2}$$

At the time t_0, each input pulse produces three output pulses, one per waveguide, which propagate away from the junction. This means that for the 2 input pulses present in the waveguides before t_0, there are now 6 output pulses present after t_0. These outgoing pulses will then constructively or destructively interfere based on their polarities to produce the overall output signal seen in each waveguide. In both series and parallel scenarios, if the two input pulses are of the same polarity, then the pulses generated in the input waveguides (waveguides 1 and 2) will destructively interfere, reducing the magnitude of the overall signals. On the other hand, the pulses generated in waveguide 3 will constructively interfere, increasing the magnitude of the output signal in this waveguide. This is reversed when the input signals instead have opposite polarities. In this case, the pulses in the input waveguides constructively interfere, while those in waveguide 3 destructively interfere. This scenario is exploited to perform a comparison operation between two input pulses, with amplitudes which are representative of two numbers φ_1 and φ_2. Importantly, Eq. 3.2 is valid for coherent TEM pulses. If this does not hold spurious pulses will appear with durations depending on the decorherence of the pulses.

3.1.1 TEM pulse comparator: Theory and operating principles

The role of a comparator is to consider two input numbers φ_1 and φ_2 ($\varphi_1, \varphi_2 \in \mathbb{R}$) and then to return one of three possible output states[109]. State 1 when $\varphi_1 < \varphi_2$, state 2 when $\varphi_1 > \varphi_2$ and the state 3 when $\varphi_1 = \varphi_2$. This operation is implemented with TEM pulses by exploiting the destructive superposition of pulses in waveguide 3 when the input pulses from P_1 and P_2 have opposite polarity. To do this φ_1 and φ_2 are mapped onto the amplitude of the input pulses from P_1 and P_2 with $x_1 = \varphi_1$ and $x_2 = -\varphi_2$, respectively. Here, x_1 and x_2 are the input pulses excited at ports 1 and 2 of the waveguide network, respectively. With this input mapping, the amplitude of the output pulse propagating towards P_3 is:

$$y_3 = \pm\frac{2}{3}(\varphi_1 - \varphi_2) \tag{3.3}$$

Importantly, the polarity of the output pulse calculated using Eq. 3.3 will depend on the relationship between φ_1 and φ_2. For instance, in the parallel implementation Eq. 3.3 returns a positive polarity output pulse if $\varphi_1 > \varphi_2$ and a negative polarity output pulse if $\varphi_1 < \varphi_2$. Additionally, if $\varphi_1 = \varphi_2$ then both pulses generated in waveguide 3 destructively interfere completely, producing no output pulse towards P_3. The TL schematic representation of the splitting and superposition of the various input and output pulses described above is presented in Fig. 3.2A-C for the parallel implementation. Additionally, Fig. 3.2D shows the decision-tree for the comparator operation performed by this device showing the three distinct categorization regions which the output pulses are separated into.

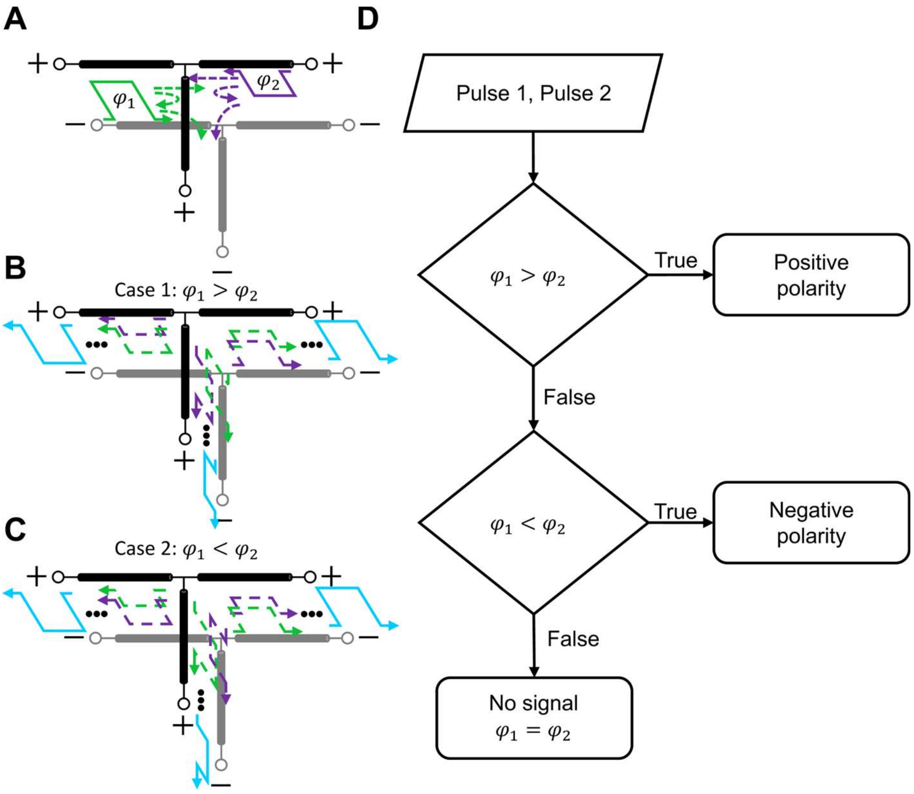

Figure 3.2 Parallel junction implementation of a TEM pulse *comparator*. **A.** Input pulses from P_1 and P_2. **B.**, **C.** Splitting and superposition of TEM pulses in the cases when $\varphi_1 > \varphi_2$ and $\varphi_1 < \varphi_2$, respectively. **D.** Decision tree of the TEM pulse *comparator* in the parallel configuration.

The implementation of the TEM pulse comparator when instead using series junctions is presented in Fig.3.3. In this scenario, the operating principle is the same as the parallel scenario however the output classification regions will be reversed due to the sign flip between the scattering matrices of the series and parallel junctions (i.e. $\boldsymbol{A}_{series} = -\boldsymbol{A}_{parallel}$ for N input perfect splitting junctions)[23,25]. The TL representation of the splitting and superposition of pulses in the series implementation of the TEM pulse comparator is presented in in Fig.3.3A-C. Likewise the decision tree for the series implementation is presented in Fig. 3.3D, showing how between the parallel and series scenarios the output classification regions for $\varphi_1 > \varphi_2$ and

$\varphi_1 < \varphi_2$ are reversed (in both scenarios $\varphi_1 = \varphi_2$ returns no output pulse towards P_3), however in both implementations the two cases are clearly distinguishable from one another.

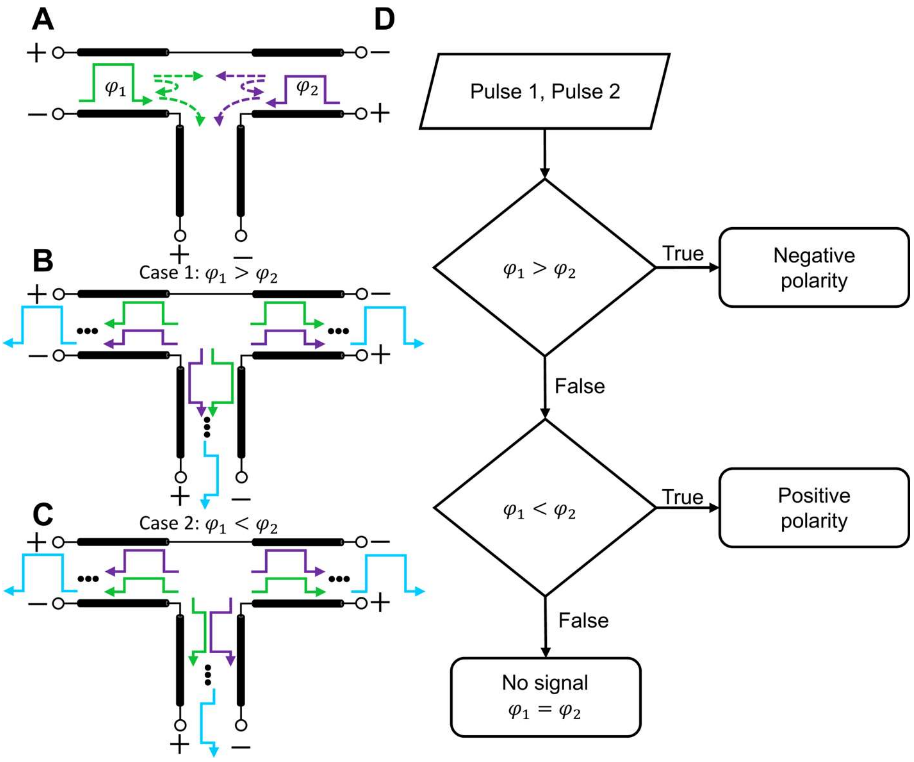

Figure 3.3 Series junction implementation of a TEM pulse *comparator*. **A.** Input pulses from P_1 and P_2. **B.**, **C.** Splitting and superposition of pulses in the $\varphi_1 > \varphi_2$ and $\varphi_1 < \varphi_2$, respectively. **D.** Decision tree for the TEM pulse *comparator* in the series configuration.

To demonstrate the generality of this approach, the theoretical amplitude of the output pulses seen at P_3 when considering a range of input combinations between $\varphi_1, \varphi_2 = -1$ and $\varphi_1, \varphi_2 = 1$ is presented in Fig. 3.4 for both the parallel (Fig. 3.4A) and series (Fig. 3.4B) cases respectively. Here the red and blue regions of the figure indicate an output pulse which is classified as positive or negative, respectively. As this technique exploits the linear superposition of pulses and is thus emulating a quasi-digital operation with an analogue system, there is a range of potential output magnitudes. This is different than a digital comparator as the output pulses are not classified as a binary 1 or 0.

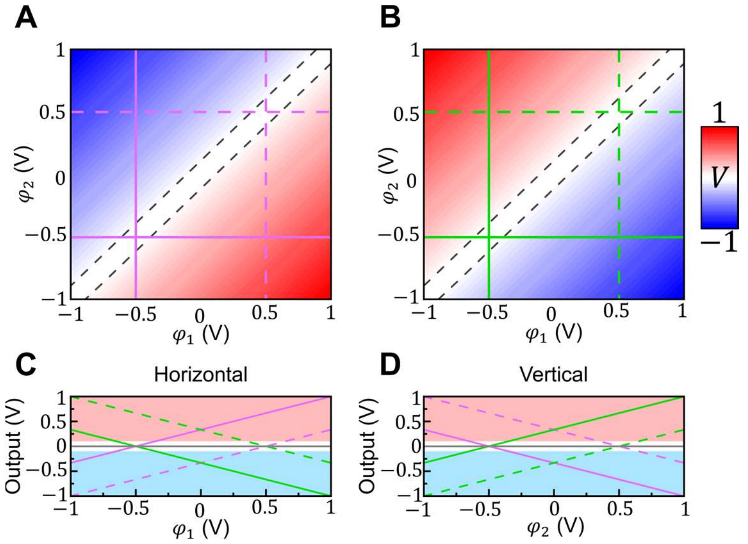

Figure 3.4 Theoretical output states of the parallel and series TEM pulse *comparator*. **A.**, **B.** Output pulse amplitude seen as P_3 in the parallel and series configurations respectively. **C.**, **D.** Output pulse amplitudes along the horizontal and vertical lines in **A** and **B**, respectively.

3.1.2 TEM pulse comparator: Numerical results

To corroborate the performance of the comparator as a decision-making process, full-wave numerical simulations of the scenarios discussed above were carried out using the transient solver of the commercial software CST Studio Suite®. These simulations were conducted for both the parallel (Fig. 3.5) and series (Fig. 3.6) scenarios. In both configurations the waveguide junctions are constructed using waveguides with a 3 mm × 3 mm cross section in the transverse plane and vacuum as the filling material ($\varepsilon_r = 1, \mu_r = 1$). The waveguides are then connected in a T-shaped junction. In Fig. 3.5 and Fig. 3.6 P_1, P_2 and P_3 are at the left, right and top, respectively. The length of waveguide between the waveguide ports and the waveguide junction is 250 mm. At time $t = 2$ ns two TEM pulses with a duration of 0.4 ns are excited, one at P_1 and one at P_2, respectively. These TEM pulses thus encounter the junction between waveguides at $t_0 = 2.83$ ns.

In both Fig. 3.5 and Fig. 3.6 two scenarios are presented. The first (Fig. 3.5A and Fig. 3.6A) is when $\varphi_1 < \varphi_2$. Here $\varphi_1 = 3$ and $\varphi_2 = 5$. Using the pulse amplitude mapping discussed above, this means that 3 V and -5 V pulses are excited at P_1 and P_2, respectively. In the second scenario (Fig. 3.5B and Fig. 3.6B) this relationship is reversed, now with $\varphi_1 = 5$ and $\varphi_2 = 3$ (i.e. $\varphi_1 < \varphi_2$) meaning the input pulse amplitudes are now 5 V and -3 V at P_1 and P_2, respectively. In Fig. 3.5 snapshots are presented of the out-of-plane E_z field at a time before ($t = 2.5$ ns) and after ($t = 3.4$ ns) t_0 for the parallel scenario. Likewise, in Fig. 3.6 snapshots of the out-of-plane H_z-field are presented for the same times, now in the series scenario. In both figures the results presented are normalised to the maximum field value obtained at the centre of the 3 V pulse. Looking at the polarity of the pulses in the $t = 3.4$ ns snapshot of Fig. 3.5A,B it can be seen that between the $\varphi_1 < \varphi_2$ and $\varphi_1 > \varphi_2$ scenarios the comparator successfully outputs a negative and positive pulse, respectfully, as expected. Furthermore, by observing the voltage values seen at each of the connected ports (bottom panels), the output pulses have an amplitude of -1.338 V and 1.338 V, respectively. These results are in excellent agreement with the theoretical values predicted by Eq. 3.3: $-4/3$ V and $4/3$ V, respectively. In the series, scenario (Fig. 3.6), the output pulses in case 1 and case 2 are now positive and negative, respectively with calculated pulse amplitudes of 1.342 V and -1.350 V. These results are also in agreement with the predicted amplitudes of $4/3$ V and $-4/3$ V, respectively.

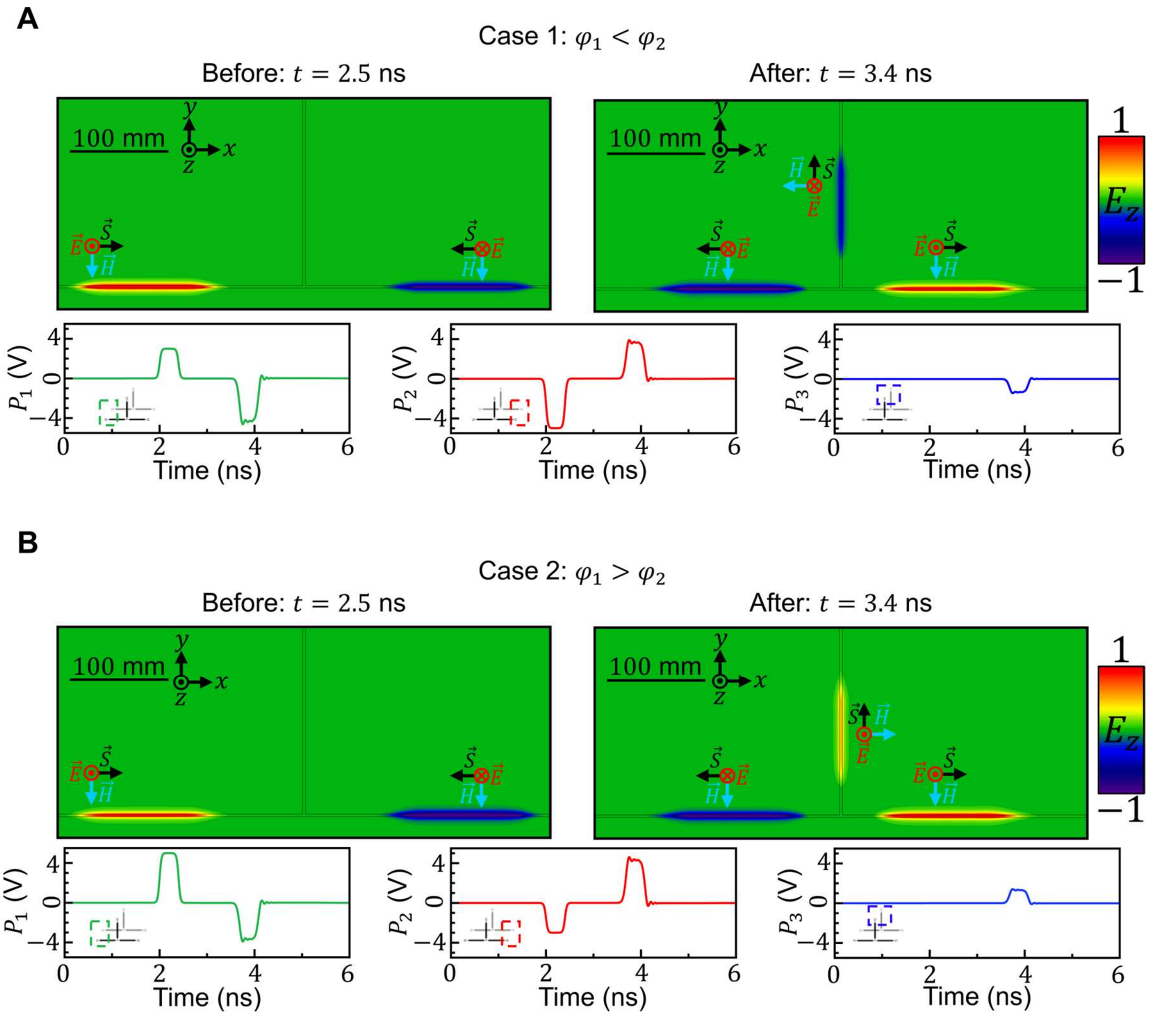

Figure 3.5 Numerical results for the out-of-plane E_z-field for the TEM pulse *comparator* in the parallel configuration. The top-left and top-right panels shown the field distributions at a time before and after the pulses interact with the waveguide junction, respectively. The bottom panels show the voltage observed at P_1-P_3 from left to right, respectively. **A.**, **B.** Results of the cases when $\varphi_1 < \varphi_2$ ($\varphi_1 = 3$, $\varphi_2 = 5$) and $\varphi_1 > \varphi_2$ ($\varphi_1 = 5$, $\varphi_2 = 3$), respectively.

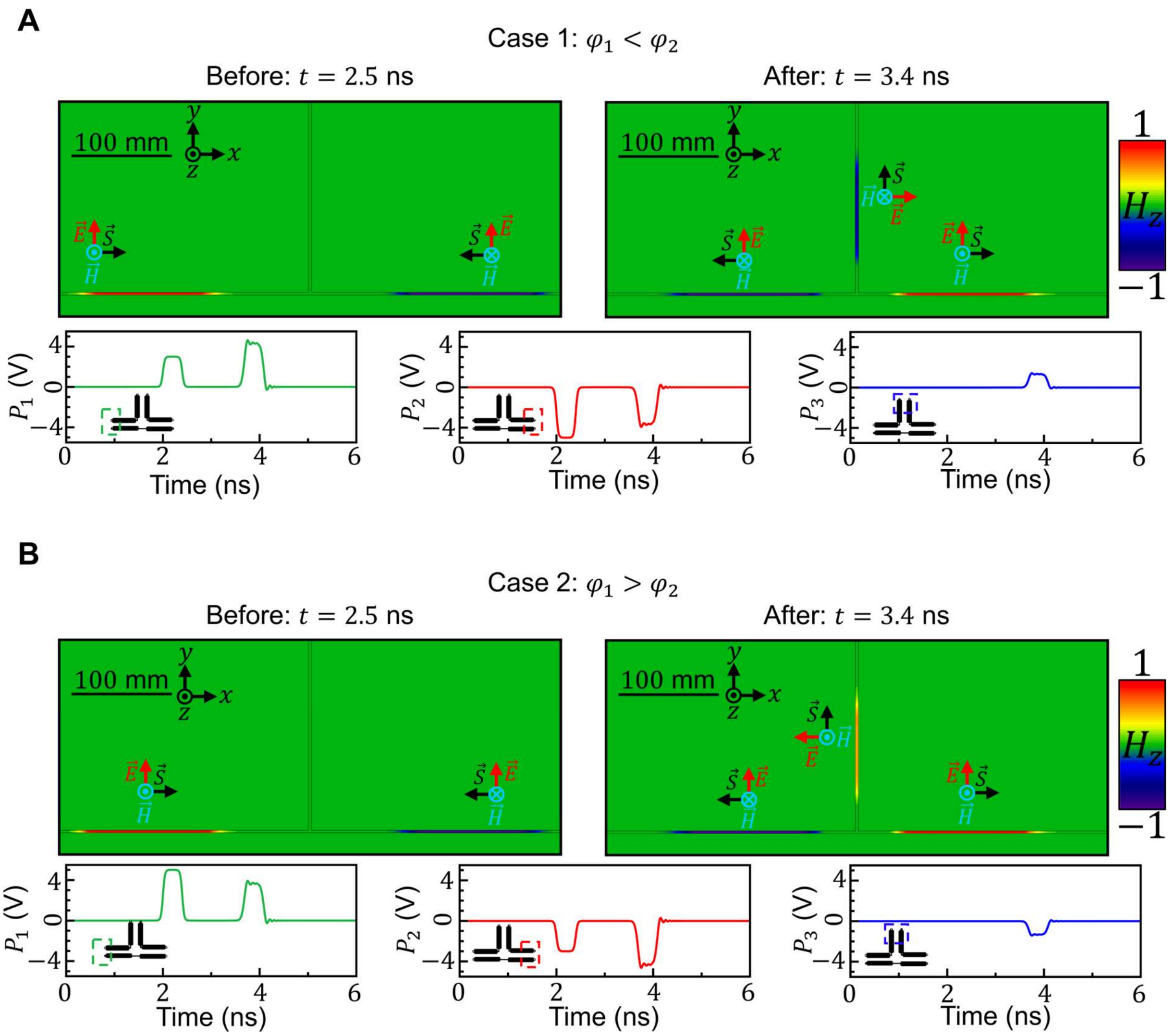

Figure 3.6 Numerical results for the out-of-plane H_z-field for the TEM pulse *comparator* in the series configuration. Panels have the same layout as in Fig. 3.5.

3.1.3 TEM pulse director: Theory and operating principles

Another example of decision-making processes with TEM pulses is the TEM pulse *director*. This technique exploits a combination of input pulses which produce only a single output pulse directed towards a single port to calculate decision making processes with many input pulses. This combination of input pulses (input vector $\boldsymbol{x}$) is referred to as a *matched* input vector. As it will be shown, the concept of a *matched* input vector may be extended to a waveguide junction with N connected waveguides. However, to demonstrate how this may be exploited for decision making processes, first consider the three-waveguide example. To calculate the matched condition, the reciprocity of the scattering matrix shown in Eq. 3.1 is exploited. In this context a desired output vector y is used to reconstruct an input vector $\boldsymbol{x}$ by using $\boldsymbol{x} = \boldsymbol{Ay}$. For example, consider the output vector $\boldsymbol{y} = [0,0,\zeta]$ V, where ζ is an arbitrary real number. The input vector required to construct this output vector is:

$$\boldsymbol{x} = \pm \begin{pmatrix} \frac{-1}{3} & \frac{2}{3} & \frac{2}{3} \\ \frac{2}{3} & \frac{-1}{3} & \frac{2}{3} \\ \frac{2}{3} & \frac{2}{3} & \frac{-1}{3} \end{pmatrix} \begin{pmatrix} 0 \\ 0 \\ \zeta \end{pmatrix} = \zeta \begin{pmatrix} \frac{2}{3} \\ \frac{2}{3} \\ \frac{-1}{3} \end{pmatrix} \tag{3.4}$$

Meaning that the input TEM pulses excited at P_1-P_3 should have amplitudes of $2\zeta/3$ V, $2\zeta/3$ V and $-1\zeta/3$ V, respectively to ensure all the power from the input pulses is redirected towards P_3. Additionally, if one (or more) of these pulse amplitudes does not conform to this *matched* condition then a portion of the input power will be instead directed towards P_1 and P_2. A schematic representation of the splitting and superposition of pulses in this scenario is presented in Fig. 3.7A,B and Fig. 3.8A,B for parallel and series three-input TEM pulse directors. The decision tree of the decision-making process which is calculated by this structure is presented in Fig. 3.7C. Here ϕ_1 and ϕ_2 are the numbers encoded into the two input pulses with $x_1 = \phi_1$ and $x_2 = \phi_2$, respectively. The output states are distinguished based on the presence of (or lack of) reflected output signals directed towards P_1 and P_2.

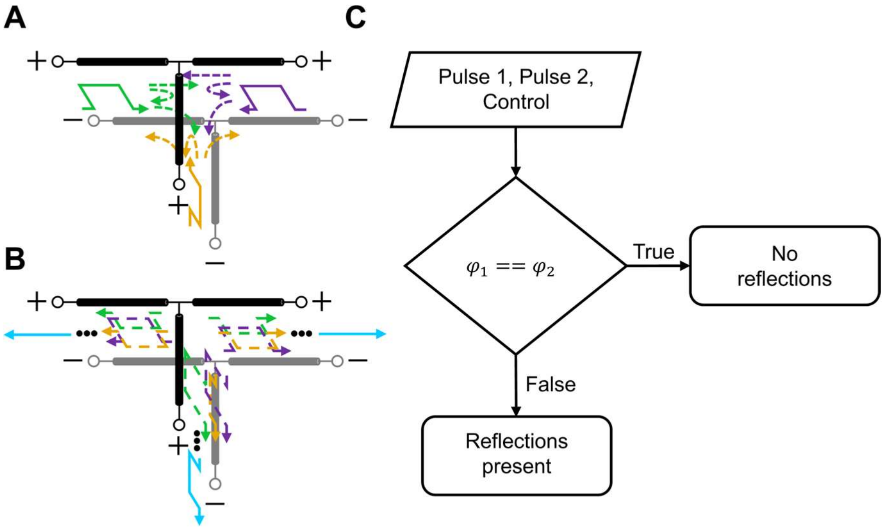

Figure 3.7 TL schematic representation of the parallel junction implementation of a TEM pulse *director*. **A.** Input pulses excited at P_1-P_3 for a matched input vector. **B.** Splitting and superposition of the TEM pulses in **A** after the interaction with the junction. **C.** decision tree of the TEM pulse *director*.

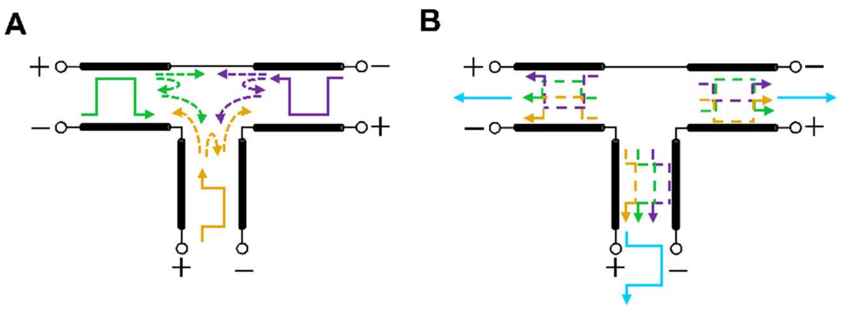

Figure 3.8 TL schematic representation of the series implementation of the TEM pulse *director*. **A.** Input pulses excited at P_1-P_3 for a matched input vector. **B.** Splitting and superposition of TEM pulse in **A** after the junction interaction. The decision tree of this scenario is the same as in Fig. 3.7C.

The TEM pulse *director* can be exploited to emulate an AND-like operation. For instance, if a TEM pulse with an amplitude of $-1/2$ V is excited at P_3 as a control signal (i.e. a signal which is excited independently to the input signals), then the input vector $\boldsymbol{x}$ is only a *matched* vector if the pulse amplitudes at P_1 and P_2 are both 1 V. This leads to the conditional statement "*If* (Input pulse amplitude at $P_1 == 1$ V) AND (Input pulse amplitude at $P_2 == 1$ V) *Then* return (No reflected pulses) *Else* return (Reflected pulses)" which is analogous to the performance of an AND gate where "no reflected pulses" is interpreted as logical 1 and "reflected pulses" is interpreted as logical 0. This is different than the performance of a digital AND gate as, similar to the TEM pulse *comparator*, the inputs of the TEM pulse *director* are analogue and thus may take a wide range of values.

The theoretical output pulse amplitudes seen at P_1-P_3 in this scenario are presented in Fig. 3.9 for the parallel (Fig. 3.9A) and the series (Fig. 3.9B) cases, respectively. Here the input pulse amplitudes can vary in the range from -2 V to 2 V and the control pulse at P_3 is $-1/2$ V. This control value is chosen so that the matched input vector is when $x_1 = x_2 = 1$ V. As it can be seen, each port has its own unique line of zero output amplitude. For P_1, P_2 and P_3 these lines are $x_2 = x_1/2 + 1/2$, $x_2 = 2x_1 - 1$ and $x_2 = -x_1 + 1/4$, respectively. The input combination which produces a matched input vector is thus the intersection of the zero output lines for P_1 and P_2. This position is marked with a star. Additionally, Fig. 3.10 show the portion of input power which is directed towards P_1, P_2 (Fig. 3.10A) and P_3 (Fig. 3.10B), respectively. As expected, only when the input vector is *matched* will 100% of the input power be directed towards P_3, indicated by the minimum in Fig. 3.10A or the maximum in Fig. 3.10B.

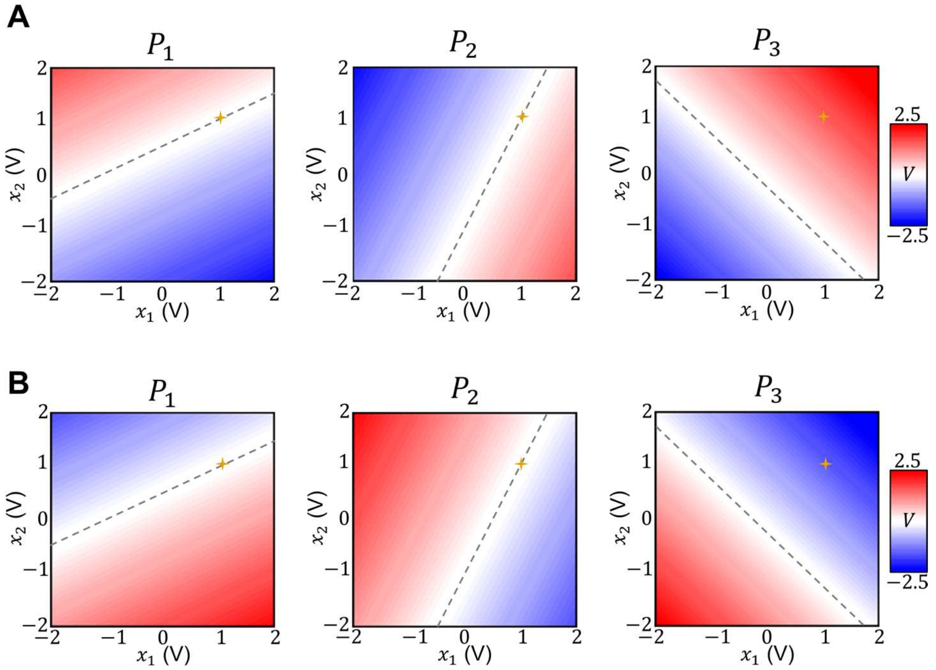

Figure 3.9 A., B. Theoretical output pulse amplitudes for the three-port TEM pulse director in the parallel and series configurations when excited with an input vector $\boldsymbol{x} = [x_1, x_2, -1/2]$ V. The left, middle and right panels show the output pulse amplitude at P_1, P_2 and P_3 after the interaction with the waveguide junction, respectively. The dashed lines in panel are the 0 V contour lines. These are $x_2 = x_1/2 + 1/2$, $x_2 = 2x_1 - 1$ and $x_2 = -x_1 + 1/4$ for the left, middle and right panels, respectively. The star indicates the intersection point between the dashed lines in the left and middle panels.

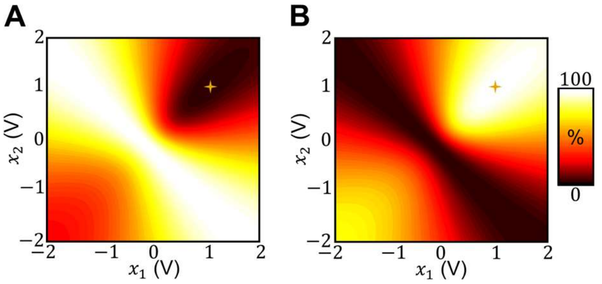

Figure 3.10 A., B. Theoretical percentage of total input power which is directed towards the input and output waveguides, respectively. As in Fig. 3.9 the input vector is $\boldsymbol{x} = [x_1, x_2, -1/2]$ V.

3.1.4 TEM pulse director: Numerical results

To corroborate the performance of the TEM pulse director, a numerical study of the scenario presented in Fig. 3.7 and 3.8 is conducted. Using the same structure and simulation setup as discussed in section 3.2.2, numerical results considering four different input vectors $\boldsymbol{x}$ are calculated. These are as follows: 1) $\boldsymbol{x} = [1,1,-1/2]$ V, 2) $\boldsymbol{x} = [-1,1,-1/2]$ V, 3) $\boldsymbol{x} = [1,-1,-1/2]$ and 4) $\boldsymbol{x} = [-1,-1,-1/2]$. The numerical results of these cases are presented in Fig. 3.11A-D, respectively for the parallel implementation and Fig. 3.12A-D, respectively for the series implementation. The theoretical and numerical output signals for these combinations are presented in Table. 3.1. As can be seen, the numerical results are in clear agreement with the theoretical results.

Input signals (V)		Port 1 output (V)		Port 2 output (V)		Port 3 output (V)	
Port 1	Port 2	Theo.	Num.	Theo.	Num.	Theo.	Num.
-1	-1	0	$2.44E-3$	0	$2.2E-3$	$-3/2$	1.509
-1	1	$-2/3$	0.675	$4/3$	-1.344	$-1/6$	0.168
1	-1	$4/3$	-1.344	$-2/3$	0.675	$-1/6$	0.168
1	1	$-2/3$	-0.673	$-2/3$	-0.672	$-7/6$	-1.172

Table 3.1 Theoretical and numerical output pulse amplitudes of the TEM pulse director for multiple input combinations. For each combination the amplitude of the pulse excitted at port 3 is $-1/2$ V.

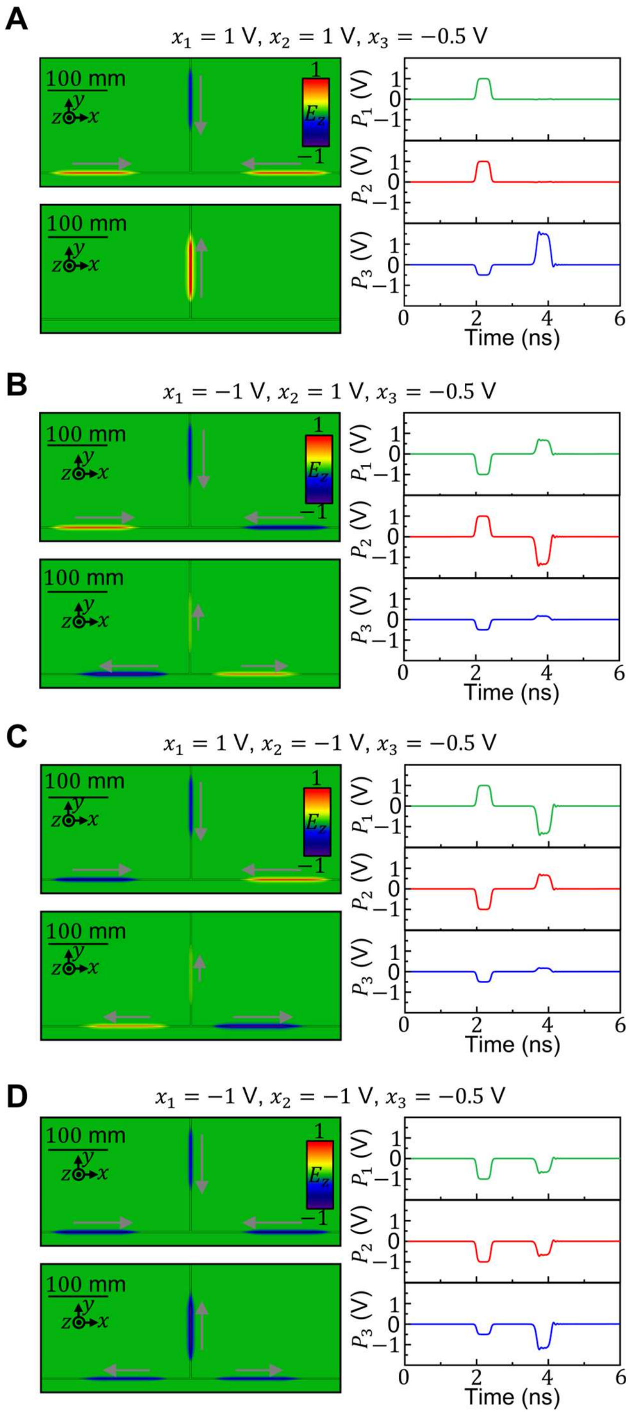

Figure 3.11 Numerical results for the out-of-plane E_z-field in the parallel implementation of the TEM pulse *director*. **A.**, **B.**, **C.**, **D.** Numerical results for the input vectors $\boldsymbol{x} = [1,1,-1/2]$, $\boldsymbol{x} = [-1,1,-1/2]$, $\boldsymbol{x} = [1,-1,-1/2]$ and $\boldsymbol{x} = [-1,-1,-1/2]$, respectively. The top-left and bottom-left panels show the field distribution at a time before and after the pulses interact with the junction, respectively. The right panels show the voltage calculated at P_1-P_3 from top to bottom, respectively.

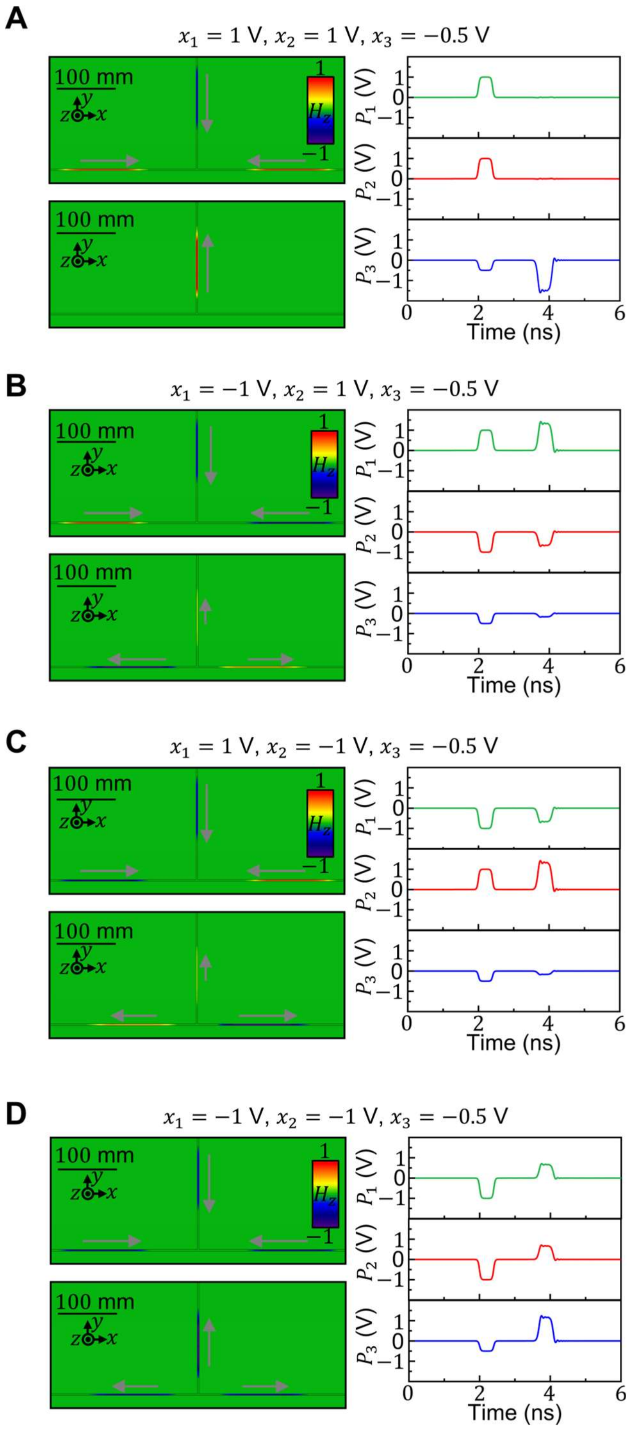

Figure 3.12 Numerical results for the out-of-plane H_z-field in the series implementation of the TEM pulse *director*. Panels are arranged the same as in Fig. 3.11

3.1.5 TEM pulse director with N inputs

The TEM pulse *director* technique for decision making processes can also be extended to an N waveguide junction, where $N = [1,2,3,...]$. In this scenario, the TEM pulses are to be directed towards port N (i.e., P_N). Meaning the control signal is applied from P_N while P_1-P_{N-1} act as inputs to the decision-making process. As before the *matched* condition is calculated by considering a single input pulse of amplitude ζ from P_N. This produces an output vector $\boldsymbol{y} = \pm[-2\zeta/N, -2\zeta/N, \ldots, \zeta(N-2)/N]$ V with $+$ and $-$ for parallel and series junctions respectively. Renormalizing this for an input pulse amplitude of 1 V gives the *matched* input vector of an N waveguide junction as:

$$\boldsymbol{x}_{matched} = \pm[1,1,\ldots,\frac{(2-N)}{2}] \tag{3.5}$$

Numerical simulations of this scenario are presented in Fig. 3.13 for an $N = 8$ waveguide junction in the series configuration. These simulations are conducted using the time domain solver of the commercial software COMSOL Multiphysics® (see Appendix A for more details). COMSOL Multiphysics® is used for this simulation instead of CST Studio Suite® as COMSOL Multiphysics allows for input ports with arbitrary orientation (i.e. off axis). As in the previous section, the waveguide junction is constructed using waveguides with square 3 mm × 3 mm cross section and a length of 250 mm between the waveguide ports and the waveguide junction. In this scenario the *matched* input vector is $\boldsymbol{x}_{matched} = [1,1,1,1,1,1,1,-3]$ V. As observed, after the interaction with the junction only a single TEM pulse is present, propagating towards P_8. This pulse has an amplitude of -3.999 V which is in good agreement with the theoretical output pulse amplitude of -4 V, demonstrating how this technique may be extended to a waveguide junction with an arbitrary number of connected waveguides.

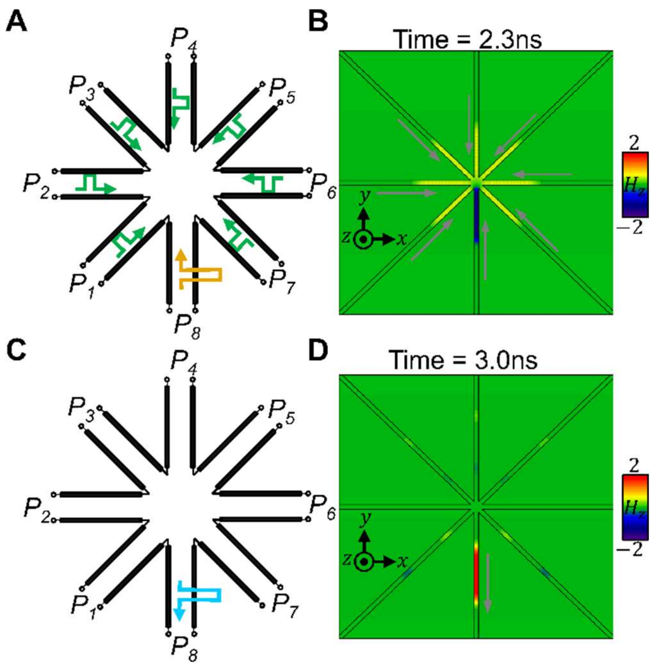

Figure 3.13 Numerical results for the out-of-plane H_z-field in the series implementation of the eight-waveguide TEM pulse *director*. **A.**, **C.** TL schematic representation of the pulses before and after they interact with the junction, respectively. **B.**, **D.** H_z-field distribution at a time before and after the pulses interact with the junction, respectively.

3.2 Mimicing linear logic gates with EM waves

Linear logic gates are systems which exploit the linear superposition of EM signal to emulate the performance of a digital logic gate using an analogue system[25,128]. This is desirable due to the high switching speeds, an inherent potential for parallel operations and energy efficiency as external power sources are not required[22,128]. As discussed in the introduction this can done by tailoring the relative path lengths of signals in order to enforce their constructive or destructive interference at the output of a system. In this realm it has been shown how digital operations such as the 7 elementary logic gates[128], NOT, AND, OR, XOR, NAND, NOR and XNOR, can be emulated using linear systems such as MZI networks[130], dielectric waveguides[82,129] and plasmonic waveguides[82,128,131,132,134] among others. For completeness, the truth tables of these 7 elementary logic operations is shown in Table. 3.2. In this section of the thesis the implementation of linear logic gates using the networks of parallel plate waveguides will be investigated. For completeness, this section begins with an overview of the core principles of linear logic gates. This includes numerical simulations of the elementary logic gates NOT, OR and AND when implemented using parallel plate waveguide networks, as examples. It is then shown how the same principles may be exploited to produce N-input linear logic gates with cascaded AND, OR and XOR gates presented as an example. Finally, it is shown how linear logic gates with many inputs and outputs may be produced with examples including a half-adder, 2-bit adder presented. At the time of writing a manuscript based on these results is currently in preparation. As such further examples, such as a linear full adder and 8-input AND gate and numerical field results for all-input combinations of the 2-bit adder structure have been omitted where necessary.

Inputs		Outputs						
Bit 1	Bit 2	NOT	AND	OR	XOR	NAND	NOR	XNOR
0	0	1	0	0	0	1	1	1
0	1	1	0	1	1	1	0	0
1	0	0	0	1	1	1	0	0
1	1	0	1	1	0	0	0	1

Table 3.2 Truth table for all 7 elementary logic operations. Here the NOT operation is applied to only input Bit 1.

As in conventional digital electronics, linear logic gates consider input signals excited with one of two possible values, representative of a logical high and logical low input, respectively. However, unlike conventional electronics where logical values may be represented by a 0 or 5 V pulse[172], linear logic gates may exploit different encoding schemes to assist in implementing different logical operations. In practice, the voltage values in the electronic system may be defined differently and also have a range of input values, however this is associated with the switching threshold values of the MOSFETs used to construct the logic gate instead of the operation itself[75]. For instance, in the literature it has been shown how by encoding information into the phase of an input signal such as $L = 1\angle\pi$ V and $H = 1\angle 0$ V, where L and H are the low and high input values, one can emulate the performance of an XOR or XNOR gate[128,136,173]. On the other hand, when realizing a linear OR gate it is instead convenient to encode input data into the magnitude of an input signal with $L = 0$ V (no signal) and $H = 1\angle 0$ V[128,135], respectively. Additionally, an offset signal which is constantly applied from one input may be used to assist in implementing the logical operation. The signal seen at the output of an N-input linear logic system is then as follows[128]:

$$y_{out} = A_{out,offset}x_{offset} + \sum_{a}^{N} A_{out,a}x_a \tag{3.6}$$

where $A_{out,a}$ is the scattering coefficient between the input port a and the output of the system. x_a is the input value at port a which may take the value L_a or H_a when representing a logical low or logical high input signal, respectively. x_{offset} is the monochromatic offset signal which is applied independently of the input signals with the scattering coefficient towards the output as $A_{out,offset}$. Eq. 3.6 is then exploited to emulate digital operations by tailoring the values of $A_{out,a}$, the encoding of x_a and the applied offset signal x_{offset} for instance by tailoring the impedances and lengths of waveguides within an interconnected waveguide network. In this scenario x_a is the phasor value of a monochromatic source.

One key distinction between a linear logic system and one which exploits non-linearities is the range of potential output values which may be attained. In a non-linear system it is conceptually possible to control the output values of each input combination independently[109]. This is not possible with a linear system as there are not enough independent variables in Eq. 3.6 to achieve this. It is however still possible to emulate digital operations by engineering the structure such that output values are separated into distinct regions which may then be classified as logical high and logical low, respectively. For instance, an output signal may be classified as high or low if it has a magnitude > 1 V or < 0.5 V, respectively. This is different than a true digital system as here the phases of the output signals are not considered and may take any value. Additionally, the output classification of signals may differ from the input encoding of signal, which poses a challenge when cascading linear logic gates together. To evaluate the performance of a linear logic gate the contrast ratio is defined as follows:

$$Contrast\ ratio = |20 \log_{10}\left(\frac{Threshold_{High}}{Threshold_{Low}}\right)| \tag{3.7}$$

where $Threshold_{High,low}$ are the threshold voltages of the high and low classification regions. Eq. 3.7 represents the distinguishability of the high and low output states in dB. When designing a linear logic gate, it is preferable to optimise the structure and the encoding scheme to maximize the value of Eq. 3.7. This is to minimize the possibility of an output signal being misclassified. As an example, it has been shown in previous works that the maximum attainable value of $Threshold_{High}/Threshold_{low}$ for a linear system is 3 (when considering voltages) meaning that the theoretical maximum contrast ratio of a linear AND operation is 9.542 dB[127,128].

3.2.1 Linear elementary logic gates

To begin with, first consider how the elementary logic gates may be implemented using Eq. 3.6. These gates are as follows: NOT, AND, OR, XOR, NAND, NOR and XNOR. The NOT gate is a one-to-one logic gate while the remaining are all two-to-one logic gates. Schematic representations of the waveguides structures which are exploited to emulate these operations are presented in Fig. 3.14. Fig. 3.14A shows the one-to-one structure used to emulate a NOT gate. This structure consists of three waveguides: one input, one output and an offset. The lengths of the input and offset waveguides are L_1 and $L_1 + \Delta L_{off}$, respectively. These values are defined from the center of the waveguide port to the center of the waveguide junction. In this example each waveguide has the same characteristic impedance Z_0. The signal seen at the output waveguide is thus:

$$|y_{out}| = |\frac{2}{3}\left(x_1 + x_{off}e^{ik\Delta L_{off}}\right)| \tag{3.8}$$

where k is the wavenumber of the EM wave inside the parallel plate waveguides. Fig. 3.14B shows the general structure of a two-to-one logic gate. This is the same structure as in Fig. 3.14A, now with the addition of a fourth waveguide which acts as a second input. This waveguide has a characteristic impedance of Z_0 and a length of $L_1 + \Delta L_2$. The signal seen at the output waveguide of this structure is:

$$|y_{out}| = |\frac{1}{2}\left(x_1 + x_2e^{ik\Delta L_2} + x_{off}e^{ik\Delta L_{off}}\right)| \tag{3.9}$$

Using these structures all 7 of the elementary linear logic gates can be emulated. As examples to demonstrate the key principles of linear logic gates, the implementation of the NOT, AND and OR operations is presented in the following section.

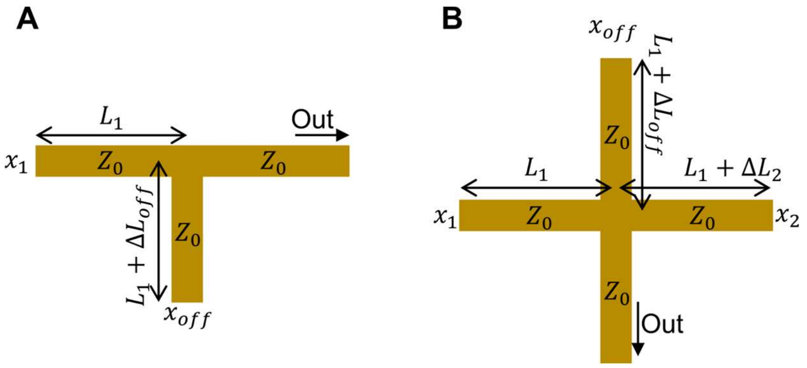

Figure 3.14 Structure of elementary logic gates. **A.** One-input logic gate (NOT gate) **B.** Two-input logic gates without offset (XNOR, XOR and OR). **C.** Two input logic gates with offset (AND NAND and NOR).

Linear NOT gate

A NOT gate is a structure which takes a single input signal and returns an output signal in the opposite state to the input signal i.e. for the input signals representing digital 0 and 1 the output signal should be classified as 1 and 0 respectively. Now, how can this performance be emulated using the structure in Fig. 3.14A and Eq. 3.8? To answer this, consider the simple encoding scheme for x_1, $L_1 = 0$ V and $H_1 = 1\angle 0$ V. This means that the magnitude of the output signal is $|(2/3)x_{off}|$ and $|(2/3)\left(1 + x_{off}e^{ik\Delta L_{off}}\right)|$ when x_1 is in the low and high input states respectively. Clearly if $x_{off}e^{ik\Delta L_{off}} = -1$ then the high input signal will destructively interfere with the offset signal. This produces no output signal, which may then be classified as the low output state. This is the case when $\Delta L_{off} = \lambda/2$ and $x_{off} = 1$, where λ is the wavelength of the CW signal inside the waveguides.

Numerical simulations of this scenario are presented in Fig. 3.15. Here monochromatic $\lambda = 30$ mm input signals are used and $L_1 = \lambda$. In this scenario and as will be the case for all numerical simulations presented in section 3.3.1 the waveguides used to construct the junction have a 1 mm × 1 mm cross section and the junction is connected in series. Fig. 3.15 shows the power distribution for the low and high input cases respectively. As it can clearly be seen when the high signal H_1 is excited from the left waveguide it destructively interferes with the offset signal from the lower waveguide producing no output signal. On the other hand, when the low signal L_1 is excited, the offset signal is free to propagate towards the output. These two output scenarios are classified as logical low and high respectively. The voltage signals seen at the output waveguide are $|y_{out}| = 0.666$ V and $|y_{out}| = 0.0406$ V for the low and high input cases. These values are in good agreement with the theoretical values of $|y_{out}| = 2/3$ V, and

$|y_{out}| = 0$ V, respectively. Using Eq. 3.7 the contrast ratio using of the linear NOT operation is calculated as 24.303 dB.[128,174]

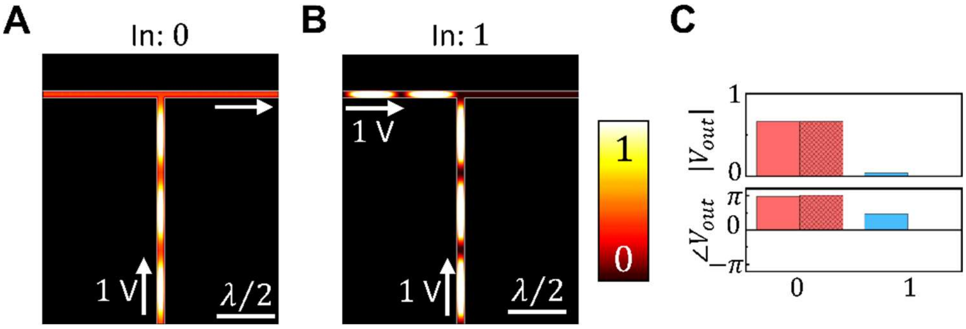

Figure 3.15 Linear NOT gate. **A.**, **B.** Power distribution of the low and high input cases, respectively. Results are normalized to the input power of a 1 V signal. **C.** Amplitude (top) and phase (bottom) of the numerically calculated output signals. Hashed and solid bars show the theoretical and numerical results, respectively.

Linear AND gate

Next, is the implementation of a linear AND gate. This is an operation which should return a high output state if and only if both of the input signals are high. Using the structure presented in Fig, 3.14b and Eq. 3.9, one can envision a linear AND gate using the input encoding $L_1 = L_2 = 0$ V, $H_1 = H_2 = 1$ V in which the waveguide lengths are designed to that the high input signals are in-phase when they arrive at the junction (i.e., $\Delta L_2 = 0$). Using Eq. 3.9 the output magnitudes of the 00, 01, 10 and 11 input combinations are calculated as 0 V, 1/2 V, 1/2 V and 1 V, respectively. This means the theoretical contrast ratio of this operation is 6.021 dB. In this scenario there are two possible output magnitudes which are classified as low, 0 V and 1/2 V. It is possible to improve the contrast ratio of this operation, either by changing the input encoding or by including an offset signal, by reducing the range of potential low outputs. The optimal contrast ratio is achieved when using an offset signal $x_{off} = 0.5$ V and an offset waveguide length $\Delta_{off} = \lambda/2$.

Numerical simulations of this scenario are presented in Fig. 3.16. This shows the power distribution for the four possible input combinations. As it can be seen, the high output signal for the 11 input combination is clearly distinguishable from the other inputs. The numerically calculated output signals for the 00, 01, 10 and 11 input combinations where 0.25 V, 0.251 V 0.251 V and 0.751 V, respectively. This means that the contrast ratio of the AND operation is 9.497 dB, which is close to the known theoretical maximum contrast ratio of 9.54 dB[128] for a linear AND gate. One important detail to note is the phase of the output signals. In this scenario, though both being classified as low, the 00 output signal is $\sim\pi$ rad out-of-phase with the 01 and 10 output signals. This means that while the output signals may be successfully classified as low based on their magnitude, they are not the same output state. This is a consequence of the linearity of the system, which for a two-input linear logic gate imposes the following constraint onto the possible output values[109]

$$y_{0,0} + y_{1,1} = y_{0,1} + y_{1,0} \tag{3.10}$$

where $y_{0,0}$, $y_{0,1}$, $y_{1,0}$ and $y_{1,1}$ are the output values for the 00, 01, 10 and 11 input cases, respectively.

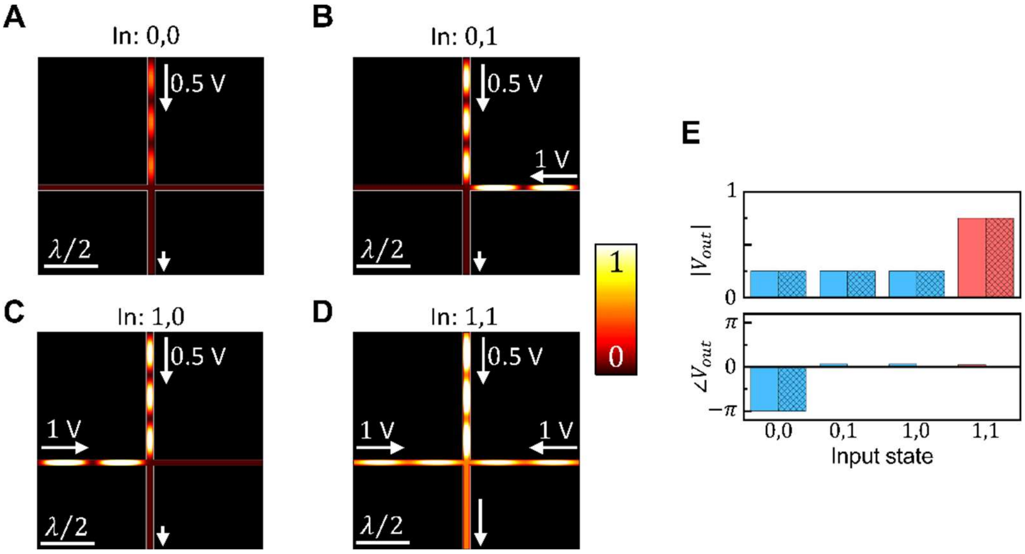

Figure 3.16 Linear AND gate. **A.**, **B.**, **C.**, **D.** Power distribution of the 00, 01, 10 and 11 input cases, respectively. Results are normalized to the input power of a 1 V signal. **E.** Amplitude (top) and phase (bottom) of the output signals in each case. Hashed and solid bars show the theoretical and numerical results, respectively.

Linear OR gate

Finally, consider the implementation of a linear OR gate. For this logic gate the output should return high if one or more of the input signals are high. As with the AND gate this operation can also be emulated using the encoding scheme $L_1 = L_2 = 0$ V, $H_1 = H_2 = 1$ V with $\Delta L_2 = 0$. However, in this case the minimum voltage threshold for a high output signal should be chosen to also include the $1/2$ V, 01 and 10 signals. Using this encoding and structure, it can be seen that there are two possible values of a high output signal ($2/3$ V and $4/3$ V). This does not affect the distinguishability of the operation (i.e., the contrast ratio), however when designing linear logic gates, it is desirable to minimize the range of the output classification regions, so that an output state is easily identifiable[128]. For the linear OR operation, the range of potential high output signals is minimized when $\Delta L_2 = 2\lambda/3$. Full-wave numerical simulations of this scenario are presented in Fig. 3.17. In this example, as no offset signal is necessary (i.e., $x_{off} = 0$ V), the offset waveguide has been removed. This means that Eq. 3.9 is now modified to replace the factor of $1/2$ with $2/3$. As it can be seen the three high output combinations are clearly distinguishable from the 00 combination meaning the OR operation is successfully emulated. The calculated output signals for the 00, 01, 10 and 11 input combinations are 0 V (No input signals), 0.666 V, 0.666 V and 0.665 V, respectively. These are in good agreement with the theoretical values from the modified Eq. 3.9, which are 0 V and $2/3$ V for the low and high output signals respectively. In this example a contrast threshold cannot be easily defined as the low output threshold is 0 V. In practice, one could calculate a contrast ratio by defining an upper limit for signals classified as low. However, this definition would be application specific depending on the noise of the system.

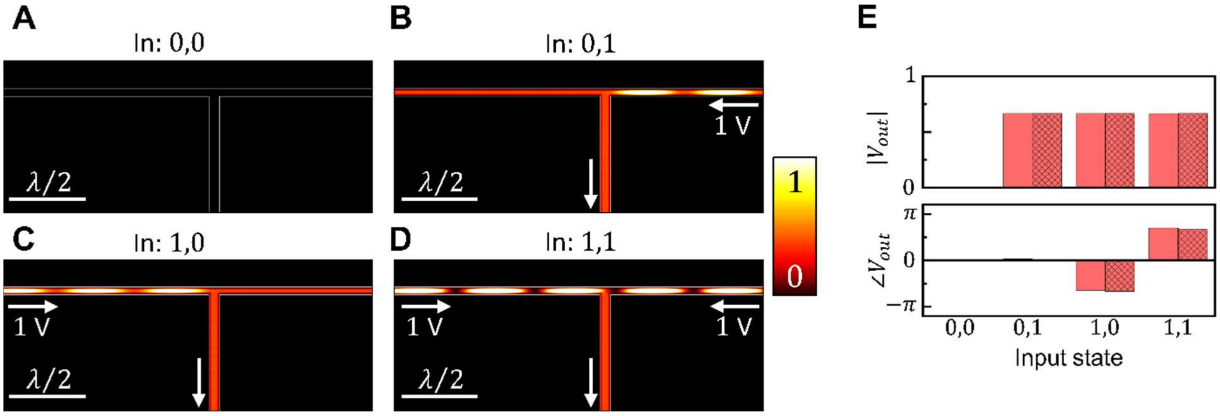

Figure 3.17 Linear OR gate. **A.**, **B.**, **C.**, **D.** Power distribution of the 00, 01, 10 and 11 input cases respectively. Results are normalized to the input power of a 1 V signal. **E.** Amplitude (top) and phase (bottom) of the theoretical (hashed) and numerical (solid) output signals.

3.2.2 Cascaded and N-input logic gates.

One of the advantages of conventional electronic logic gates is that the output signals of one logic gate may be connected to the inputs of another in a process called cascading. This enables one to produce more complicated Boolean operations with many inputs. This is a challenge for linear logic gates, as the classification of output signals may differ from the input encoding used to enable that operation. Furthermore, due to the constraint imposed by Eq. 3.10 a two-input logic gates will have at least three unique output states. This means that in general linear logic gates cannot be cascaded in the same way as electronic logic gates, while ensuring the distinguishability of the high and low output classification regions (no overlap). To overcome this challenge one can instead consider a desired operation with many inputs, not as a system of connected logic gates, but instead as a single structure emulating the overall operation. The encoding, scattering parameters and offset values may then be optimized in the same way as the two-input case to achieve the desired functionality.

A schematic representation of one potential implementation of a three and four input linear logic gate is presented in Fig. 3.18A,B, respectively. These structures exploit a series of T-junctions (and X-junctions where appropriate) to route the input signals towards a single output port. This allows for the path lengths between each input and the output to be independently controlled. Additionally, the magnitude of the signal arriving at the output port may be controlled, either by designing the waveguides with specific impedance values using Eq. 1.24 or by tailoring the input encoding at each port individually. These structures may also be extended by adding additional layers to construct linear logic gates with more inputs. For the examples presented in this section, these structures have been constructed using networks of waveguides connected in series. In these networks, each waveguide has the dimensions $w = h = 1$ mm and vacuum ($\varepsilon_r = \mu_r = 1$) as the filling material. The characteristic impedance of these waveguides is labelled as Z_0. This is with the exception of waveguides which are used as quarter-wave transformers (QWTs)[30]. These waveguides have a characteristic impedance of $\sqrt{2}Z_0$, which is achieved by changing the plate separation from 1 mm to 1.41 mm and a length of $\lambda/4$. The role of these waveguides is to enforce impedance matching between the two input waveguides at one of the T-junctions and the output waveguide of that T-junction.

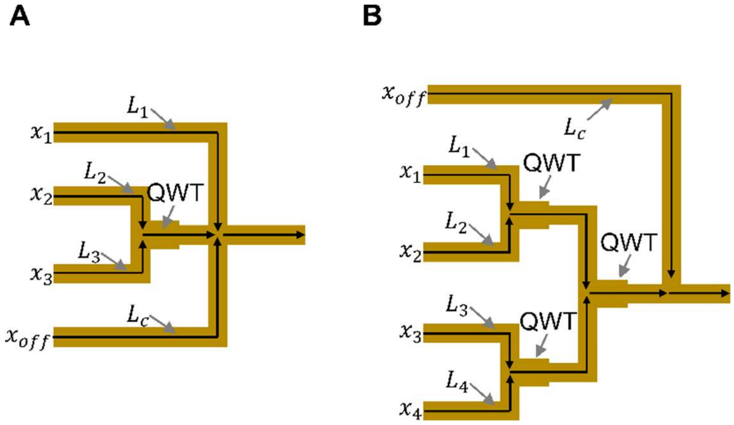

Figure 3.18 N-input linear logic gate general structure. **A.**, **B.**, General structure of 3 and 4 input logic gates with QWTs and an offset signal.

N-input AND gate

Consider for instance, the implementation of an N input AND operation. This operation should return a high output signal if and only if all the input signals are high. As in the two-input case this can be achieved with an $L_a = 0$ V, $H_a = 1$ V input encoding (where $a = 1,2 \ldots N$ is the input number) by designing the path lengths of the structure to enforce constructive interference between the high input signals i.e., the scattering coefficient between each input and the output is the same ($A_{out,in}$). This will ensure that the largest magnitude output signal will be when all input signals are high. In this scenario the upper limit of the low output classification region is as follows:

$$y_{low,threshold} = A_{out,in}(N-1) \tag{3.11}$$

i.e. the largest magnitude output signal which is classified as low is the result of $N-1$ high input signals constructively interfering. The high output state is:

$$y_{high,threshold} = A_{out,in}N \tag{3.12}$$

From Eq. 3.11 and Eq. 3.12 it can be seen that the separation between high and low classification regions (and thus contrast ratio of the operation) decreases as the total number of inputs increases. This can be improved by the addition of an optimized offset signal. As before, the offset signal should destructively interfere with the high input signals, thus reducing the magnitude of the low classification threshold. The maximum contrast ratio is attained when the magnitude of the output signal for all low and $N-1$ high input combinations (i.e., the two extremes of the low classification region) are equal to one another. This is expressed as:

$$|A_{out,off}x_{off}| = |A_{out,in}(N-1) - A_{out,off}x_{off}| \tag{3.13}$$

the optimal value of the offset signal is thus calculated as

$$x_{off} = \frac{|A_{out,in}|(N-1)}{2|A_{out,off}|} \tag{3.14}$$

Eq. 3.14 is then used with Eq. 3.6 and Eq. 3.7 to calculate the theoretical maximum contrast ratio as:

$$Contrast\ ratio = 20\log_{10}\left(\frac{2N-(N-1)}{N-1}\right) \tag{3.15}$$

As an example, a numerical study of a linear AND gate with four inputs has been conducted using the structure presented in Fig. 3.18B. Here, the scattering coefficients are

$A_{out,in} = 1/\sqrt{8}$ and $A_{out,off} = 1/\sqrt{2}$. This means using Eq. 3.14 the optimal value of the offset signal is calculated as $x_{off} = 1/2$ V. From Eq. 3.15 the theoretical contrast ratio is 4.447 dB. Numerical results for the power distribution of the four input AND are presented in Fig. 3.19. Here only the 0000, 0001, 0011, 0111 and 1111 input combinations have been shown. This is as these input combinations cover all theoretically attainable output states. It is expected that the remaining output states will have the same output signal as those with the same number of high inputs (i.e., 1011 and 1110 would have the same output signal as 0111). As it can be seen, the output signal for the 1111 input combination is clearly distinguishable from the other input combinations. This input combination has an output magnitude of 0.941 V while the upper limit of the low classification region is calculated to be 0.588 V meaning the contrast ratio is 4.08 dB. The difference between the numerically calculated and the theoretical contrast ratios can be attributed to the increased complexity of the structure compared to the elementary operations, allowing for imperfect splitting effects, such as path length differences though the waveguide junction[26,77,83], to have a more significant impact of the performance of the linear logic gate.

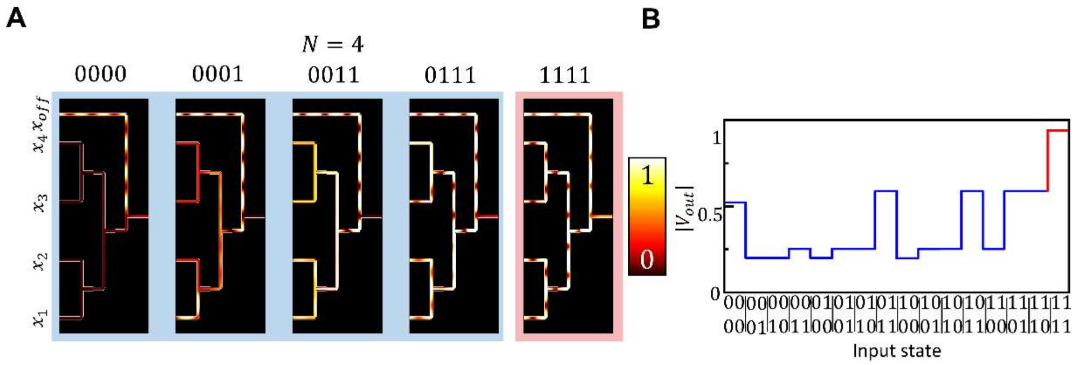

Figure 3.19 4-input AND gate. **A.** Normalized power distribution for the $N = 4$ AND gate with 0 to 4 high input states (from left to right). **B**. Magnitude of the output signals seen for each input combination.

N-input OR gate

Another example of a cascadable linear logic gate is an N-input OR operation. This operation should return a high output signal if any of the input signals are high. As with the 2-input OR gate this operation can be realized with an $L_a = 0$ V and $H_a = 1$ V input encoding. This is similar to the N-input AND operation, however now the path lengths between the input and output signals should be slightly altered so that the high-input signals are slightly out-of-phase when they arrive at the output waveguide. For the 2-input logic gate the phase difference was

$2\pi/3$ between the two high input signals. For the N-input OR gate the path lengths are instead chosen such that:

$$\varphi_a = \frac{2\pi}{3}\frac{a-1}{N-1} \tag{3.16}$$

where φ_a is the phase of the signal from input a when arriving at the output port. This means that from $a = 1$ to $a = N$ there is an even distribution of added path lengths from L_1 to $L_1 + \lambda/3$. This is done so that each high input signal will be slightly out-of-phase with the other high input signals, thus reducing the overall size of the high output classification region. The maximum phase difference between any two high input signals is chosen to be $2\pi/3$. This is chosen as the upper limit to prevent two input signals from destructively interfering and in doing so reducing the distinguishability of the operation. Numerical simulation results of the $N = 4$ linear OR operation is presented in Fig. 3.20. As it can be seen, the high output states are clearly distinguishable from the low 0000 input combination where there are no signals present. As the low output state is 0 V a contrast ratio cannot be easily defined. The lower and upper bounds of the high classification region were calculated to be 0.358 V and 1.03 V, respectively. This means that any output signal within this range should be classified as high.

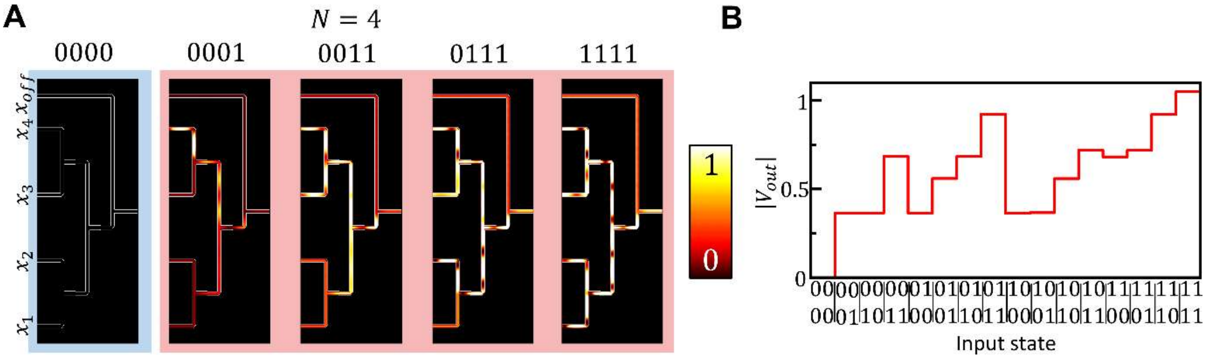

Figure 3.20 4-input OR gate. **A.** Normalized power distribution for the $N = 4$ OR gate with 1 to 4 high inputs (from left to right). **B.** Magnitude of the output signals seen for each input combination.

Three input XOR gate

Finally, the implementation of a 3-input XOR operation is also presented. This highlights a scenario where it is beneficial to exploit different encoding schemes at each input port. For the 8 possible input combinations 000, 001, 010, 011, 100, 101, 110 and 111 the output states of the 3-input XOR should be classified as 0, 1, 1, 0, 1, 0, 0 and 1, respectively. The output resembles an XOR operation between inputs 2 and 3 when input 1 is low and an XNOR when input 1 is high. To being with consider the case where $L_1 = 0$ V and input 1 is low. In this scenario the output signal is calculated as:

$$|y_{out}| = |A_{out,2}x_2 + A_{out,3}x_3 + A_{out,off}x_{off}| \tag{3.17}$$

where $A_{out,2}$ and $A_{out,3}$ is the coupling between inputs 2,3 and the output waveguide, respectively. If $A_{out,2} = A_{out,3}$ (as is the case for the structure in Fig. 3.18A) then the XOR operation may be emulated using the following input encoding $L_2 = H_3 = 1\angle 0$ V and $L_3 = H_2 = 1\angle\pi$ V, when $x_{off} = 0$ V. In this scenario the low and high output signals are 0 V and $|2A_{out,2}|$ V, respectively. Now, how can one implement the NOT operation when input 1 is high? For this to be possible H_1 should be selected to destructively interfere with the 01 or 10 input combination from input 2 and 3. Take for example the 10 input combination. With the addition of the high signal from input 1 the output in this case becomes: $|y_{out,101}| = |2A_{out,2} + A_{out,3}H_1|$, where $y_{out,101}$ is the value of y_{out} calculated from Eq. 3.17 for the 101 input combination. And thus, the required value of H_1 is calculated as:

$$H_1 = -\frac{A_{out,1}}{2A_{out,2}} \tag{3.18}$$

Using this encoding scheme, a numerical study of the 3-input XOR gate is conducted, and the calculated power distributions of the various input combinations are presented in Fig. 3.21. As it can be seen the 3-input XOR operation is successfully emulated with the low signals at ~ 0 V with the exception of the 101 input combination. In this case the H_1 input signal constructively interferes with the 01 input combination from inputs 2 and 3. This is a consequence of the constraints imposed by Eq. 3.10. However, this does not prevent the XOR operation from being distinguishable. Instead, it places an upper limit onto the high classification region. From the results presented in Fig, 3.21 an output signal is classified as high if it has a magnitude between 0.809 V and 0.891 V. The low output signal for the 101 input combination has a magnitude of 1.623 V. This means that in this case the low output will have a higher output voltage than the high output signal. The contrast ratio of the overall operation is then calculated using Eq. 3.7 by considering the two threshold values which produce the smallest contrast ratio. For this example, this is the upper bound of the high region 0.891 V and the 1.623 V low output signal. The means that the contrast ratio of this operation is calculated to be 5.202 dB.

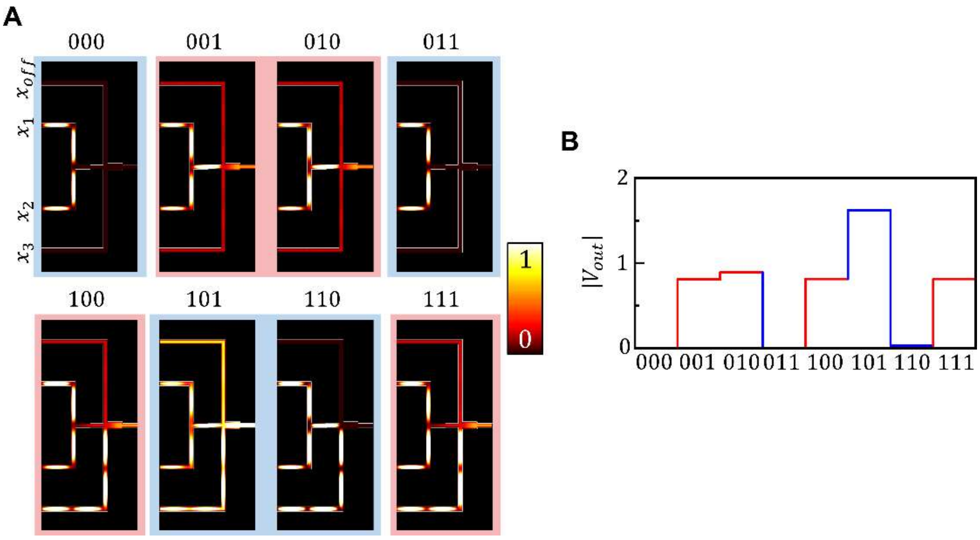

Figure 3.21 3-input XOR gate. **A.** Normalized power distribution for the $N = 3$ XOR operation for all 8 input combinations. **B.** magnitude of the numerically calculated output signals for each input combination.

3.2.3 Multiple-output logic gates: adders

Thus far the discussion of linear logic gates has focused on operations with multiple inputs but only a single output. As will be discussed in this section, this technique may also be extended to produce logic operations with multiple outputs. When doing so, it is important to design the waveguide structure and select the input encodings such that the logic operations at each output is successfully implemented simultaneously. To demonstrate this the designs of two multiple-output logic operations will be presented and a numerical study to corroborate their performance will be conducted. These operations are as follows: a half-adder and a 2-bit adder. Here the structure and performance of these linear logic gates will be discussed, however full simulation results of the various input combinations have been omitted. This is as, at the time of writing, a manuscript is currently being prepared based on these results.

EM wave-based half-adder

The first example to be discussed is the EM wave-based half-adder. This is a two-input two-output operation in which the first and second output are XOR and AND operations, respectively. A schematic representation of the waveguide structure used to implement this operation can be seen in Fig. 3.22A-C. Fig. D,E shows numerical simulations of the signal paths between the input and output ports. In this structure, quarter-wave transformers have been used at the input waveguides to match the impedance of the input waveguide to the impedance of the two connected waveguides. This allows for the implementation of a fan-out operation (the splitting of input signals into two or more paths) without any loss due to reflections. Signals from either input are then combined at the two outputs via the use to a Wilkinson power divider (WPD). This allows for one-way coupling between the input and the output waveguides. Between this design and a conventional WPD, the $2Z_0$ Ω resistor has instead been replaced with a pair of dump ports which direct any unnecessary signals out of the network. This is important as it prevents any potential crosstalk between the two logic operations which would impact the distinguishability of both.

When considering the splitting/superposition of signals and the various signal path lengths through the half-adder structure, the signal seen at the two output waveguides is calculated using TL theory[30] as follows:

$$|y_{SUM}| = |\frac{1}{2}(x_1 - x_2)| \tag{3.19a}$$

$$|y_{CARRY}| = |\frac{1}{2}(x_1 + x_2)| \tag{3.19b}$$

where y_{SUM} and y_{CARRY} are the output signals at the SUM and CARRY ports, respectively. i.e. the path length from inputs 1,2 to the CARRY output is the same, while there is a $\lambda_0/2$ difference to the SUM output. This results in the $-$ and $+$ in Fig. 3.19a and Fig. 3.19b, respectivley. Using Eq. 3.19 the input encoding $L_1 = 1/3\ \angle\pi$ V, $L_2 = 1/3\ \ \angle\pi$ V, $H_1 = 1\angle0$ V and $H_2 = \angle1$ V is selected to enable both operations simultaneously. With this encoding scheme, the theoretical outputs for the various input combinations are as follows: $|y_{SUM,00}| = |y_{SUM,11}| = 0$ V, $|y_{SUM,01}| = |y_{SUM,10}| = 2/3$ V, $|y_{CARRY,00}| = |y_{CARRY,01}| = |y_{CARRY,10}| = 1/3$ V and $|y_{CARRY,11}| = 1$ V. This means that the theoretical contrast ratios of the SUM and $CARRY$ operations are undefined (due to the division by 0) and 9.542 dB, which is the theoretically optimal value for a linear XOR and AND operation[128]. The contrast ratios of the simulated EM-wave based half adder was 43.049 dB and 9.236 dB for the SUM and CARRY operations, respectively.

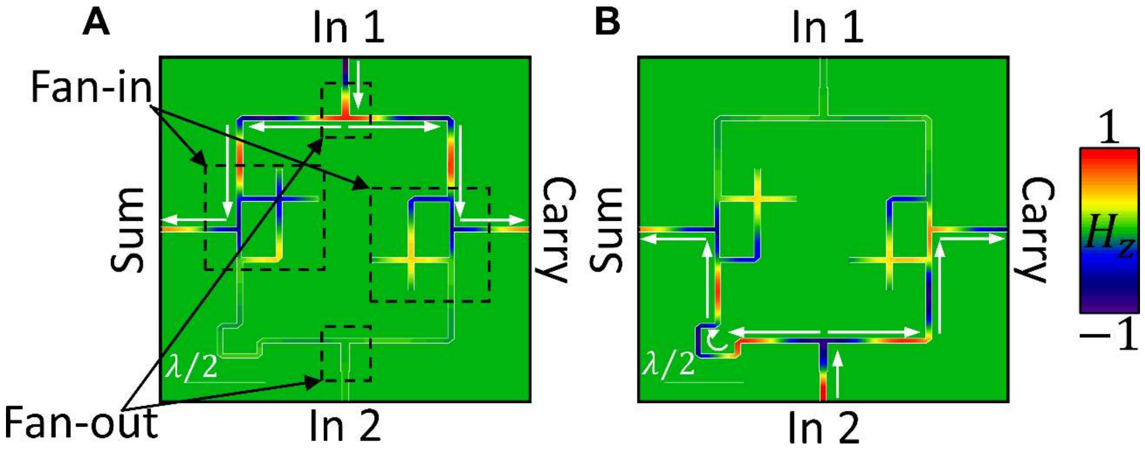

Figure 3.22 EM wave-based half adder. **A.**, **B**. Signal paths though the structure originating from input 1 and input 2, respectively.

EM wave-based 2-bit adder

Finally, the structure of the EM wave-based 2-bit adder is presented in Fig. 3.23 which shows the various path length taken by input signals though this structure. The purpose of the 2-bit full adder is to take two 2-bit binary numbers $B1$ and $B2$, respectively and then to output the sum of these two numbers. This means that the structure has four inputs, $B1_1$, $B2_1$, $B1_2$ and $B2_2$ which are the first bit of $B1$, the first bit of $B2$ the second bit of $B1$ and the second bit of $B2$, respectively. The structure also has three outputs, $CARRY$, $SUM1$ and $SUM2$ which are the first, second and third bits of the of the output number. These outputs are to the left, top and bottom of the structure presented in Fig. 3.23, respectively. Using this structure, the theoretical output signals at these three inputs are as follows:

$$|y_{CARRY}| = |\frac{1}{2\sqrt{2}}(x_3 + x_4 + \frac{x_1 + x_2}{\sqrt{2}})| \tag{3.20a}$$

$$|y_{SUM1}| = |\frac{1}{2\sqrt{2}}(-x_3 + x_4 + \frac{x_1 + x_2}{\sqrt{2}})| \tag{3.20b}$$

$$|y_{SUM2}| = |\frac{1}{2}(x_1 - x_2)| \tag{3.20c}$$

where x_1, x_2, x_3 and x_4 are the high/low values of $B1_1$, $B2_1$, $B1_2$ and $B2_2$, respectively. Eq. 3.20 may be exploited to implement the 2-bit adder operation when the following encoding scheme is used: $L_1 = L_2 = 1/3\angle\pi$ V, $H_1 = H_2 = 1\angle 0$ V, $L_3 = L_4 = \sqrt{2}/3\angle\pi$ V and $H_3 = H_4 = \sqrt{2}\angle 0$ V. Then, considering all the input combinations in Eq. 3.20, the theoretical threshold values of the high and low classification regions are obtained.

Regarding the CARRY operation the theoretical classification regions are as follows: low if $|y_{CARRY}| < 1/2$ V and high if $|y_{CARRY}| > 5/6$ V. This means that the theoretical contrast ratio is 4.437 dB. The classification regions of the CARRY operation in the numerically simulated structure were: low if $|y_{CARRY}| < 0.564$ V and high if $|y_{CARRY}| > 0.821$ V and the numerical contrast ratio is 3.071 dB. The theoretical classification regions of the SUM1 operation are as follows: low if $|y_{SUM1}| < 1/6$ V or $|y_{SUM1}| > 7/6$ V and high if $5/6$ V $> |y_{SUM1}| > 1/2$ V. Using these values, the theoretical contrast ratio is 2.923 dB. The classification regions of the numerical SUM1 operation were: low if $|y_{SUM1}| < 0.138$ V or $|y_{SUM}\ \ | > 1.194$ V and high if 0.865 V $> |y_{SUM}\ \ | > 0.497$ V meaning the numerical contrast ratio is 2.816 dB. Finally, the theoretical classification regions of the SUM2 operation are: low if $|y_{SUM1}| = 0$ V and high if $|y_{SUM1}| > 2/3$ V. This means that the theoretical contrast ration is undefined. The simulated classification regions of this operation were: low if $|y_{SUM1}| = 4.905 \times 10^{-2}$ V or $|y_{SUM1}| > 0.658$ V meaning the contrast ratio is 22.55 dB.

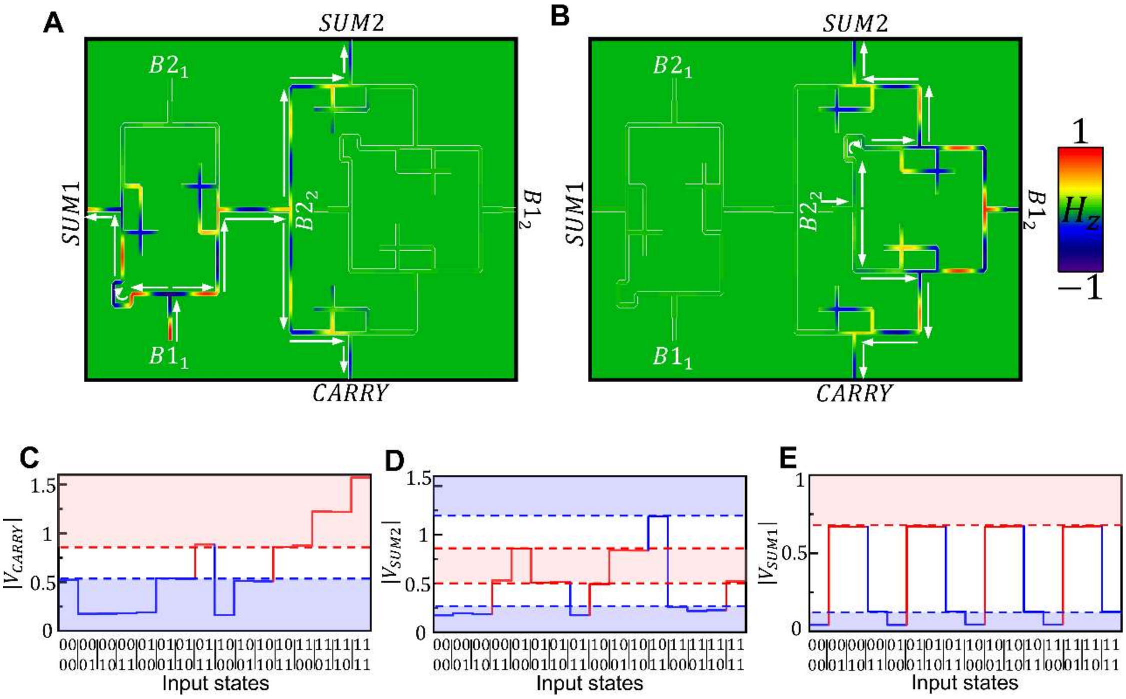

Figure 3.23 EM wave-base full adder. **A.**, **B.** Signal paths though the structure originating at the $B1_1$ and $B1_2$ inputs, respectively. **C.**, **D.**, **E.** Magnitude of the output signals at CARRY, SUM2 and SUM1, respectively. High and low regions are shown in red and blue, respectivley.

3.3 Chapter 3 conclusions

In this chapter, the results of two studies have been presented. The first study describes how the superposition of TEM pulses at the junctions between PPWs may be exploited to calculate the outcomes of $if\ldots then\ldots else\ldots$ statements. To demonstrate the technique two example applications have been presented. These are 1) a TEM pulse comparator and 2) a TEM pulse director. The first is designed to compare the values of two numbers and the second is designed to achieve a performance analogous to an AND operation. These designs are corroborated via full-wave numerical simulation results, which have been presented throughout the chapter. This study has been published by Advanced Intelligent Systems in the manuscript titled "Amplitude-Controlled Electromagnetic Pulse Switching Using Waveguide Junctions for High-Speed Computing Processes."

The second study details how one may emulate the performance of traditional logic gates by exploiting the linear superposition of monochromatic EM-waves. These operations are referred to as "linear logic" operations. This study begins with an exploration of elementary linear logic operations before expanding to include many-input one-output and many-input many-output operations such as an N-input AND and a 2-bit full adder, respectively. At the time of submission, a manuscript is currently being prepared based on the results of this study.

Chapter 4. One-dimensional Analogue Computing: Waveguide-based Differentiators

As discussed in the introduction section of this thesis, the advantages of computing with EM-waves have also been exploited in the realm of analogue computing. In this realm, the solutions to mathematical operations are calculated by designing structures capable of applying said operators directly onto the wavefront of an incident signal in either spatial or temporal domains. Two common techniques used to implement these operations were discussed in the introduction section. In this realm, operations such as integration, convolution and differentiation have been demonstrated exploiting structures such as metamaterials[149,153,175], metasurfaces[154,176], fibre gratings[159,160,177] and MZI networks[166], among others[163,165,167,168,178]. To achieve this, techniques such as parameter optimization is commonly used when designing structures to achieve a desired response. Furthermore, inverse design techniques[175,178,179] and machine learning approaches[21,162,180] have also seen application.

In this chapter, the application of interconnected waveguide networks and TL filtering techniques to analogue computing will be explored. This is done with a focus on analogue differentiation due to the prevalence of this operation in practical applications. Examples of this include edge detection algorithms for image recognition[155] or throughout many different areas of physics and mathematics. This work has been published in Scientific Reports as the manuscript entitled "Time derivatives via interconnected waveguides"[26]. To begin with, this chapter discusses the performance of a hypothetical analogue differentiator before exploring how TL filtering techniques[30,181] may be exploited to emulate this behaviour. After this the impact of imperfect splitting at waveguide junctions is discussed including methods which may be exploited to mitigate this. Finally, this chapter discusses how these techniques may be exploited to enable arbitrary order analogue differentiation including fractional/non-integer order differentiators[182].

4.1 TL Filtering Techniques for Green’s Function Analogue Computing

To begin with, consider the required behaviour of a hypothetical analogue processor which has been designed to implement a first order differentiation operation in the time domain. This operation is illustrated in Fig. 4.1A. As discussed in the introduction, time domain operations such as this example can be implemented by tailoring the EM response of a structure in the frequency domain (i.e. by tailoring the profile of $T(f)$ in Eq. 1.30). Regarding analogue differentiation, the output signal of the structure will resemble the first order derivative of the incident signal if $T(f) = 2\pi i f$,[157,162] where i is the imaginary unit. For signals which are modulated by a carrier frequency f_0 this transfer function is instead $2\pi i(f - f_0)$.[30] It is important to note that this chapter considers linear and passive structures. Due to this, the values of $|T(f)|$ of all the designed structures are bound within the range 0-1. This is not the case for $2\pi i(f - f_0)$ and thus it is necessary to normalise the target transfer function to also be bound within the range 0-1[30]. This then means that the transfer function of the hypothetical analogue processor should be designed to resemble a linear and symmetrical V-shaped dip centred at the carrier frequency of the incident signal f_0 (as shown in the top left insert of Fig. 4.1A).

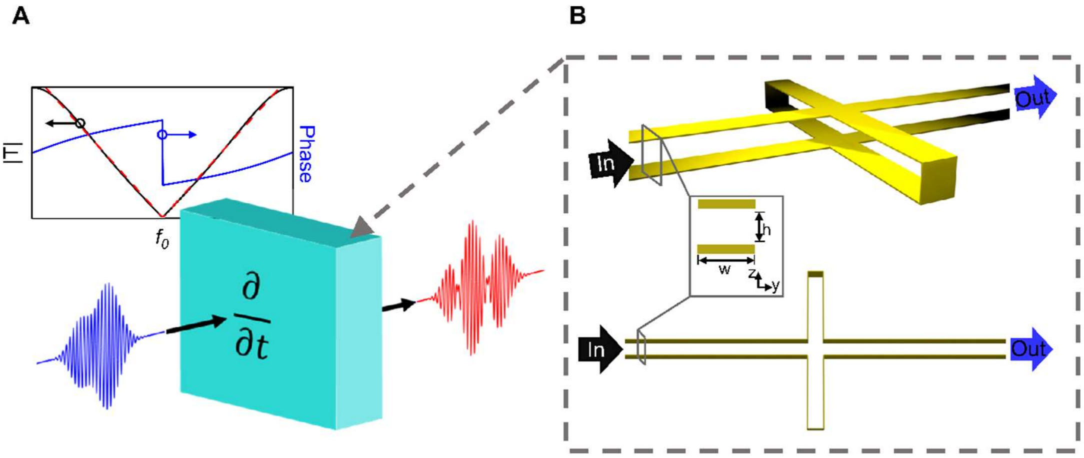

Figure 4.1 Introduction to waveguide-based time-domain analogue computing. **A.** Performance of a hypothetical differentiator. **B.** Schematic representation of stub-based differentiators with stubs connected in parallel (top) and series (bottom).

Now how can one design a structure capable of emulating the required V-shaped transfer function? To answer this one can exploit TL filtering techniques such as waveguide stubs[30,181]. A schematic representation of these structures is presented in Fig. 4.1B for stubs exploiting parallel (top) and series (bottom) junctions, respectively. The purpose of these stub waveguides is to split an incident signal into multiple copies and then to feed these “copies” of the incident signal back into the original with a small temporal delay, which may be controlled by the length and filling materials of the stub waveguides. This delay is $\Delta t = 2L_s\sqrt{\varepsilon_r \mu_r}/c$, where ε_r and μ_r

are the relative permittivity and permeability of the stub filling material and L_s is the length of the stub. In this chapter, stubs with vacuum ($\varepsilon_r = \mu_r = 1$) as the filling material are used. Considering the structures presented in Fig. 4.1B, when an incident signal arrives at the waveguide junction it is split into four outgoing signals, one reflected, one transmitted and one traveling within each connected stub waveguide. If these waveguides have equal characteristic impedance, then from Eq. 1.26 these outgoing signals are all of equal magnitude[23–25,84]. Specifically for an incident signal $x_{in}(t)$, the transmitted signals to the stubs and output waveguides are $x_{in}(t)/2$. This process is referred to as the "*first split".* Now, when the signals propagating within the stub waveguides encounter the end of the stubs they are reflected and thus redirected back into the waveguide junction. They arrive at the waveguide junction for a second time after a time delay of Δt, at which point they are once again split into four signals. This is referred to as the "*second split*". If the two waveguide stubs are chosen to have the same electrical length, then the two reflected signals involved in the *second split* will thus be in phase with each other as they arrive back at the waveguide junction. Using Eq. 1.26, in this scenario the outgoing signals in the waveguide stubs after the *second split* will destructively interfere and cancel out. As a result, all of the signals involved in the *second split* are then transmitted towards the input and output waveguides respectively. The final outward signal seen at these two waveguides is thus the superposition of the signals produced by the *first split* and the *second split*, respectively. For PEC ended stubs connected at a parallel junction this is as follows:

$$y_{out}(t) = \frac{1}{2}[x_{in}(t) - x_{in}(t - \Delta t)] \tag{4.1a}$$

$$y_{in}(t) = \frac{1}{2}[x_{in}(t) + x_{in}(t - \Delta t)] \tag{4.1b}$$

where $y_{out}(t)$ and $y_{in}(t)$ and the outgoing signals at the output and input waveguides respectively. In both equations the *first* and *second* terms are the output signals produced by the first and second split, respectively.

To understand how this structure may be used to calculate derivatives, compare Eq. 4.1a to the well-known first order finite difference equation[183]:

$$\frac{dy}{dx} = \lim_{\Delta x \to 0} \frac{y(x) - y(x - \Delta x)}{\Delta x} \tag{4.2}$$

As it can be seen, Eq. 4.1a is analogous to Eq. 4.2, differing only be a normalization factor[137,149,162].This means that if the stub length is chosen such that Δt is small (compared to the timescale of the variation in the envelope of the incident signal) then Eq. 4.1a can be used to calculate first order derivatives by analogy to Eq. 4.2. Furthermore, this analogy can also be extended to apply to modulated signals. However, in this case Δt should be engineered to ensure that the output signals produced by the *first* and *second split* are π rad out-of-phase. This is to enforce the minus sign applied to the $x_{in}(t-\Delta t)$ term. For the case of PEC ended stubs this occurs when L_s is an even and odd integer multiple of $\lambda_0/2$ for parallel and series junctions, respectively. Likewise of vacuum terminated (open) stubs this occurs when L_s is an odd and even integer multiple of $\lambda_0/2$ for parallel and series junctions, respectively.

The discussion above details how a junction of four interconnected waveguides (one input, one output and two stubs) may be exploited to produce the required V-shaped transmission coefficient. However, it is also possible to tune the shape of the transfer function to better meet the needs of specific tasks, such as to control the usable bandwidth of the differentiation operator. To do this, consider the transmission (and reflection) coefficient produced by a junction with M connected stubs. This means that the total number of junctions connected at the junction is $N = M + 2$. In this scenario, the input and output waveguides are chosen to have the same characteristic impedance Z_0, however the characteristic impedance of the stub waveguides Z_{sa} is allowed to vary freely. Furthermore, the length of these stubs is defined as L_{sa}, where $a = 1,2,3 \dots M$ and the reflection coefficient at the end of each stub is $\Gamma_{a,\pm 1}$ (i.e., $+1$ and -1 for open ended and PEC ended stubs, respectively). Using these parameters, the scattering matrix of the waveguide junction $\boldsymbol{A}$ can be calculated using Eq. 1.23 and Eq. 1.24 for parallel and series junctions respectively with the input and output vectors $\boldsymbol{x}$ and $\boldsymbol{y}^T$, respectively. For the sake of simplicity, the terms of $\boldsymbol{x}$ and $\boldsymbol{y}$ are arranged such that the first 1 to M values refer to incoming and outgoing signals within the waveguide stubs while the $M+1$ and $M+2$ values are the signals in the input and output waveguides respectively. The transmitted and reflected signal at either waveguide is thus written as:

$$y_{M+2} = A_{M+2,M+1}x_{in} + \sum_{a=1}^{M} A_{M+2,a}x_a \tag{4.3a}$$

$$y_{M+1} = A_{M+1,M+1}x_{in} + \sum_{a=1}^{M} A_{M+1,a}x_a \tag{4.3b}$$

where x_{in} is the input signal which is to be differentiated. In Eq. 4.3 the first and second terms describe the output signals which are produced by the *first* and *second splits*, respectively.

The inward traveling signals involved in the *second split* are related to the outward traveling signals produced by the *first split* by considering the phase change and reflection coefficient of each individual stub. This can be expressed as follows:

$$x_a = \Gamma_{a\pm 1} x_{in} e^{-2i\varphi_a} y_a \tag{4.4}$$

where $\varphi_a = \omega L_{sa}\sqrt{\varepsilon_{r,a}\mu_{r,a}}/c$ is the phase difference between the junction to the end of stub a and $\varepsilon_{r,a}$, $\mu_{r,a}$ are the relative permittivity and permeability values of the stub filling materials, respectively. The structures presented in Fig. 4.1B and discussed above are special cases in which the outgoing signals after the *second split* are all directed towards the input and output waveguides. However, in general, a portion of these signals will also be directed into the stub waveguides. This means that the outgoing signals in each stub can also be written as a superposition of the signals involved in the *first* and *second splits* as follows:

$$y_a = A_{a,M+1} x_{in} + \sum_{b=1}^{M} A_{a,b} x_b \tag{4.5}$$

which is similar to Eq. 4.3a,b however now selecting the elements of $\boldsymbol{A}$ which describe the scattering of signals towards the stub waveguides. By combining Eq. 4.4 and Eq. 4.5 this is rewritten as:

$$y_a = A_{a,M+1} x_{in} + \sum_{b=1}^{M} A_{a,b} \Gamma_b e^{-2i\varphi_b} y_b \tag{4.6}$$

which are a set of simultaneous equations which may be solved to express the outgoing signals y_a in terms of the input signal x_{in} and the structural parameters (Γ_{sa}, φ_{sa} and $\boldsymbol{A}$) only. To assist in this the matrix $\boldsymbol{C}$ is defined as follows:

$$C_{a,b} = \delta_{a,b} - A_{a,b} \Gamma_{b\pm 1} e^{-2i\varphi_b} \tag{4.7a}$$

$$\sum_{b=1}^{M} C_{a,b} y_b = A_{a,M+1} x_{in} \tag{4.7b}$$

Substituting Eq. 4.7 into Eq. 4.6 and rearranging for y_a gives:

$$y_a = \sum_{b=1}^{M} (\boldsymbol{C})_{a,b}^{-1} A_{b,M+1} x_{in} \tag{4.8}$$

Then by combining Eq. 4.8, 4.4 and 4.3, the final signals observed at the input and output waveguides is:

$$y_{M+2} = [A_{M+2,M+1} + \sum_{a=1}^{M}\sum_{b=1}^{M} A_{M+2,a}\Gamma_{a\pm1}e^{-2i\varphi_a}(\boldsymbol{C})_{a,b}^{-1}\, A_{b,M+1}]x_{in} \tag{4.9a}$$

$$y_{M+1} = [A_{M+1,M+1} + \sum_{a=1}^{M}\sum_{b=1}^{M} A_{M+1,a}\Gamma_{a\pm1}e^{-2i\varphi_a}(\boldsymbol{C})_{a,b}^{-1}\, A_{b,M+1}]x_{in} \tag{4.9b}$$

From Eq. 4.9a and Eq. 4.9b the transmission and reflection coefficients of the overall structure can then be obtained.

$$T = \frac{y_{M+2}}{x_{in}} = A_{M+2,M+1} + \sum_{a=1}^{M}\sum_{b=1}^{M} A_{M+2,a}\Gamma_{a\pm1}e^{-2i\varphi_a}(\boldsymbol{C})_{a,b}^{-1}\, A_{b,M+1} \tag{4.10a}$$

$$\Gamma_{total} = \frac{y_{M+1}}{x_{in}} = A_{M+1,M+1} + \sum_{a=1}^{M}\sum_{b=1}^{M} A_{M+1,a}\Gamma_{a\pm1}e^{-2i\varphi_a}(\boldsymbol{C})_{a,b}^{-1}\, A_{b,M+1} \tag{4.10b}$$

Eq. 4.10 is a general expression which may be applied to a wide range of potential designs. This provides a great deal of control over the transfer function of these stub-based differentiators. Eq. 4.10 may also be simplified by imposing restrictions onto the candidate designs such that symmetries in the structure may be exploited. For instance, enforcing $Z_{sa} = Z_0$ the scattering matrix of the waveguide junction can instead be expressed using Eq. 1.25. With this restriction Eq. 4.10 can instead be rewritten as:

$$T = \frac{2\phi}{M+2} + \frac{4}{(2+M)^2}\sum_{a=1}^{M}\sum_{b=1}^{M} \Gamma_{a\pm1}e^{-2i\varphi_a}(\boldsymbol{C})_{a,b}^{-1} \tag{4.11a}$$

$$\Gamma_{total} = \frac{2\phi}{M+2} - \phi + \frac{4}{(2+M)^2}\sum_{a=1}^{M}\sum_{b=1}^{M} \Gamma_{a\pm1}e^{-2i\varphi_a}(\boldsymbol{C})_{a,b}^{-1} \tag{4.11b}$$

where $\phi = \pm1$ has been introduced to distinguish between the parallel and series junctions with $\phi = 1$ and $\phi = -1$, respectively. Additionally, Eq. 4.7 is now as follows:

$$C_{a,b} = \delta_{a,b} - \frac{2\phi}{M+2}\Gamma_{b,\pm1}e^{-2i\varphi_b} \tag{4.12}$$

Eq. 4.11 can be simplified further if the connected stubs are identical, i.e., $\Gamma_{sa} = \Gamma_s$ and $\varphi_a = \varphi_s$ which are the reflection coefficients and electrical length of all the stub waveguides. Then, due to the symmetry of the restricted system it is expected that the outgoing signals (produced by the *first split*) and the incoming signals (involved in the *second split*) in each of the stub waveguides will be the same. This then means that Eq. 4.4 can be rewritten as:

$$x_s = \Gamma_s e^{-2i\varphi_s} y_s \tag{4.13}$$

Using Eq. 4.13, Eq. 4.6, 4.8 and 4.9 can also be rewritten as:

$$y_{M+2} = \frac{2\phi}{2+M}(x_{in} + Mx_s) \tag{4.14a}$$

$$y_{M+1} = \frac{2\phi}{2+M}(x_{in} + Mx_s) - \phi \tag{4.14b}$$

$$y_s = \frac{2\phi}{2+M}[x_{in} + (M-1)x_s] - \frac{\phi M}{M+2}x_s \tag{4.14c}$$

$$y_s = \frac{2\phi x_{in}}{M+2-(M-2)\Gamma_s e^{-2i\varphi_s}} \tag{4.14d}$$

Which may be combined to reveal the simplified transmission and reflection coefficients as:

$$T = \frac{2\phi}{2+M}[1 + \phi\frac{2M\Gamma_s e^{-2i\varphi_s}}{M+2-(M+2)\Gamma_s e^{-2i\varphi_s}}] \tag{4.15a}$$

$$\Gamma_{total} = \frac{2\phi}{2+M}[1 + \phi\frac{2M\Gamma_s e^{-2i\varphi_s}}{M+2-(M+2)\Gamma_s e^{-2i\varphi_s}}] - 1 \tag{4.15b}$$

Using Eq. 4.15, an analytical study of various stub-based differentiation setups is conducted. Here, the transfer functions (magnitude and phase of the transmission and reflection coefficients) are calculated for junctions with one to five identical connected stubs. These stubs all have a length of $\lambda_0/2$, where λ_0 is the modulation wavelength (in free space) of an incident signal to be differentiated. The results of this study are presented in Fig. 4.2 and Fig. 4.3 for parallel and series junctions with closed and open-ended stubs respectively. As it can be seen, the regions around the minima of the transfer functions is approximately a linear V-shape. For the PEC-ended parallel junctions and open-ended series junctions, these minima occur when f/f_0 is an integer value. Conversely, for PEC-ended series junctions and open-ended parallel junctions they occur when f/f_0 is a half-integer value. This means that these minima may be targeted to perform the differentiation operation. This behaviour is also confirmed by looking at the phase continuity in the transfer functions at these frequencies. This is characteristic of a first-order differentiation operation[168]. Furthermore, as the reflection and transmission coefficients of these structures are complementary it is also possible to instead exploit the reflection coefficient as a means of performing first order differentiation. The frequencies at which the linear and symmetrical V-shaped dips appear in the reflection coefficients are $f/f_0 = 1$ and $f/f_0 = 0.5$ for the PEC-ended series junctions, the open-ended parallel junctions and the PEC-ended parallel junctions, open-ended series junctions, respectively. It can also be seen how by controlling the number of connected stubs (effective stub impedance value) the bandwidth (spectral range around the minima in which the transfer function can be approximated as linear) of the differentiation operation may be controlled. This means by combining open and closed stubs or series and parallel junctions it is possible to design first order differentiators with a desired operational bandwidth. As will be explained later, these same principles may also be exploited by cascading multiple junctions together in order to produce higher order or even fractional order differentiation operations.

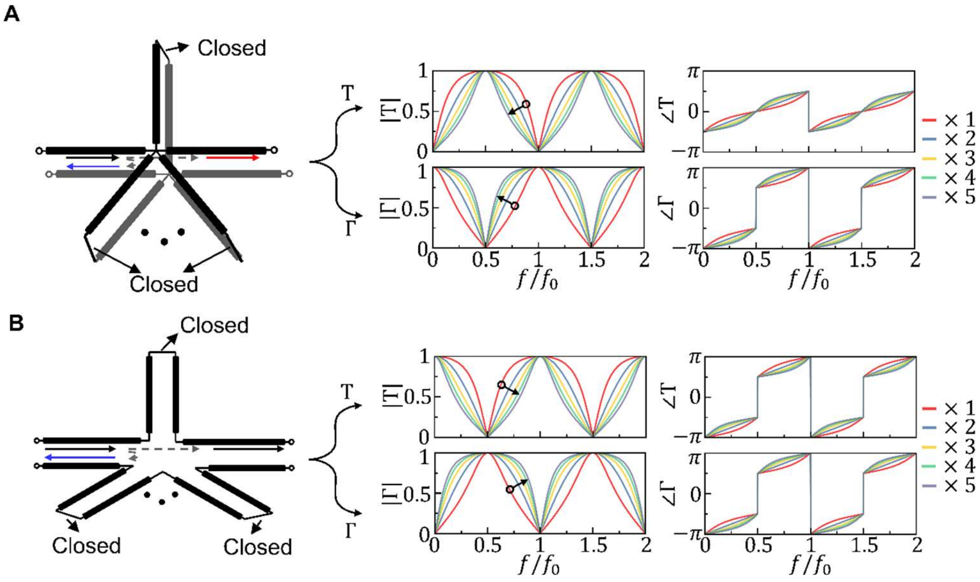

Figure 4.2 Star-stub differentiators using closed stubs. **A.**, **B.** Parallel and series junctions with 1-5 identical connected stubs.

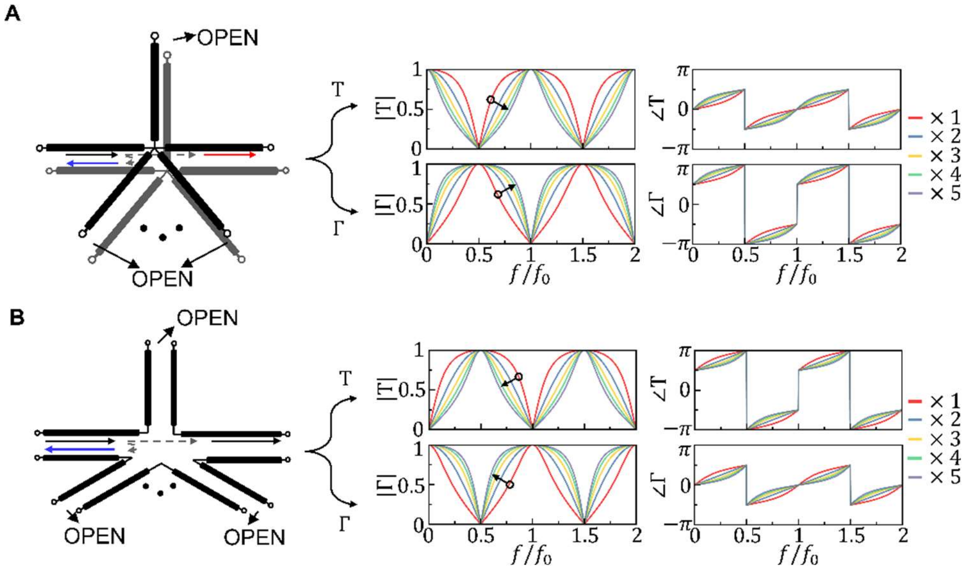

Figure 4.3 Star-stub differentiators using open stubs. **A.**, **B.** Parallel and series junctions with 1-5 identical connected stubs.

4.2 Impact of Non-Ideal Junction Splitting on the Performance of Waveguide Differentiators

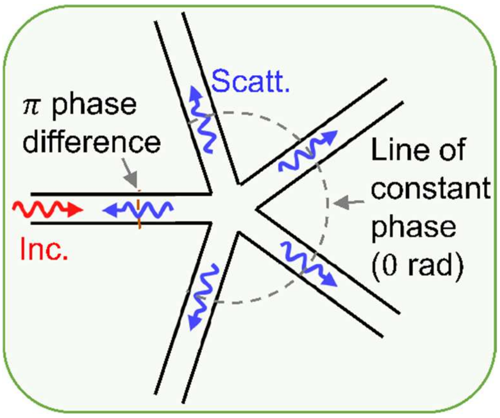

Figure 4.4 Origin of non-ideal junction scattering behaviour. Schematic representation of ideal junction scattering.

Thus far all the results present in this section have considered ideal waveguides modelled as TLs which thus obey the perfect splitting equations presented in Eq. 1.25. This is a valid approximation when the cross-section of the waveguide junction is small compared to the wavelength of the incident signal and the waveguide mode is tightly confined[76,77]. A schematic representation of this scenario is presented in Fig. 4.4 where an incident signal from the left waveguide is split among the connected waveguides with four transmitted signals and one reflected. One important detail to note is that the magnitude of all the transmitted signals is the same, but also if one where to draw a circle around the junction centred at the middle of the junction, then each of the transmitted signals will be in-phase at the point where they meet the edge of the circle (see Fig. 4.4). Additionally, the reflected signal will be π rad out-of-phase with the transmitted signals at this point. If any of these conditions are broken, then the performance of the differentiator will be affected potentially leading to lower calculation accuracy. A numerical study of the scenarios presented in Fig. 4.2-4.3 was conducted and two main sources of non-ideal behaviour where identified. 1) Non-ideal splitting due to the non-zero junction size and 2) transfer function distortion caused by asymmetry of the waveguide junction. A schematic representation of these effects is presented in Fig. 4.5

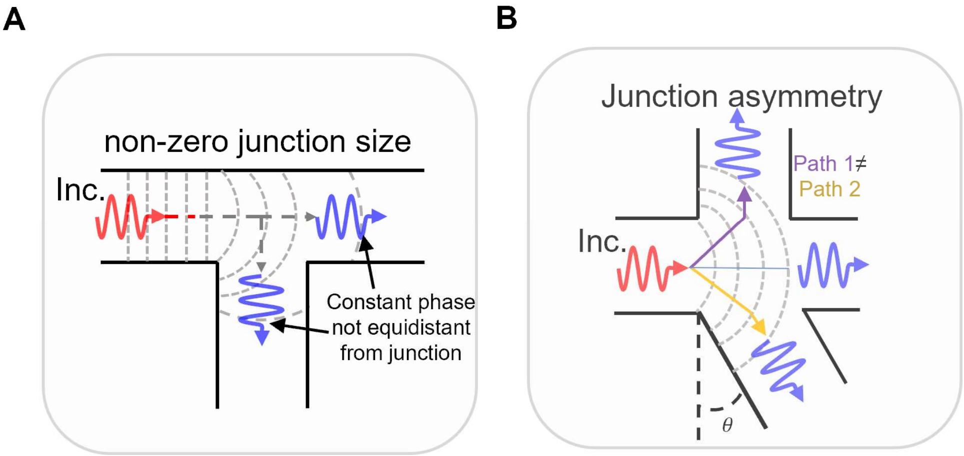

Figure 4.5 Realistic junction scattering with non-ideal behaviour. **A.** originating from the non-zero junction area. **B.** originating from junction asymmetry.

4.2.1 Non-ideality due to a non-zero junction cross section

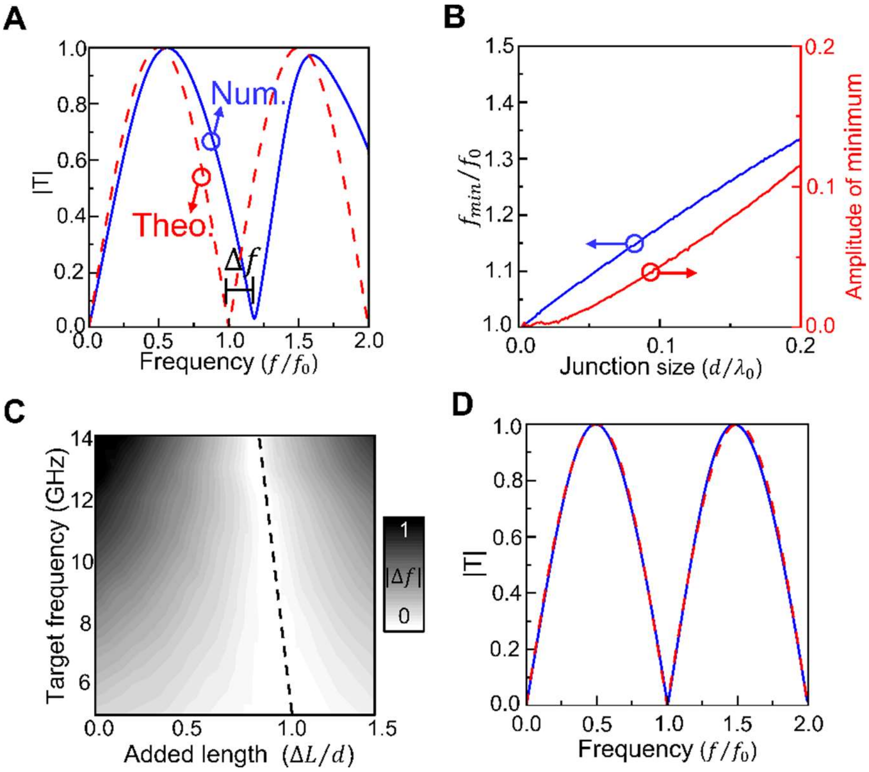

Figure 4.6 Impact of non-zero junction size on waveguide-differentiator performance. **A.** Numerical and theoretical simulation results for the transmission coefficient of a two-stub waveguide differentiator designed to operate at 8 GHz. **B.** Shift in the frequency of the calculated minimum in the transmission coefficient and the value of the amplitude of that minimum for varying junction sizes. **C.** Frequency difference between the ideal transfer function and the numerical transfer function for a range of target frequencies and added stub lengths. **D.** Transfer function of the structure from **A** now with the additional length from **C.**

To being with, consider the non-ideal splitting behaviour which originates from the non-zero junction size. Conceptually, this can be thought of in terms of the available signal paths though the waveguide junction[77,83]. If the waveguide junction has a non-zero cross section, then an incident signal does not need to travel towards the centre of the junction and may instead take a shorter path between the input-waveguide and the stub-waveguide. This means that the *effective* length of the stub waveguide is reduced which manifests as a shift in the operational frequency of the differentiator. Additionally, at larger junction sizes when the incident signal is no longer tightly contained Eq. 1.25 is no longer valid as a larger portion of the signal is transmitted through to the output waveguide[76,184,185] (positioned opposite to the input waveguide) than to the stub waveguides (positioned to the left and right of the input waveguide).

Numerical simulations using CST Studio Suite® of these effects can be seen in Fig. 4.6. Here, a differentiator is constructed from two PEC-ended stubs connected at a parallel junction. The length between the centre of the junction and the end of the stubs is chosen to be $\lambda_0/2$ (Here $\lambda_0 = 37.5$ mm i.e. $f_0 = 8$ GHz). From Eq. 4.15 this means the first minima in the transmission spectra is expected to be at f_0. The waveguides in question are designed to have a square cross section in the transverse plane with $w = h = d$ where d is a scaling parameter used during the parametric sweep. The results for the simulated transmission coefficient when $d = 1$ mm $(0.0267\lambda_0)$ are presented in Fig. 4.6A. As it can be seen the numerically simulated results resemble the theoretical results however there is a clear shift in the frequency at which the minimum is observed. The shift in frequency between the numerical and theoretical results is $\Delta f = f_{min} - f_0$. Here the numerical minimum is shifted towards higher frequencies, this is expected and a result of the shorter path length though the waveguide junction reducing the *effective* length of the waveguide stub. Fig. 4.6B shows how the ratio between the frequency of the numerical minimum and the theoretical minimum varies with the scaling parameter d. As expected, as the size of the connected waveguides (and thus the area of the waveguide junction) increases the frequency shift becomes more pronounced. Additionally, the minimum value of the amplitude of the transmission coefficient increases with junction size. This is indicative of a larger portion of the incident signal being transmitted towards the output port instead of being split evenly among all connected waveguides.

One method to minimize the impact of this frequency shift is to increase the length of the connected stubs L_s in order to compensate for the reduction in the *effective* length of the stubs. This is demonstrated in Fig. 4.6C where the magnitude of the frequency shift for a range of target frequencies and added stub lengths (ΔL) is presented. Here target frequency refers to the frequency at which the differentiator is designed to operate at. The black dashed line shows the minimum in Δf for each target frequency. For instance, using Fig. 4.6C the added path length required to minimize the frequency shift present in Fig. 4.6A (Target frequency = 8 GHz, $d = 1$ mm) is calculated to be $0.0227\lambda_0$. The transfer function of this structure after this length has been added onto the stub-waveguides is presented in Fig. 4.6D where it can be seen there is now a clear agreement between the numerical results and those produced using Eq. 4.15.

4.2.2 Non-ideality due to junction asymmetry

Next, the same optimized structure which was used to produce the results in Fig. 4.6D is used to investigate the impact of junction asymmetry onto the shape of the transfer function. This is done by rotating one of the connected stubs by θ from the initial position considered in Fig. 4.6D (90°). A schematic representation of this scenario is presented in the right panel of Fig. 4.5B. The numerically calculated transfer function of this structure is presented in Fig. 4.7A for the angles $\theta = 0°$ (ideal scenario), $\theta = 25°$ and $\theta = 45°$, as examples. As it can be seen, the introduction of asymmetry into the junction produces a distortion in the linear V-shape of the transmission coefficient. This would reduce the accuracy of the differentiation operation. The origin of this distortion is similar to the frequency shift discussed in Fig. 4.6 in that the non-zero size of the waveguide junction produces a reduced *effective* stub length. However, in this scenario, the reduction of the *effective* stub length is also affected by the angle at which the stub is connected to the junction. This presents a challenge when multiple stubs are connected at different angles to the waveguide junction as the different *effective* stub lengths produce a phase mismatch between the reflected signals from either stub (signals involved in the *second split*). To quantify the impact of this distortion the root mean square error (RMSE) between the ideal transmission coefficient of a first order differentiator ($|T_{ideal}| = C|f - f_0|$ where C is a normalization factor used to constrain the transfer function from 0 to 1) and the numerically calculated transfer function is presented in Fig. 4.7B. Here it can be seen that the increase in angle leads to a greater distortion in the transmission coefficient as expected. Additionally, the distortion produced by the phase mismatch is symmetrical around $\theta = 0°$. This symmetry can be understood from a path length perspective by considering the impact of the angle on the signals involved in the *first* and *second* splits. When an input signal first encounters the junction, it interacts with two stub waveguides: one at an angle of 90° and the other at $\theta + 90°$. The ideal structure (when $\theta = 0°$) has two stub waveguides at 90° angles to the input waveguide, directly 180° opposite from one another. When these signals return to the junction as an inputs of the *second split* the angles between the stubs and output waveguide is now $90°$ and $90° - \theta$. The distortion in the signal is then due to the combined reduction in path length from both the *first* and *second split*, respectively. This produces the symmetry seen in Fig. 4.7B as the combined path length is the same for positive and negative angles, only changing the order in which the reduced paths are encountered.

As discussed in Fig. 4.6, it is also possible to minimize the impact of this non-ideal behaviour by adjusting the length of the stub waveguides. This is done by choosing the value of ΔL for each angle to ensure that the *effective* length of each stub is the same. An example of this for the case where $\theta = 25°$ is presented in Fig. 4.7. Here an additional 0.2 mm, 0.4 mm and 0.6 mm is added onto the length of the angled stub and the calculated transmission coefficient is presented. In this scenario the distortion (RMSE) was minimized for an added length of 0.6 mm. A parametric sweep of added length was performed for angles ranging from $-60°$ to $60°$. The path lengths which were calculated to minimize the impact of the distortion in the transmission coefficient is presented in Fig. 4.7D. Interestingly no additional length was required from $-15°$ to $15°$, which means that the distortion in the transmission coefficient will be negligible within this range.

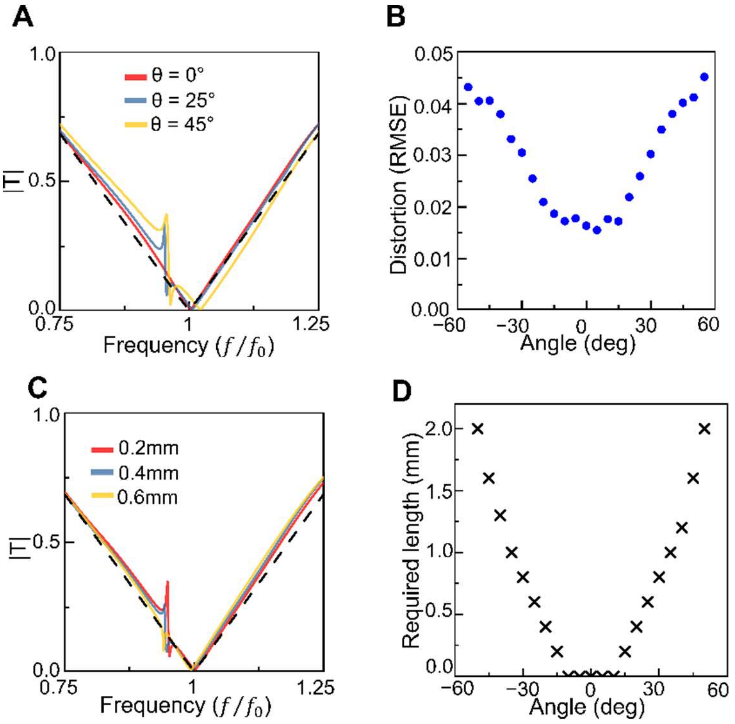

Figure 4.7 Impact of junction asymmetry on waveguide-differentiator performance. **A.** Distortion observed in the transmission coefficient of the differentiator for three asymmetry angles $\theta = 0°$, $\theta = 25°$ and $\theta = 45°$, respectively. **B.** Distortion (RMSE) produced by asymmetry angles from $\theta = -60°$ to $\theta = 60°$. **C.** Transmission coefficients with reduced distortion due to the increase in the length of the angled stub. **D.** Additional length required to minimize the impact of the distortion in the transmission coefficient.

4.3 First Order Waveguide Differentiators: Numerical Study

4.3.1 Transmission and reflection mode differentiators

To corroborate the performance of the proposed structures as first order differentiators, a numerical study is performed using the time domain solver of CST Studio Suite®. The results of this study are presented in this section. To being with a first order differentiator is constructed using two identical PEC-ended stubs ($w = h = 1$ mm) connected at a parallel junction. These stubs are connected at a $\theta = 0°$ angle (i.e. perpendicular to the input and output waveguides, see Fig. 4.5B). The lengths of these waveguides are also adjusted according to Fig. 4.6C so that the calculated minimum in the numerical transmission coefficient is at $f_0 = 8$ GHz (i.e., $L_s = 0.5227\lambda_0$). From Fig. 4.2A it can also be seen that the transmission and reflection coefficients of the $M = 2$ scenario are complementary with the minimum in the reflection coefficient occurring at 4 GHz. This means that if the incident signal is instead modulated with $f_0 = 4$ GHz then the first order derivative will instead be calculated using the reflected signal instead of the transmitted signal.

The numerical simulation results of this scenario are presented in Fig.4.8-4.10. Here a gaussian incident signal with a standard deviation of $\sigma = 0.5$ ns and a maximum voltage of 1 V is excited in the input waveguide of the differentiator structure. Two simulations are conducted in which the incident signal is modulated with $f_0 = 8$ GHz and $f_0 = 4$ GHz, respectively. Space-time plots showing the electric field calculated along a line at the centre of the input and output waveguides are presented in Fig. 4.8. Here, it can be seen that by changing the modulation frequency the location of the calculated derivative has shifted from the transmitted signal (top-panel, $f_0 = 8$ GHz) to the reflected signal (bottom-panel, $f_0 = 4$ GHz). Furthermore, the input and output voltage signals for the $f_0 = 8$ GHz and the $f_0 = 4$ GHz simulations are presented in Fig. 4.9 and Fig. 4.10, respectively. As it can be seen, in both scenarios there is a good agreement between the numerically calculated output signal and the normalized value of the analytically calculated derivative in both time (top panels) and frequency (bottom panels) domains. There is a slight asymmetry in the frequency domain output signal calculated in the $f_0 = 4$ GHz scenario. This is as the structure was optimized using Fig. 4.6C to work using the transmission coefficient at 8 GHz. Due to this the position of the minima in the reflection coefficient differs slightly from the predicted 4 GHz.

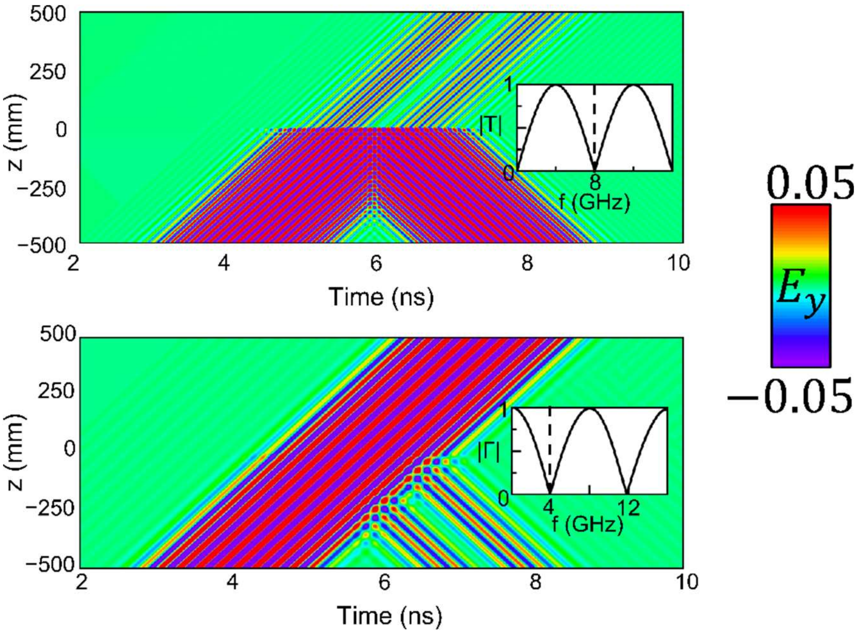

Figure 4.8 Space-time plots of first order differentiation in transmission (top, 8 GHz) and reflection (bottom, 4 GHz) configurations.

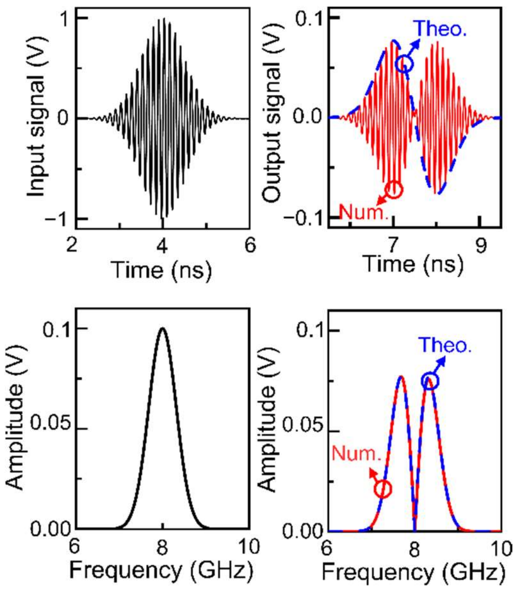

Figure 4.9 Differentiation of a gaussian incident signal in the transmission configuration (8 GHz central frequency). (top-left, bottom-left) incident signals in the time and frequency domains. (top-right, bottom-right) Output signals in the time and frequency domains.

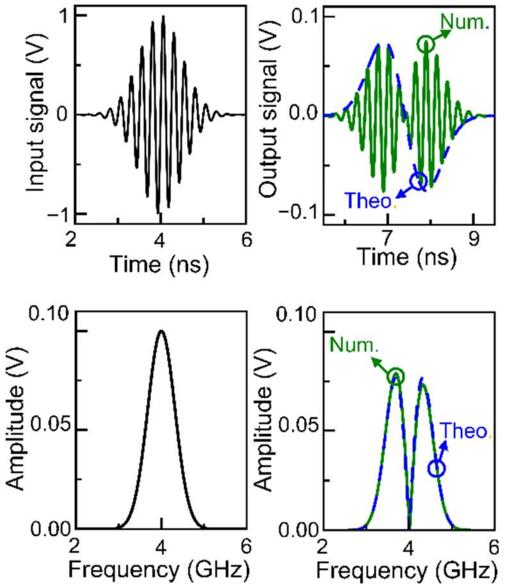

Figure 4.10 Differentiation of a gaussian incident signal in the reflection configurations (4 GHz central frequency). (top-left, bottom-left) incident signals in the time and frequency domains. (top-right, bottom-right) Output signals in the time and frequency domains.

For completeness and to demonstrate that the proposed structure can calculate the derivative of any incident signal (provided that the frequency content of that signal is constrained within the region of the transmission/reflection coefficient which may be approximated as linear), a numerical study of two arbitrary incident signals was conducted. The results of which can be seen in Fig. 4.11. The first incident signal (Fig. 4.11A) resembles a pyramid, a smooth step function (0 V to -1 V and back to 0 V), a gaussian and finally the first order derivative of the gaussian. This signal is then modulated at 8 GHz so that the derivative is calculated in the transmitted signal. The second incident signal (Fig. 4.11C) is constructed by converting the profile of a local landmark from Newcastle Upon Tyne, the Tyne Bridge, into an unmodulated time domain signal. This is done by manually converting the height of the bridge (measured from the road) into an input voltage and judiciously normalizing so that results are within a reasonable voltage range. The duration of the signal is also judiciously selected to be 25 ns. This signal is not modulated with a carrier frequency, however as the transfer function of this structure is also linear around $f = 0$ the derivative may still be calculated. The transmitted signals for both these scenarios are presented in Fig. 4.11B,D, respectively along with the theoretical normalized differentiated signal calculated via the finite difference method (Eq. 4.2). In all instances there is a good agreement between the calculated and theoretical output signals. Furthermore, it can be seen how the derivative of the Tyne-bridge incident signal has successfully identified the location of the towers at the start and end of the bridge, demonstrating how analogue differentiators may be used to perform edge detection.

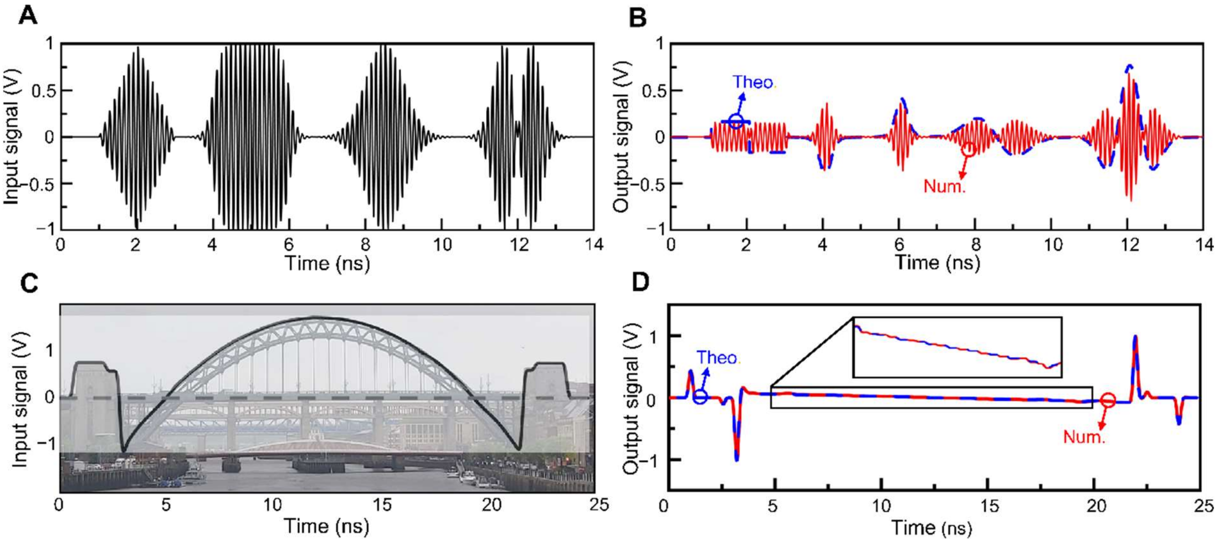

Figure 4.11 Differentiation of arbitrary incident signals in the transmission configuration. **A.**, **C.** Incident signals in the time domain. Here **C** has been constructed by converting the profile of a local landmark in Newcastle Upon Tyne into a time domain signal. **B.**, **D.** the calculated transmitted signals corresponding to **A** and **C**, respectively.

4.3.2 Impact of signal bandwidth on operation accuracy

Finally, a numerical study is conducted to investigate the impact of signal bandwidth onto the accuracy of the first order differentiation operation. From Fig. 4.2-4.3 it can be seen that the transmission/reflection coefficient is only linear in a finite region around the minimum. The bandwidth of this linear region can be adjusted by tailoring the length, number, and impedances of the connected stubs. It is expected that signals with frequency content outside of the linear region will produce a less accurate result than those that are confined within it. To investigate this the structure discussed in Fig. 4.8-4.11 is exploited, now with three stub lengths. These were as follows $L_s = 0.5227\lambda_0$ (i.e., the same as in Fig. 4.8-4.11), $L_s = 1.0222\lambda_0$ and $1.5205\lambda_0$, respectively. These structures are designed to produce a minimum at 8 GHz. This being the first, second and third minima, respectively (see Fig. 4.12B). These three minima may all be exploited to perform temporal differentiation; however, the bandwidth of the linear region is different for each design. For instance, from Fig. 4.12A it can be seen that in the range $0.8f_0$-$1.2f_0$ the transmission coefficient of the $L_s = 0.5227\lambda_0$ remains approximately linear. However, the transmission coefficients of the $L_s = 1.0222\lambda_0$ and $L_s = 1.5205\lambda_0$ designs begin to curve towards the edges of the region. It should be noted that there is a trade-off between the bandwidth of the differentiation operation and the magnitude of the output signal due to the shallower V-shape of the transfer function.

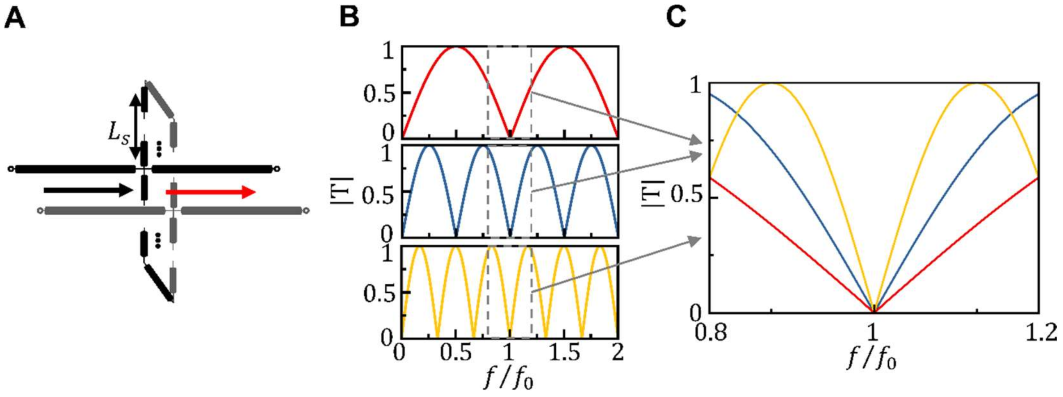

Figure 4.12 Impact of stub length of TF bandwidth. **A.** TL schematic representation of the three differentiators designed used in this section. **B.** Transmission coefficients of the designs from **A**. **C.** Transmission coefficients in the region around f_0.

These structures where simulated when excited with several Gaussian input signals, modulated at $f_0 = 8$ GHz, with frequency domain full width half maximums (FWHMs) in the range of $0.05f_0$ to $0.4f_0$. The performance of the differentiators was then evaluated by calculating the RMSE between the numerically calculated time domain output signal and the normalized analytically calculated derivative. The results of which are shown in Fig. 4.13. Fig. 4.13A shows the normalized frequency content of the numerically calculated output signal of the three structures when excited with the $0.4f_0$ FWHM signal. As it can be seen, the output signal of the $L_s = 0.5227\lambda_0$ structure accurately calculates the first order derivative of the input signal while the output signals of the $L_s = 1.0222\lambda_0$ and $L_s = 1.5205\lambda_0$ begin to deviate away from f_0. In the case of the $1.0222\lambda_0$ structure this is due to the curving of the transmission coefficients towards the edges of the frequency range. For the $L_s = 1.5205\lambda_0$ structure additional minima in the output spectra (not located at $f_0 = 1$) can also be observed. This indicates that the frequency content of the gaussian signal spans over multiple periods of the transmission coefficient and thus the accuracy of the differentiation operation is reduced. Fig. 4.13B shows the RMSE for the three structures as a function of the FWHM of the incident signal. For the $L_s = 0.5227\lambda_0$ and $L_s = 1.0222\lambda_0$ structures, there is little difference in the RMSE of the calculated derivative for the lowest FWHM signal. This is as in both cases the frequency content is constrained within the spectral region which may be approximated as linear. In all cases the accuracy of the differentiation operation decreases for more broadband incident signals as is expected.

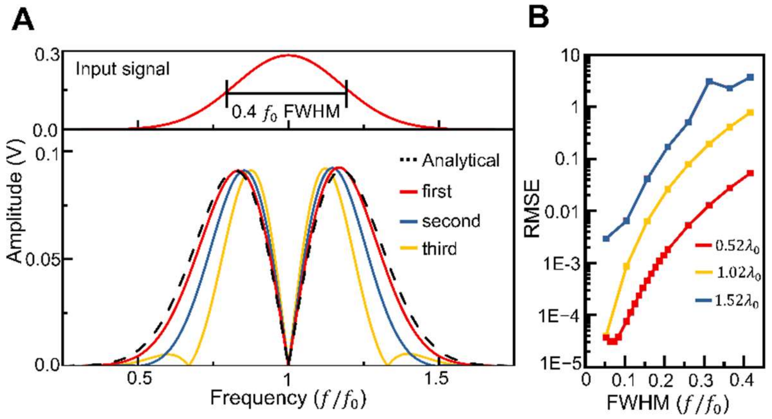

Figure 4.13 Impact of signal gaussian signal bandwidth on differentiation accuracy. **A.** Normalized frequency content of the calculated output signals of the $L_s = 0.5227\lambda_0$, $L_s = 1.0222\lambda_0$ and $1.5205\lambda_0$ structures respectively. **B.** Calculated RMSE in the output signals of three structures when excited with Gaussian signals of varying FWHMs.

4.4 Design of Arbitrary m^{th} Order Differentiators

Thus far, this chapter has discussed the use to TL filtering techniques to enable first order differentiation. It is also possible to use the same techniques to achieve higher order differentiation. One method of doing so is to cascade multiple first order differentiators together by connecting the output of one differentiator to the input of another. This then means that the first order differentiation operation is performed multiple times in series. The ideal transmission coefficient of this operation is as follows:

$$T_m = |[2\pi i(f - f_0)]^m| \tag{4.16}$$

where m is the order of differentiation to be performed. Eq. 4.16 is also valid for fractional differentiation operations in which the order m can be a non-integer value. One method of calculating these fractional derivatives in the time domain is by using the Riemann-Liouville equation as follows[186]:

$$\left.\frac{\partial^m f(t)}{\partial t^m}\right|_{t>b} = \frac{1}{\Gamma(\lceil m \rceil - m)} \frac{d}{dt^{\lceil m \rceil}} \int_b^t (t - x)^{\lceil m \rceil - m - 1} f(x) dx \tag{4.17}$$

where, in this instance Γ is the gamma function, which is commonly used to describe the factorials of complex numbers[187], $\lceil m \rceil$ indicates rounding m upwards towards the next integer and b is the basepoint of the system, which is important to describe the non-locality of fractional derivatives[188].

4.4.1 Cascading first-order waveguide differentiators.

The TL schematic representation of a second order cascaded differentiator is presented in Fig. 4.14A. Here each individual differentiator is represented as a “black box” which applies the differentiation operation to any incident signal. To construct the second order differentiator these individual first order differentiators are connected via a TL (waveguide). Importantly, as differentiation is performed using the minima of transmission coefficients, the majority of any incident signal will be reflected. In the context of cascaded operations, this means that a standing wave is produced between the two differentiators due to high reflection coefficient of the individual structures. These reflections can then interfere with the transmitted signal such that it no longer resembles the second order derivative of the input signal. Using TL theory, the impact of this interference can be reduced by choosing the length of the connected waveguide

L_c such that the reflections produced by the individual differentiators destructively interfere and cancel out.

To investigate this, an analytical study of the impact of the connection length on the transmission coefficient of the cascaded structure is performed. To evaluate the transmission coefficient of the combined structure the Redheffer star product method is exploited[189–191]. This method considers a pair of connected 2 × 2 scattering matrices $\boldsymbol{A_1}$ and $\boldsymbol{A_2}$ with a connection between a single input/output (as is shown in Fig. 4.14A). These scattering matrices are expressed as follow:

$$\begin{pmatrix} y_{1L} \\ y_{1R} \end{pmatrix} = \begin{pmatrix} \Gamma_1(f) & T_1(f) \\ T_1(f) & \Gamma_1(f) \end{pmatrix} \begin{pmatrix} x_{1L} \\ x_{1R} \end{pmatrix} \tag{4.18a}$$

$$\begin{pmatrix} y_{2L} \\ y_{2R} \end{pmatrix} = \begin{pmatrix} \Gamma_2(f) & T_2(f) \\ T_2(f) & \Gamma_2(f) \end{pmatrix} \begin{pmatrix} x_{2L} \\ x_{2R} \end{pmatrix} \tag{4.18b}$$

where $\Gamma_{1,2}(f)$ and $T_{1,2}(f)$ are the frequency dependent reflection and transmission coefficients, respectively of the first and second differentiator calculated using Eq. 4.15. Here L and R indicate an input/output signal which arrives/departs from the left and right of the individual differentiator respectively. Additionally, to account for the length of the connection, a phase change should be applied to one of the scattering matrices (for instance $\boldsymbol{A_1}$). This is done using the following conversion: $T_1(f) \rightarrow T_1(f)e^{-i\varphi_c(f)}$, $\Gamma_1(f)e^{-2i\varphi_c(f)}$ where $\varphi_c = 2\pi f L_c/c$ is the electrical length of the connection. The connection between the two structures is then expressed as:

$$x_{1R} = y_{2L} \tag{4.19a}$$

$$x_{2L} = y_{1R} \tag{4.19b}$$

By combining Eq. 4.18-4.19 the reflection and transmission coefficients of the combined structure can be written as:

$$T_{combined}(f) = \frac{T_1(f)T_2(f)}{1 - \Gamma_2(f)\Gamma_1(f)} \tag{4.20a}$$

$$\Gamma_{combined}(f) = \frac{T_1(f)^2\Gamma_2(f)}{1 - \Gamma_2(f)\Gamma_1(f)} + \Gamma_1(f) \tag{4.20b}$$

Using Eq. 4.20 the calculated transmission coefficient (magnitude and phase) can be seen in Fig. 4.14B. These results are calculated when two two-stub parallel differentiators (same structure used in Fig. 4.8-4.11) are connected together via a parallel plate waveguide with $w = h = 1$ mm and vacuum ($\varepsilon_r = 1$, $\mu_r = 1$) as the filling material. This study is performed in the frequency range from $3f_0/4$ to $5f_0/4$ (i.e., the region around the minima) for connection lengths from $\lambda_0/5$ to λ_0. From these results it can be seen that for the majority of connection lengths the combined transmission coefficient is non symmetrical around f_0. This would reduce the accuracy of the differentiation operation as symmetry around f_0 is a characteristic of Eq. 4.16. In fact, from TL theory transmission coefficient of the combined structure is only symmetrical around f_0 when $L_c = a\lambda_0/4$, where $a = 1,2,...$. To demonstrate this, the calculated transmission coefficients when $L_c = \lambda_0/4$, $2\lambda_0/4$, $3\lambda_0/4$ and $4\lambda_0/4$ are presented in Fig. 4.14C. These results have also been separated into the odd (left-panel) and even (right-panel) multiples of $\lambda_0/4$. This is as, while symmetry around f_0 is preserved in both cases, only the odd integer multiples of $\lambda_0/4$ show the characteristic U-shaped transmission coefficient of a second order differentiator. When L_c is instead an even integer multiple of $\lambda_0/4$ the combined structure instead still exhibits a V-shaped transmission coefficient around f_0. This is due to the destructive and constructive interference of the reflected signals when L_c is an odd and even multiple of $\lambda_0/4$, respectively. This can be understood in terms of the splitting of time domain signals. Like in Eq. 4.1 destructive interference between the first and second split is required to produce the differentiation operation which only occurs when L_C is an odd integer multiple of λ_0/4. It should also be noted that the U-shaped (second order) transfer functions produced by Eq. 4.20 are not the same as two first order operations and the structure should still be optimized to best implement the desired operation. Fig. 4.14D shows how the transmission coefficient at a pair of fixed frequencies, $f = (1 - 0.125)f_0$ and $f = (1 + 0.125)f_0$ varies with the connection length. This highlights the symmetry of the transmission coefficient when $L_c = a\lambda_0/4$ as these are the only intersection points of the two functions.

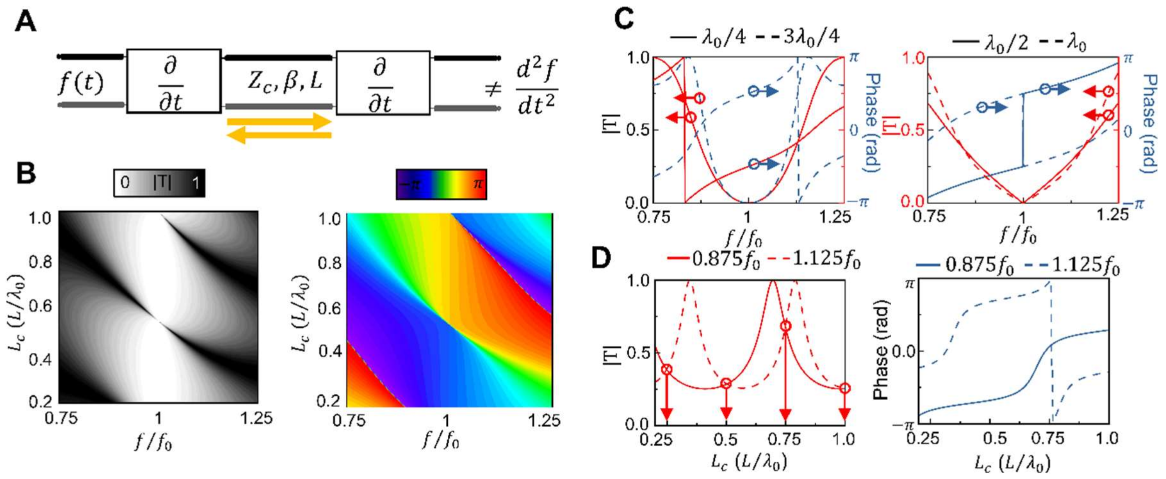

Figure 4.14 Cascading first order differentiators: impact of connection length on TF shape. **A.** TL schematic representation of two cascaded first order differentiators. **B.** Magnitude (left) and Phase (right) of the transmission coefficient of the cascaded structure presented in **A** for a range of connection lengths. **C.** Transmission coefficients for odd-integer (left) and even-integer (right) multiples of $\lambda_0/4$. **D.** Transmission coefficients at $f = (1 - 0.125)f_0$ and $f = (1 + 0.125)f_0$ connection lengths between $0.25\lambda_0$ and λ_0.

4.4.2 mth *order example operations*

Based on the principle of cascading first order differentiators, the general structure of an mth order differentiator is presented in Fig. 4.15. This structure consists of multiple layers of individual first order differentiators cascaded together. At each layer, the number of stubs, the length of the stubs and the PEC/open ended nature of the stubs can all be individually controlled. Additionally, the length of each of the connecting waveguides can also be individually defined. This produces a highly parameterized system which allows for a great deal of control over the shape and spread of the minima in the transmission/reflection coefficient. To solve for the reflection and transmission coefficients of this structure, the same principles as those discussed in Chapter 2 are used. Here Eq. 4.20 is applied to combine the scattering matrices of two connected differentiators into a new scattering matrix. This is written as:

$$\boldsymbol{A}_{combined} = \begin{pmatrix} \Gamma_{combined} & T_{combined} \\ T_{combined} & \Gamma_{combined} \end{pmatrix} = \boldsymbol{A_1} \star \boldsymbol{A_2} \tag{4.21}$$

where "⋆" denotes the Redheffer star product operation[190]. Then through repeatedly applying Eq. 4.21, at each stage combining two connected scattering matrices, the transmission and reflection coefficients of the overall structure are calculated. This is a simplification of the algorithm described in Chapter. 2 and is used here to reduce the computing time required to calculate the transmission coefficients of many designs.

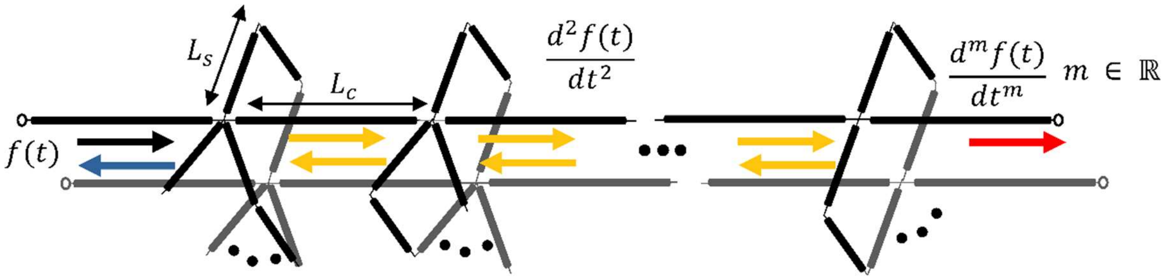

Figure 4.15 TL schematic representation of the general structure of an arbitrary order differentiator

Using the structure presented in Fig. 4.15 and Eq. 4.21, the transmission coefficients of various candidate designs are calculated. The suitability of these designs as a differentiator is evaluated by calculating the RMSE between the transfer function of the candidate design and that of an ideal mth order derivative as follows:

$$RMSE = \sqrt{\frac{1}{2\Delta f}\int_{f_0-\Delta f}^{f_0+\Delta f} W(f)[|T(f)| - C|f - f_0|^m]^2 df} \tag{4.22}$$

where Δf is the frequency range around f_0 in which the structure is designed to operate (i.e., from $f_0 - \Delta f$ to $f_0 + \Delta f$). $W(f)$ is a weighting function which is used to enthesis the RMSE between the two functions for frequencies near f_0. For the designs presented in this chapter the function $W(f) = |(f - f_0)/\Delta f|$ is used. The required normalization factor is calculated by selecting the value of C which minimized the RMSE, with the restriction that $C \geq 0.2$. This is to prevent the trivial case of $T(f) = 0$ and $C = 0$ returning an RMSE value of 0. From these candidate designs the top 5% are selected and a parameter optimisation is conducted using the optimization toolbox from MATLAB®. Two examples of designs produced using this method are presented in Fig. 4.16A and Fig. 4.17A, respectively. These designs where optimised to perform $m = 2$ and $m = 0.717$ order differentiation respectively. The value of $m = 0.717$ was chosen at random between the range of 0 to 1. These structures are also adjusted to minimize the impact of the effects discussed in Section 4.2. The numerically simulated transmission coefficients using the frequency domain solver of CST Studio Suite® are presented in the right panel of Fig. 4.16A and Fig. 4.17A respectively.

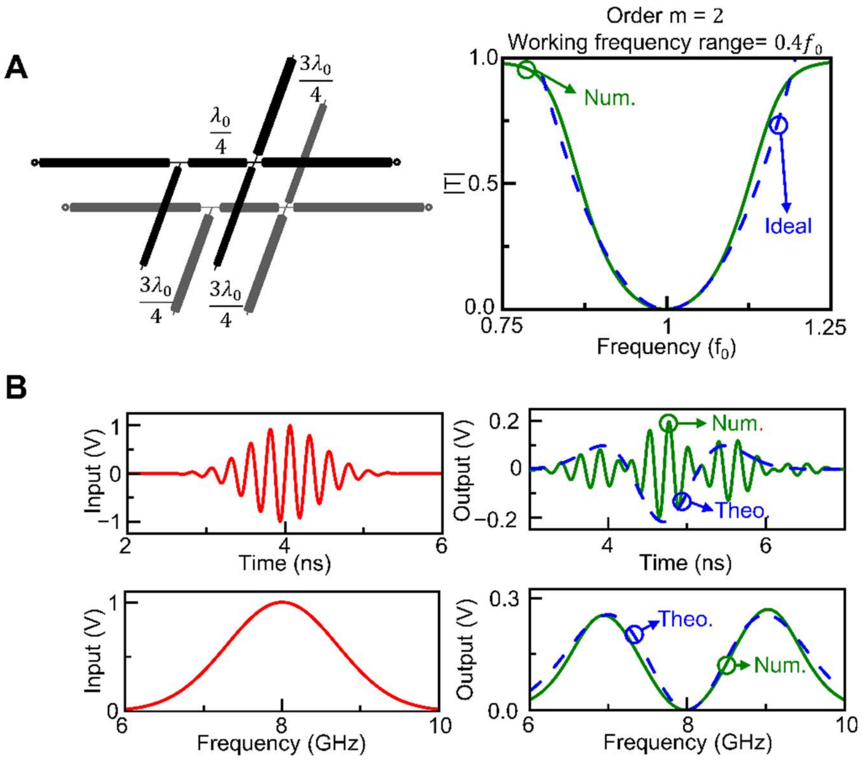

Figure 4.16 Design and numerical simulation of a second order differentiator. **A.** TL schematic representation of the optimized design and the numerically simulated transmission coefficient. **B.** Time domain results of the structure from **A** performing $m = 2$ differentiation onto an incident Gaussian signal.

For completeness, a numerical study of these structures is performed using the time domain solver of CST Studio Suite®. In both cases a Gaussian input signal was excited in the left-hand waveguide (input waveguide) and the differentiated signal was observed in the signal transmitted through to the right-hand waveguide (output waveguide). For the $m = 2$ differentiator, the envelope of the incident Gaussian was chosen to have a standard deviation in the time domain of $\sigma = 0.3536$ ns and a maximum value of 1 V. This is so that the frequency content of the incident signal would be confined within the working frequency range of the structure. This is defined as the frequency range in which the numerical and ideal transmission coefficients are within 10% of each other. The calculated output signal of this scenario is presented in the Fig. 4.16B in both time (top-right) and frequency (bottom-right) domains along with the analytically calculated value of the second order derivative. As can be seen there is a clear agreement between the numerical and analytical results indicating that the structure is indeed performing second order differentiation. This study is also conducted for the $m = 0.717$ structure now using a Gaussian input signal with $\sigma = 0.4632$ ns and a maximum value of 1 V. The numerically calculated output signals of this scenario are presented in Fig. 4.17B in both time (top-right) and frequency (bottom-right) domains along with the analytically calculated fractional derivative using Eq. 4.17. Again, there is a clear agreement between the numerical and analytical results. Furthermore, the envelope of the time domain signal has two “lobes”. The second of these “lobes” has a reduced amplitude and a longer duration than the first, which is a characteristic of the fractional derivatives of Gaussian signals[182,192] when $0 < m < 1$. This indicates that the structure is indeed calculating the second order derivative as intended.

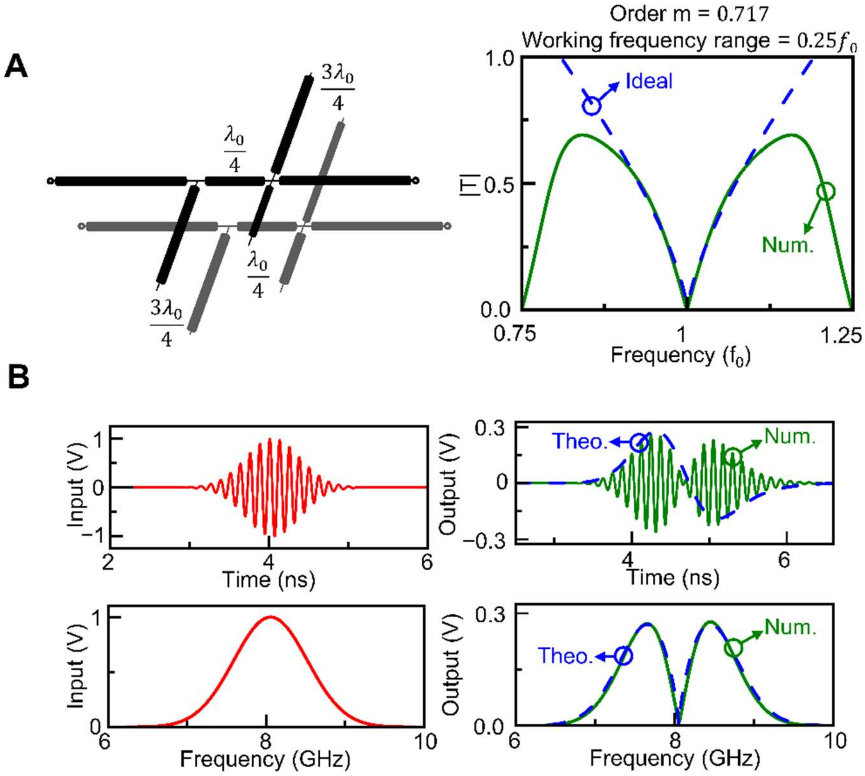

Figure 4.17 Design and numerical simulation of an $m = 0.717$ order differentiator. **A.** TL schematic representation of the optimized design and the numerically simulated transmission coefficient. **B.** Time domain results of the structure from **A** performing $m = 0.717$ differentiation onto an incident Gaussian signal.

4.5 Chapter 4 conclusions

A method of performing analogue time domain differentiation onto the envelope of an incident EM-signal has been presented. This is done by exploiting TL filtering techniques, specifically stubs, to tailor a transmission (or reflection) function to resemble the greens function of a differentiation operation. A full mathematical description of this technique has been presented for completeness. This technique has been extended to mth order (where m is any positive real number i.e. not necessarily an integer) differentiation by connecting multiple layers of first order differentiators together sequentially. Numerical simulation results of this technique have been presented and are in agreement with theoretical values. These operations are performed in one-shot (as the signal propagates though the network) and thus has the potential to enable high speed computing of differential operators within an application specific processor. This work has been published in the Scientific Reports article titled “Time derivatives via interconnected waveguides”.

Chapter 5. Calculating the Solutions to PDEs Using Waveguide-based Metatronic Circuits

In addition to structures exploiting the Greens function method[21], as was discussed in chapter. 4, EM wave-based structures have also been exploited to calculate the solutions to iterative computing tasks. These include performing matrix inversion[193], solving integral equations[175,178,194] and solving PDEs[185,195–197]. In this realm, calculating the solutions to PDEs is of particular importance due to their prevalence through physics, mathematics and engineering. In general, the solutions to arbitrary PDEs cannot be expressed in a closed form, meaning specialized simulation software packages are required to produce approximate numerical solutions. Much research effort has been dedicated to optimizing these tools, however, due to the inherent size and iterative nature of the calculations, this remains a computationally intensive task, via conventional computing systems. In recent years EM wave-based PDE solvers have been demonstrated to solve equations in the form of the Poisson equation ($\nabla^2 g(x, y) = 0$, where g is the function to be solved for and x,y are the independent variables of g) by exploiting structures including, dielectric ring resonators[185], inverse design wave splitters[185] and metatronic circuits using epsilon-near-zero materials[197]. In this chapter, networks of waveguide-based metatronic circuits are exploited to calculate the solution of PDE boundary value problems. This work has been uploaded to ArXiv[27] and at the time of writing is currently under review to be published in a scientific journal. Different to previous works, this technique exploits metatronic circuits constructed from thin dielectric slabs without the use of epsilon-near-zero materials. This allows for PDEs in the form of the Helmholtz wave equation ($\nabla^2 g(x,y) + k^2 g(x,y) = 0$ where k is the wavenumber) to be solved.

To being with, this chapter introduces the core concepts behind analogue PDE solving for both the Poisson and Helmholtz equations. After this, the proposed method for PDE solving with metatronic circuits is introduced alongside a small-scale example solution. It is then explained how the geometric parameters and EM properties of the proposed metatronic circuit may be optimized to obtain more accurate PDE solutions. Next, the scaling and sampling rate of the PDE solution is discussed. Then finally, it is shown how this method of PDE solving may be exploited to calculate the solution to both closed and open boundary value problems.

5.1 Solving PDEs via an Analogy with the Finite Difference Method

5.1.1 Solutions to Poisson's equation using lumped impedances

To begin with, first consider how a network of conventional lumped circuit elements (resistors, inductors, and capacitors) may be exploited to compute solutions to the Poisson equation ($\nabla^2 g(x,y) = 0$). This equation is commonly used to model phenomena such as heat transfer or electro/magnetostatics[198]. In previous works it has been shown that this may be done by arranging the circuit elements into a periodic network of circuit junctions[145,146]. A section of this network is shown in Fig. 5.1A. As it can be seen, each junction between lumped elements is connected to the four nearest junctions (up, right, down and left), in this way forming a grid-like network. The impedances, voltages, and currents at one of these circuit junctions is shown in Fig. 5.1B. Here the central junction is connected to each of the four adjacent junctions via an RLC circuit connected in series[146]. The impedance of these circuits are Z_1, Z_2, Z_3 and Z_4 where 1, 2, 3 and 4 refers to the top, right, bottom and left circuits respectively. Likewise, the currents though these circuits (and into the centre junction) are I_1, I_2, I_3 and I_4. Considering Kirchhoff's current law[71] at the centre junction, the governing equation of this network can be written as follows:

$$\sum_{a=1}^{4} I_a = \frac{V_1}{Z_1} + \frac{V_2}{Z_2} + \frac{V_3}{Z_3} + \frac{V_4}{Z_4} - \left(\frac{1}{Z_1} + \frac{1}{Z_2} + \frac{1}{Z_3} + \frac{1}{Z_4}\right) V_0 = 0 \qquad (5.1)$$

where V_1, V_2, V_3, V_4 and V_0 are the voltage values at the top, right, bottom, left and centre junction in Fig. 5.1. Importantly as the network is periodic, Eq. 5.1 holds for all junctions of the network Eq. 5.1 can be simplified when considering the special case where $Z_1 = Z_2 = Z_3 = Z_4 = Z_L$. In this scenario the governing equation becomes:

$$\frac{1}{Z_L}(V_1 + V_2 + V_3 + V_4 - 4V_0) = 0 \qquad (5.2)$$

To understand how this structure may be exploited for PDE solving, compare Eq. 5.2 with the well-known finite difference formula for the discretized two-dimensional Laplacian[183]. This is as follows:

$$\nabla^2 g(x,y) \approx \frac{1}{h^2}[g(x+h,y) + g(x-h,y) + g(x,y+h) + g(x,y-h) - 4g(x,y)] \qquad (5.3)$$

where h is the step size of the discretization of $g(x,y)$. As it can be seen, Eq. 5.2 is analogous to Eq. 5.3 if the impedance value of the connecting circuits Z_L is chosen to be representative of the step size of the solution with $Z_L = \sqrt{h}$. This means that the overall network of lumped elements may be conceptualised as an area of simulation space and the junctions between the lumped elements as the discretized sampling points of this network.

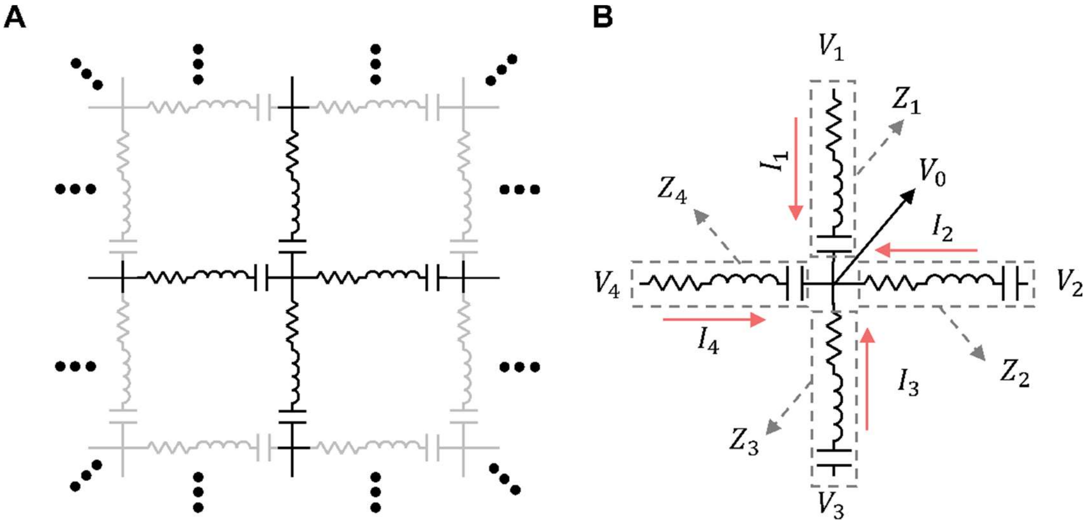

Figure 5.1 Poisson equation solving with networks of lumped elements. **A.** Periodic arrangement of lumped elements connected in a grid-like network. **B.** Lumped elements connecting a central node 0 to the four nearest neighbouring nodes, 1 (top), 2 (right), 3 (bottom) and 4 (left).

5.1.2 Solutions to the Helmholtz equation using T-circuits

Conceptually, this method of PDE solving presented in Fig. 5.1 may also be exploited to solve PDEs in the form of the Helmholtz equation. i.e., PDEs which may be represented as $\nabla^2 g(x,y) + k^2 g(x,y) = 0$. This may be done by altering the structure presented in Fig. 5.1 to also include the $k^2 g(x,y)$ term. The finite difference representation of this equation is as follows:

$$\nabla^2 g(x,y) + k^2 g(x,y) =$$

$$\frac{1}{h^2}[g(x+h,y) + g(x-h,y) + g(x,y+h) + g(x,y-h)] + k^2 g(x,y) = 0 \qquad (5.4)$$

Now, how can the structure presented in Fig. 5.1 be modified to emulate Eq. 5.4 instead of Eq. 5.3? To answer this, two structures presented in Fig. 5.2A and Fig. 5.3 are proposed. As in Fig. 5.1A these structures also consist of a periodic arrangement of circuit elements connected at junctions, however in these examples the RLC circuit has instead been replaced by a T-circuit and a π-circuit, respectively. Additionally in Fig 5.2 the T-circuits are connected at the junction in series while in Fig. 5.3 the π-circuits are connected in parallel. This discussion will focus on the series structure presented in Fig. 5.2 as this is the structure which is exploited to produce the later results in this chapter. The choice of the structure in Fig. 5.2 over Fig. 5.3 is to assist in the implementation of metatronic circuit elements which are used to emulate the performance of the T-circuit. This will be discussed in more detail in section 5.2.1.

Now, as the T-circuit from Fig. 5.2A are connected in series, the flow of current through them will form a rotating current around the centre of the series junction[30,70] I_0. This means that the magnetic field at the centre of the junction is out-of-plane. The rotating currents around the adjacent connected junctions are I_1, I_2, I_3 and I_4, respectively. Then, by looking into one of the connected T-circuits, the voltage across the circuit (see Fig. 5.2B) is calculated as:

$$V_a = Z_p(I_a - I_0) - Z_s I_0 \tag{5.5}$$

where $a = 1,\ 2,\ 3,\ 4$ and Z_p, Z_s are the parallel and series impedances of the connecting T-circuit, respectively (see Fig. 5.2B). The governing equation of this network can then be calculated by considering Kirchhoff's voltage laws[71] using the voltage values calculated from Eq. 5.5 as follows:

$$\sum_a^4 V_a = Z_p(I_1 + I_2 + I_3 + I_4 - 4I_0) - 4Z_s I_0 = 0 \tag{5.6}$$

Now by comparing Eq. 5.6 with Eq. 5.4 it can be seen that the two equations are analogous if the impedances of the T-circuit are chosen to be $Z_p = 1/h^2$ and $Z_s = -k^2/4$. With this selection of impedances, the first and second terms of Eq. 5.6 are analogous to the $\nabla^2 g(x,y)$ and the $k^2 g(x,y)$ terms of Eq. 5.4, respectively. A schematic representation of a finite difference grid is presented in Fig. 5.2C. Here the top, left, bottom, right and centre junctions of Fig. 5.2 are analogous to the $(0,1)$, $(1,0)$, $(0,-1)$, $(-1,0)$ and $(0,0)$ points of the finite difference grid respectively.

It is important to note that while the selection of impendences $Z_p = 1/h^2$ and $Z_s = -k^2/4$ allows for an analogy to be made between the two equations an additional transformation is required in order for this analogy to be strictly valid. This is as $h \in \mathbb{R}$ while $Z_p \in \mathbb{C}$. To address this mismatch the current values from Eq. 5.6 are renormalized using the transformation $I_a' = I_a/Z_p^*$ where * indicates the complex conjugate and I_a' is the transformed impedance value. With this Eq. 5.6 can be rewritten as:

$$|Z_p|^2(I_1' + I_2' + I_3' + I_4' - 4I_0') - 4Z_s Z_p^* I_0 = 0 \tag{5.7}$$

which is analogous to Eq. 5.4 if the impedances are instead chosen to be $\left|Z_p\right| = h$ and $Z_s = -4k^2/Z_p^*$, respectively. Furthermore, as the currents in Eq. 5.7 are rotating around the junction a solution to Eq. 5.7 is also valid when considering the out-of-plane H_z-field at the centre of the waveguide junctions.

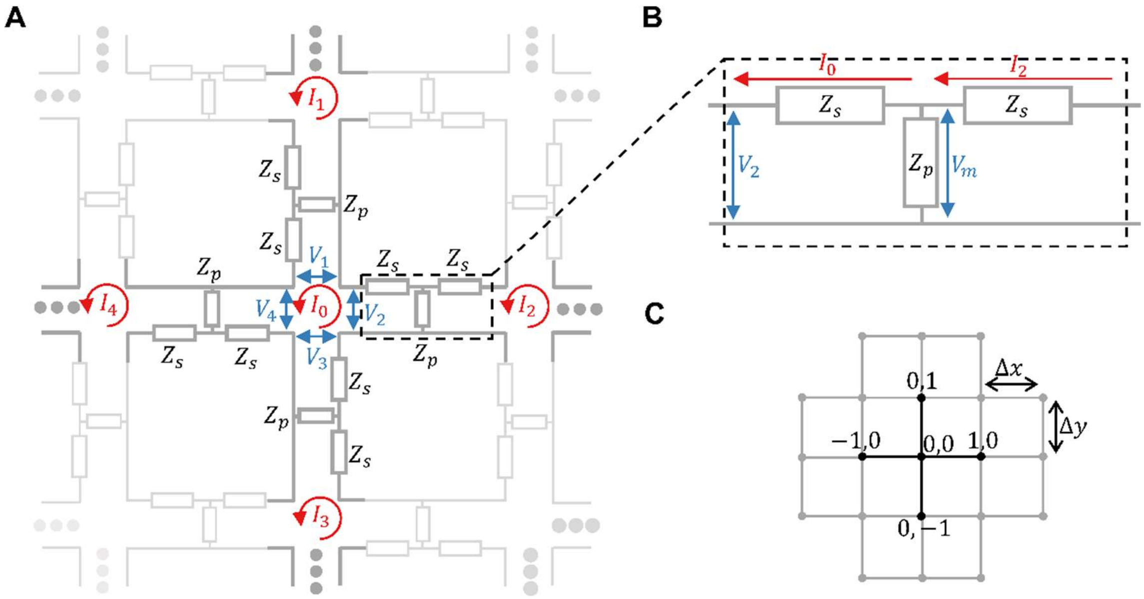

Figure 5.2 Equivalent circuit of the proposed PDE solving structure exploiting T-circuits connected in series. **A.** Periodic network of T-circuits arranged in a grid-like network. Each junction is connected to the four nearest neighbouring junctions as in Fig. 5.1A **B.** Circuit representation of a T-circuit connecting two junctions together. **C.** Schematic representation of a finite difference grid calculating Laplace's equation.

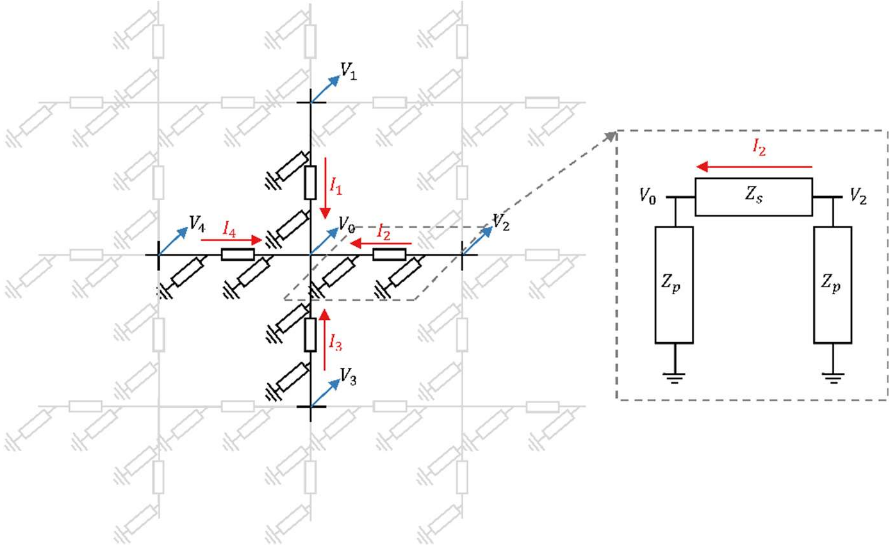

Figure 5.3 Equivalent circuit of a PDE solving structure exploiting a periodic network of π-circuits connected in parallel.

5.2 Emulating the Performance of an Electrical T-circuit Using Metatronic Circuits

5.2.1 General structure of the metatronic T-circuits and numerical study of a 3×3 network

To implement the structure presented in Fig. 5.2 metatronic circuits are exploited. As discussed in the introduction these are subwavelength structures of dielectric or metallic elements which may be used to emulate the performance of electrical lumped elements at higher frequencies[88,89,199] (in this case microwaves). Using the principles discussed in section 1.3 and Eq. 1.27-1.28, a metatronic circuit capable of emulating the electrical T-circuit from Fig. 5.2B is constructed[96,97]. A schematic representation of this structure is presented in Fig. 5.4A. This structure consists of three thin dielectric slabs, one per impedances of the electronic T-circuit. The parallel impedance is emulated by a slab with a thickness of w_p and a relative permittivity of ε_p. The equivalent impedance of this slab is calculated using Eq. 1.27. The two series impedances are emulated by dielectric slabs sandwiched between two $\lambda_0/4$ regions of vacuum ($\varepsilon_r = 1$). Here, λ_0 is the operating wavelength of the PDE solving structure in free space (for all calculations presented in this chapter $\lambda_0 = 30$ mm). The dielectric slabs have relative permittivity values and thicknesses of ε_s and w_s, respectively. The combined structure of the two $\lambda_0/4$ regions and the ε_s dielectric slab acts as a single series impedance with a value calculated using Eq. 1.28. Here, the host medium is vacuum, meaning that $Z_h = Z_0 = 120\pi\ \Omega$.

This structure (three dielectric slabs, four $\lambda_0/4$ regions) is then embedded within a parallel plate waveguide to enable the circuits to be connected at series junctions. The entire structure then emulates the performance of the electrical T-circuit presented in Fig. 5.4B Importantly, Eq. 1.27-1.28 are valid when considering a TEM incident signal as is the case for parallel plate waveguides. However, when selecting the dimensions of the parallel plate waveguides it was found that the cross-section should be wide compared to the operating wavelength to limit the impact of fringing fields at the edges of the waveguide as is explained in [27]. This informed the choice of series junctions from Fig. 5.2 instead of parallel as in Fig. 5.3, as to ensure perfect splitting at the junction the cross-sectional area of the junction should also be small compared to the operating wavelength. This is possible with series junctions as it is the plate separation, not the waveguide width, which determined the junction cross-section. It is also possible to emulate the performance of a π-circuit for the parallel implementation of the PDE solving structure. For instance, this can be done by modifying the structure presented in Fig. 5.4A by removing the left and right $\lambda_0/4$ regions. In this scenario the parallel to series impedance transform associated with these regions is instead applied to the centre slab and thus the structure instead emulates a π-circuit[30].

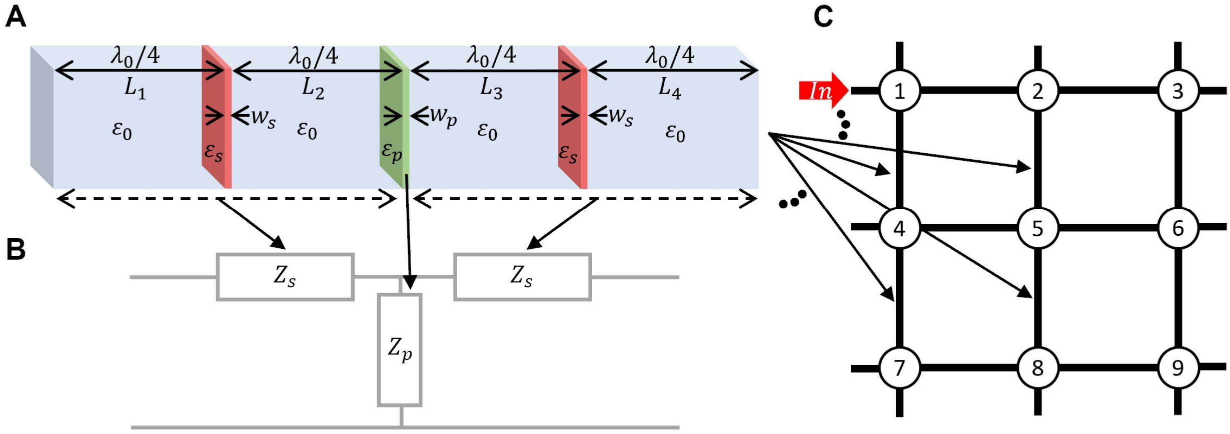

Figure 5.4 A. Proposed structure for the emulation of the electrical T-circuit by exploiting metatronic circuits. **B.** Equivalent circuit of the structure presented in **A**. **C.** Schematic representation of a 3×3 network of waveguide junctions for PDE solving. Here each node represents a series parallel plate junction, and each line represents where the waveguide-based metatronic filters from **A** have been inserted.

As an example, and to demonstrate the potential of this method of PDE solving, a numerical study of a 3×3 network of metatronic T-circuits is conducted. A schematic representation of this structure is presented in Fig. 5.4C. In this example, the waveguide based metatronic T-circuit is designed with $w_s = w_p = 0.2$ mm ($\lambda_0/150$) and $\varepsilon_p = 9.54$ and $\varepsilon_s = 21.44$ respectively. From Eq. 1.27-1.28 the calculated impedance values are $Z_p = 2.5iZ_0$ and $Z_s = -0.9iZ_0$, respectively. This means that the PDE parameters are $h = 0.4$ and $k = 3$. It should be noted that the units of h and k are informed by the physics of the PDE to be solved. For example, if the PDE is representative of an EM wave then h and k would have units of m and m^{-1}, respectively. However, in this chapter they will be left as unitless values so that a general solution to a PDE may be obtained. To corroborate the performance of the metatronic T-circuit a full ABCD matrix analysis of the three-slab structure was conducted to extract the emulated impedance values. The details of this calculation are discussed in section 5.22. In this calculation it was found that the designed three-slab structure emulated a T-circuit with the impedance values $Z_p = 2.51522iZ_0$ and $Z_s = -0.9311iZ_0$, respectively. The difference between these values and the theoretical values calculated using Eq. 1.27-1.28 is due to the thickness of the dielectric slabs used to construct the metatronic T-circuit. Eq. 1.27-1.28 are only valid for thin dielectric slabs and while 0.2 mm is within this regime, there is still a slight deviation between the ideal and actual results associated with the thickness. As will be discussed the emulated impedances of the three-slab structure may be altered to better match the desired values by optimizing the geometric parameters and EM properties of the three-slab structure. However, in this initial example the unoptimized structure will be used.

To excite this structure a 10 GHz monochromatic signal is excited from the left-waveguide of the top-left junction of the waveguide network (labelled as junction 1 in Fig. 5.4C). The numerical results of the out-of-plane H_z-field calculated at the centre of the waveguide junctions is presented in Fig. 5.5. These results have been normalized with respect to the out-of-plane H_z-field at the centre of the top-left waveguide junction and are presented alongside the theoretical values for the out-of-plane H_z-field in Fig. 5.5B. In this chapter, "theoretical" refers to values calculated using the waveguide network solving algorithm outlined in Chapter. 2. The arrows in Fig. 5.5 show the deviation between the numerically calculated and the theoretical results.

One important detail to note is that for a junction to conform to Eq. 5.7, it must be connected to four adjacent junctions. This means that for the 3×3 example only the central junction (junction 5) will conform to Eq. 5.7 and thus calculate a solution to the PDE. The remaining junctions are *boundary junctions* which are used to implement the desired PDE boundary conditions. As will be discussed in detail in section 5.5, if a boundary value is not provided then these junctions may produce unwanted reflections in the PDE solution. Although these reflections do impact the PDE results, the system must still conform to Eq. 5.7 and thus the calculated solution is still a valid solution of the Helmholtz equation. The analytical value of the H_z-field may be calculated at this point by considering the numerical values calculated at junctions 2, 4, 6 and 8, respectively. From Eq. 5.7 this value is calculated as $H_5 = (H_2 + H_4 + H_6 + H_8)/(4 - h^2 k^2)$. Using this value, the difference between the numerical value of H_5 and the analytical value of H_5 is calculated as $\sim 7.23\%$. This demonstrates how this structure may indeed be used to produce an approximate solution to the Helmholtz equation.

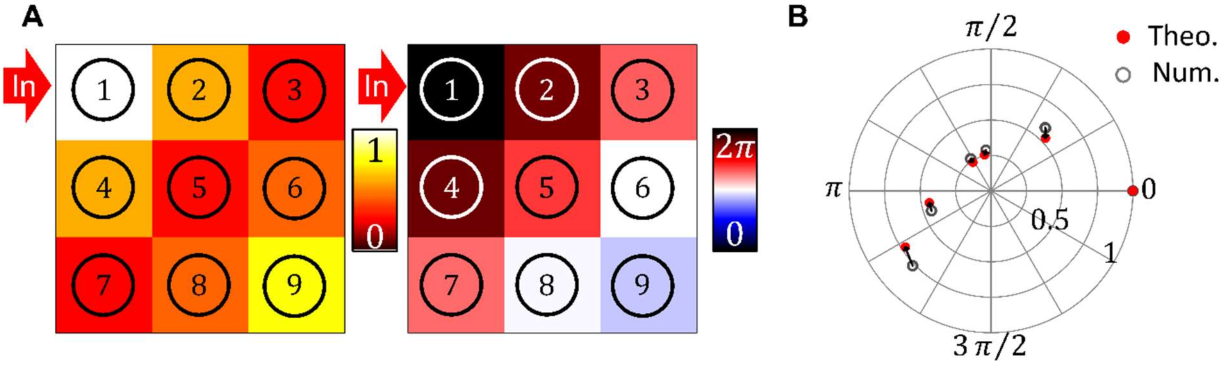

Figure 5.5 Numerical results for a 3 × 3 PDE solving structure when excited from the left waveguide of junction 1. **A.** Magnitude (Left) and Phase (right) of the out-of-plane H_z-field calculated at the centre of the 9 junctions. **B.** Theoretical (blue-dot) and Numerical (red-circle) results in phasor form. The arrows show the variation between the two sets of results.

5.2.2 Optimization of the metatronic T-circuits

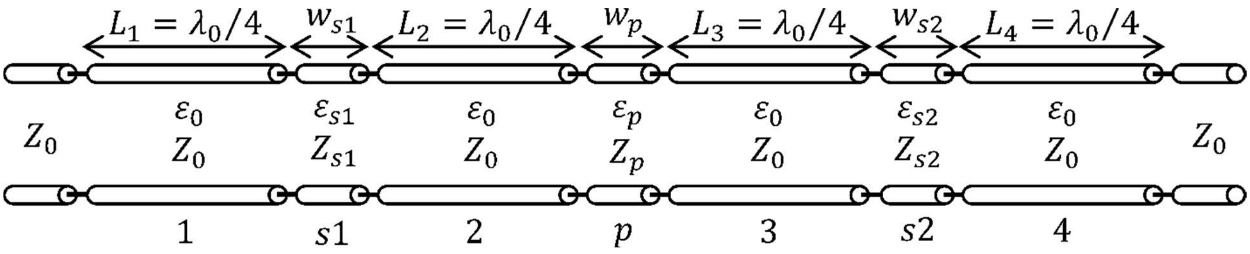

Figure 5.6 TL schematic representation of the proposed metatronic T-circuit structure.

As mentioned in section 5.2.1 a full ABCD matrix analysis is conducted to evaluate the performance of the three-slab structure. The TL schematic representation of this structure is presented in Fig. 5.6. It consists of 7 TL segments representing the 4 $\lambda_0/4$ regions and the three dielectric slabs. Using the values defined above, the ABCD matrix of the total structure may be calculated using the method outlined in section 1.3.4. For comparison, the ABCD matrix elements of an electrical T-circuit using the theoretical impedance values are calculated as follows[30]:

$$A_{T-circuit} = 1 + \frac{Z_{s1}}{Z_p} \tag{5.8a}$$

$$B_{T-circuit} = Z_{s1} + Z_{s2} + \frac{Z_{s1}Z_{s2}}{Z_p} \tag{5.8b}$$

$$C_{T-circuit} = \frac{1}{Z_p} \tag{5.8c}$$

$$D_{T-circuit} = 1 + \frac{Z_{s2}}{Z_p} \tag{5.8d}$$

where Z_{s1} and Z_{s2} are the left and right series impedance values. Thus far, the examples presented have considered networks where $Z_{s1} = Z_{s2} = Z_s$, however in general Z_{s1} and Z_{s2} may differ as is explored in section 5.5.3. Clearly, if the three-slab structure is correctly emulating the performance of a T-circuit with the designed values of Z_s and Z_p then the two ABCD matrices (calculated using Eq. 1.20 and Eq. 5.8, respectively) should be the same. However, as mentioned above, it was found that there was indeed a slight variation in these two matrices which would impact the accuracy of the calculated PDE solution. The true impedance values emulated by the three-slab structure can be found by substituting the ABCD parameters of the three-slab structure into Eq. 5.8 and solving for Z_p, Z_{s1} and Z_{s2}. For instance, using the geometric parameters and EM properties discussed in section 5.2.1 the emulated impedance values were calculated as $Z_{s1} = Z_{s2} = -0.9311iZ_0$ and $Z_p = 2.51522iZ_0$.

To better emulate the desired impedance values this design is optimised using the optimisation toolbox in MATLAB®. Using the structure presented in Fig. 5.6, the following geometric parameters and EM properties are allowed to vary: L_1, L_2, L_3, L_4, w_{s1}, w_{s2}, w_p, ε_{s1}, ε_{s2} and ε_p, while the permittivity of the connecting $\lambda_0/4$ regions is fixed at $\varepsilon_r = 1$. Here, L_1, L_2, L_3 and L_4 are the lengths of the four $\lambda_0/4$ regions from left to right (the initial value of these parameters is $\lambda_0/4$, however they may change during the optimisation process). Additionally, if in the desired T-circuit $Z_{s1} = Z_{s2}$ then the following restrictions are also imposed: $w_{s1} = w_{s2}$, $\varepsilon_{s1} = \varepsilon_{s2}$, $L_1 = L_4$ and $L_2 = L_3$. The objective function which is minimized by this optimisation process is as follows:

$$O(Z_{s1}, Z'_{s1}, Z_{s2}, Z'_{s2}, Z_p, Z'_p) = |Z_{s1} - Z'_{s1}| + |Z_{s2} - Z'_{s2}| + |Z_p - Z'_p| \tag{5.9}$$

where Z_{s1}, Z_{s2} and Z_p are the calculated emulated impedance values and Z'_{s1}, Z'_{s2} and Z'_p are the desired impedance values, respectively. For the example presented in section 5.2.1 the optimized parameters and properties were: $\varepsilon_{s1} = \varepsilon_{s2} = 21.5$, $\varepsilon_p = 12$, $w_{s1} = w_{s2} = 0.2111$

mm, $w_p = 0.1741$ mm, $L_1 = L_4 = 7.3944$ mm and $L_2 = L_3 = 7.3074$ mm, respectively. The emulated impedance values of this optimised structure are then calculated to be $Z_{s1} = Z_{s2} = -0.9002iZ_0$ and $Z_p = 2.498iZ_0$, respectively.

5.3 Scaling of the Calculated PDE Solutions

5.3.1 Solution to a PDE at two different scales

As discussed in section 5.1.2, each junction between waveguides is representative of a single sampling point in the calculated PDE solution. Additionally, for a junction to calculate a valid PDE solution, it should be fully surrounded by adjacent junctions. This means, to increase the resolution of the calculated PDE solution it is necessary to expand the waveguide network so that more junctions are contained within the central region of the network. Here a *central junction* refers to a junction which is surrounded by four adjacent junctions and is thus used to calculate the PDE solution. The remaining junctions, which form the edge of the network and have at most 3 connected junctions, are called *boundary junctions*. As will be discussed in section 5.4, although these junctions are not used to calculate a PDE solution, they still play an important role as they can be used to enforce boundary conditions in the calculated PDE solution.

Now, let us consider an arbitrary network of size $N \times M$, where N and M are the number of horizontal and vertical junctions respectively. If Z_s and Z_p are the same for all junctions present within the network, then this network represents an area of simulation space with a size $h(N-1) \times h(M-1)$. The sampling density along a line in the PDE solution is then:

$$\rho_{sampling} = \frac{\lambda_1}{h} = \frac{2\pi|Z_p|}{\sqrt{-4Z_sZ_p^*}} \tag{5.10}$$

where λ_1 is the wavelength of the calculated PDE solution ($2\pi/k$) and $\rho_{sampling}$ is the number of sampling points per wavelength of the calculated PDE solution. When selecting h and k values (and though them Z_p and Z_s values) care should be taken to ensure that $\rho_{sampling}$ is large enough to capture the detail of the PDE solution. This typically means ensuring $\rho_{sampling}$ is between 6 and 10^{200}, however smaller or larger values may be selected depending on the desired level of accuracy. Eq. 5.10 also means that if one were to increase the network size by an arbitrary factor $\zeta \in \mathbb{Z}$ (i.e. change the network size to $\zeta N \times \zeta M$) a higher resolution solution to the same PDE as the $N \times M$ network may be calculated if $h \rightarrow h/\zeta$ while k remains unchanged. This is achieved by changing the impedance values as follows: $Z_p \to \zeta Z_p$ and $Z_s \to Z_s/\zeta$. Using Eq. 5.10 it can then be seen that in this scenario the sampling rate of the new structure has increased by a factor of ζ.

To demonstrate this, a numerical study of a pair of $N = M = 25$ PDE solving networks is presented in Fig. 5.7. This network includes 625 junctions, 96 of which are boundary junctions. The remaining junctions are central junctions, which are used to calculate a solution to the PDE in question. The first network is designed to emulate the series and parallel impedance values $Z_s = -0.9iZ_0$ and $Z_p = 2.5iZ_0$ ($h = 0.4$, $k = 3$) while the second network instead emulates $Z_s = -0.45iZ_0$ and $Z_p = 5iZ_0$ ($h = 0.2$, $k = 3$). The emulated impedance values after optimization where $Z_s = -0.9003iZ_0$, $Z_p = 2.498iZ_0$ and $Z_s = -0.4501iZ_0$, $Z_p = 5.001iZ_0$ for the first and second network, respectively. This means that the two networks are expected to calculate a solution to the same PDE (same k value). However, the solution of the second network should represent $1/4$ of the simulation area of the first network. Additionally, the sampling density of the second network (sampling points per wavelength along a line) is expected to be double that of the first network meaning the resolution of the calculated solution (sampling points per area) should be quadrupled.

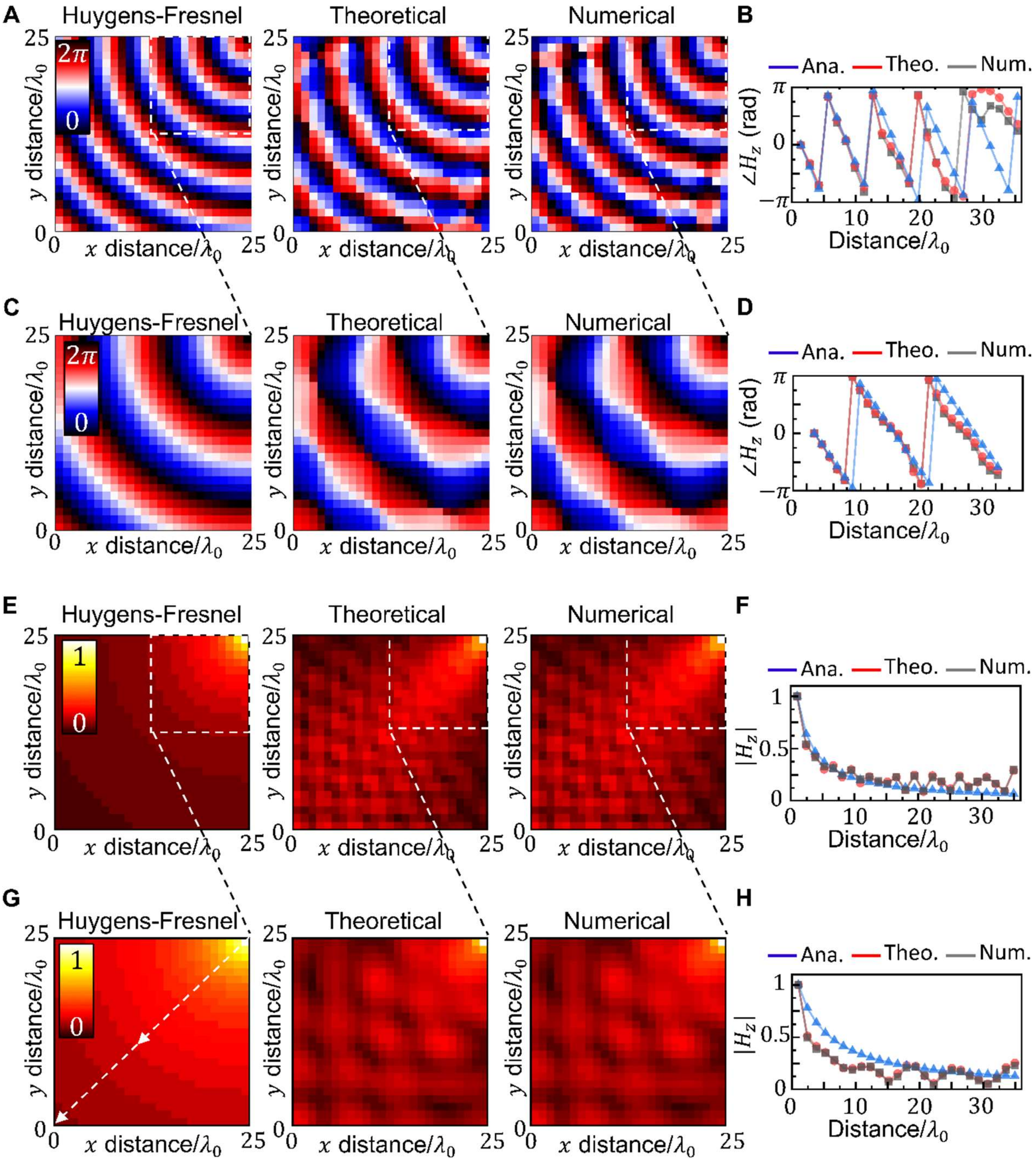

Figure 5.7 A., C. Analytical (left), theoretical (middle) and numerical (right) results for the phase of the out-of-plane H_z-field measured at the junction centres for a 25×25 junction network. This structure is excited from the right waveguide of the top-right junction. **E., G.** Same as **A** and **C** now for the magnitude of H_z. Results are normalized to the out-of-plane H_z-field calculated at the top-right junction. Here $Z_p = 2.498iZ_0$, $Z_s = -0.9003iZ_0$ and $Z_p = 5.001iZ_0$, $Z_s = -0.4501iZ_0$ for the results presented in **A, E** and **B, G**, respectively. These values correspond to the following PDE parameters: $h = 0.4004$, $k = 2.999$ ($\lambda_{sim} = 2.095$) and $h = 0.2$, $k = 3.001$ ($\lambda_{sim} = 2.094$), respectively. **B., D.,** Phase values extracted along a line from the top-right junction (distance = 0) to the bottom-left junction (distance = $25\sqrt{2}\lambda_0$) of the results presented in **A** and **C**, respectively. This path is shown as a white dashed line in the left panel of **G**. **F., H.** Same as **B** and **D** now for the results from **E** and **G**, respectively.

As in Fig. 5.5, this network is excited using a monochromatic 10 GHz signal, now from the right-waveguide of the top-right junction. The calculated values of the out-of-plane H_z-field (theoretical and numerical) are then normalized to the out-of-plane H_z-field value at the top-right junction. With these input conditions, it is expected that the solution to the PDE will resemble a radiating dipole oriented out-of-plane and located at the top-right junction. The calculated phase at the centre of the junctions is presented in Fig. 5.7A,C for the first and second network, respectively. These results are shown alongside an analytical solution to the PDE which is calculated using the Huygens-Fresnel principle[201,202], considering the top-left junction as a radiating dipole. As it can be seen there is a clear agreement between the theoretical, numerical, and analytical results for both waveguide networks. Additionally, one can see that the calculated solution from the second waveguide network resembles the top-left region of the solution from the first network, with three wavelengths visible in both regions. In both the numerical and theoretical results there is a distortion of the calculated PDE solution not seen in the analytical results. This distortion may also be seen in the magnitude of the H_z-field which is shown in Fig. 5.7E,G where it produces oscillations in the magnitude of the calculated solution. These oscillations can clearly be seen by looking at the calculated value of the H_z-field from the top-left junction (signal source) to the bottom-right junction (shown in Fig. 5.7F,G for the first and second network respectively). These oscillations are attributed to unwanted reflections at the boundary junctions which produce a standing wave in the calculated solution. The origin of these reflections and a method used to minimize their impact on the calculated solution is presented in section 5.5.

As a further example, another numerical study of the second waveguide network is conducted. This time the input signal is excited from the left waveguide of the middle-left boundary junction. The calculated H_z-field at each of the 625 junction is then normalized to the signal at the centre of this junction. This study demonstrates the potential of this method of PDE solving when using different input sources. The calculated H_z-field in this scenario is presented in Fig. 5.8. As it can be seen, this example also resembles an oscillating dipole, now located at the middle-left junction, as expected.

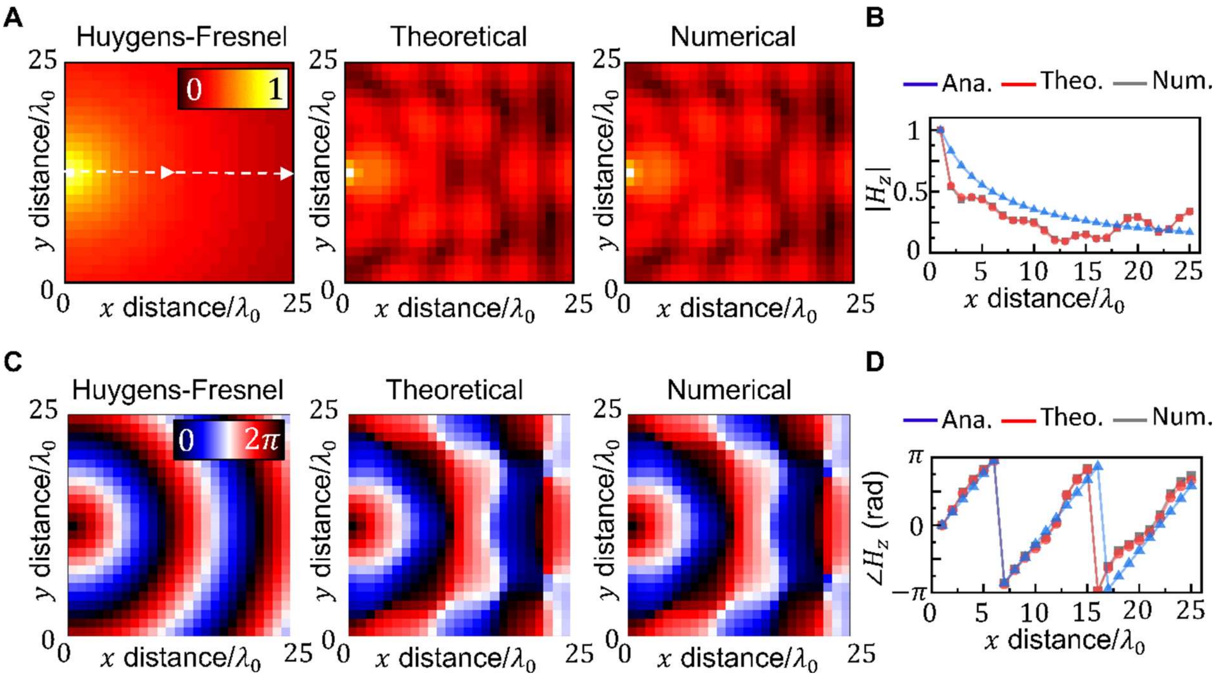

Figure 5.8 Analytical (left), theoretical (middle) and numerical (right) results for the phase of the out-of-plane H_z-field measured at the junction centres for a 25×25 junction network. **A.**, **C.**, Magnitude, and phase respectively. The PDE parameters are the same as in Fig. 5.7C,G, now with the excitation signal from the left-waveguide of the middle junction on the left boundary of the structure. The results are normalized to the out-of-plane H_z-field calculated at this junction. **B.**, **D.**, Results extracted along a line from the left-middle junction (distance = 0) to the right-middle junction (distance $= 25\lambda_0$) of the results presented in **A**, **C**, respectively. This path is shown as a white dashed line in the left panel of **A**.

5.3.2 Emulating a variable sampling rate in the PDE solution

The examples presented in Fig. 5.7-5.8 considered waveguide networks with a uniform sampling rate. This means that Z_p is chosen to be the same for every connecting T-circuit. However, when conducting finite difference simulations, it is common to vary the sampling density in different regions of the simulation domain[203]. This allows for accurate results to be computed with more efficiency by sampling complex regions of the domain, such as regions with a higher k value, with a higher density than less complex regions. This principle may also be exploited using the PDE solving network structure by instead allowing for Z_p to vary throughout the structure. An example of this is presented in Fig. 5.9, where a structure is designed to solve $\nabla^2 g(x,y) + 3^2 g(x,y) = 0$ with a vertical step size of $h_y = 0.2$ and a horizontal step size of $h_x = 0.4$. This means designing different T-circuits for the vertical and horizontal connections respectively. The finite difference representation of the PDE when using the two different sampling rates is as follows:

$$\begin{aligned}&\nabla^2 g(x,y) + k^2 g(x,y)\\ &= \frac{1}{h_x^2}\left[g(x+h_x,y) + g(x-h_x,y) - 4g(x,y)\right]\\ &+ \frac{1}{h_y^2}\left[g\left(x,y+h_y\right) + g\left(x,y-h_y\right) - 4g(x,y)\right] + k^2 g(x,y)\end{aligned} \tag{5.11}$$

Likewise, the governing equation of the PDE solving network (equivalent of Eq. 5.6) when considering separated horizontal and vertical T-circuit is:

$$Z_{px}(I_1 + I_3 - 2I_0) + Z_{py}(I_2 + I_4 - 2I_0) - 2(Z_{sx} + Z_{sy})I_0 = 0 \tag{5.12}$$

where Z_{px}, Z_{py}, Z_{sx} and Z_{sy} are the horizontal parallel, vertical parallel, horizontal series and vertical series impedance values respectively. As in Eq. 5.6 a transformation of the current values is used to ensure h_x and h_y are real numbers. In this case the transformation $I'_a = Z_p^* I_a$ is used and Eq. 5.12 is then rewritten as:

$$Z_{px}Z_{py}^*(I'_1 + I'_3 - 2I'_0) + |Z_{py}|^2(I'_2 + I'_4 - 2I'_0) - 2(Z_{sx} + Z_{sy})Z_{py}^* I'_0 = 0 \tag{5.13}$$

By comparing Eq. 5.13 and Eq. 5.11 it can be seen that the two equations are analogous if the impedances are chosen to satisfy $\left|Z_{py}\right| = 1/h_y$, $Z_{px}Z_{py}^* = 1/h_x^2$ and $-2\left(Z_{sx} + Z_{sy}\right)Z_{py}^* = k^2$. The k^2 term can be realized by selecting $Z_{sx} = Z_{sy} = -k^2/(4Z_{py}^*)$. The horizontal parallel term can then be calculated by considering $h_x = \varsigma h_y$, where ς is a real number greater than 0. From this the condition for h_x becomes $Z_{px}Z_{py}^* = 1/(\varsigma h_y)^2$, which may be combined with the condition for h_y to reveal: $Z_{px} = Z_{py}/\varsigma^2$. With this, the following impedance values are chosen to implement the scenario described above: $Z_{sx} = Z_{sy} = -0.45iZ_0$, $Z_{py} = 5iZ_0$ and $Z_{px} = 1.25iZ_0$.

Analytical and theoretical values for the out-of-plane H_z-field at the junction centres are presented in Fig. 5.9. As in Fig. 5.7 this structure is excited from the right waveguide of the top-right junction and results are normalized to the H_z-field at this junction. Fig. 10B,D shows the calculated H_z values along a horizontal (left) line from the top-left junction to the top right and a vertical line (right) from the top-left to the bottom left. As it can be seen the rate of phase change (Fig. 5.9E) and decrease in magnitude (Fig. 5.9C) in the horizontal direction is approximately twice that of the vertical, as is expected.

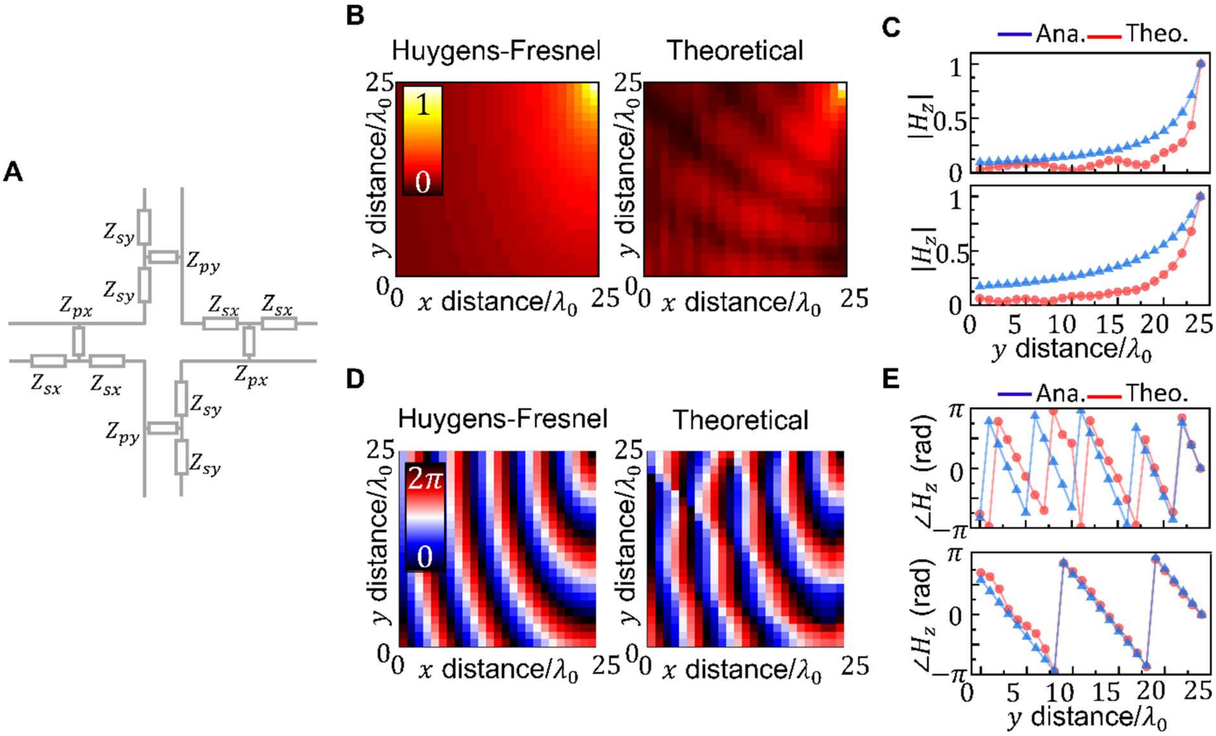

Figure 5.9 Theoretical study of a variable sampling density using a 25 × 25 PDE solving structure. **A.** Schematic representation of a single waveguide junction with anisotropic impedances. **B.**, **D.** Magnitude and phase of the out-of-plane H_z-field calculated at the centre of the waveguide junctions, respectively. Here $Z_{sx} = Z_{sy} = -0.45iZ_0$, $Z_{px} = 2.5iZ_0$ and $Z_{py} = 5iZ_0$. This corresponds to a PDE with parameters $k = 3$, $h_x = 0.4$ and $h_y = 0.2$. The structure is excited from the right-waveguide of the top-right junction and the results are normalized to this junction. **C.**, **E.** Results extracted from **B** and **D**, respectively. The top panel is shows the results along a horizontal line from the top-left junction to the top-right junction. The right panel shows the results along a vertical line from the bottom-right junction to the top-right junction.

5.4 Dirichlet Boundary Value Problems

5.4.1 Implementation of boundary conditions at boundary junctions

Thus far, all the examples presented in sections 5.2 and 5.3 have consisted of a single input signal excited at one of the boundary junctions. In this scenario the solutions are all expected to resemble radiating dipoles. As will be discussed in this section, by exciting input signals from each of the input waveguides simultaneously it is also possible to produce solutions to Dirichlet boundary value problems. This is done by tailoring the amplitude and phase ratios between the various input signals to enforce conditions such as $g(x = 0, y) = 0$ or $g(x = 0, y) = 1$ at the boundary junctions. To do this, the left-waveguide of the top-left junction is used as a reference point. The combination of incident signals required to implement these boundary conditions at the boundary junctions can be calculated directly form the scattering matrix of the PDE solving structure $\boldsymbol{A}_{PDE}$. This scattering matrix is calculated using the algorithm outlined in Chapter. 2. To do this consider the vector of incident signals (defined by their E-field) excited from the boundary waveguides connected to the boundary junctions of the waveguide network $\boldsymbol{x}_{boundary} = [x_1, x_2 \dots, x_{2(M+N)}]^T$. Here the input waveguides are labelled from 1 to $2(M+N)$ with 1 as the left input at the top-left junction. The labels then proceed around the network anti-clockwise meaning that the final label $2(M+N)$ is the top-waveguide of the top-left junction. The vector of output signals at these boundary waveguides is then[23–25,84] $\boldsymbol{y} = \boldsymbol{Ax}$. With $\boldsymbol{y} = [y_1, y_2 \dots, y_{2(N+M)}]^T$. Using these vectors, the complex values of the instantaneous H_z-field (or rotating current value) at these boundary junctions is then calculated as:

$$\boldsymbol{H}_{boundary} = (\boldsymbol{x} - \boldsymbol{y})/Z_b \tag{5.14}$$

where Z_b is the characteristic impedance of the boundary waveguide. Eq. 5.14 is also used to calculate the H_z-field at the centre of the boundary junction by removing the added phase due to the length of the boundary waveguide. It should be noted that when doing so the H_z value calculated from the two waveguides connected at the corner junctions should be the same. Using Eq. 5.14 with the scattering matrix of the structure $\boldsymbol{A}_{PDE}$ the vector of required incident signals is calculated as follows:

$$\boldsymbol{x} = Z_b(\boldsymbol{I} - \boldsymbol{A})^{-\boldsymbol{1}}\boldsymbol{H}_b \tag{5.15}$$

where $\boldsymbol{I}$ is the identity matrix of size $2(N+M) \times 2(N+M)$. Using Eq. 5.15 it is possible to define an arbitrary set of boundary values at the boundary junctions and then calculate the input vectors which will implement those values.

5.4.2 Example solution: $g = 1$ boundary value problems

One example of a Dirichlet boundary value problem which may be solved using this PDE solving structure is presented in Fig. 5.10. Here the same 25×25 junction structure as used in Fig. 5.7C,D,G,H and Fig. 5.8 is exploited to produce a solution to the Dirichlet boundary value problem with $g = 1$ at each of the boundary junctions. To do this the required vector of incident signals is calculated using Eq. 5.15 when $\boldsymbol{H}_b = [1,1, \dots 1,1]^T$ is the all 1 vector of length $2(N+M)$. The results for the calculated out-of-plane H_z-field values are presented in Fig. 5.10B. Here, “analytical” results to this boundary value problem have been calculated using the PDE Toolbox in MATLAB®[204]. This toolbox uses the finite element method (FEM) to calculate a numerical solution to the PDE. This is referred to as analytical as it is an accurate solution produced by conventional PDE solving techniques. In this scenario the solution resembles the probability distribution of an electron trapped within a two-dimensional square potential well. These results have been normalized to the H_z-field at the centre of the middle waveguide junction (13 junctions down and 13 junctions along). As it can be seen there is a clear agreement between the calculated PDE solution using the PDE solving network and the "analytical" solution produced via the FEM.

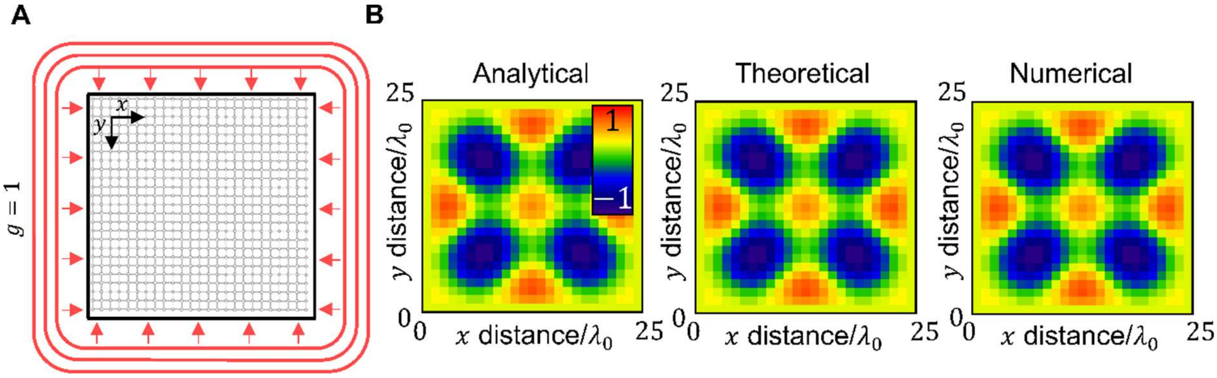

Figure 5.10 Boundary value problem solving example: $g = 1$. **A.** Schematic representation of the PDE boundary value problem to be solved. Here the input signals at each of the boundary waveguide are chosen such that the boundary junctions of the network enforce a $\partial\Omega = 1$ boundary value around the entire network. **B.** Analytical (left), theoretical (middle) and numerical (right) results for the out-of-plane H_z-field at the centre of the waveguide junctions. Here $Z_s = -0.4501iZ_0$, $Z_p = 5.001iZ_0$, meaning that $h = 0.2$ and $k = 3.001$, respectively. These results are normalized with respect to the maximum out-of-plane magnetic field within the network.

5.4.3 Example solution: variable boundary value problem

Another example of a Dirichlet boundary value problem is presented in Fig. 5.11. This highlights the scenario where the boundary values at the boundary junction can vary from junction to junction. In this example the same 25×25 network as in Fig. 5.10 is exploited. The inputs from the boundary waveguides are then designed such that the boundary values around the network have a magnitude of 1 and a phase which completes one full cycle around the network. This phase cycle starts at the top-left junction and then proceeds clockwise (when viewed from above) so that the phases at the top-right, bottom-right and bottom-left junctions are $\pi/2$ rad, π rad and $3\pi/2$ rad, respectively. A schematic representation of this is presented in Fig. 5.11A. The calculated magnitude and phase of the H_z-field at the junction centres is presented in Fig. 5.11B,C, respectively. As can be seen both theoretical and numerical results are in agreement with the analytical results (calculated using the FEM in the PDE toolbox from

MATLAB®). Additionally key features, such at the ring structure in both magnitude and phase successfully recovered.

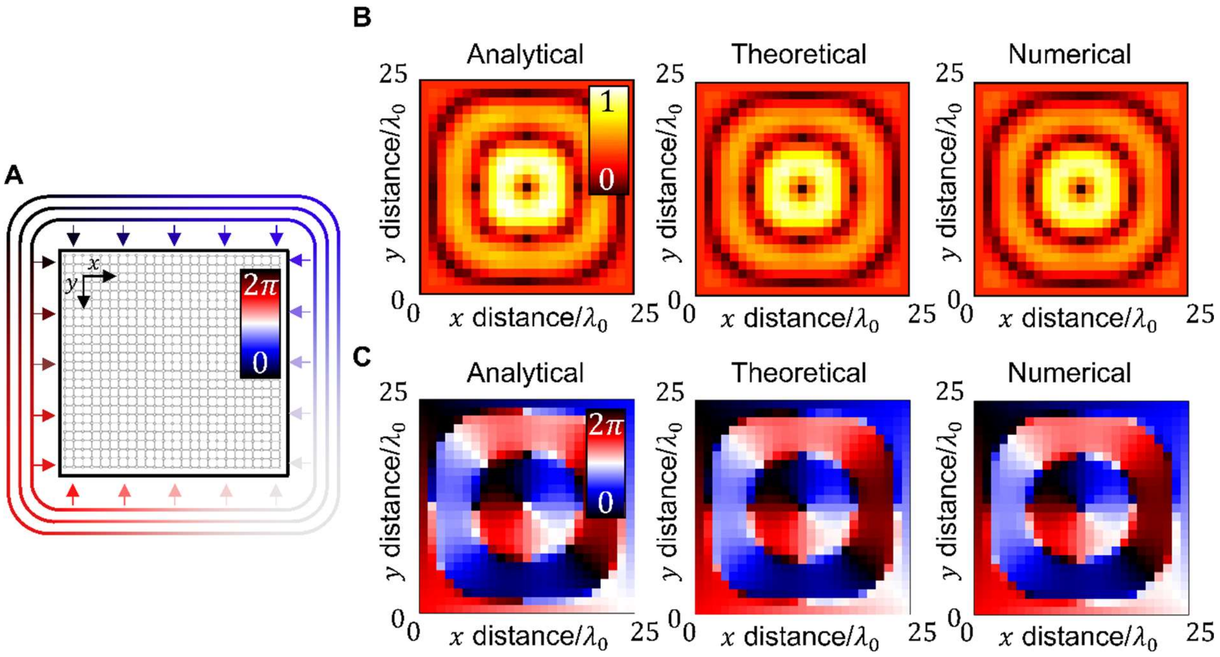

Figure 5.11 Boundary value problem solving example: Varying phase. **A.** Schematic representation of the PDE boundary value problem to be solved. Here the input signals at each of the boundary waveguides are chosen such that the boundary values at the boundary waveguides have a magnitude of 1 and a phase which varies from 0 to 2π clockwise around the boundary (starting at the top-left junction). **B.**, **C.** Analytical (left), theoretical (middle) and numerical (right) values for the out-of-phase H_z-field calculated at the centre of the junctions. **B.**, **C.** Magnitude and phase, respectively. These results are normalized to the maximum magnitude value which was located at $x = 15\lambda_0$, $y = 11\lambda_0$.

5.5 Open Boundary Value Problems

5.5.1 Impedance mismatches produced at open boundary junctions

As a final study, the implementation of open boundary value problems using this PDE solving structure is also investigated. To implement open boundaries, it is required that any signal incident upon the boundary be fully absorbed. In a conventional software based PDE solver, this may be done using perfectly matched layers (PMLs)[205]. However, in attempting to mimic this behaviour using waveguide ports at the end of the boundary waveguides unwanted reflections were obtained in the PDE solution. These reflections are visible in the results presented in Fig. 5.7-5.9. These reflections are not present when calculating the solution to Dirichlet boundary value problems. This is as when defining a boundary value for the boundary junction, the calculated input signal at the boundary waveguide will destructively interfere with the reflections. A schematic representation of the origin of these reflections is presented in Fig.

5.12. As can be seen between the centre and boundary junctions of the network there are four and three connected junctions respectively. This means that when a signal which is propagating through the centre of the network encounters a boundary junction, there is an impedance mismatch between the two regions. If a waveguide port is placed at the boundary waveguides, only a portion of the signal is absorbed as the reflection is produced at the boundary junction.

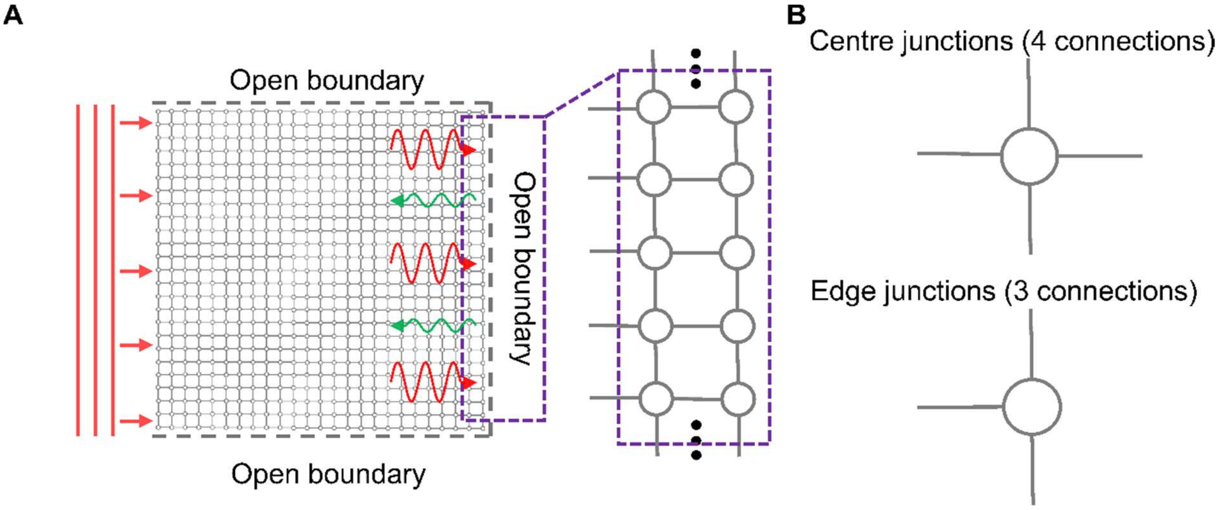

Figure 5.12 A. Schematic representation of the origin of reflections open boundary value simulations using a 50×50 PDE solving structure. **B.** Schematic representation of the differences between a centre junction (top) and a boundary junction (bottom) which leads to the anomalous reflection at the network boundary.

One method to minimize the impact of these reflections is to further extend the network by including more waveguide junctions and in doing so increasing the areas of simulation space. This allows for the signals within the network to propagate and decay within the extended region of the network similar to the behaviour of a PML. The desired solution to the open boundary value problem can then be extracted from a subnetwork of the overall network. A schematic representation of this is presented in Fig. 5.13A. Here a 50×50 subnetwork is used as the simulation space of the PDE solving structure. The network is then extended by a further 50 junctions from the top, right and bottom boundaries of this region, in doing so creating a 150×100 network. It should be noted that as the network cannot be extended infinitely there are still some reflections produced at the boundary junctions of the overall network. However due to the larger area of simulation space, the impact of these reflection is reduced. These reflections could be reduced further via the addition of loss in the extended region of the waveguide network, however for the examples presented in section 5.5.2-5.5.3 the extended region of the network is lossless.

To calculate the theoretical values of the PDE solution produced by this network the algorithm outlined in chapter 2 is used. However, to solve for the performance of the entire 150×100 network directly would be a computationally intensive task. To avoid this the periodicity of the network is exploited. A schematic representation of this method is presented in Fig. 5.13B. Here, the waveguide network is separated into 6 identical 50×50 subnetworks. Then using the waveguide network solving algorithm, the scattering matrix of a single 50×50 region is calculated $\boldsymbol{A}_{50\times50}$. This scattering matrix is then copied over to the remaining 5 regions in doing so forming a network of 6 interconnected nodes which may be solved as a new network. Here each pair of connected nodes share 50 connections between them. Additionally, care is taken to ensure that the metatronic T-circuit within each of these connections is also correctly modelled.

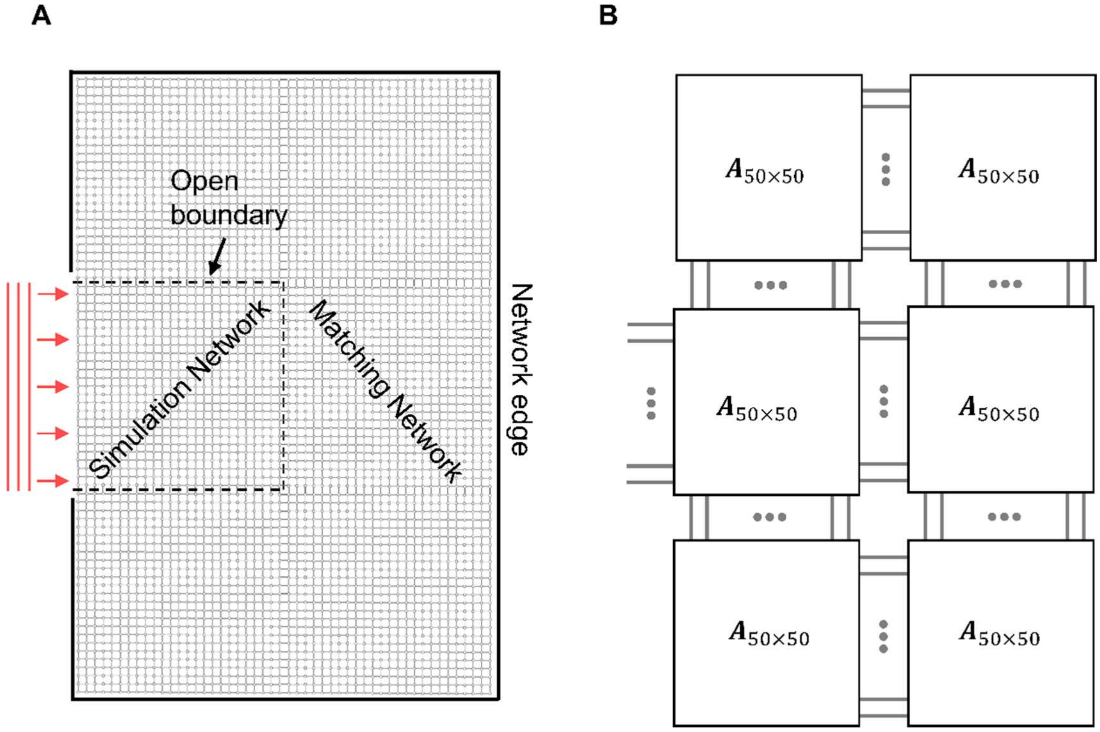

Figure 5.13 Proposed solution to minimize the anomalous reflection for open boundary value problems. **A.** A 50×50 subnetwork extended at the top, right and bottom boundaries to form a 150×100 network. **B.** Schematic representation of the method used to evaluate the theoretical performance of this network.

5.5.2 Open boundary example: Focusing/Lensing

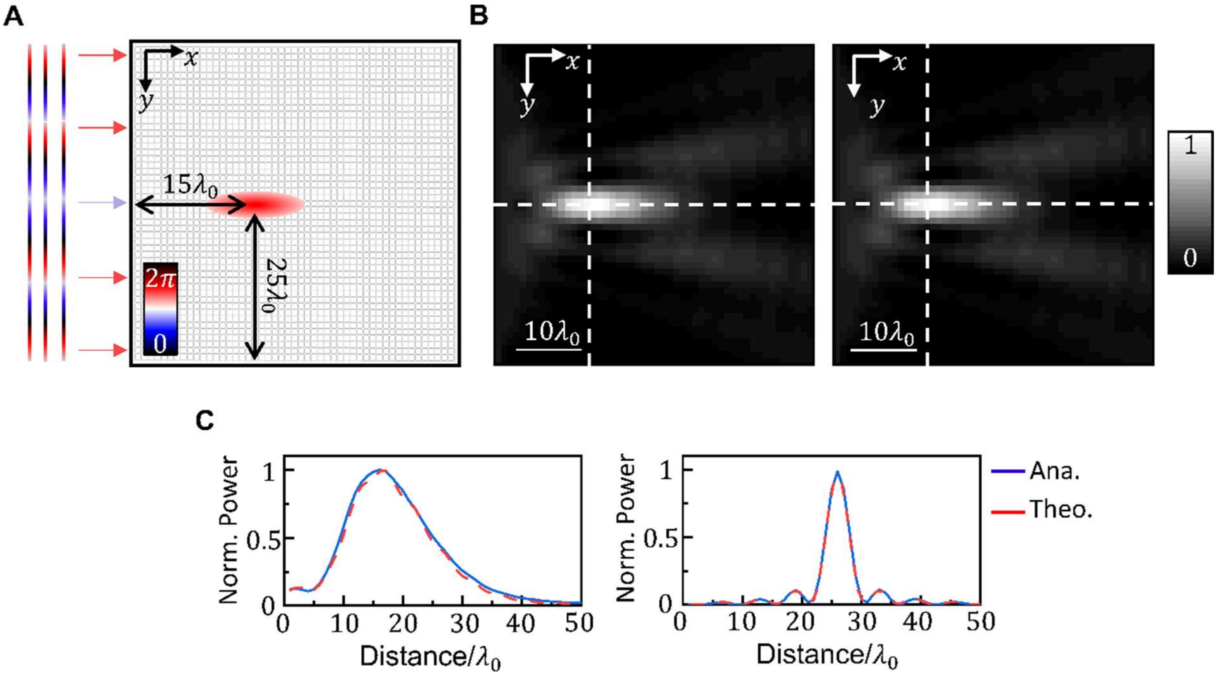

Figure 5.14 Open boundary value problem example: Focusing/lensing**.** **A.** Schematic representation of the input conditions of the focusing/lensing using a 50 × 50 subnetwork of the 100 × 150 network presented in Fig. 5.13. Here $Z_p = 5.001iZ_0$, $Z_s = -0.4501iZ_0$ meaning $h = 0.2$ and $k = 3.001$. The inputs at the lefthand-boundary of the 50 × 50 subnetwork are designed to produce a focus 15 junctions along and 25 junctions down in the PDE solving network. **B.** Analytical (left) and theoretical (right) results for power distribution calculated from the out-of-plane H_z-field at the junction centres. Here results have been normalized to the maximum power of the focus. **C.** Results extracted along and down the horizontal (left) and vertical (right) white lines shown in **B**.

To demonstrate the potential of this method for solving open boundary value problems an example of a focusing/lensing problem is presented in Fig. 5.14. Here the 150 × 100 network presented in Fig. 5.13A is evaluated when $Z_p = 5.001iZ_0$ and $Z_s = -0.4501iZ_0$ ($h = 0.2, k = 3$). The solution to the PDE is then extracted from the 50 × 50 subnetwork labelled as "simulation network" in Fig. 5.13A. Input signals are then excited in the left-waveguides connected to the boundary junctions at the left-hand side of this 50 × 50 region. These input signals are calculated using Eq. 5.15 such that the boundary values implemented at these junctions resemble the output signal of a converging lens designed to produce a focus at $x = 1.432\lambda_1$, $y = 2.387\lambda_1$ with $\lambda_1 = 2.094$. Inside the waveguide network, this corresponds to a focus 15 junctions along the x direction and 25 junctions up the y direction.

Theoretical values for the PDE solution calculated using the waveguide network are presented in Fig. 5.14B alongside an analytical solution calculated using the Huygens-Fresnel principle. These results show the power distribution of the system calculated from the out-of-plane H_z-field at the junction centres. These results are then normalized to the maximum power of the calculated focus. In the theoretical results focus is calculated to be produced at $x = 1.432\lambda_1$ and $y = 2.387\lambda_1$ demonstrating a good agreement with the analytical calculations. The horizontal and vertical profiles of the calculated focus is presented in Fig. 5.14C demonstrating a clear agreement with the analytical calculations. In the theoretical calculations there are still some slight ripples visible within the calculated PDE solution. These are produced at the edge of the overall 150×100 network.

5.5.3 Open boundary example: Scattering from an obstacle

A second example of an open boundary value problem is presented in Fig. 5.15. This example show scattering produced by a square insert within the simulation space. Using the PDE solving structure, an insert may be modelled by locally changing the impedances of the metatronic T-circuit. This produces a region of simulation space with a different value of k thus emulating an insert. In the example presented in Fig. 5.15 this insert is designed to reflect all incident signals (similar to the performance of a PEC). In this example, this is done by removing the waveguide junctions within a 10×10 region at the centre of the network and replacing the connecting waveguides with PEC ended stubs with a length of $\lambda_0/4$. This has the effect of enforcing a $g = 0$ at the boundary junctions between the simulation region and the insert region of the simulation network. This structure is then excited from the left boundary of the structure by designing the input signals from the boundary waveguides to implement a $g = 1$ boundary. This emulates a propagating wave from the lefthand boundary. To evaluate the quality of this PDE solution an “analytical” solution is calculated using the PDE toolbox in MATLAB®.

The analytical and theoretical results for the power distribution of this structure are presented in Fig. 5.15. As it can be seen the reflection and scattering of signals due to the presence of the insert within the simulation domain closely resembles the analytical solution. This can be further confirmed by comparing the two sets of results along the vertical and horizontal lines. Here it can be seen that the periodicity and the magnitude of the standing wave produced between the insert and the lefthand boundary is in good agreement. Additionally, the two lobes of the scattered signal have the correct profile. Between these results and those presented in Fig. 5.14 there is a larger disagreement between the theoretical and analytical results. This can be attributed to two factors. 1) The impact of the reflections. In both examples there is a small amount of reflection produced at the edge of the 150×100 network, however these are expected to have a more significant impact on the results presented in Fig. 5.16 as the magnitude of the focus in Fig. 5.14 is significantly larger than the magnitude of the reflections. 2) The coarseness of the PDE solving grid. As each junction of the PDE solving network represents a single sampling point within the simulation space, the size of the insert is effectively rounded up to an integer multiple h. This means that the insert simulated by the PDE solving network is slightly larger than the designed insert used in the analytical calculation. The impact of this could be reduced by considering a mesh with a higher sampling density using the methods outlined in section 5.3.

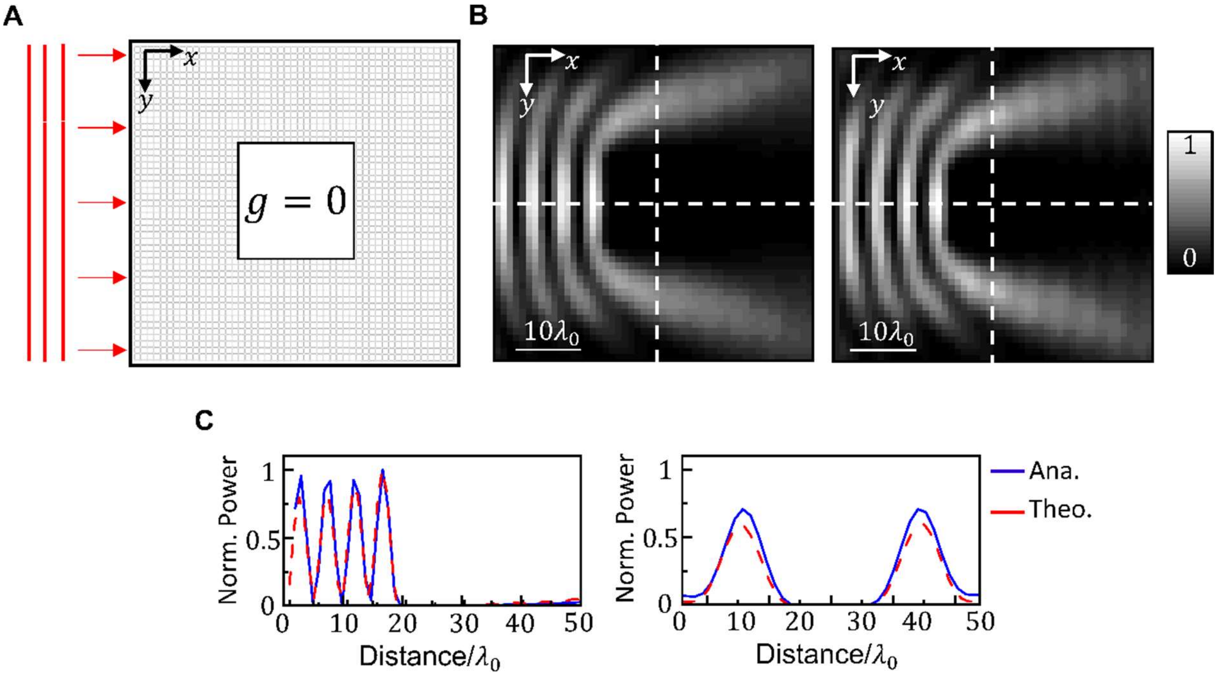

Figure 5.15 Open boundary value problem example: Scattering from a square insert. **A**. Schematic representation of simulation setup using the 50×50 subnetwork of the 100×150 structure. Here the PDE parameters are the same as in Fig. 5.14. The input signals from the left-waveguides of the left-junctions of the 50×50 subnetwork are chosen to implement a $\partial\Omega = 1$ boundary. Additionally, a $0.9549\lambda_1 \times 0.9549\lambda_1$ (10×10 junctions) $g = 0$ insert has been included at the centre of the waveguide network. This is realized by removing the waveguide junctions within that area of the network. **B.** Analytical (left) and theoretical (results) for the power distribution calculated from the out-of-plane H_z-field at the centre of the waveguide junctions. **C.** Results extracted along and down the horizontal (left) and vertical (right) white lines shown in **B**.

5.6 Chapter 5 conclusions

In summary, a method of EM-wave-based analogue PDE solving using interconnected networks waveguide-based metatronic circuits has been presented. This is done by constructing the network such that the governing equation resembles the 2D Helmholtz wave equation. The parameters of the equation to be solved are controlled by tailoring the emulated impedance values of the waveguide-based metatronic circuit elements which are emulating the performance of an electrical T-circuit. The solution to the PDE is extracted at the centre of the waveguide junctions and is thus a discretized approximate PDE solution, similar to the results from an FDTD simulation using a hexahedral mesh. It is also shown how the boundary conditions of the PDE to be solved are implemented via external signals at the boundary junctions, demonstrating how a single PDE solver may be used to solve multiple boundary value problems. Finally, this method is also extended to solve open boundary value problems, such as focusing and scattering of light. Analytical, theoretical, and numerical results are presented for a range of scenarios and are in good agreement.

In future work, the technique demonstrated here using numerical simulation could be implemented using current microwave technologies[30] in order to demonstrate the technique experimentally. Additionally, this technique may also be translated to other spectral regimes where metatronic circuits have been demonstrated[88,96] (such as Thz or optics) and can thus potentially be miniaturized to achieve higher processing speeds.

Chapter 6. Conclusions and Future Directions

In this thesis, interconnected networks of parallel plate waveguides have been exploited for EM wave-based computing applications. To this end, four main studies have been presented between chapters 3 and 5. These studies have led to the publication of two manuscripts, with a third currently under review and a fourth in preparation, at the time of submission.

Following an introduction to EM theory and the TL techniques used throughout the thesis, chapter 2 presented an overview of a theoretical tool produced to assist in the characterization of interconnected waveguide networks. This tool, based on signal flow diagram decomposition rules[30,169], was designed to algorithmically reduce a network of interconnected scattering matrices into a single effective scattering matrix that describes the behavior of the overall system. The mathematics which forms the basis of this algorithm have been presented in this chapter and the accuracy of the tool has been evaluated by comparing it to full-wave numerical simulation results. These simulations are in excellent agreement with the theoretical results produced using the tool. Throughout this thesis, this tool has been exploited when considering interconnected networks to produce theoretical results. This includes modeling the behavior of the N-input and many-to-many linear logic gates presented in chapter 3, as well as large periodic networks presented in chapter 5. Potential future developments for this tool include the implementation of a user interface and further expanding the functionality. For instance, resolving the band diagrams of periodic networks or the behavior of active structure via an iterative process.

In chapter 3, the focus was to emulate the functionality of some select digital electronic computing systems by exploiting the linear superposition of EM waves within waveguide networks[23–25,84]. This chapter presented the results of two studies. In the first study a method exploiting the splitting and superposition of TEM pulses at PPW junctions to emulate decision making processes in the form of *if…then…else…* statements were presented. This was done through the use of two example operations. The first, called a *comparator*, was designed to compare the magnitude of two input numbers φ_1 and φ_2 and then return one of three output states when $\varphi_1 < \varphi_2$, $\varphi_1 > \varphi_2$ and $\varphi_1 = \varphi_2$, respectively. The second, called a *director*, exploited reciprocity to perform a decision-making process analogous to an N-input AND operation. This operation differs from a digital AND operation in that both input and output signals are continuous and thus may take a wide range of values. This work has been published in *Advanced Intelligent Systems*[25]. Further applications of this method could also be explored to enable the emulation of additional *if…then…else* statements by increasing the complexity of the waveguide networks or via the addition of active elements to introduce non-linearity. Additionally, this technique could be potentially merged with existing electronic systems to produce TEM pulse-based processors.

The second study presented in chapter 3, explores how the linear superposition of monochromatic waves within networks of waveguides may be exploited to emulate the performance of linear logic operations[127,128,132]. In this realm, binary information is encoded into features of the monochromatic input signals, such as phase and amplitude[128]. Logic operations are then performed by tailoring the path lengths between input and output ports to enforce constructive or destructive interference between signals. Examples of elementary logic gates have been presented, demonstrating how one may optimize the structure and encoding scheme to maximize the contrast ratio of the operation. Additionally, a method of extending this method to produce logic gates with more inputs has been presented. This is different to cascading operations, as is common for electronic systems, as now the structure and encoding of the system as a whole should be optimized to best implement the N-input operation. Finally, this section also discusses the implementation of many-to-many linear logic gates with the examples of a linear half-adder and 2-bit adder presented. At the time of submission a manuscript based on these results is currently being prepared. Future work in this area would begin with the publication of this manuscript. In future work, these principles could be applied to other waveguide-based structures in order to minimize the footprint of the proposed devices. This could include exploiting structures such as plasmonic waveguides[128,132,137], dielectric waveguides[106,108,118], or topological waveguides[136].

In chapter 4, TL filtering techniques were exploited to perform analogue differentiation via the Green's function[21] technique. Here, it was shown how by exploiting a series of waveguide junctions with connected stubs[30,181], it is possible to tailor the profile of a minimum in the transmission or reflection coefficient to resemble the Green's function of a differentiation operation[162]. This technique is also extended to produce m^{th} order differentiators including fractional differentiators[182] where m may be a positive non-integer value. During this chapter, two sources of non-ideal splitting behavior which may impact the performance of a differentiator were identified and investigated. These sources are 1) non-ideality due to a non-zero junction cross section and 2) due to junction asymmetry. The theoretical differentiator designs may then be adjusted to minimize the impact of these effects. These results have been published in *Scientific Reports*. Future work regarding this project would include expanding the range of potential operations to include examples such as integration and convolution, investigating the potential use of phase shifters inside the stub waveguides in order to create a reconfigurable device and exploiting multiple minima simultaneously in order to enable multiple parallel operations with a single device.

Finally, in chapter 5 periodic networks of parallel plate waveguide junctions were exploited to calculate solutions to PDE boundary value problems. This was done by constructing an analogy between the governing equations of the waveguide network and the finite difference representation of the Helmholtz equation in two dimensions[145,146,206]. Here, the waveguide network was shown to act as an area of simulation space. To implement the desired PDE metatronic circuits have been exploited. In this chapter it was shown how my tailoring the effective impedance of the metatronic circuit elements it is possible to control both the scaling and sampling density of the calculated PDE solution. It was also shown how the input signals applied at the edges of this network may be controlled to enforce boundary conditions in the calculated PDE solution. Two examples of this were presented with calculated analytical, theoretical, and numerical solutions in agreement for both cases. Finally, two examples of open boundary value problems were also presented demonstrating the versatility of this method of PDE solving. A manuscript based on this work has been prepared and is, at the time of writing, currently under review[27]. This work has also been presented to the community at Metamaterials 2023 and has also been accepted for a presentation at AT-RASC 2024. In the future, this method could also be expanded via the addition of non-local connections (waveguides which connect junctions which are not adjacent) to enable higher order PDE solutions. Another potential avenue to explore would be exploiting non-reciprocal structures such as topological waveguides or circulators.

Appendix A. Numerical Methods

Nowadays, a multitude of commercial simulation tools are available for evaluation of EM wave-base structures as well as other applications. These tools produce approximate numerical solutions to maxwells equations, evaluated in either differential (Eq. 1.2) or integral forms. In this appendix section, a brief overview of the numerical tools which have been exploited throughout this project will be provided. These tools are as follows: CST Studio Suite®, COMSOL Multiphysics® and the PDE toolbox in MATLAB®.

A.1 CST Studio Suite®

CST Studio Suite® is the numerical simulation tool which has been exploited to produce the majority of numerical results presented throughout this thesis. For the sake of consistency between models and results, this tool has been used wherever possible, with other simulation tools only being used when necessary. This is possible, due to the variety of numerical solvers available in CST Studio Suite®. In this thesis, two of these solvers have been exploited. The first is the Transient Solver and the second is the Frequency Domain Solver. Both of these solvers use the Finite Integration Technique (FIT)[207] to produce approximate solutions to Maxwells's equations in integral form.

A.1.1 CST Studio Suite® Transient solver

In chapter 3, TEM pulse simulations where presented. These results were calculated using the transient (time domain) solver in CST Studio Suite®. This solver uses the FIT and the leap-frog integration method[208] to calculate the propagation of signals though EM structures. The waveguide junctions presented in this chapter were constructed using PPWs with a 3×3 mm cross-section in the transverse plane. The metallic plates of the PPWs were made from PEC and had zero-thickness. Vacuum ($\varepsilon_r = \mu_r = 1$) was used as both the filling material between the two PEC plates and as the background medium of the simulation space. Both boundary conditions in the z-direction (out of the junction plane) were set to "open-(add space)". The remaining boundary conditions were all set to "open". Additionally, when using the parallel and series structures, electric and magnetic symmetry was applied in the xy-plane, respectively. This structure can be seen in Fig. A.1 which shows the tetrahedral mesh at the centre of the waveguide junction for both the parallel and series scenarios.

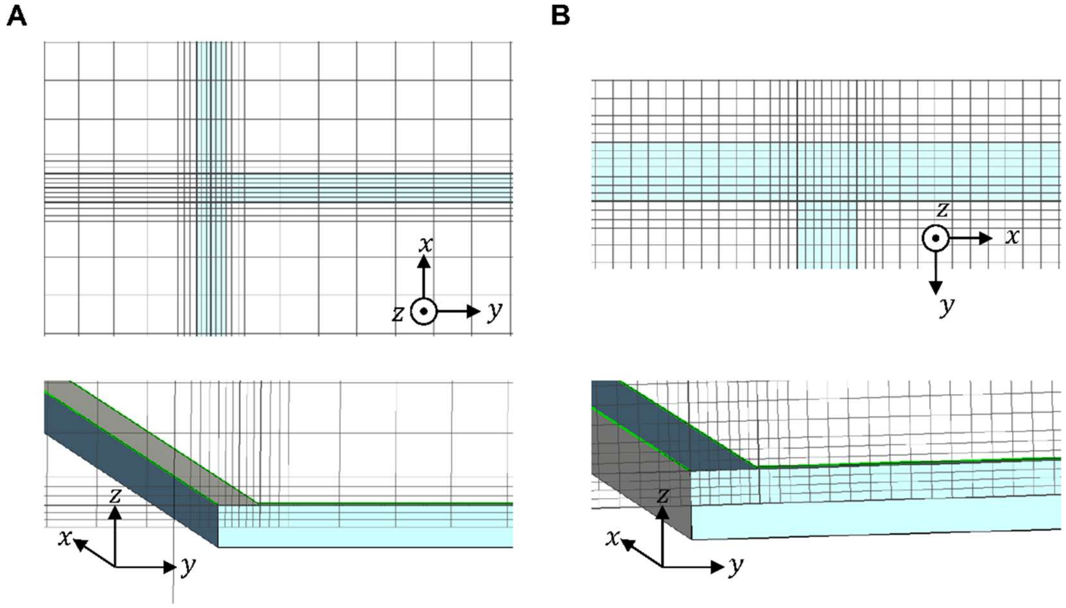

Figure. A.1 A., B. Hexahedral mesh view of parallel and series three-waveguide junction

To excite this structure waveguide ports were connected at the ends of the input waveguides. These waveguides had a length of 250 mm between the port and the waveguide junction. The TEM pulses presented throughout this chapter were constructed with the following input profile:

$$P(t) = A[\frac{1}{1+e^{-st}} - \frac{1}{1+e^{-s(t-\Delta t)}}] \tag{A.1}$$

where A is the amplitude of the pulse, s is a constant which controls the slope of the pulses, t is time and and Δt is the duration of the pulse. In this chapter $\Delta t = 0.4$ ns and $s = 400$ GHz.

A similar setup was used to produce the time domain results presented in chapter 4, now using waveguides with a 1×1 mm cross-section unless stated otherwise. Additionally, the length of the input/output waveguides was changed to 25 mm ($2\lambda_0/3$), with the exception of the Fig. 4.8 in which this length was instead 500 mm ($13.3\lambda_0$). The gaussian input signals presented throughout this chapter are defined using the following equation:

$$G(t) = e^{-(t-4)^2/2\sigma^2}\sin(2\pi f_0 t) \tag{A.2}$$

where f_0 is the modulation frequency of the input signal and σ is the standard deviation of the gaussian in the time domain.

A.1.2 CST Studio Suite® Frequency domain solver

The frequency domain solver in CST Studio Suite® is used to calculate the solution to Maxwells equations for time harmonic signals. This allows for the efficient computing of S-parameters. Additionally, this solver allows for tetrahedral meshing, which is preferable for subwavelength structures as it may adjusted to better match the geometry of the structure. In this thesis, this solver was used in chapter 3 to simulate the linear logic gates, in chapter 4 to extract transmission and reflection coefficients and in chapter 5 to evaluate the PDE solving structure.

When simulating the linear logic gates, series waveguides with a cross-sectional area of 1×1 mm are used, unless stated otherwise. These are constructed using PEC for the metallic plates and vacuum as both the waveguide filling and background materials. The boundary conditions were the same as for the series junction in the transient solver. Likewise, when calculating the transmission and reflection coefficients of the differentiator structures presented in chapter 4, the same structure, background and boundary conditions as the time domain solver were used. However, in this case the mesh was regenerated to use a tetrahedral mesh cell.

Regarding the PDE solving structure presented in chapter 5, the 3×3 and 25×25 waveguide networks were constructed using waveguides with 0.1 mm $(\lambda_0/150)$ of plate separation and a width of 2 mm. Here, magnetic boundary conditions are applied at the top and bottom boundaries of the z-direction, which has the effect of extending the width of the waveguides in this direction. In this example, the waveguides are modelled by blocks of vacuum inserted into a PEC background medium. The metatronic elements are then modelled by replacing sections of this vacuum structure with a dielectric. For this study, the dielectric permittivity is modelled without losses, at the operating frequency. The tetrahedral mesh used for this simulation can be seen in Fig. A.2. Here Fig. A.2A,B shows the mesh at the junctions between waveguides, while Fig. A.2C show the mesh of the metatronic circuit elements.

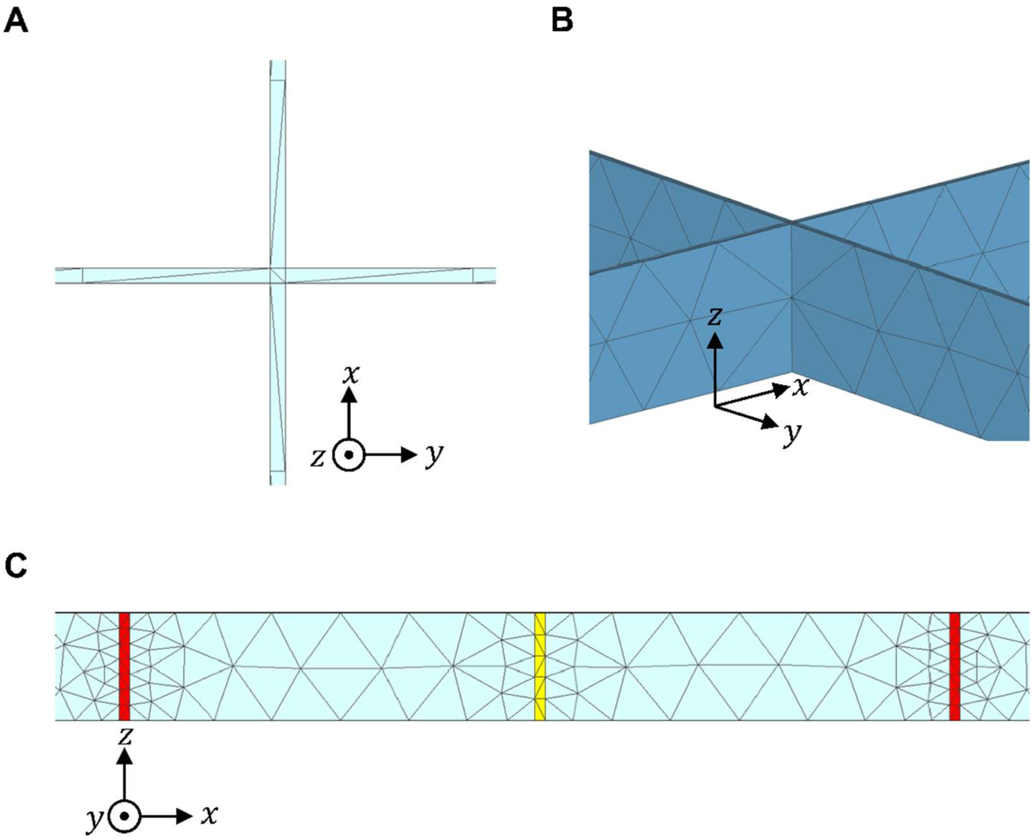

Figure. A.2 Tetrahedral mesh view of the PDE solving structure. **A.**, **B.** The four-way waveguide junction when viewed from above and from the side, respectively. **C.** A portion to the metatronic T-circuit, when viewed from the side.

A.2 COMSOL Multiphysics®

In Fig. 3.13 the time-domain solver from RF module in COMSOL Multiphysics®[209] was used to produce the results for the 8-input TEM pulse director. This method was used as time Transient Solver in CST Studio Suite® requires input ports to be aligned along the cartesian directions, whereas COMSOL Multiphysics does not. This simulation tool is similar to the Transient Solver in CST Studio Suite®, however now maxwells equations are solved in their differential form (Eq. 1.2) using the Backward Differentiation Formula[210]. These results were calculated using the same materials as in the CST simulations, however the separation between waveguide plates was changed to 10 mm so that the pulses would be more easily visible when viewed from above. Scattering boundary conditions were used at the ends of each waveguide, both to excite the input pulses and to absorb the output pulses. In this case, the TEM input pulse has a duration of 0.4 ns and a rise/fall time of 0.08 ns with second derivative smoothing.

A.3 PDE Toolbox from MATLAB®

The PDE Toolbox is a general PDE solving tool capable of calculating solutions to parabolic and hyperbolic PDEs as well as eigenvalue problems via the FEM[211,212]. In this thesis, this tool is exploited to calculate the "analytic" solution to the boundary value problems presented in chapter 5. This is done by solving a PDE of the form.

$$d\frac{\partial u}{\partial t} - \nabla \cdot (c\nabla u) + au = f \tag{A.4}$$

where u is the function to be solved for f is a forcing function and d, c and a are PDE parameters. For the calculations in chapter 5, $d = 0$, $c = 1$, $a = -k^2$ and $f = 0$, except at the boundaries of the simulation domain where f is used to enforce the boundary conditions of the PDE to be solved. The simulation domain was a square region with a size of $(N-1)h \times (M-1)h$ where N, M and h are the number of junctions in the x direction, the number of junctions in the y direction and the step size in simulation space of the PDE solving structure. The results produced by this method are sampled at intervals of h (i.e., sampled at the points which the waveguide junctions are modelling). This is so that a fair comparison may be made between the analytical, numerical, and theoretical results.

Appendix B. Scaling of the Waveguide Network Solving Algorithm

The waveguide network solving algorithm outline in chapter 2, is designed to be a tool which may be exploited to efficiently calculate the S-parameters of complex interconnected networks (as will be presented in later chapters). This means that it is important understand how the run-time of the algorithm scales with the size of the network being modelled. To this end, two investigations were conducted. The first was to study the impact of network size (number of junctions within the network) on run-time for a fully connected network and the second was to repeat this task, now for a locally connected network. In the fully connected network, each junction in the network is connected to each other junction in the network, meaning that for a network of N junctions, each junction has $N - 1$ connections (see Fig. B.1). This network may be unfeasible to construct in reality, however this is an important study as it is the most computationally intensive scaling of the system. On the other hand, in the locally connected network, the number of connections per junction does not scale with the size of the system. In this study, each junction is connected to two other junctions, in this way forming a network which resembles a line. In both networks input and output waveguides are also connected to the first and last junction of the network.

The results of the run-time scaling investigations for the fully-connected and locally-connected networks are presented in Fig. B.1B,D, respectively. Here, the time-scaling of two stages of the algorithm have been investigated 1) the time taken to generate the scattering matrices of each junction and 2) the time taken to calculate the combined scattering matrix of the network after 1) has been completed, shown in the left and right plots of Fig. B.1B,C respectively. Each plot shows the time taken to complete 1) and 2) as a function of the number of junctions in the network. A log scale has been used to represent the data and using the built in curve fitting toolbox in MATLAB®, a linear line of best fit has been fit has been matched to the results. The gradient of this line reveals the scaling power p of the system written in big O notation[213] as $O(N^p)$ where N is the number of junctions in the network. For the fully connected network the scaling power of the matrix generation portion of the algorithm was $p = 1.927$. When calculating the scatting matrix of the total system, it was found that there were two distinct scaling regimes, with the transition occurring at approximately 30 junctions. Below 30 junctions the scaling can be modelled with $p = 1.307$, however above 30 junctions the system is modelled by $p = 5.12$. This can also be seen in the locally connected network, now with $p = 1.205$ and $p = 1.721$ for networks with less than and more than 30 junctions respectively. In both regimes the scaling of the locally connected network is smaller than the fully connected network. This is expected as from Eq. 2.17, the number of calculations required per matrix combination scales with the number of connections between the junctions. The time taken to generate the matrices of the locally connected network is shown in the left panel of Fig. B.1D. This has been shown without a log scale as in this instance, this operation is completed in linear time (i.e. $p = 1$). This is expected, as the size of the individual scattering matrices do not vary with the network size.

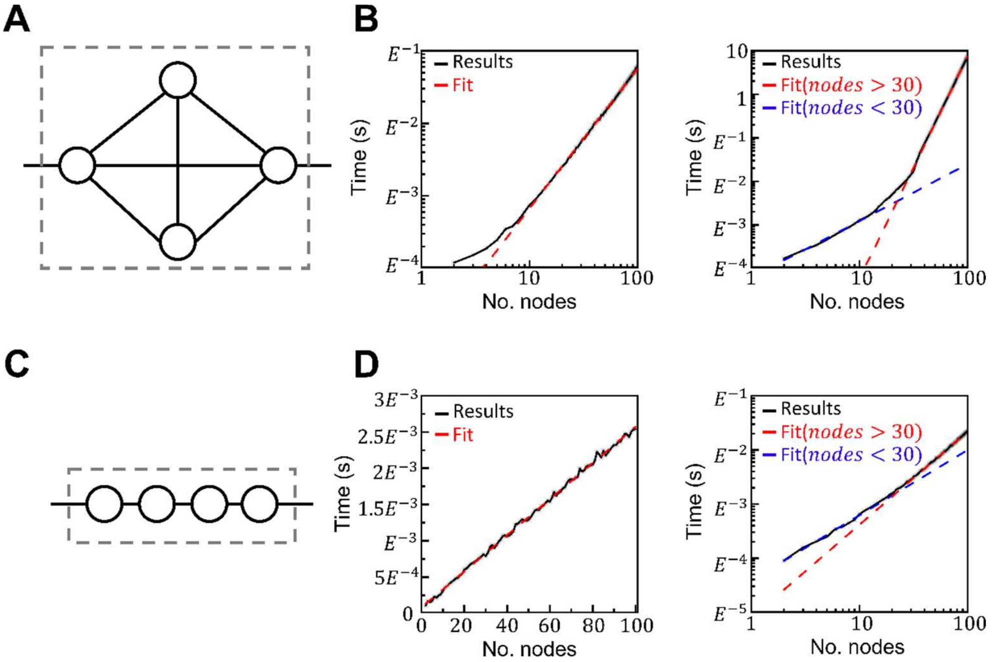

Figure. B.1 Time-scaling of the waveguide solving algorithm for a fully connected and locally connected network. **A, C.** Schematic representation of a fully connected and locally connected network made from four junctions. **B, D.** Time-scaling results for the fully connected and locally connected networks, respectively.

Appendix C. Comparing time to solve between waveguide solving tool and full-wave simulation results.

Chapter 2 detailed the development of a tool which could solve for the scattering parameters of arbitrarily connected waveguide networks. This tool was used to assist in the design of the various structures presented throughout this thesis by providing an alternative solution method to numerical simulation which can be used to corroborate results. It is expected that the waveguide network solving algorithm will be faster than full-wave simulation due to the relative simplicity of the calculations (series of matrix multiplications). However, proving this requires comparison between the time to solve of various waveguide networks (of different sizes and complexities) using both the tool and a full-wave simulation software. This is conceptually difficult due to the generality of the tool meaning networks of any shape, size and number of nodes can be resolved. For instance, this tool can solve for a network of N fully connected nodes (each node is connected to each other), which for large N may not be physically possible to construct. Alternatively, if each node was only connected to two other nodes (the minimum possible number of connections), then the network would essentially be a single waveguide, as is discussed in appendix section B. This would not be a fair comparison as the tool would be doing needless calculations which could instead be replaced by a single multiplication (to account for a change in phase). Instead, to compare the two techniques an $N \times N$ network of equally spaced junctions is used. Here, each junction is connected to it's nearest neighbouring junctions only (up, down, left and right) meaning the complexity of the connections does not grow with the total number of nodes (as it would do in the fully connected case). A schematic representation of this network is presented in Fig. 2.9A.

The time to solve for the scattering parameters (at 1001 frequency samples) of this network when $N = [2,3,4,5,6]$ is presented in Fig. 2.9B. In this case the full-wave simulation software used for comparison is CST Studio Suite®. These results show the total time for this calculation as a function of the total number of junctions within the waveguide network. As can be seen, in all instances the waveguide network solving tool is significantly faster (by orders of magnitude). However, a fairer comparison is to instead consider the scaling of the time to solve. This is as the time to solve for the Full-wave simulation software will also be affected by the choice of connection length. The scaling provides a better comparison as no matter the choice of connection, if doubling the number of nodes doubles the time to solve (i.e. linear scaling) in the full-wave simulation but quadruples the time to solve of the tool (i.e. scaling $O(N^2)$) then full-wave simulation would be faster for large N networks. However, as can be seen in Fig. 2.9A, as well as having a longer time to solve for low N the scaling of the full-wave simulation (gradient of time over junctions in a log-log scale) is significantly larger than the waveguide network solving algorithm, as expected. Additionally, since the full-wave simulation time to solve results have an upward curve, it cannot be simply modelled by $O(N^b)$ scaling where b is the scaling power. For a full model of the scaling, more data-points (simulation results for larger N) would be required. This is a challenging task as at $N = 6$ the time to solve is ~8 hours and expected to rise significantly for $N = 7$ and above. For the purposes of comparison to the waveguide network solving tool, these results indeed demonstrate a significant computational speedup when using the tool, especially for networks with many junctions. A further study of the time-scaling of this tool can be found in appendix section. B

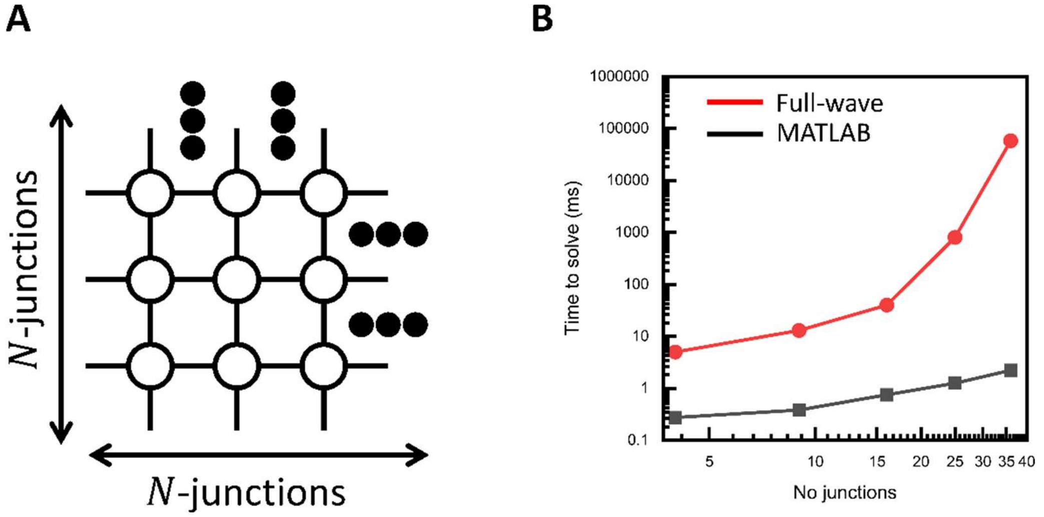

Figure. C.1 Time to solve comparison between algorithm and full-wave simulation results for an $N \times N$ network **A.** Schematic representation of the $N \times N$ network being solved by both the network solving algorithm and full-wave simulation software (CST Studio Suite®). **B.** Time to solve for the full scattering matrix parameters of the $N \times N$ network for $N = [2,3,4,5,6]$. Here the x-axis has been converted to the total number of nodes included in the network to be solved (i.e. N^2).

Appendix D. PDE solution convergence time

Thus far the results presented in this chapter have shown that this technique is capable of producing accurate PDE solutions which are in clear agreement with software-based PDE solutions. This is an important metric for a PDE solver. Another important metric is the convergence time, which is the time taken for a solution to converge within a certain tolerance value. When considering the PDE solving network to reach a steady state solution after the initial excitation of the input signals at the boundary waveguides. To quantify this the following equation is used:

$$Convergence = \frac{d}{dt}\left(\sum_{junctions} |H_z|\right) \tag{5.16}$$

Which is the rate of change of the magnitude of the out-of-plane magnetic field values calculated at the centre of the waveguide junctions. The convergence time t_c is then the time taken for $Convergence$ to approach 0, to within a certain tolerance value (while ignoring the trivial case when all $|H_z| = 0$).

To investigate this, consider the boundary value problem presented in Fig. 5.10. The numerical results presented in Fig. 5.10 were calculated using the frequency domain solver of CST Studio Suite®. To calculate the convergence time of the operation, the same study is repeated, now using the time domain solver. In this study, at time $t = 0$, the various monochromatic 10 GHz input signals required to implement the $g = 1$ boundary conditions are excited at each of the boundary waveguides. This is done simultaneously, save for small delays which are necessary to implement the correct phase difference between the input signals. The out-of-plane magnetic field is then monitored at each junction and used to calculated $Convergence$ using Eq. 5.16. The results of which can be seen in Fig. 5.12A. Here $Convergence$ has been normalized so that the maximum calculated value is 1. In addition to this the out-of-plane H-field values at the centres of two example junctions are presented in Fig. 5.12B. These junctions are located at the top-left corner of the network (left-panel) and at the centre of the network (right-panel). From Fig. 5.12 it can be seen that there is an initial rapid rise in $Convergence$ as the input signals first enter the network and begin to spread throughout. This can also be seen in the field plots in Fig. 5.12B. In this example the maximum

$Convergence$ value occurs at ≈2.2 ns. After this initial peak, the $Convergence$ value beings to reduce as the structure approaches a steady state solution. From Fig. 5.12 it can be seen that for this example this occurs after $t_c \approx 30$ ns. It should be noted that this value of t_c is specific to this waveguide network and if one where to, for instance, change the size or shape of the network, then this study would need to be repeated. However, it is expected that changing the PDE parameters of the network (by controlling the parameters of the dielectric slabs) would not have a significant impact on the convergence time since the dielectric slabs are thin in the direction of wave propagation.

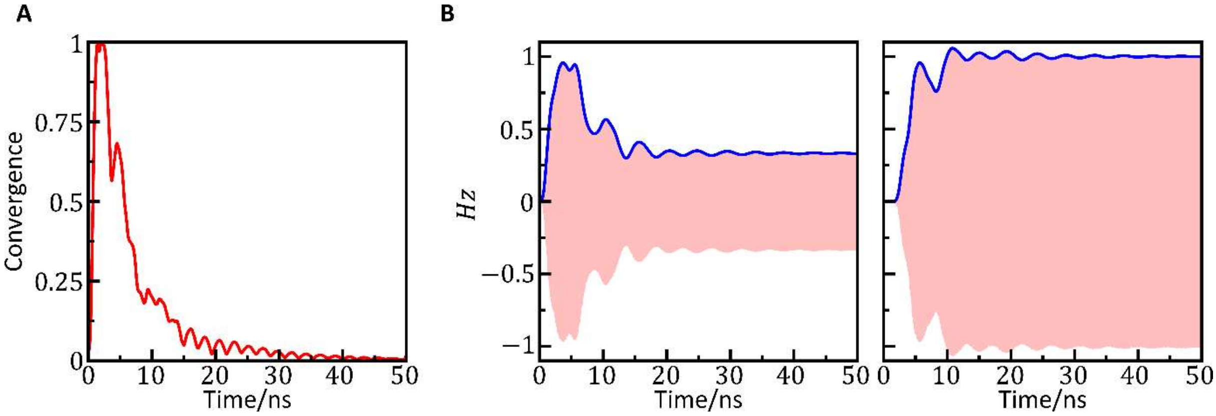

Figure D.1 Convergence time of a 25×25 PDE solving network. **A**. $Convergence$ value over time. **B**. Calculated out-of-plane magnetic field (H_z) values at the centre of junctions located at the top-left (left panel) and centre (right panel) of the waveguide network.

Author Merits and Awards

Journal articles

- **MacDonald, R. G**., Yakovlev, A. & Pacheco-Peña, V. Amplitude-Controlled Electromagnetic Pulse Switching Using Waveguide Junctions for High-Speed Computing Processes. *Adv. Intell. Syst.* **2200137**, 2200137 (2022).
- **MacDonald, R. G**., Yakovlev, A. & Pacheco-Peña, V. Time derivatives via interconnected waveguides. *Sci. Rep.* **13**, 13126 (2023).
- **MacDonald, R. G**., Yakovlev, A. & Pacheco-Peña, V. Solving partial differential equations with waveguide-based metatronic networks. *arXiv* (2023) (*Under Rev.*).

Conferences

- Metamaterials' 2021: 15th International Congress on Artificial Materials for Novel Wave Phenomena
    - Yakovlev, A., **MacDonald, R. G.**, Ventisei, A., Knightley, T. & Riley, J. A. TEM pulse routing and switching via series and parallel interconnected waveguide crossings. (2021).
- AT-AP-RASC 2022: 3rd URSI Atlantic / Asia-Pacific Radio Science Meeting – 2022
    - Yakovlev, A., **MacDonald, R. G.**, Ventisei, A., Knightley, T., Aljuid, W., Rogers, J., Riley, J. A. & Pacheco-Peña, V. From TEM pulse switching to computing with light. (2022)
    - **MacDonald, R. G.**, Yakovlev, A. & Pacheco-Peña, V. Exploiting transmission line theory to calculate temporal derivatives. (2022)
    - **MacDonald, R. G.**, Yakovlev, A. & Pacheco-Peña, V. Exploiting waveguide junctions for the switching of transverse electromagnetic pulses of nonconstant amplitude. (2022)
- Uk Semiconductors 2022
    - **MacDonald, R. G.**, Yakovlev, A. & Pacheco-Peña, V. Computing temporal derivatives with waveguide networks. (2022)
- Metamaterials' 2022: The 16th International Congress on Artificial Materials for Novel Wave Phenomena

  - **MacDonald, R. G.**, Yakovlev, A. & Pacheco-Peña, V. TEM pulse splitting and routing in waveguide networks for decision making processes in computing. (2022)
  - **MacDonald, R. G.**, Yakovlev, A. & Pacheco-Peña, V. Utilizing transmission line techniques for the calculation of temporal derivatives. (2022)
  - Riley, J. A., **MacDonald, R. G.**, Ventisei, A., Knightley, T., Aljuid, W., Rogers, W., Yakovlev, A. & Pacheco-Peña, V. Modelling and computing decision-making processes and temporal derivatives with electromagnetic waves. (2022)
- URSI GASS 2023: 35th URSI General Assembly and Scientific Symposium
  - **MacDonald, R. G.**, Yakovlev, A. & Pacheco-Peña, V. Arbitary order analogue differentiation using transmission line techniques. (2023)
  - Rogers, W., Johnson-Richards, C., **MacDonald, R. G**., Yakovlev, A. & Pacheco-Peña, V. Ideal splitting in rectangular waveguides enabled by evanescent coupling. (2023)
- Metamaterials' 2023: 17th International Congress on Artificial Materials for Novel Wave Phenomena
  - **MacDonald, R. G.**, Yakovlev, A. & Pacheco-Peña, V. Exploiting waveguide networks to calculate solutions of partial differential equations. (2023)
- URSI UK Symposium 2024
  - **MacDonald, R. G.**, Yakovlev, A. & Pacheco-Peña, V. Towards partial differential equation solvers using light-matter interactions. (2024)
- AT-RASC 2024: 4th URSI Atlantic Radio Science Meeting
  - **MacDonald, R. G.**, Yakovlev, A. & Pacheco-Peña, V. Exploiting waveguide-based metatronic circuits for partial differential equation solving. (2024) [Abstract accepted for presentation at the time of submission].

Awards/achievements

- The “Amplitude-Controlled Electromagnetic Pulse Switching Using Waveguide Junctions for High-Speed Computing Processes” journal article was highlighted as editors choice in Advanced Intelligent Systems.
- The “Time derivatives via interconnected waveguides” was in the top 100 (17th) most viewed articles from *scientific reports* in 2023.
- The “Exploiting waveguide networks to calculate solutions of partial differential equations” conference paper was selected as a finalist of the student paper competition at the Metamaterials’ 2023 conference.
- The “Exploiting waveguide networks to calculate solutions of partial differential equations” conference presentation was awarded “Best contribution related to photonics whose first author is a student” during the conference Metamaterials’ 2023. This award was sponsored by Nature Photonics.
- Awarded the “Young Scientist Award” at the conference AT-RASC 2024. At the time of submission this award has been confirmed but not presented.

References

1. Moore, G. E. Cramming More Components Onto Integrated Circuits. *Proceedings of the IEEE* **86**, 82–85 (1998).
2. Dennard, R. *et al.* Design of Ion-Implanted Small MOSFET ' S Dimensions with Very. *IEEE Journal of Solid State Circuits* **9**, 257–268 (1974).
3. Manfrinato, V. R. *et al.* Resolution Limits of Electron-Beam Lithography toward the Atomic Scale. *Nano Lett* **13**, 1555–1558 (2013).
4. Zhang, J.-F. & Ducree, J. Proposition of atomic and close-to-atomic scale manufacturing. *Adv Manuf* (2023) doi:10.1007/s40436-023-00442-4.
5. Rotman, D. We're not prepared for the end of Moore's Law | MIT Technology Review. *MIT Review* https://www.technologyreview.com/2020/02/24/905789/were-not-prepared-for-the-end-of-moores-law/ (2020).
6. Shalf, J. M. & Leland, R. Computing beyond Moore's Law. *Computer (Long Beach Calif)* **48**, 14–23 (2015).
7. Theis, T. N. & Wong, H.-S. P. The End of Moore's Law: A New Beginning for Information Technology. *Comput Sci Eng* **19**, 41–50 (2017).
8. Chatterjee, J. M. O. Y. & Dewangan, S. Bio Computers - Trends & Applications. *International Journal of Advanced Computational Engineering and Networking* **5**, 28–32 (2017).
9. Benenson, Y. Biomolecular computing systems: principles, progress and potential. *Nat Rev Genet* **13**, 455–468 (2012).
10. Akula, B. & Cusick, J. Biological Computing Fundamentals and Futures. 1–7 (2009).
11. Hirohata, A. *et al.* Review on spintronics: Principles and device applications. *J Magn Magn Mater* **509**, 166711 (2020).
12. Finocchio, G. *et al.* The promise of spintronics for unconventional computing. *J Magn Magn Mater* **521**, 167506 (2021).
13. AbuGhanem, M. & Eleuch, H. Two-qubit entangling gates for superconducting quantum computers. *Results Phys* **56**, 107236 (2024).
14. Arute, F. *et al.* Quantum supremacy using a programmable superconducting processor. *Nature* **574**, 505–510 (2019).
15. Gyongyosi, L. & Imre, S. A Survey on quantum computing technology. *Comput Sci Rev* **31**, 51–71 (2019).
16. Bertels, K. *et al.* Quantum Computer Architecture Toward Full-Stack Quantum Accelerators. *IEEE Transactions on Quantum Engineering* **1**, 1–17 (2020).
17. O'Brien, J. L. Optical Quantum Computing. *Science (1979)* **318**, 1567–1570 (2007).

18. Kim, T. *et al.* Progress, Challenges, and Opportunities in Oxide Semiconductor Devices: A Key Building Block for Applications Ranging from Display Backplanes to 3D Integrated Semiconductor Chips. *Advanced Materials* **35**, 1–50 (2023).

19. Shalf, J. The future of computing beyond Moore's Law. *Philosophical Transactions of the Royal Society A: Mathematical, Physical and Engineering Sciences* **378**, 20190061 (2020).

20. Lau, J. H. Recent Advances and Trends in Advanced Packaging. *IEEE Trans Compon Packaging Manuf Technol* **12**, 228–252 (2022).

21. Zangeneh-Nejad, F., Sounas, D. L., Alù, A. & Fleury, R. Analogue computing with metamaterials. *Nat Rev Mater* **6**, 207–225 (2020).

22. Singh, P., Tripathi, D. K., Jaiswal, S. & Dixit, H. K. All-Optical Logic Gates: Designs, Classification, and Comparison. *Advances in Optical Technologies* **2014**, 1–13 (2014).

23. Yakovlev, A. & Pacheco-Peña, V. Enabling High-Speed Computing with Electromagnetic Pulse Switching. *Adv Mater Technol* **5**, 2000796 (2020).

24. Pacheco-Peña, V. & Yakovlev, A. Computing with Square Electromagnetic Pulses. in *Handbook of Unconventional Computing,* (ed. Adamatzky, A.) 465–492 (World Scientific, London, 2021). doi:10.1142/9789811235740_0016.

25. MacDonald, R. G., Yakovlev, A. & Pacheco-Peña, V. Amplitude-Controlled Electromagnetic Pulse Switching Using Waveguide Junctions for High-Speed Computing Processes. *Advanced Intelligent Systems* **2200137**, 2200137 (2022).

26. MacDonald, R. G., Yakovlev, A. & Pacheco-Peña, V. Time derivatives via interconnected waveguides. *Sci Rep* **13**, 13126 (2023).

27. MacDonald, R. G., Yakovlev, A. & Pacheco-Peña, V. Solving partial differential equations with waveguide-based metatronic networks. *arXiv:2401.00861* (2023).

28. Jackson, J. D. *Classical Electrodynamics*. (Wiley, New York, NY, 1999).

29. Moore, R. K. Radio communication in the sea. *IEEE Spectr* **4**, 42–51 (1967).

30. Pozar, D. M. *Microwave Engineering*. (John wiley & sons, Hoboken, NJ, USA, 2011).

31. Kateb, B., Yamamoto, V., Yu, C., Grundfest, W. & Gruen, J. P. Infrared thermal imaging: A review of the literature and case report. *Neuroimage* **47**, T154–T162 (2009).

32. Born, M. *et al. Principles of Optics*. (Cambridge University Press, 1999). doi:10.1017/CBO9781139644181.

33. Silver, S. *Microwave Antenna Theory and Design*. *Electronics and Power* vol. 23 (Institution of Engineering and Technology, 1984).

34. Levy, R., Snyder, R. V. & Matthaei, G. Design of microwave filters. *IEEE Trans Microw Theory Tech* **50**, 783–793 (2002).

35. Pacheco-Peña, V., Beruete, M., Rodríguez-Ulibarri, P. & Engheta, N. On the performance of an ENZ-based sensor using transmission line theory and effective medium approach. *New J Phys* **21**, 043056 (2019).

36. Kaiser, W. & Garrett, C. G. B. Two-photon excitation in CaF2: Eu2+. *Phys Rev Lett* **7**, 229–231 (1961).

37. Murti, Y. V. G. S. & Vijayan, C. *Physics of Nonlinear Optics*. *Physics of Nonlinear Optics* (Springer International Publishing, Cham, 2021). doi:10.1007/978-3-030-73979-9.

38. Wei, J. L., Hamie, A., Giddings, R. P. & Tang, J. M. Semiconductor Optical Amplifier-Enabled Intensity Modulation of Adaptively Modulated Optical OFDM Signals in SMF-Based IMDD Systems. *Journal of Lightwave Technology* **27**, 3678–3688 (2009).

39. Schawlow, A. L. & Townes, C. H. Infrared and Optical Masers. *Physical Review* **112**, 1940–1949 (1958).

40. Hecht, J. A short history of laser development. *Appl Opt* **49**, F99 (2010).

41. Feng, Q. *et al.* Enhanced optical Kerr nonlinearity of graphene/Si hybrid waveguide. *Appl Phys Lett* **114**, (2019).

42. He, B., Yan, S.-B., Wang, J. & Xiao, M. Quantum noise effects with Kerr-nonlinearity enhancement in coupled gain-loss waveguides. *Phys Rev A (Coll Park)* **91**, 053832 (2015).

43. Vukovic, N. *et al.* Ultrafast optical control using the Kerr nonlinearity in hydrogenated amorphous silicon microcylindrical resonators. *Sci Rep* **3**, 2885 (2013).

44. Chen, H. *et al.* Nanoscale Kerr Nonlinearity Enhancement Using Spontaneously Generated Coherence in Plasmonic Nanocavity. *Sci Rep* **5**, 18315 (2015).

45. Djurišić, A. B. & Li, E. H. Modeling the index of refraction of insulating solids with a modified lorentz oscillator model. *Appl Opt* **37**, 5291 (1998).

46. Silaeva, E., Saddier, L. & Colombier, J.-P. Drude-Lorentz Model for Optical Properties of Photoexcited Transition Metals under Electron-Phonon Nonequilibrium. *Applied Sciences* **11**, 9902 (2021).

47. Ordal, M. A., Bell, R. J., Alexander, R. W., Long, L. L. & Querry, M. R. Optical properties of fourteen metals in the infrared and far infrared: Al, Co, Cu, Au, Fe, Pb, Mo, Ni, Pd, Pt, Ag, Ti, V, and W. *Appl Opt* **24**, 4493 (1985).

48. Tao, L. *et al.* Experimental Investigation of the Dielectric Constants of Thin Noble Metallic Films Using a Surface Plasmon Resonance Sensor. *Sensors* **20**, 1505 (2020).

49. Johnson, P. B. & Christy, R. W. Optical Constants of the Noble Metals. *Phys Rev B* **6**, 4370–4379 (1972).

50. Sehmi, H. S., Langbein, W. & Muljarov, E. A. Optimizing the Drude-Lorentz model for material permittivity: Method, program, and examples for gold, silver, and copper. *Phys Rev B* **95**, 115444 (2017).

51. Drude, P. Zur Elektronentheorie der Metalle. *Ann Phys* **306**, 566–613 (1900).

52. Alabastri, A. *et al.* Molding of Plasmonic Resonances in Metallic Nanostructures: Dependence of the Non-Linear Electric Permittivity on System Size and Temperature. *Materials* **6**, 4879–4910 (2013).

53. Kock, W. E. Metal-Lens Antennas. *Proceedings of the IRE* **34**, 828–836 (1946).

54. Brown, J. Artificial dielectrics having refractive indices less than unity. *Proceedings of the IEE - Part IV: Institution Monographs* **100**, 51–62 (1953).

55. Rotman, W. Plasma simulation by artificial dielectrics and parallel-plate media. *IRE Transactions on Antennas and Propagation* **10**, 82–95 (1962).

56. Pendry, J. B., Holden, A. J., Robbins, D. J. & Stewart, W. J. Magnetism from conductors and enhanced nonlinear phenomena. *IEEE Trans Microw Theory Tech* **47**, 2075–2084 (1999).

57. Smith, D. R., Padilla, W. J., Vier, D. C., Nemat-Nasser, S. C. & Schultz, S. Composite Medium with Simultaneously Negative Permeability and Permittivity. *Phys Rev Lett* **84**, 4184–4187 (2000).

58. Ahmadi, A. & Mosallaei, H. All-dielectric metamaterials: double negative behavior and bandwidth-loss improvement. in *2007 IEEE Antennas and Propagation Society International Symposium* 5527–5530 (IEEE, 2007). doi:10.1109/APS.2007.4396800.

59. Alu, A. & Engheta, N. Radiation from a traveling-wave current sheet at the interface between a conventional material and a metamaterial with negative permittivity and permeability. *Microw Opt Technol Lett* **35**, 460–463 (2002).

60. Smith, D. R. & Kroll, N. Negative Refractive Index in Left-Handed Materials. *Phys Rev Lett* **85**, 2933–2936 (2000).

61. Durant, S., Liu, Z., Steele, J. M. & Zhang, X. Theory of the transmission properties of an optical far-field superlens for imaging beyond the diffraction limit. *Journal of the Optical Society of America B* **23**, 2383 (2006).

62. Wegener, M., Dolling, G. & Linden, S. Backward waves moving forward. *Nat Mater* **6**, 475–476 (2007).

63. Pacheco-Peña, V., M. Solís, D. & Engheta, N. Time-varying electromagnetic media: opinion. *Opt Mater Express* **12**, 3829 (2022).

64. Ptitcyn, G., Mirmoosa, M. S. & Tretyakov, S. A. Time-modulated meta-atoms. *Phys Rev Res* **1**, 023014 (2019).

65. Stefanini, L. *et al.* Temporal interfaces by instantaneously varying boundary conditions. *Phys Rev B* **106**, 094312 (2022).

66. Pacheco-Peña, V. & Engheta, N. Temporal aiming. *Light Sci Appl* **9**, 129 (2020).

67. Pacheco-Peña, V. & Engheta, N. Effective medium concept in temporal metamaterials. *Nanophotonics* **9**, 379–391 (2020).

68. Liberal, I., Vázquez-Lozano, J. E. & Pacheco-Peña, V. Quantum antireflection temporal coatings: quantum state frequency shifting and inhibited thermal noise amplification. (2022) doi:https://doi.org/10.48550/arXiv.2208.10089.

69. Collin, Robert. E. *Foundations for Microwave Engineering*. (Wiley-IEEE Press, Hoboken, NJ, USA, 2000).

70. Christopoulos, C. *The Transmission-Line Modeling (TLM) Method in Electromagnetics*. *Synthesis Lectures on Computational Electromagnetics* vol. 1 (Springer International Publishing, Cham, 2006).

71. Quintela, F. R., Redondo, R. C., Melchor, N. R. & Redondo, M. A General Approach to Kirchhoff’s Laws. *IEEE Transactions on Education* **52**, 273–278 (2009).

72. Capmany, J., Pastor, D., Sales, S. & Muriel, M. a. Pulse distortion in optical fibers and waveguides with arbitrary chromatic dispersion. *Journal of the Optical Society of America B* **20**, 2523 (2003).

73. Chandrashekhar, K. & Attimarad, G. V. Mode Patterns of Parallel plates & Rectangular wave guides. *Int J Sci Eng Res* **3**, 1–6 (2012).

74. Della Giovampaola, C. & Engheta, N. Plasmonics without negative dielectrics. *Phys Rev B* **93**, 195152 (2016).

75. Dally, W. J. & Poulton, J. W. *Digital Systems Engineering*. *Digital Systems Engineering* (Cambridge University Press, California, 1998). doi:10.1017/CBO9781139166980.

76. Feigenbaum, E. & Orenstein, M. Perfect 4-way splitting in nano plasmonic X-junctions. *Opt Express* **15**, 17948 (2007).

77. Feigenbaum, E. & Atwater, H. A. Resonant Guided Wave Networks. *Phys Rev Lett* **104**, 147402 (2010).

78. Martin-Sanchez, D., Li, J., Zhang, E. Z., Beard, P. C. & Guggenheim, J. A. ABCD transfer matrix model of Gaussian beam propagation in plano-concave optical microresonators. *Opt Express* **31**, 16523 (2023).

79. Dupraz, K. *et al.* The ABCD matrices for reflection and refraction for any incident angle and surface. *Opt Commun* **443**, 172–176 (2019).

80. Liu, H., Liu, L., Xu, R. & Luan, Z. ABCD matrix for reflection and refraction of Gaussian beams at the surface of a parabola of revolution. *Appl Opt* **44**, 4809 (2005).

81. Hwang, Y., Kim, J.-E. & Park, H. Y. Frequency selective metal-insulator-metal splitters for surface plasmons. *Opt Commun* **284**, 4778–4781 (2011).

82. Burgos, S. P., Lee, H. W., Feigenbaum, E., Briggs, R. M. & Atwater, H. A. Synthesis and Characterization of Plasmonic Resonant Guided Wave Networks. *Nano Lett* **14**, 3284–3292 (2014).

83. Feigenbaum, E. & Atwater, H. A. Dielectric based resonant guided wave networks. *Opt Express* **20**, 10674 (2012).

84. Ventisei, A., Yakovlev, A. & Pacheco-Peña, V. Exploiting Petri Nets for Graphical Modelling of Electromagnetic Pulse Switching Operations. *Adv Theory Simul* **2100429**, 2100429 (2021).

85. Rogers, W., Johnson-Richards, C., Yakovlev, A. & Pacheco-Peña, V. Perfect splitting in rectangular-waveguide junctions for analog computing. *Phys Rev Appl* **21**, 054054 (2024).

86. Zhou, Z. & Li, Y. N -Port Equal/Unequal-Split Power Dividers Using Epsilon-Near-Zero Metamaterials. *IEEE Trans Microw Theory Tech* **69**, 1529–1537 (2021).

87. Zhang, F., Song, K., Fan, M. & Fan, Y. All-Metal-Waveguide Power Divider with High Power-Combining Efficiency. *J Infrared Millim Terahertz Waves* **37**, 258–266 (2016).

88. Engheta, N. Circuits with Light at Nanoscales: Optical Nanocircuits Inspired by Metamaterials. *Science (1979)* **317**, 1698–1702 (2007).

89. Caglayan, H., Hong, S.-H., Edwards, B., Kagan, C. R. & Engheta, N. Near-Infrared Metatronic Nanocircuits by Design. *Phys Rev Lett* **111**, 073904 (2013).

90. Li, Y., Liberal, I., Della Giovampaola, C. & Engheta, N. Waveguide metatronics: Lumped circuitry based on structural dispersion. *Sci Adv* **2**, 1–8 (2016).

91. Engheta, N., Salandrino, A. & Alù, A. Circuit Elements at Optical Frequencies: Nanoinductors, Nanocapacitors, and Nanoresistors. *Phys Rev Lett* **95**, 095504 (2005).

92. Li, Y., Liberal, I. & Engheta, N. Metatronic analogues of the Wheatstone bridge. *Journal of the Optical Society of America B* **33**, A72 (2016).

93. Rashed, A. R. *et al.* Highly-Sensitive Refractive Index Sensing by Near-infrared Metatronic Nanocircuits. *Sci Rep* **8**, 11457 (2018).

94. Alù, A., Young, M. E. & Engheta, N. Design of nanofilters for optical nanocircuits. *Phys Rev B* **77**, 144107 (2008).

95. Qin, X. *et al.* Negative capacitors and inductors enabling wideband waveguide metatronics. *Nat Commun* **14**, 7041 (2023).

96. Li, Y., Liberal, I. & Engheta, N. Dispersion synthesis with multi-ordered metatronic filters. *Opt Express* **25**, 1937 (2017).

97. Sun, W., Qin, X., Li, H., Zhou, Z. & Li, Y. Impedance matching via ultrathin metatronic layer assisted by Smith Chart. *Opt Express* **30**, 25567–25580 (2022).

98. Liu, N. *et al.* Individual Nanoantennas Loaded with Three-Dimensional Optical Nanocircuits. *Nano Lett* **13**, 142–147 (2013).

99. Abbasi, F. & Engheta, N. Roles of epsilon-near-zero (ENZ) and mu-near-zero (MNZ) materials in optical metatronic circuit networks. *Opt Express* **22**, 25109 (2014).

100. Das, S. *Microwave Engineering*. (Oxford University Press, New Delhi, 2014).

101. Ryf, R., Neilson, D. T. & Aksyuk, V. A. MEMS Based Optical Switching. in *Optical Switching* 169–213 (Springer US, Boston, MA, 2006). doi:10.1007/0-387-29159-8_6.

102. Mei, X., Huang, X. G. & Jin, T. A Sub-wavelength Electro-optic Switch Based on Plasmonic T-Shaped Waveguide. *Plasmonics* **6**, 613–618 (2011).

103. Ooi, K. J. A., Chu, H. S., Bai, P. & Ang, L. K. Electro-optical graphene plasmonic logic gates. *Opt Lett* **39**, 1629 (2014).

104. Chen, W. *et al.* Electro-optical logic gates based on graphene–silicon waveguides. *Opt Commun* **372**, 85–90 (2016).

105. Lin, C.-E., Lu, Y.-H., Zhou, M.-T. & Chen, C.-C. Reconfigurable electro-optical logic gates using a 2-layer multilayer perceptron. *Sci Rep* **12**, 14203 (2022).

106. Alizadeh, A. H. & Rashidi, A. Implementation of optical OR and NOR gates using Mach-Zehnder interferometers. *J Phys Commun* **4**, 085014 (2020).

107. Kumar, A., Kumar, S. & Raghuwanshi, S. K. Implementation of XOR/XNOR and AND logic gates by using Mach–Zehnder interferometers. *Optik (Stuttg)* **125**, 5764–5767 (2014).

108. Raghuwanshi, S. K., Kumar, A. & Rahman, A. Implementation of high speed optical universal logic gates using the electro-optic effect-based Mach–Zehnder interferometer structures. *J Mod Opt* **62**, 978–988 (2015).

109. Zhang, W. *et al.* Performing photonic nonlinear computations by linear operations in a high-dimensional space. *Nanophotonics* **12**, 3189–3197 (2023).

110. Webb, R. P., Yang, X., Manning, R. J. & Giller, R. All-optical 40 Gbit⁄s XOR gate with dual ultrafast nonlinear interferometer. *Electron Lett* **41**, 1396 (2005).

111. Chen, X., Yu, Y. & Zhang, X. All-Optical Logic Minterms for Three-Input Demodulated Differential Phase-Shift Keying Signals at 40 Gb/s. *IEEE Photonics Technology Letters* **23**, 118–120 (2011).

112. Chattopadhyay, T. & Roy, J. N. Semiconductor optical amplifier (SOA)-assisted Sagnac switch for designing of all-optical tri-state logic gates. *Optik (Stuttg)* **122**, 1073–1078 (2011).

113. Jae Hun Kim *et al.* All-optical XOR gate using semiconductor optical amplifiers without additional input beam. *IEEE Photonics Technology Letters* **14**, 1436–1438 (2002).

114. Stubkjaer, K. E. Semiconductor optical amplifier-based all-optical gates for high-speed optical processing. *IEEE Journal of Selected Topics in Quantum Electronics* **6**, 1428–1435 (2000).

115. Singh, P., Dixit, H. K., Tripathi, D. K. & Mehra, R. Design and analysis of all-optical inverter using SOA-based Mach–Zehnder interferometer. *Optik (Stuttg)* **124**, 1926–1929 (2013).

116. Singh, P., Tripathi, D. K., Jaiswal, S. & Dixit, H. K. Designs of all-optical buffer and OR gate using SOA-MZI. *Opt Quantum Electron* **46**, 1435–1444 (2014).

117. Kang, I. *et al.* All-optical XOR and XNOR operations at 864 Gb/s using a pair of semiconductor optical amplifier Mach-Zehnder interferometers. *Opt Express* **17**, 19062 (2009).

118. Ye, X., Ye, P. & Zhang, M. All-optical NAND gate using integrated SOA-based Mach–Zehnder interferometer. *Optical Fiber Technology* **12**, 312–316 (2006).

119. Serajmohammadi, S. & Absalan, H. All optical NAND gate based on nonlinear photonic crystal ring resonator. *Information Processing in Agriculture* **3**, 119–123 (2016).

120. Singh, L., Pareek, P., Kumar, G. M. & Revathi, D. A Microscale Numerical Analysis of Ex-OR and Ex-NOR Logic Gates by Using Single Plasmonic MZI. *Plasmonics* **16**, 1127–1136 (2021).

121. Vali-Nasab, A.-M., Mir, A. & Talebzadeh, R. Design and simulation of an all optical full-adder based on photonic crystals. *Opt Quantum Electron* **51**, 161 (2019).

122. Maleki, M. J., Mir, A. & Soroosh, M. Design and analysis of a new compact all-optical full-adder based on photonic crystals. *Optik (Stuttg)* **227**, 166107 (2021).

123. Maleki, M. J., Mir, A. & Soroosh, M. Designing an ultra-fast all-optical full-adder based on nonlinear photonic crystal cavities. *Opt Quantum Electron* **52**, 196 (2020).

124. Lu, C. *et al.* All-optical logic gates and a half-adder based on lithium niobate photonic crystal micro-cavities. *Chinese Optics Letters* **17**, 072301 (2019).

125. Neisy, M., Soroosh, M. & Ansari-Asl, K. All optical half adder based on photonic crystal resonant cavities. *Photonic Network Communications* **35**, 245–250 (2018).

126. Moradi, M., Danaie, M. & Orouji, A. A. Design and analysis of an optical full-adder based on nonlinear photonic crystal ring resonators. *Optik (Stuttg)* **172**, 127–136 (2018).

127. Qian, L. & Caulfield, H. J. What can we do with a linear optical logic gate? *Inf Sci (N Y)* **176**, 3379–3392 (2006).

128. Peng, C. *et al.* Universal Linear-Optical Logic Gate with Maximal Intensity Contrast Ratios. *ACS Photonics* **5**, 1137–1143 (2018).

129. Li, Z., Chen, Z. & Li, B. Optical pulse controlled all-optical logic gates in SiGe/Si multimode interference. *Opt Express* **13**, 1033 (2005).

130. Chen, J. *et al.* Optical logic operations using a meshed Mach-Zehnder interference array. *Opt Laser Technol* **167**, 109703 (2023).

131. Dutta, S. *et al.* Proposal for nanoscale cascaded plasmonic majority gates for non-Boolean computation. *Sci Rep* **7**, 17866 (2017).

132. Birr, T., Zywietz, U., Chhantyal, P., Chichkov, B. N. & Reinhardt, C. Ultrafast surface plasmon-polariton logic gates and half-adder. *Opt Express* **23**, 31755 (2015).

133. Fu, Y. *et al.* All-Optical Logic Gates Based on Nanoscale Plasmonic Slot Waveguides. *Nano Lett* **12**, 5784–5790 (2012).

134. Wei, H., Wang, Z., Tian, X., Käll, M. & Xu, H. Cascaded logic gates in nanophotonic plasmon networks. *Nat Commun* **2**, 387 (2011).

135. Pal, A., Ahmed, M. Z. & Swarnakar, S. An optimized design of all-optical XOR, OR, and NOT gates using plasmonic waveguide. *Opt Quantum Electron* **53**, 84 (2021).

136. He, L., Zhang, W. X. & Zhang, X. D. Topological all-optical logic gates based on two-dimensional photonic crystals. *Opt Express* **27**, 25841 (2019).

137. He, L. *et al.* Topology-Optimized Ultracompact All-Optical Logic Devices on Silicon Photonic Platforms. *ACS Photonics* **9**, 597–604 (2022).

138. Seiradakis, J. H. & Edmunds, M. G. Our current knowledge of the Antikythera Mechanism. *Nat Astron* **2**, 35–42 (2018).

139. Sugden, K. F. A HISTORY OF THE ABACUS. *Account Hist J* **8**, 1–22 (1981).

140. Williams, M. R. From Napier to Lucas: The Use of Napier's Bones in Calculating Instruments. *IEEE Annals of the History of Computing* **5**, 279–296 (1983).

141. Barrell, F. R. The Slide Rule. *The Mathematical Gazette* **2**, 83–91 (1901).

142. Small, J. S. General-purpose electronic analog computing: 1945-1965. *IEEE Annals of the History of Computing* **15**, 8–18 (1993).

143. Hartree, D. R. The Differential Analyser. *Nature* **135**, 940–943 (1935).

144. MacNee, A. B. An Electronic Differential Analyzer. *Proceedings of the IRE* **37**, 1315–1324 (1949).

145. Save, Y. D., Narayanan, H. & Patkar, S. B. Solution of Partial Differential Equations by electrical analogy. *J Comput Sci* **2**, 18–30 (2011).

146. Kron, G. Electric circuit models of partial differential equations. *Electrical Engineering* **67**, 672–684 (1948).

147. Uy, R. F. & Bui, V. P. A metalens-based analog computing system for ultrasonic Fourier transform calculations. *Sci Rep* **12**, 17124 (2022).

148. Abdollahramezani, S., Hemmatyar, O. & Adibi, A. Meta-optics for spatial optical analog computing. *Nanophotonics* **9**, 4075–4095 (2020).

149. Silva, A. *et al.* Performing Mathematical Operations with Metamaterials. *Science (1979)* **343**, 160–163 (2014).

150. Ebrahimi, S. & Dashtdar, M. Quantitative phase imaging based on Fresnel diffraction from a phase plate. *Appl Phys Lett* **115**, (2019).

151. Tanriover, I., Dereshgi, S. A. & Aydin, K. Metasurface enabled broadband all optical edge detection in visible frequencies. *Nat Commun* **14**, 6484 (2023).

152. Emkey, W. & Jack, C. Analysis and evaluation of graded-index fiber lenses. *Journal of Lightwave Technology* **5**, 1156–1164 (1987).

153. Zangeneh-Nejad, F. & Fleury, R. Performing mathematical operations using high-index acoustic metamaterials. *New J Phys* **20**, 073001 (2018).

154. Momeni, A., Rouhi, K. & Fleury, R. Switchable and simultaneous spatiotemporal analog computing with computational graphene-based multilayers. *Carbon N Y* **186**, 599–611 (2022).

155. Wang, Z. *et al.* Single-layer spatial analog meta-processor for imaging processing. *Nat Commun* **13**, 2188 (2022).

156. Hwang, Y., Davis, T. J., Lin, J. & Yuan, X.-C. Plasmonic circuit for second-order spatial differentiation at the subwavelength scale. *Opt Express* **26**, 7368 (2018).

157. Zhu, T. *et al.* Plasmonic computing of spatial differentiation. *Nat Commun* **8**, 15391 (2017).

158. Zhang, J., Ying, Q. & Ruan, Z. Time response of plasmonic spatial differentiators. *Opt Lett* **44**, 4511 (2019).

159. Rajabalipanah, H., Momeni, A., Rahmanzadeh, M., Abdolali, A. & Fleury, R. Parallel wave-based analog computing using metagratings. *Nanophotonics* **11**, 1561–1571 (2022).

160. Dong, Z., Si, J., Yu, X. & Deng, X. Optical spatial differentiator based on subwavelength high-contrast gratings. *Appl Phys Lett* **112**, (2018).

161. Azana, J., Slavik, R., Park, Y. & Kulishov, M. Ultrafast All-Optical Differentiators Based on Fiber Gratings. in *2007 9th International Conference on Transparent Optical Networks* vol. 00 101–104 (IEEE, 2007).

162. Knightley, T., Yakovlev, A. & Pacheco-Peña, V. Neural Network Design of Multilayer Metamaterial for Temporal Differentiation. *Adv Opt Mater* **11**, 2202351 (2023).

163. Zangeneh-Nejad, F., Khavasi, A. & Rejaei, B. Analog optical computing by half-wavelength slabs. *Opt Commun* **407**, 338–343 (2018).

164. Bezus, E. A., Doskolovich, L. L., Bykov, D. A. & Soifer, V. A. Spatial integration and differentiation of optical beams in a slab waveguide by a dielectric ridge supporting high-Q resonances. *Opt Express* **26**, 25156 (2018).

165. Youssefi, A., Zangeneh-Nejad, F., Abdollahramezani, S. & Khavasi, A. Analog computing by Brewster effect. *Opt Lett* **41**, 3467 (2016).

166. Dong, J. *et al.* Compact, flexible and versatile photonic differentiator using silicon Mach-Zehnder interferometers. *Opt Express* **21**, 7014 (2013).

167. Zangeneh-Nejad, F. & Fleury, R. Topological analog signal processing. *Nat Commun* **10**, 2058 (2019).

168. Sol, J., Smith, D. R. & del Hougne, P. Meta-programmable analog differentiator. *Nat Commun* **13**, 1713 (2022).

169. Walther, H. Signal flow graphs. in *Ten Applications of Graph Theory* 187–196 (Springer Netherlands, Dordrecht, 1984). doi:10.1007/978-94-009-7154-7_9.

170. Bapat, R. B. *Graphs and Matrices*. *Graphs and Matrices* (Springer London, London, 2010). doi:10.1007/978-1-84882-981-7.

171. MacDonald, R. G., Yakovlev, A. & Pacheco-Peña, V. Amplitude controlled electromagnetic pulse switching using waveguide junctions for high-speed computing processes. *arXiv:2205.04814* (2022) doi:10.1002/aisy.202200137.

172. Block, D. Digital Electronics. in *SAE Technical Papers* 313–408 (1974). doi:10.4271/740013.

173. Sharma, P. & Kumar, V. D. All Optical Logic Gates Using Hybrid Metal Insulator Metal Plasmonic Waveguide. *IEEE Photonics Technology Letters* **30**, 959–962 (2018).

174. *CMOS, the Ideal Logic Family*. www.fairchildsemi.com (1998).

175. Mohammadi Estakhri, N., Edwards, B. & Engheta, N. Inverse-designed metastructures that solve equations. *Science (1979)* **363**, 1333–1338 (2019).

176. Pors, A., Nielsen, M. G. & Bozhevolnyi, S. I. Analog Computing Using Reflective Plasmonic Metasurfaces. *Nano Lett* **15**, 791–797 (2015).

177. Berger, N. K. *et al.* Temporal differentiation of optical signals using a phase-shifted fiber Bragg grating. *Opt Express* **15**, 371 (2007).

178. Camacho, M., Edwards, B. & Engheta, N. A single inverse-designed photonic structure that performs parallel computing. *Nat Commun* **12**, 1466 (2021).

179. Rodríguez, J. A. *et al.* Inverse Design of Plasma Metamaterial Devices for Optical Computing. *Phys Rev Appl* **16**, 014023 (2021).

180. Li, L. *et al.* Machine-learning reprogrammable metasurface imager. *Nat Commun* **10**, 1082 (2019).

181. Ma, Y. H., Yuan, Y. & Yuan, N. A Novel Method to Design Stub-loaded Microstrip Filters with Arbitrary Passband Based on the Reflection Theory and Monte Carlo Method. *Radioengineering* **27**, 136–146 (2019).

182. Yarman, C. E. Approximating fractional derivative of Faddeeva function, Gaussian function, and Dawson’s integral. *Math Methods Appl Sci* **44**, 8042–8056 (2021).

183. Fornberg, B. Generation of Finite Difference Formulas on Arbitrarily Spaced Grids. *Math Comput* **51**, 699 (1988).

184. Razinskas, G., Biagioni, P. & Hecht, B. Limits of Kirchhoff’s Laws in Plasmonics. *Sci Rep* **8**, 1921 (2018).

185. Sun, S. *et al.* Induced homomorphism: Kirchhoff’s law in photonics. *Nanophotonics* **10**, 1711–1721 (2021).

186. Owolabi, K. M. Riemann-Liouville Fractional Derivative and Application to Model Chaotic Differential Equations. *Progress in Fractional Differentiation and Applications* **4**, 99–110 (2018).

187. Lanczos, C. A Precision Approximation of the Gamma Function. *Journal of the Society for Industrial and Applied Mathematics Series B Numerical Analysis* **1**, 86–96 (1964).

188. Tarasov, V. E. No nonlocality. No fractional derivative. *Commun Nonlinear Sci Numer Simul* **62**, 157–163 (2018).

189. Gosse, L. Redheffer Products and Numerical Approximation of Currents in One-Dimensional Semiconductor Kinetic Models. *Multiscale Modeling & Simulation* **12**, 1533–1560 (2014).

190. Liu, V. On scattering matrices and the Redheffer star product. 21–23 (2013).

191. Tervo, J. *et al.* Efficient Bragg waveguide-grating analysis by quasi-rigorous approach based on Redheffer's star product. *Opt Commun* **198**, 265–272 (2001).

192. Pu, Y., Wang, W., Zhou, J., Wang, Y. & Jia, H. Fractional differential approach to detecting textural features of digital image and its fractional differential filter implementation. *Science in China Series F: Information Sciences* **51**, 1319–1339 (2008).

193. Wu, K., Soci, C., Shum, P. P. & Zheludev, N. I. Computing matrix inversion with optical networks. *Opt Express* **22**, 295 (2014).

194. Tzarouchis, D. C., Mencagli, M. J., Edwards, B. & Engheta, N. Mathematical operations and equation solving with reconfigurable metadevices. *Light Sci Appl* **11**, 263 (2022).

195. Anderson, J. *et al.* Virtualizing a Post-Moore's Law Analog Mesh Processor: The Case of a Photonic PDE Accelerator. *ACM Transactions on Embedded Computing Systems* **22**, 1–26 (2023).

196. Ye, J. *et al.* Reconfigurable application-specific photonic integrated circuit for solving partial differential equations. *Nanophotonics* **13**, 2231–2239 (2024).

197. Miscuglio, M. *et al.* Approximate analog computing with metatronic circuits. *Commun Phys* **4**, 196 (2021).

198. Nandakumaran, A, K. & Datti, P, S. Heat Equation. in *Partial Differential Equations* 216–251 (Cambridge University Press, 2020). doi:10.1017/9781108839808.009.

199. Li, Y. & Engheta, N. Microwave analogues of multi-ordered metatronic filters with waveguide metamaterials. in *2016 URSI Asia-Pacific Radio Science Conference (URSI AP-RASC)* 530–533 (IEEE, 2016). doi:10.1109/URSIAP-RASC.2016.7601273.

200. Marburg, S. Discretization Requirements: How many Elements per Wavelength are Necessary? in *Computational Acoustics of Noise Propagation in Fluids - Finite and Boundary Element Methods* 309–332 (Springer Berlin Heidelberg, Berlin, Heidelberg, 2008). doi:10.1007/978-3-540-77448-8_12.

201. Teperik, T. V., Archambault, A., Marquier, F. & Greffet, J. J. Huygens-Fresnel principle for surface plasmons. *Opt Express* **17**, 17483 (2009).

202. Kapralos, B., Jenkin, M. & Milios, E. Acoustical diffraction modeling utilizing the huygens-fresnel principle. in *IREE International Worksho on Haptic Audio Visual Environments and their Applications, 2005.* vol. 2005 39–44 (IEEE, 2005).

203. Cendes, Z. & Shenton, D. Adaptive mesh refinement in the finite element computation of magnetic fields. *IEEE Trans Magn* **21**, 1811–1816 (1985).

204. Burstein, L. *PDE Toolbox Primer for Engineering Applications with MATLAB® Basics*. (CRC Press, Boca Raton, 2022). doi:10.1201/9781003200352.

205. Basu, U. Explicit finite element perfectly matched layer for transient three-dimensional elastic waves. *Int J Numer Methods Eng* **77**, 151–176 (2009).

206. Liebmann, G. Solution of Partial Differential Equations with a Resistance Network Analogue. *British Journal of Applied Physics* **1**, 92–103 (1950).

207. Weiland, T. Finite Integration Method and Discrete Electromagnetism. in 183–198 (2003). doi:10.1007/978-3-642-55745-3_12.

208. Shampine, L. F. Stability of the leapfrog/midpoint method. *Appl Math Comput* **208**, 293–298 (2009).

209. RF module user guide v6.0. 1–270 https://www.comsol.com/rf-module (2021).

210. Stewart, K. A model for stability of the semi-implicit backward differentiation formulas. *J Comput Appl Math* **33**, 245–259 (1990).

211. Kwon, Y. W. & Bang, H. *The Finite Element Method Using MATLAB*. (CRC Press, 2018). doi:10.1201/9781315275949.

212. Bofang, Z. *The Finite Element Method*. (Wiley, 2018). doi:10.1002/9781119107323.

213. Chivers, I. & Sleightholme, J. An Introduction to Algorithms and the Big O Notation. in *Introduction to Programming with Fortran* 359–364 (Springer International Publishing, Cham, 2015). doi:10.1007/978-3-319-17701-4_23.